Numerical modelling of the coupling of thermal and photoelectric effects for the photovoltaic modules under low concentration

Marko Pavlov

NNT : 2016SACLS361

These de Doctorat

de

l'Universite Paris-Saclay

preparee a

l'Universite Paris-Sud

ÉCOLE DOCTORALE N°579

Sciences mécaniques et énergétiques, matériaux et géosciences

Spécialité de doctorat : Énergétique

Par

M. Marko Pavlov

Modélisation numérique du couplage thermique-photoélectrique pour des modules photovoltaïques sous faible concentration

Thèse présentée et soutenue à Orsay, le 25 octobre 2016 :

Composition du Jury :

M. Pere Roca i Cabarrocas, Directeur de Recherche, École Polytechnique, Président
M. Philippe Blanc, Directeur de Recherche, MINES ParisTech, Rapporteur
M. Daniel Lincot, Directeur de Recherche, IPVF, Rapporteur
M. Radovan Kopecek, Deputy Chairman, ISC Konstanz, Allemagne, Examinateur
Mme Anne Migan-Dubois, Maître de Conférences, UPMC, Examinateur
M. Michel Pons, Directeur de Recherche, CNRS, Directeur de thèse
M. Vincent Bourdin, Ingénieur de Recherche, CNRS, Invité

Executive Summary

(See Appendix A for a summary in French)

The "Aleph" project (Amélioration de l'Efficacité Photovoltaïque) was inspired by the design constraints of conventional horizontal-plane photovoltaic (PV) installations, such as rooftop installations and large-scale solar farms installed in the field. In a typical installation, the ground coverage ratio (the ratio between the PV cell and ground surfaces) is limited by the need to minimize shading periods which occur in the morning and evening periods. The resulting system is of a relatively low angle of inclination of the PV modules (typically 10° less than the latitude) and an inter-row spacing equal to 2-5 times the module height. This arrangement results in the inter-row space being illuminated during the periods of highest solar irradiation (around solar noon) without contributing to electricity production. The Aleph project aims to explore the benefit of adding inter-row planar reflectors to increase the system yield, and define clear rules for optimal settings of such systems in a given location and under a given climate.

Existing literature shows that the use of planar reflectors is an already established technique for increasing the solar flux incident on a collector. Various studies have been performed for estimating the increase in irradiation from a given collector-reflector system geometry, most frequently focusing on solar thermal systems. However, very few extensive studies have been carried out on planar reflector-equipped PV systems. Existing studies rarely involve both numerical and experimental parts or test more than one PV module technology in parallel.

This work combines experiments on PV module behavior in an outdoor environment on the SIRTA (Site Instrumental de Recherche par Télédétection Atmosphérique) meteorology platform (Palaiseau, France, 48.71°N, 2.21°E) and a multiphysics numerical model used to simulate the system behaviour considering all the important physical phenomena (notably the optical, photoelectric, and thermal effects). Two prominent PV technologies are tested for performance with this type of system: hydrogenated amorphous silicon (*a*-Si:H) and polycrystalline silicon (*p*-Si). The experimental data show significant gains in produced energy brought by the reflectors, and highlight the advantage of *a*-Si:H modules compared to *p*-Si modules. The model is built in a modular way, allowing for testing of several modelling approaches of a given physical phenomenon (e.g. analytical vs. stochastic optical model). Some of the highlights of the modelling work include a Monte-Carlo

ray-tracing optical model and a cell-level photo-electric model. The proposed integrated model is calibrated with outdoor measurements using an evolutionary algorithm. Once calibrated, the model demonstrates good performance in predicting the module power output as a function of atmospheric and irradiance data.

Several model applications are demonstrated through case studies, such as designing for a specific reflector performance, evaluating achievable gains under different climates, and evaluating the impact of string mismatch.

Acknowledgements

The first acknowledgements go to the SOLEMS company and the LABEX LaSIPS for their kind contributions of financial and material means, allowing for the successful construction and installation of the experiment. Thank you ED SMEMAG for having given me the opportunity to pursue my thesis.

I would like to thank my immediate supervisors − Michel Pons (thesis director), Anne Migan-Dubois, and Vincent Bourdin − for providing outstanding guidance throughout my dissertation. They dedicated their time for regular and spontaneous meetings where they shared their individual knowledge, experiences, and perspectives to point me in the right direction. Working with these great people made the doctoral work a wonderful experience.

I wish to thank the following individuals for their kind contributions to the project: Jordi Badosa, Martial Haeffelin, Alexandre Jaffré, Christophe Spiesser, Thomas Mambrini, Emeric Tapachez, Paul Narchi, Christophe Longeaud, Lionel Mathelin, Aurore Brézard Oudot, Anne Labouret, and others who I may have omitted. Thank you everyone in Mines ParisTech for the solar training and your kind advice.

I am thankful to all the staff at the LIMSI, the GeePs, and the LMD, for providing excellent administrative, informatics and other services allowing for a smooth execution of the thesis including the presentation of obtained results in numerous conferences.

Last but not least, I wish to thank my dear family and friends for their continuous support throughout this endeavour.

THIS PAGE INTENTIONALLY LEFT BLANK

Contents

Nomenclature

a	Fraction of ohmic current involved in avalanche breakdown	–
a-Si:H	Amorphous silicon (hydrogenated)	–
A	Area	m^2
AM	Air mass	–
AOD	Aerosol optical depth	–
b	Vertical distance between the ground and the highest point of the system	m
BHI	Beam (direct) horizontal irradiance	W/m^2
BNI	Beam (direct) normal irradiance	W/m^2
BPD	Bypass diode	–
C	Concentration factor	–
c-Si	Crystalline silicon	–
d_i	Thickness of the i-layer of a PIN semiconductor	cm
D	Inter-row spacing	m
DHI	Diffuse horizontal irradiance	W/m^2
E	Incident solar flux	W/m^2
EoT	Equation of time	min
F	View factor	–
FF	Fill factor	–
FOA	Frontal obstruction angle	°
GHI	Global horizontal irradiance	W/m^2
H	Solar time	h
H_l	Local time	h
ΔH_L	Difference between local time and UTC	h
ΔH_G	Difference between local time and the Greenwich Mean Time (4 min per degree East from reference meridian)	h
I	Current	A
I_0	Dark saturation current	A
I_{SC}	Short-circuit current	A
I_{MPP}	Current at the maximum power point	A
I_{phot}	Photogenerated current	A
I_{rec}	Recombination current	A
J	Day of the year (1 on January 1st)	–
J'	1 on 1.1.2013, 366 on 1.1.2014, etc. up to 1.1.2023	–
J_0	Dark saturation current density	A/cm^2
k	Boltzmann's constant	J/K
k_D	Ratio of diffuse to global horizontal irradiance	–
L	PV-module height	m

L'	Reflector height	m
m	Avalanche breakdown exponent	–
n	Diode ideality factor	–
P	Power	W
P_{MPP}	Power at the maximum power point	W
p-Si	Polycrystalline silicon	–
q	Charge of an electron	C
R_S	Series resistance	Ω
R_{SH}	Shunt (parallel) resistance	Ω
s	Inclination angle of the PV-module	°
s'	Inclination angle of the reflector	°
T	Temperature	°C
V	Voltage	V
V_{bi}	Built-in voltage	V
V_{br}	Breakdown voltage	V
V_j	Junction voltage	V
V_{OC}	Open-circuit voltage	V
V_{MPP}	Voltage at the maximum power point	V
w	Vertical distance to the point marking the useful zone of the reflector	m
WS	Wind speed	m/s
y	Vertical distance to the point marking the shaded zone	m
z	Vertical distance to the point marking the highlighted zone	m

Greek symbols

α	Solar elevation angle (solar altitude)	°
α_{Isc}	I_{SC} temperature coefficient	°C $^{-1}$
β	Evans efficiency temperature coefficient	°C $^{-1}$
γ	Evans efficiency irradiance coefficient	–
γ_0	Azimuth angle of a surface (orientation)	°
γ_S	Azimuth angle of the Sun	°
δ	Declination angle	°
η	Conversion efficiency	–
θ	PV-module angle of incidence	°
θ'	Reflector angle of incidence	°
θ"	PV-module angle of incidence after reflection	°
λ	Wavelength	nm
λ_g	Latitude	°
ρ	Reflectance of the reflector	%
σ	Standard deviation	(any)
$\mu\tau$	Effective mobility-lifetime product	cm^2/V
τ	Transmittance of the front glass of the module	%
ϕ	Solar flux	W/m^2
ϕ_g	Longitude	°
ω	Hour angle	°

Subscripts and superscripts

a	Air
amb	Ambient
br	Breakdown
B	Beam irradiance
D	Diffuse irradiance
eff	Effective
exp	Experimental
cal	Calculated
grnd	Ground
loc	Localised
M	Module
MPP	Maximum power point
phot	Photogenerated
POA	Plane of array (plane of PV cells)
ref	Reflector

Chapter 1

Introduction

Photovoltaic (PV) systems, which convert sunlight directly into electricity, have the potential to provide a significant portion of the energy mix in supplying an ever-increasing global energy demand [1] (see Fig. 1-1a).

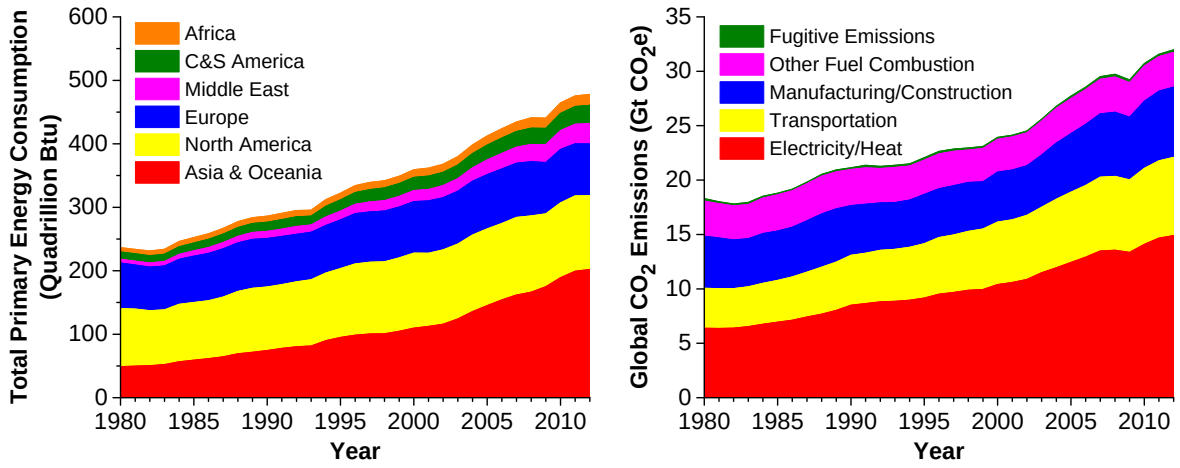

(a) Global energy demand

(b) Energy-related CO_2 emissions

Figure 1-1: (a) Global energy demand by continent. Source of data: U.S. Energy Information Administration, 2016 [1], (b) Absolute energy-related CO_2 emissions, by sector. Source of data: World Resources Institute, 2015 [2]

Figure 1-1b presents the global energy-related CO_2 emissions, by subsector [2]. The combined electricity and heat production is the highest contributor to energy-related CO_2 emissions due to the widespread use of fossil fuels for their generation. A recent report from the Intergovernmental Panel on Climate Change estimated that this component accounts for 25% of total CO_2 emissions [3]. An advantage of PV electricity generation is that it does not produce greenhouse gas (GHG) emissions during operation.

Although the PV effect was first observed in the 19th century, it was not until the 1950s and 1960s that solar cells found practical use as electricity generators, taking advantage of silicon semiconductor technology. Today, a range of PV technologies are available on the market and many other are under development in laboratories (see Appendix B for

a graph of best research-cell efficiencies maintained by NREL).

Figures 1-2 and 1-3 present the recent trends in the global cumulative and annual installed PV capacities, respectively. The global PV cumulative installed capacity in 2015 was over 229 GW, with over 50 GW installed that same year. Europe has historically possessed, and still is associated with the highest cumulative PV installed capacity. Until 2011, Europe has also been the leader in annual capacity installations, after which it saw a declining trend over the years. Today's annual installations are dominated by the APAC (Asia-Pacific) countries and China.

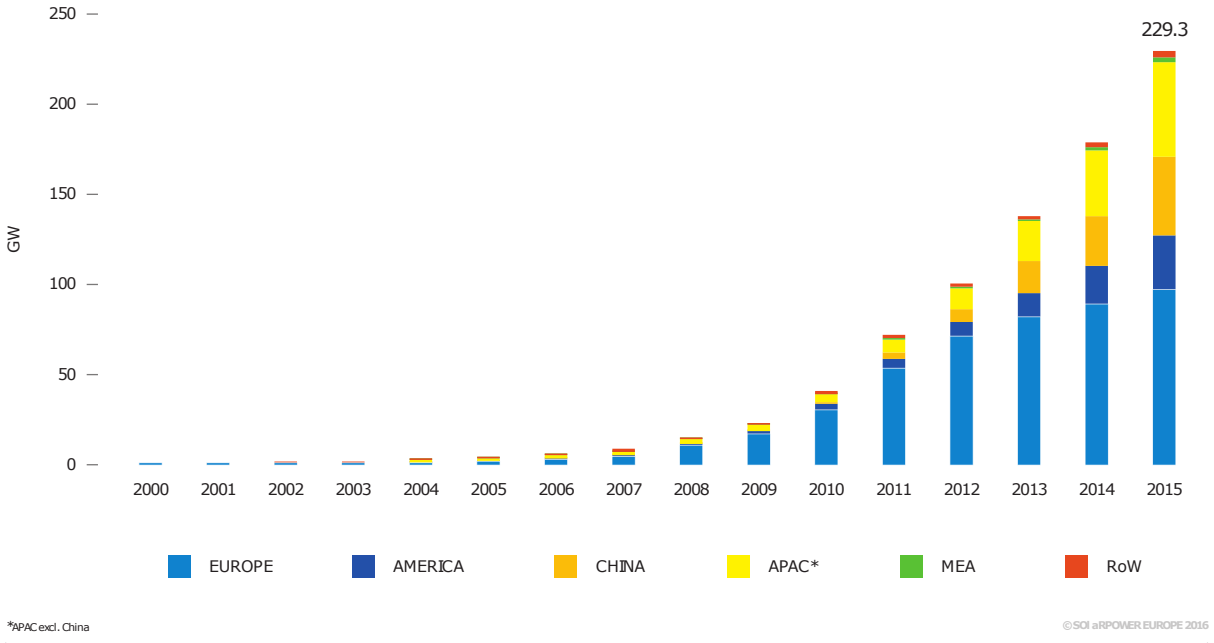

Figure 1-2: Evolution of global cumulative PV installed capacity 2000-2015 (GW). Source: SolarPower Europe, 2016 [4]

Figure 1-4 illustrates the total (finite) energy potential of non-renewable energy sources (4 spheres on the right-hand side) present on planet Earth, and the annual energy potential of renewable energy sources (spheres in the middle). To achieve a sense of scale, the 2015 annual global energy consumption (18.4 TW-yr) is included in the figure. Assuming no growth in the energy demand, it could be sustained with the available fossil fuels for another 100 years. With a constantly increasing global energy demand however, fossil fuels will not sustain the global energy needs in this time-frame, and upon declined availability resources will become more costly. As seen in the figure, solar energy is the most substantial energy source, being several orders of magnitude greater than others, and over 1000 times greater than the global energy demand. Solar energy, being clean, renewable and distributed over the globe, is the best candidate for satisfying the energy demand of tomorrow.

Despite this potential, solar energy is one of the least utilized energy sources for electricity production, as evident in Figure 1-5. Solar PV accounts for less than 1%

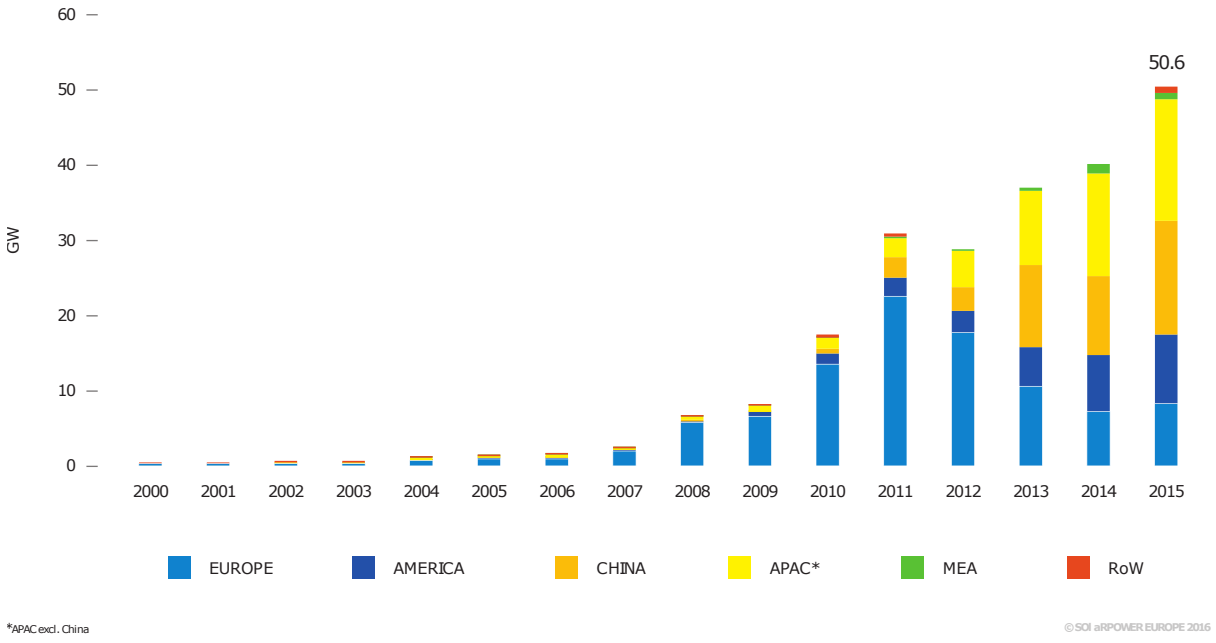

Figure 1-3: Evolution of the global annual PV installed capacity 2000-2015 (GW). Source: SolarPower Europe, 2016 [4]

fuel share in the global electricity production. The small share of solar energy can be attributed to the high cost per unit of solar generated energy as compared to other sources (e.g. fossil fuel-derived and nuclear energy).

The point at which PV technologies become economically competitive (without government subsidy) with the energy sources currently used to power the electricity grid is termed "grid parity" of PV. Grid parity depends on many factors, and is reached at different points in time across different countries (it even varies within countries in some cases). For example, it will greatly depend on the retail price of electricity in that country, the amount of annual insolation the region receives, and the efficiency of sunlight conversion to electricity.

Fig. 1-6 presents grid parity estimates for Europe [7]. The movement of the grid-parity frontier to the left, encompassing more and more countries, is associated with the cost reductions of PV generated electricity resulting from technological advances and economies of scale. According to the study, the French industrial sector should reach grid parity by 2020. Despite the trend of decreasing installed cost of PV, this form of energy often remains more expensive compared to conventional sources, limiting its deployment. The cost of the modules accounts for a big part of the total installed cost of the system (for crystalline silicon (c-Si)-based PV technologies it is around one half of the total installed cost [8]). Independently of the module cost, the cost of PV-generated electricity is inversely proportional to the yield of the PV system. Recognising this, a potential method for decreasing the cost of PV electricity is a more efficient use of the PV modules. For example, if adding mirrors to the system increases the capital investment

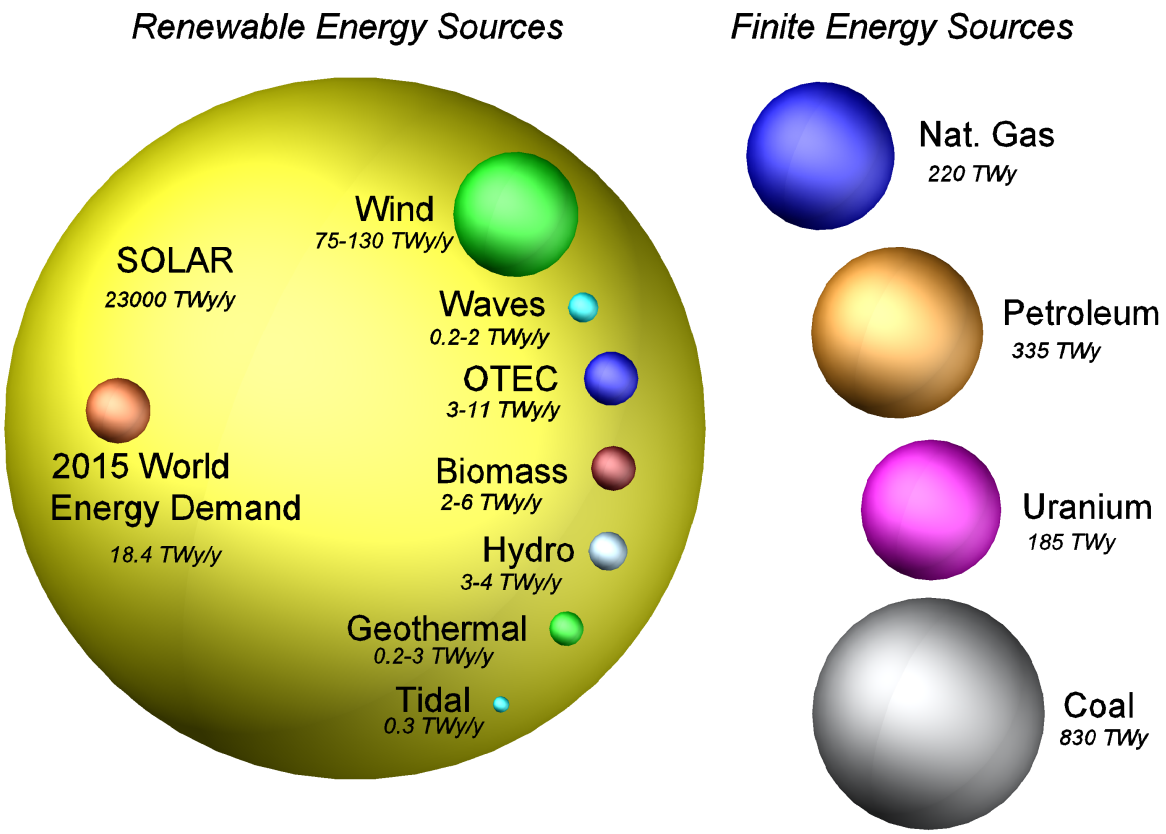

Figure 1-4: (left, orange) 2015 world energy use in TW-year/year, (center) renewable energy sources, shown in annual potential (TW-year/year), and (right) finite energy resources representing total recoverable reserves (TW-year). The solar resource over 1000 times greater than the world energy demand. Source of data: R. Perez, 2015 [5]

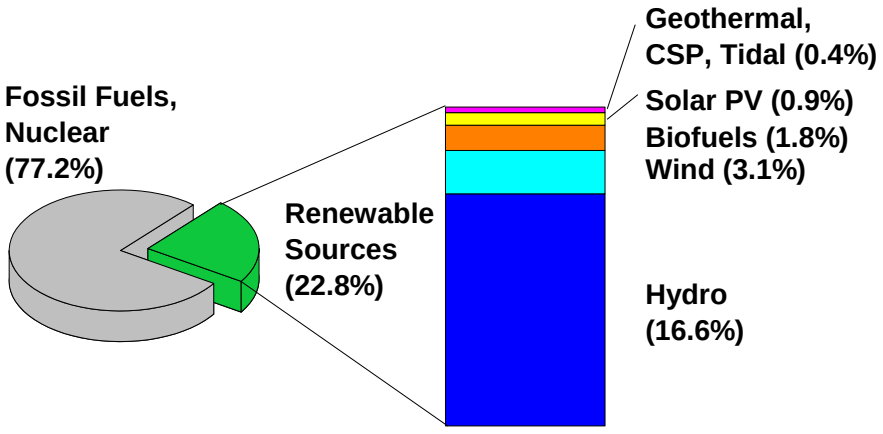

Figure 1-5: 2014 estimated fuel shares of global electricity production. Source of data: Ren21, 2016 [6]

by 5% but results in a 30% increase in electricity production, the cost per unit of energy is reduced by more than 19%.

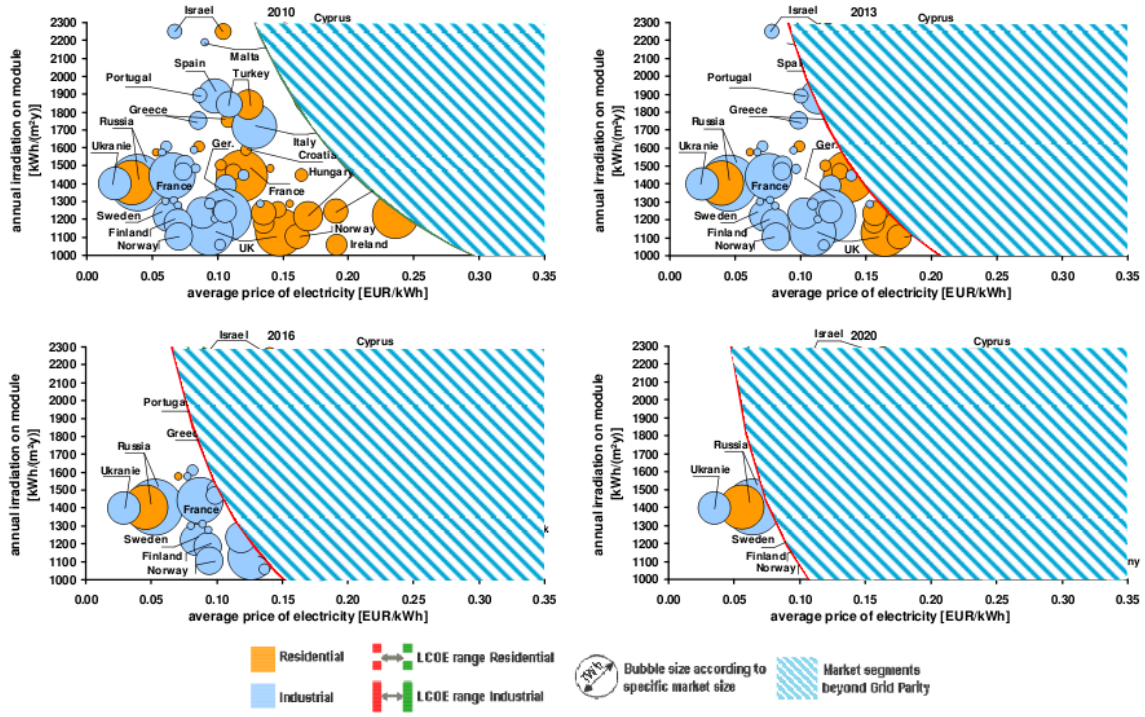

Figure 1-6: Grid-parity analysis for Europe in 2010, 2013, 2016 and 2020, showing the time at which PV becomes economically competitive in different countries. The movement of the grid-parity frontier to the left is associated with the cost reductions of PV generated electricity resulting from technological advances and economies of scale. Source: Breyer and Gerlach, 2010 [7]

1.1 State of the Art: Solar Concentrator Systems

The idea behind achieving efficiency gains through concentrating incoming solar radiation has been explored in great detail starting in the second half of the 20th century [9]. Today, several different approaches exist in increasing electrical yield through concentration. The research on solar concentrators is mainly divided into three categories: high, medium, and low concentration systems.

High concentration systems typically refer to systems with concentration ratios from 100 to 1000. Due to the small acceptance angles, it is necessary for the systems to have precise two-axis tracking of the Sun to achieve such high concentrations. This certainly increases the capital and operating costs of the system. The high flux that is generated by the concentrators can be used to generate very high temperatures. At these temperatures, it is possible to generate electricity in a number of ways, e.g. using steam turbines or sterling cycles. If the concentrator is used to concentrate the irradiation onto a photovoltaic cell (i.e. high-concentration PV, or HCPV), the cell can be extremely small due to the small spot size. However, the cell must be designed for concentrator applications due to the high intensities and therefore high photogenerated currents. To

avoid permanent damage to the cells, they must be actively cooled (convective heat transfer to a moving fluid)[10]. This increases capital and operating costs of the system, although the levelised cost of electricity can be reduced if the heat is recovered and used to generate electricity. High concentrations are generally obtained with parabolic dishes [11] or lenses [12, 13].

Fresnel lenses present an effective means of achieving high concentrations as they use significantly less material compared to conventional lenses (see Fig. 1-7). With the improvements of lens material since the invention of the Fresnel lenses in the early 19th century (particularly polymethylmetacrylate (PMMA) which has a much higher transmissivity than glass), interest in Fresnel lenses for concentrated PV applications entered a rising trend in the latter half of the 20th century [9]. At the beginning of the

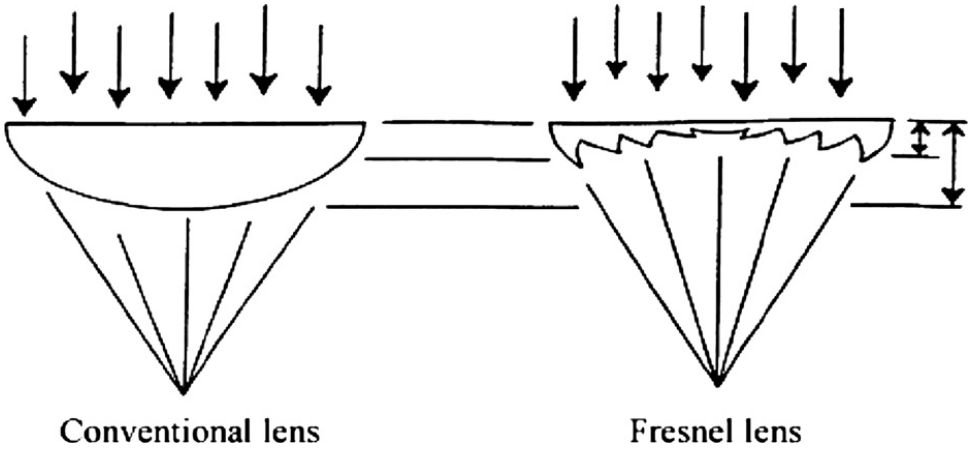

Figure 1-7: Conventional lens and Fresnel lens. The advantage of Fresnel lens is a lower material consumption. Source: Sierra and Vazquez, 2005 [14]

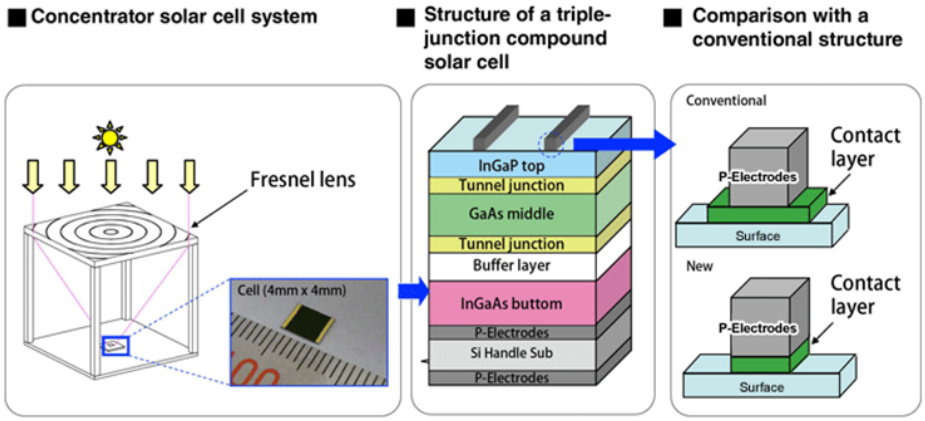

Figure 1-8: Sharp Concentrator solar cell system, operating at 44.4% efficiency. Source: Sharp, 2013 [15]

thesis, the world's highest conversion efficiency of 44.4% was held by a concentrator solar cell produced by SHARP [15, 16] (see Appendix B for the best research-cell efficiencies

graph by NREL). As seen in Figure 1-8, the system essentially relies on the Fresnel lens and a high performance triple-junction solar cell optimised for high concentration. The concentrator system achieves a light-concentrating magnification of 302x [15]. At the time of writing, the record conversion efficiency of 46% is held by Fraunhofer Institute, with a four-junction concentrator solar cell and 508x concentration.

Medium concentration photovoltaic (MCPV) systems refer to systems concentrating light 10-100 times. In this case, only single-axis tracking is required [10]. The existing systems are based on parabolic reflectors [17, 18] (see 1-9a and 1-9b) and Fresnel lenses [19]. The reflectors used are typically translationally symmetric (e.g. trough shaped), whose production may require expensive manufacturing techniques resulting in increased capital costs. Medium concentration systems generally require at least passive cooling (e.g. heat sinks) [10], increasing capital costs.

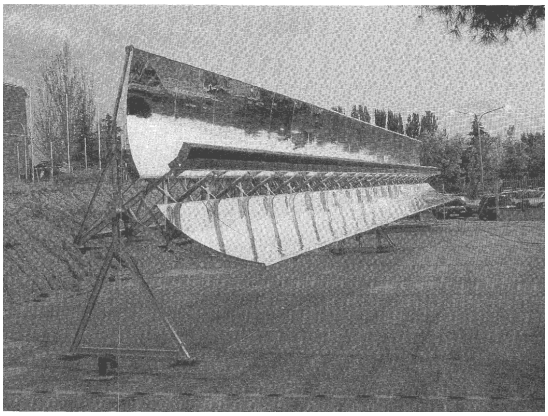

(a) EUCLIDES prototype

(b) CHAPS prototype

Figure 1-9: (a) EUCLIDES prototype [17]: PV installation including a 24 m long reflective parabolic trough with 1-axis tracking, and modules consisting of 12 BP Solar SATURN concentrator cells. Cooling is achieved passively using a lightweight aluminum finned heat sink. The system achieves concentration ratios of up to 32x. (b) CHAPS prototype [18]: PV/T installation including a 15 m long reflective parabolic trough with 1-axis tracking, and ANU monocrystalline concentrator cells designed to have a low internal series resistance. The working fluid is water mixed with anti-freeze and anti-corrosive additives, which serves the purpose of cooling the cells and collecting thermal energy. The system achieves concentration ratios of up to 37x (excluding the shading due to the receiver).

Fig. 1-9 shows two examples of MCPV systems: the EUCLIDES prototype [17], relying on passive heat sinks, and the CHAPS prototype [18], relying on a working fluid to cool the cells and collect thermal energy. While the two prototypes exhibit similar concentration ratios, the CHAPS system is more likely to have a higher combined thermal and electrical efficiency due to the exploitation of the thermal energy collected by the working fluid. The corresponding authors report that under typical operating conditions, the thermal efficiency of around 58% and the electrical efficiency of about 11% result in

a combined efficiency of 69% (the PV cells in questions are rated as 20% efficient under 25 °C and 30x concentration).

Low concentration photovoltaic (LCPV) systems achieve concentration ratios of 1 to 10. Due to the low factors of concentration, these systems are often constructed stationary to remove the dependance on moving parts. Capital and operating costs are therefore reduced compared to systems relying on tracking. Another benefit of the low concentration factor is that it allows the use of standard PV cells made for non-concentrating applications [20]. This is very important, since standard cells are more likely to be mass-produced and therefore drop in price due to economies of scale. Most LCPV systems are based on compound parabolic concentrators (CPC) [10, 21–23] and V-troughs [24–29]. Cooling can be used to increase cell efficiency, but in the case of low concentrations of just several suns (e.g. with planar reflectors) it can be fully omitted [20].

The use of planar reflectors is an established technique for increasing the solar flux incident on a collector, and various studies have been performed for estimating the increase in irradiation from a given collector-reflector system geometry [8, 20, 30–60].

Ronnelid et al. [47] performed a theoretical study of the planar reflector system. For a latitude of 60° N and a specular reflector with a reflectivity of 0.8, a gain in annual output from *a*-Si:H PV modules of up to 25% was predicted. Matsushima et al. [41] explored the benefit of adding booster reflectors by placing the reflector at a 90° angle with a *c*-Si PV module and varying the inclination of the assembly. With a latitude of about 35° N (Tokyo, Japan) and a specular reflector with a reflectance of 0.95, a gain of 50% in produced electricity was estimated. Andrews et al. [20] experimentally tested the PV-booster system over a year. For the latitude of 44° N (Kingston, Canada), a specular reflector with a reflectance of 0.90 and a *c*-Si module, a gain of 45% of produced energy was estimated based on I_{SC} measurements. Pavlovic and Kostic [55] have performed a geometrical optimisation of a flat plate solar collector with four adjacent reflector surfaces. Tina and Ventura [56] developed an integrated model of a PV+Reflector installation and validated it with experimental measurements. For the latitude of 37.5° N, a specular reflector with a reflectance of 0.85 and a *mc*-Si module, a maximum monthly gain of 34% is predicted.

The United States-based company tenKsolar has demonstrated the concept of the planar reflector-equipped PV-system in the industry, and currently offers the service of installing it on rooftops or in the field [61] (see Fig. 1-10). The company 3M from the U.S. [62] specialises in optimising reflector films for a given solar application, and is the direct supplier of reflectors to tenKsolar. For example, they offer reflectors which reduce heating or ageing of PV modules by only reflecting selected wavelengths of light.

It should be noted that the PV module and cell efficiencies are certified at standard

Figure 1-10: A tenKsolar system. Source: TenKsolar, 2013 [61]

conditions, which assume an operating temperature of 25 °C and an in-plane irradiance of 1000 W/m^2. However, under normal operating conditions and especially under concentration, the cell temperature tends to increase. As shown with the example of Spectrolab CDO-100 concentrator PV cell, efficiency greatly drops with increasing temperatures (see Fig. 1-11). The same pattern is observed for non-concentrator cells, whose efficiencies drop linearly (to the first order) with temperature - see Fig. 1-12. Beyond efficiency degradations, extreme temperatures can lead to permanent damage to the solar cells. For these reasons, a means of cooling the PV cells is often implemented.

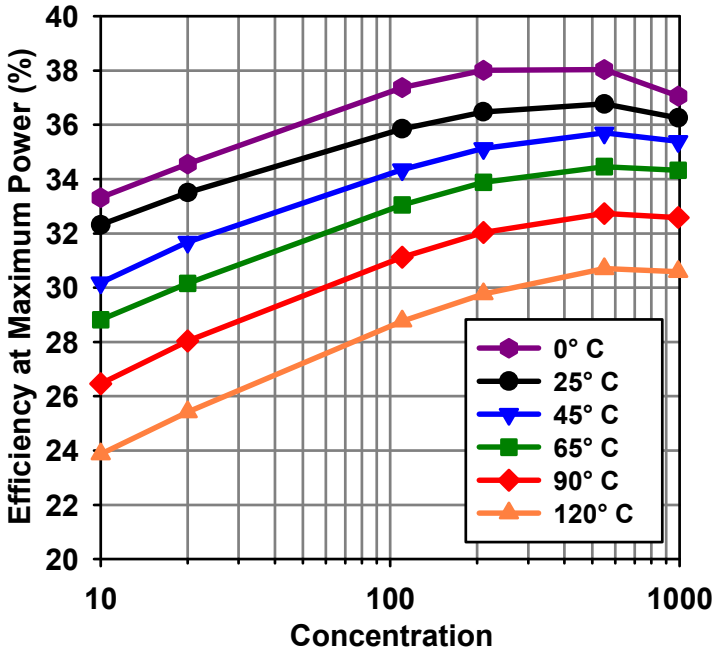

Figure 1-11: Relationship between the efficiency and the concentration factor for Spectrolab's CDO-100 concentrator solar cell at different operating temperatures. Source: Spectrolab, 2008 [63]

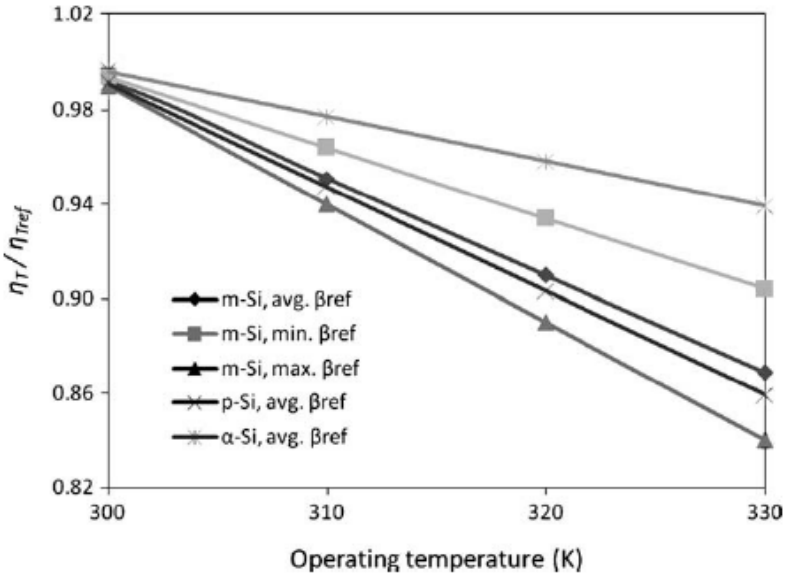

Figure 1-12: The ratio of temperauture-adjusted to reference efficiency, as predicted by the Evans-Florschuetz efficiency correlation for typical silicon-based PV modules. Source: Skoplaki, 2009 [64]

Passive cooling through heat sinks is the most common means of dissipating heat. Heat sinks often involve metalic fins, but can also be liquid. For instance, Rosa et al. and Bahaidarah et al. studied the behaviour of a PV panel submerged in water (serving as a heat sink) and observed an average increase in electrical efficiency of 11% and 10%, respectively [65, 66].

Active cooling can be advantageous if the heated fluid can be used for additional electricity generation. For instance, Erdil et al. [67] constructed a hybrid PV module and solar thermal collector system in north Cyprus. The system heated water by collecting the heat from a 0.6 m^2 PV module, producing about 2.8 kWh of thermal energy daily. The payback period of the modification (from PV to hybrid) was estimated at just 2 years.

Finally, filters such as the ones described by Sabry et al. [68] may be used to inhibit unwanted solar radiation from reaching the cell and thus limit cell operating temperatures.

1.2 Project Description

The core concept behind the Aleph project is to create a low-concentration PV system where electricity production is increased compared to conventional systems without significantly increasing the capital and operating costs.

GeePs (Laboratoire Génie électrique et électronique de Paris, previously LGEP), focusing in the field of photovoltaics, and LIMSI (Laboratoire d'Informatique pour la Mécanique et les Sciences de l'Ingénieur), focusing in the fields of fluid mechanics, heat

transfer, and energy, have developed an experiment demonstrating the potential of adding planar reflectors to photovoltaic modules in order to increase their power output. The demonstrator (further detailed in Chapter 3) was installed in the SIRTA meteorological station in Palaiseau (see Figs. 1-13 and 1-14), allowing for a direct use of locally-measured environmental variables (i.e. ground irradiances, wind characteristics, ambient temperature, etc.).

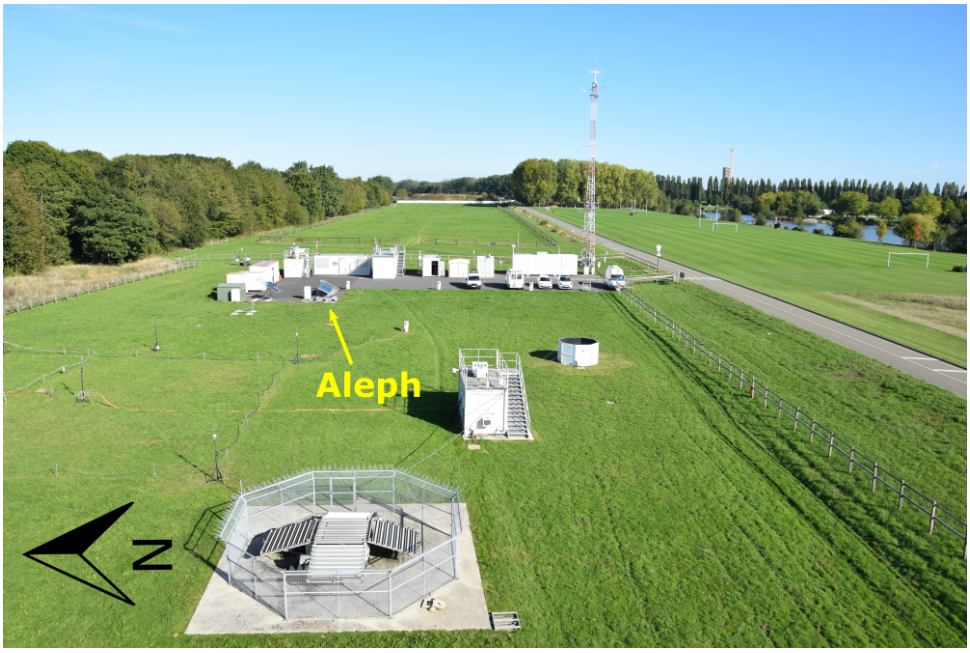

Figure 1-13: Aerial view of zone 1 of SIRTA with the position of the Aleph system indicated. Photo credit: Jordi Badosa

With the goal of reducing costs and environmental impacts, Aleph relies on PV modules that:

- are readily available on the market
- depend on abundant raw materials (e.g. silicon) and do not depend on scarce inputs (e.g. indium, tellurium, etc.)
- do not depend on toxic inputs (e.g. cadmium). Even if the encapsulant is made to prevent leaks of toxic substances, the presence of toxins can render the end-of-life treatment very difficult (reducing the potential of material recycling).

Currently, the PV market is dominated by poly-crystalline, mono-crystalline, and thin film (amorphous) silicon devices, whose electrical productions can be increased with low concentration without the need to alter them. For this reason, poly-crystalline and amorphous silicon modules were decided to be tested with this system.
Compared to conventional systems, the Aleph system results in:

- significant gains in annual production per unit area of PV module, or alternatively a reduction in PV module area to satisfy a given annual demand. With the assumption of a relatively low cost of reflector area compared to that of PV modules,

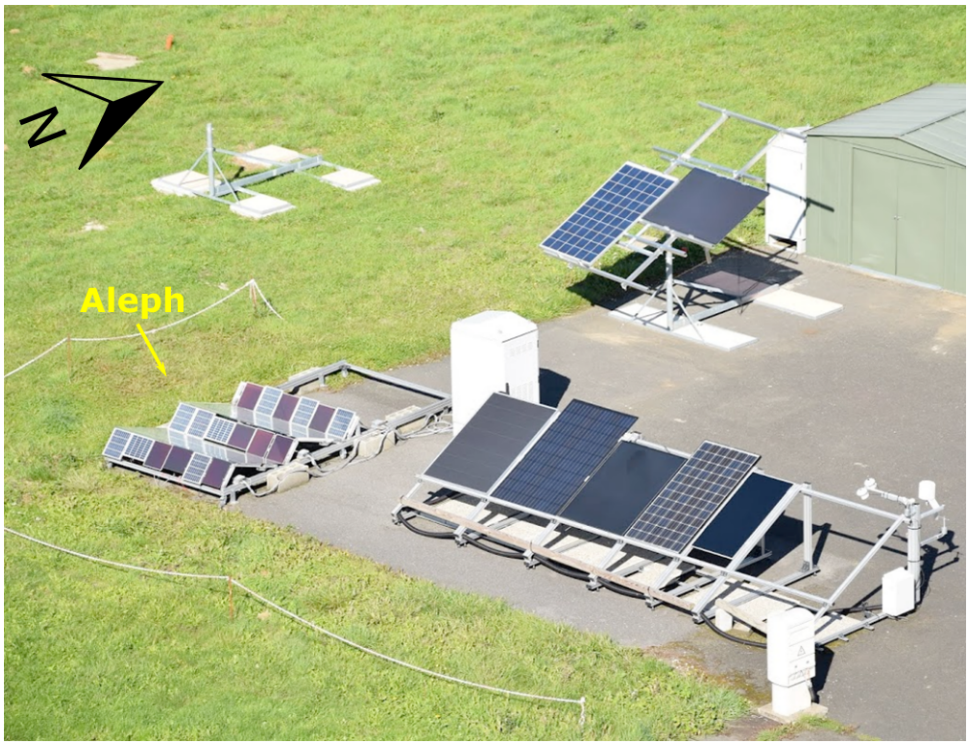

Figure 1-14: Aerial view of the three PV systems installed in SIRTA: Aleph (left center), tracker (right top) and classical fixed-mount (right bottom). Photo credit: Jordi Badosa

the levelised cost of electricity (LCOE) is decreased.

- less land use for satisfying a given demand. This can be of great importance for roof-top applications where roof area may be limited or costly.
- an annual production profile that better corresponds to the French electricity demand (i.e. high production around the equinoxes). Conventional systems result in peak production in the summer.

Compared to other concentrator systems, Aleph has the following advantages:

- incorporates low-cost planar reflectors rather than curved or Fresnel lenses (reducing capital costs)
- planar reflectors contribute to the concentration of diffuse irradiance (increase in view factor), which is not the case for curved reflectors. This is important since a large fraction of annual global irradiation in mid-latitude climates is diffuse.
- remains fixed, eliminating the need for tracking systems (reducing capital and operating costs)
- achieves sufficient cooling with natural convection, requiring no active or passive cooling (reducing capital and operating costs)
- operates with cells and modules readily available on the market instead of depending on concentrator cells (reducing capital costs)

A rooftop Aleph system in particular has additional advantages compared to a conventional rooftop system. Due to the complete coverage of the roof, the heating of the

building envelope is reduced. In the summer periods with high solar altitudes, the mirrors reflect a part of the irradiation back to space, reducing the heat island effect. The triangular cavity formed by the roof, PV module, and the reflector can be completely closed, with the hot air trapped inside being used to heat the building.

The experimental data collected by the demonstrator are of great scientific value. They give an insight into the achievable gains in produced energy brought by the reflectors compared to the frontal (control) modules. With access to environmental variables measured at SIRTA, the gains can be correlated to different seasons and weather conditions. The unique experimental setup allows for a direct comparison of PV module performances based on their technologies (amorphous and polycrystalline), positions within the row (e.g. distance from the edge), and orientations (portrait or landscape). With temperature probes attached to the backs of each module, the experiment allows for a direct evaluation of the rise in module temperature due to concentration. Continuous long-term measurements give an insight into the effects of ageing and soiling on the system performance.

The collected data are used in the development and calibration of a numerical model of this system, capable of evaluating the electric power output of PV modules as a function of key inputs (environmental variables, PV module properties, reflector properties, and the geometric configuration of the PV modules and reflectors). The performance of the Aleph system depends on several physical phenomena - including optical aspects, heat transfers, and the photoelectric effect - which are often coupled (depend on each other). For this reason, a coupled "multi-physics" model is developed to describe the system behaviour.

The scientific contribution of the work compared to similar studies include the consideration of more than one PV technology, precise measurement of complete I-V characteristics (compared to just I_{SC} measurements [20]), and a parallel experimental and numerical investigations of the system.

The authors hope that the industrialisation of the Aleph system will contribute to a rapid achievement of global grid parity of PV, in view of enabling a global large scale integration of PV systems.

THIS PAGE INTENTIONALLY LEFT BLANK

Chapter 2

Theoretical Background and Conventions

This section provides the reader with some basic principles essential to understanding the report, establishes certain conventions (e.g. for the solar azimuth and solar hour angles), and gives resources to access more information about each topic. Refer to Appendix C for additional theoretical background.

2.1 Astronomical and Geometrical Calculations

The equations and the conventions for the most important astronomical and geometrical variables are summarised in this section.

2.1.1 Solar Declination, δ

Solar declination is the angle between a plane perpendicular to incoming solar radiation and the rotational axis of the earth [69]. It is illustrated in Figure 2-1. Due to the Earth's axis being tilted by about 23.45°, the solar declination angle varies from +23.45° on June 21/22 (summer solstice) to −23.45° on December 21/22 (winter solstice). The solar declination angle is 0° on equinox dates (March 21/22 and September 21/22).

The solar declination can be calculated as a function of the day of the year, J, according to Equation 2.1 by Cooper [70].

$$\delta\,(degrees) = 23.45 \sin\left(\frac{2\pi\,(J{+}284)}{365}\right) \tag{2.1}$$

The error in the solar declination as calculated by (2.1) is in the interval $[-1.9° \,;+0.77°]$.

Bourdin [71] proposed an empirical correlation for the declination angle (Equation 2.2) based on the IMCCE data [72].

$$\delta\,(degrees) = 0.38 + 23.26 \sin\left(\frac{2\pi J'}{365.24} - 1.395\right) + 0.375 \sin\left(\frac{4\pi J'}{365.24} - 1.47\right) \tag{2.2}$$

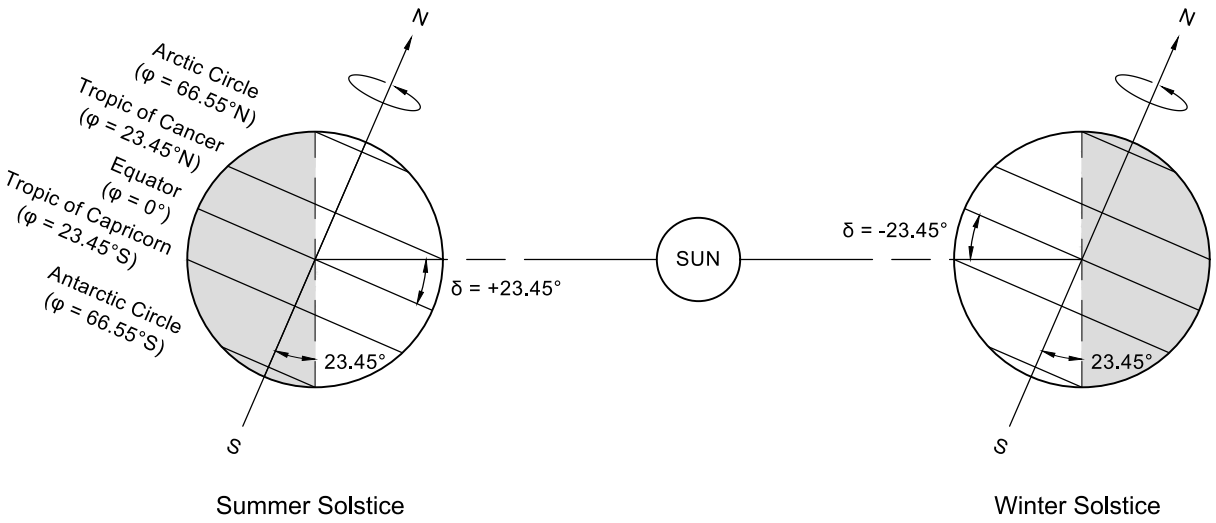

Figure 2-1: Sketch illustrating the solar declination. The Sun and Earth sizes and distances are not to scale.

where J' is 1 on the first of January 2013, 366 on the first of January 2014, 731 on the first of January 2015, etc. up to and including the first of January 2023.

The correlation was developped using least-square fitting of IMCCE data for the period January 1^{st} 2013 to January 1^{st} 2023. It aims to provide a good compromise between accuracy and calculation cost. The corresponding error is in the interval $[-0.20° ; +0.20°]$, which was considered small enough for the purpose of this project.

2.1.2 Local hour angle, ω

The local hour angle is an angle equalling zero at solar noon, and increasing in the westward direction by one hour for each 15° of longitude (see Figure 2-2). In this formulation, the hour angle is negative in the morning, and positive in the afternoon. Furthermore,

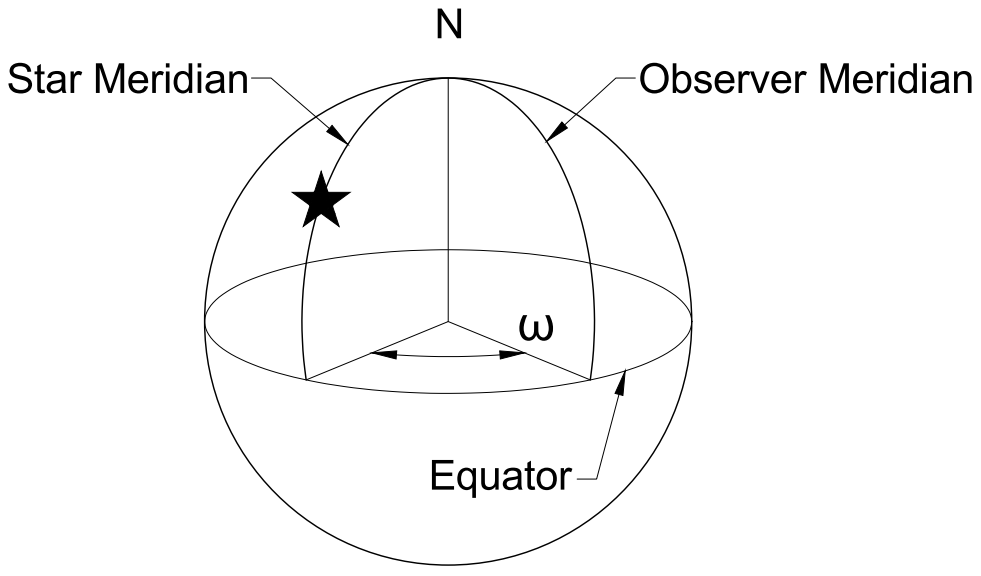

Figure 2-2: Sketch illustrating the local hour angle

the local hour angle can be obtained as a function of the local solar time, H, expressed in hours:

$$\omega(rad) = \frac{\pi\,(H-12)}{12} \tag{2.3}$$

or

$$\omega(deg) = \frac{180\,(H-12)}{12} \tag{2.4}$$

2.1.3 Solar time, H

Unlike the common time, which is for simplicity shared within geographically defined time-zones, solar time at a certain location strictly depends on the longitude (local meridian). It can be expressed as follows:

$$H{=}H_l - \Delta H_L + (4min/deg)\phi_g - EoT \tag{2.5}$$

where H_l is the local time in hours; ΔH_L is the advance[1] of the local time compared to the Coordinated Universal Time (UTC) in hours; ϕ_g is the local longitude (positive towards East) in degrees; and EoT is the equation of time in hours.

The equation of time, EoT, is used to describe the difference between the apparent and mean solar time. The difference is a result of two factors: 1) the obliquity of the earth axis, and 2) the eccentricity of the Earth's orbit around the Sun. Both factors follow a sinusoidal relationship throughout the year, and slowly change over the long term. The combined effect of these two components is commonly expressed with an empirical relationship.

Bourdin [71] proposed an empirical correlation for the Equation of Time (Equation 2.6) based on the IMCCE data [72].

$$\begin{aligned} EoT\,(seconds) = 7.36\ \sin\left(\frac{2\pi \mathrm{J}^{'}}{365.242}{-}0.071\right) \\ + 9.92\ \sin\left(\frac{4\pi \mathrm{J}^{'}}{365.242}{+}0.357\right) \\ + 0.305\ \sin\left(\frac{6\pi \mathrm{J}^{'}}{365.242}{+}0.256\right) \end{aligned} \tag{2.6}$$

where J' is 1 on the first of January 2013, 366 on the first of January 2014, 731 on the first of January 2015, etc. up to and including the first of January 2023.

The correlation was developped using least-square fitting of IMCCE data for the period January 1^{st} 2013 to January 1^{st} 2023. It aims to provide a good compromise

[1]Note: For countries following daylight savings, this parameter has two values depending on the time of the year. For example, for France, ΔH_L is 2h from the last Sunday of March to the last Sunday of October, and 1h otherwise (e.g. in the winter).

between accuracy and calculation cost. The correlation has a mean absolute error of 8.4 s, and a maximum error of 16 s, which was considered suitable for the purposes of this project.

2.1.4 Angle of incidence on a surface, θ, as a function of time (indirectly through ω)

The angle of incidence of beam radiation on a surface is the angle between the beam and the normal to the plane [69], as illustrated in Fig. 2-3.

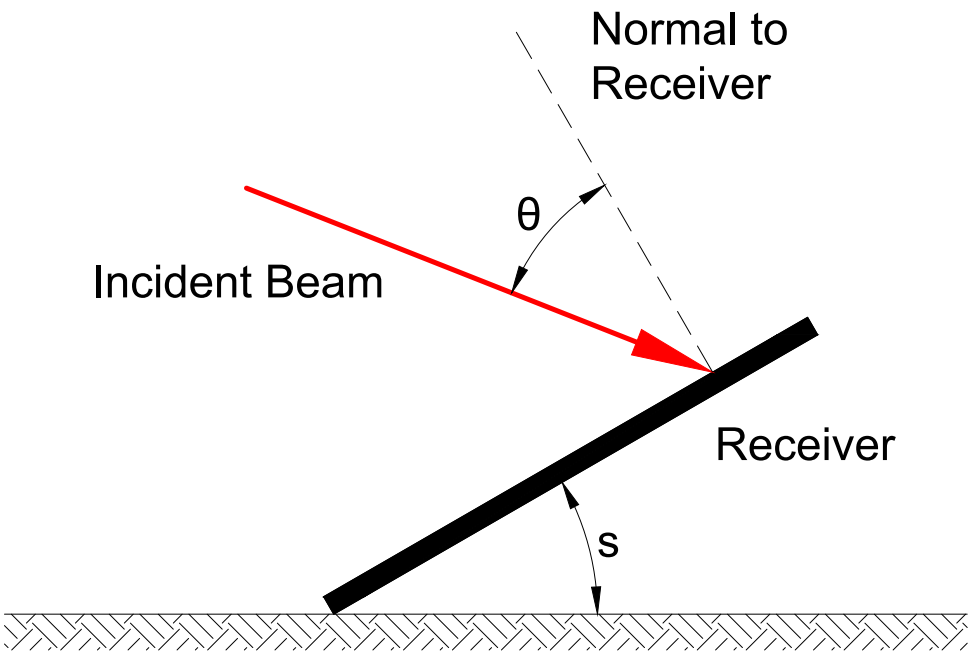

Figure 2-3: Sketch illustrating the angle of incidence on a surface

Furthermore, it can be calculated as a function of the other angles, using (2.7).

$$\begin{aligned}\cos(\theta) =& \sin(\delta)\sin(\lambda_g)\cos(s)\\ &-\sin(\delta)\cos(\lambda_g)\sin(s)\cos(\gamma_0)\\ &+\cos(\delta)\cos(\lambda_g)\cos(s)\cos(\omega)\\ &+\cos(\delta)\sin(\lambda_g)\sin(s)\cos(\gamma_0)\cos(\omega)\\ &+\cos(\delta)\sin(s)\sin(\gamma_0)\sin(\omega)\end{aligned} \tag{2.7}$$

where θ is the angle of incidence of the beam with respect to the surface; δ is the declination of the Earth; λ_g is the latitude of the receiver; s is the inclination of the receiver with respect to the horizontal; γ_0 is the surface azimuth angle of the receiver; and ω is the hour angle.

2.1.5 Solar altitude, α, and the solar azimuth angle, γ_S, as a function of time (indirectly through ω)

The solar altitude, α is the angle between the incoming beam and the horizontal plane [69]. The solar azimuth angle, γ_S is the angle (measured on the horizontal plane) between the projection of the solar vector onto the horizontal plane and the local meridian, the zero point being due South, increasing towards West, and decreasing (negative) towards East [69]. Solar altitude, α and the solar azimuth angle, γ_S are illustrated in Figure 2-4.

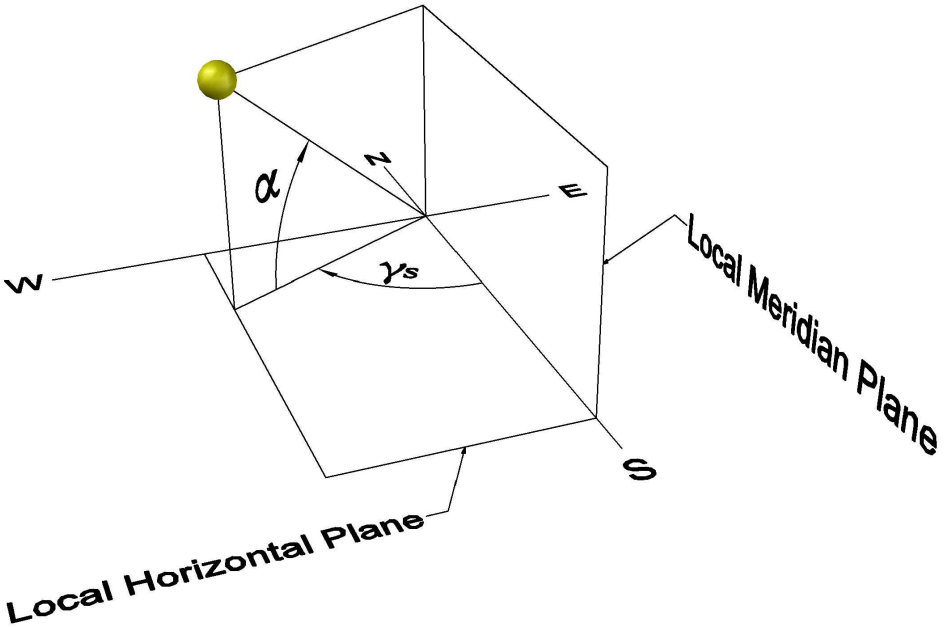

Figure 2-4: Sketch illustrating the solar altitude angle, α, and the solar azimuth angle, γ_S. The convention used for the solar azimuth angle is 0 for South, and increasing towards West.

Solar altitude and solar azimuth angles can be written as a function of time (indirectly through ω), as seen in (2.8), (2.9), and (2.10).

$$\sin(\alpha) = \sin(\delta)\sin(\lambda_g) + \cos(\delta)\cos(\lambda_g)\cos(\omega) \tag{2.8}$$

$$\sin(\gamma_S) = \frac{\cos(\delta)\sin(\omega)}{\cos(\alpha)} \tag{2.9}$$

or

$$\cos(\gamma_S) = \frac{\cos(\delta)\cos(\omega)\sin(\lambda_g) - \sin(\delta)\cos(\lambda_g)}{\cos(\alpha)} \tag{2.10}$$

2.2 Photovoltaic Conversion Process

A photovoltaic cell (often called a solar cell) is a non-mechanical and non-thermal device that converts light into electricity. While commonly used for generating electricity from sunlight, some PV cells (for example those found in pocket calculators) can convert artificial light into electricity.

Sunlight is composed of photons, containing various amounts of energy distributed along a spectrum of wavelengths (see Fig. 4-1 on page 45).

A PV cell is made of a semiconductor material (see [73] for a great introductory textbook on semiconductor physics). When photons strike the PV cell, they may be reflected, transmitted, or absorbed by the semiconductor material. Only the absorbed photons with enough energy contribute to electricity production (i.e. photons with energies higher than the material energy band gap). When sufficiently energetic photons are absorbed, electrons are freed from the material's atoms resulting in the generation of electron-hole pairs. Due to the structure of the solar cell (for example, a p-n junction with the p-layer on the bottom and the n-layer on the top), the electrons naturally move to the surface of the cell. When many electrons travel toward the front surface of the cell, the resulting imbalance of electrical charge between the top and bottom surfaces creates a voltage potential across the cell. Electrical conductors such as metallic contacts are placed on the top and bottom surfaces. When an external load or resistance is connected to the contacts completing an electrical circuit, electrical current flows in the circuit.

The efficiency at which PV cells convert sunlight to electricity:

- varies by type of semiconductor material and PV cell technology
- is a result of an integrated spectral response to a given solar spectrum (see Fig. 5-3 on page 58)
- varies with irradiance (drop in efficiency under low irradiances [74])
- varies with temperature [74]

For the sake of fair comparison, efficiencies of PV cells and modules are often tested and expressed under Standard Testing Conditions (STC), comprising of:

- solar spectrum AM1.5 (ASTM G-173-03)
- 1000 W/m^2 irradiance
- 25 °C operating temperature

The STC efficiency of most commercially available PV modules is between 5 and 15%, reaching up to 23% [75], while the cell-level laboratory efficiencies of single junction monocrystalline silicon cells reach 25.6% [76], with both records being frequently broken.

A single PV cell is capable of producing only 1 or 2 W, which is enough power only for small uses. For generating larger amounts of power, PV cells are electrically connected (generally in series, but depends on application), and encapsulated for weather protection to produce a PV module or panel. PV modules can be connected in groups to form a PV

array, which is often the case for large-scale PV power plants.

Photovoltaic cells generate direct current (DC) electricity, which can be used in its raw form for many applications, including charging batteries. However, almost all electricity in the electricity transmission and distribution systems is transported as alternating current (AC). For this reason, inverters are often used to convert DC current to AC for PV arrays (or micro-inverters on the level of PV modules).

PV cells produce the largest amount of power when they are directly facing the Sun. Tracking systems can be used to constantly orient the PV modules toward the Sun, but require larger capital and operating expenditures. Furthermore, their maintenance requires specialised knowledge, potentially rending them inappropriate in developing countries.

A classical PV module installation consists of rows PV modules that are:

- fixed (stationary)
- facing directly south (in the northern hemisphere, or facing north in the southern hemisphere)
- inclined at an angle that optimises a given objective (often economic performance) at the location where it is installed (taking into account average local weather patterns)
- spaced apart to minimise shading

2.2.1 Temperature Effects

Like all other semiconductors, PV cells are sensitive to temperature. Figure 2-5 shows the simulated current-voltage (I-V) characteristics of a typical p-Si cell under different operating temperatures. To discuss the temperature effect, let us define three key points of each I-V curve. The short-circuit current, I_{SC}, is the current output under zero voltage bias. The open-circuit voltage, V_{OC}, is the cell output voltage under open circuit conditions. The power at the maximum power point, P_{MPP}, is the cell power output when the current-voltage product is the highest.

An increased operating temperature results in a decrease in the effective semiconductor energy band gap. In practice (see Fig. 2-5), this has an overall adverse effect on conversion efficiency by:

1. decreasing the V_{OC}, and
2. slightly increasing the I_{SC},

resulting in a reduction in P_{MPP}.

To illustrate the source of the temperature effect, consider the classical single-diode model (further described in Section 6.2.1.2) for predicting the I-V characteristic:

$$I_{out} = I_{phot} - I_0\left[exp\left(\frac{q(V_{out} + I_{out}R_s)}{nkT}\right) - 1\right] - \frac{V_{out} + I_{out}R_s}{R_{sh}} \tag{2.11}$$

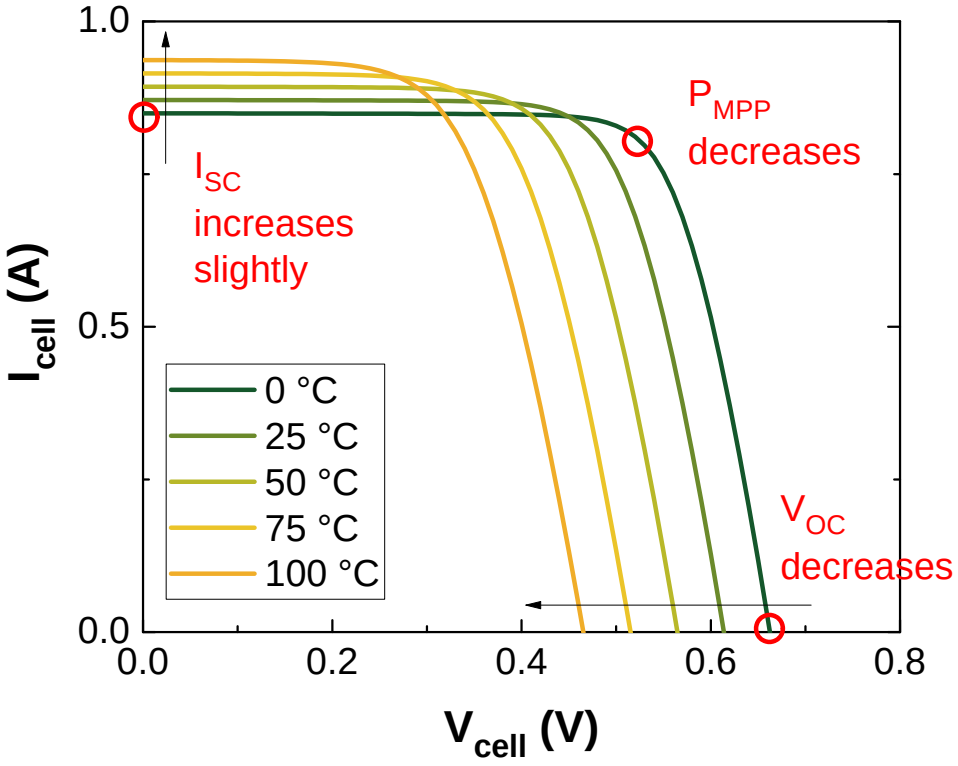

Figure 2-5: Typical p-Si cell I-V characteristic submitted to an irradiance of 1000 W/m^2 and various operating temperatures. The increased temperature decreases the open-circuit voltage, V_{OC}, while slightly increasing the short-circuit current, I_{SC}. The overall impact is a decrease in the maximum power output, P_{MPP}.

where I_{out} is the net current flowing through the diode in A, V_{out} is the output voltage in V, I_{phot} is the photogenerated current in A, I_0 is the dark saturation current (diode leakage current in the absence of light) in A, q is the absolute value of the electron charge (1.602×10^{-19} C or J/V), n is the diode ideality factor, k is the Boltzmann's constant (1.381×10^{-23} J/K), and T is the diode temperature in K, and R_s and R_{sh} are respectively the cell series and shunt resistances, in Ω. R_s represents the sum of series resistances at the base, emitter, metal grid, contacts and the current collecting bus. R_{sh} is used to reflect the leakage current due to localised shunts at the emitter layers, as well as the perimeter shunts along the cell borders. The V_{OC} decreases with temperature due to the temperature dependence of I_0. The equation for I_0 from one side of a p-n junction is given by:

$$I_0 = qA\frac{Dn_i^2}{L_D N_D} \tag{2.12}$$

where q is the charge of an electron (1.602×10^{-19} C); A is the semiconductor surface area; D is the diffusivity of the minority carrier; L_D is the diffusion length of the minority carrier; N_D is the dopant concentration; and n_i is the intrinsic carrier concentration.

Many of the parameters in (2.12) have some dependence on temperature, but the

temperature effect is dominated by the temperature dependence of n_i, given by:

$$\begin{aligned} n_i^2 &= 4\left(\frac{2\pi kT}{h^2}\right)^3 (m_e^* m_h^*)^{3/2} \exp\left(-\frac{E_{G0}}{kT}\right) \\ &\approx BT^3 \exp\left(-\frac{E_{G0}}{kT}\right) \end{aligned} \tag{2.13}$$

where T is the junction temperature; h and k are respectively Plank's and Boltzmann's constants; m_e^* and m_h^* are respectively the effective masses of electrons and holes; E_{G0} is the band gap linearly extrapolated to absolute zero temperature; and B is a constant essentially independent of temperature.

Substituting (2.13) into (2.12) yields:

$$I_0 = qA\frac{D}{LN_D}BT^3 \exp\left(-\frac{E_{G0}}{kT}\right) \tag{2.14}$$

Assuming the temperature dependencies of the other parameters can be neglected gives:

$$I_0 \approx B'T^\gamma \exp\left(-\frac{E_{G0}}{kT}\right) \tag{2.15}$$

where B' is considered as a temperature-independent constant; and γ is used (instead of the number 3) to allow the incorporation of the possible temperature dependencies of the other material parameters.

The impact of I_0 on V_{OC} can be calculated by substituting (2.15) into the equation for V_{OC}, as follows:

$$\begin{aligned} V_{OC} &= \frac{kT}{q}\ln\left(\frac{I_{SC}}{I_0}+1\right) \\ &\approx \frac{kT}{q}\ln\left(\frac{I_{SC}}{I_0}\right) \\ &= \frac{kT}{q}\ln I_{SC} - \frac{kT}{q}\ln\left[B'T^\gamma \exp\left(-\frac{E_{G0}}{kT}\right)\right] \\ &= \frac{kT}{q}\left(\ln I_{SC} - \ln B' - \gamma \ln T + \frac{E_{G0}}{kT}\right) \\ &= \frac{kT}{q}\left(\ln I_{SC} - \ln B' - \gamma \ln T + \frac{qV_{G0}}{kT}\right) \end{aligned} \tag{2.16}$$

Assuming that dV_{OC}/dT does not depend on dI_{SC}/dT, it can be written as follows:

$$\frac{dV_{OC}}{dT} = -\frac{V_{G0}-V_{OC}}{T} - \gamma\frac{k}{q} \tag{2.17}$$

yielding a linear dependence of V_{OC} on temperature.

The photogenerated current, I_{phot}, and hence the I_{SC} increase slightly with temperature as a result of a reduced effective band gap, since more photons have enough energy

to create electron-hole pairs. This dependance has been shown to be linear and material-dependent [77], and typically takes the following form:

$$I_{phot} = I_{SC,STC} \frac{G_{POA}}{1000\ W/m^2} \left[1 + \alpha_{Isc} \left(T - 25\,^{\circ}\mathrm{C}\right)\right] \tag{2.18}$$

where $I_{SC,STC}$ is the I_{SC} at STC conditions (in A); G_{POA} is the global in-plane irradiance (in W/m^2); and α_{Isc} is the I_{SC} temperature coefficient (in $^{\circ}$C^{-1}).

The series resistance, R_S, has been reported to increase with temperature according to the following expression [78]:

$$R_S(T) = R_{S0} \exp\left(B_S T\right) \tag{2.19}$$

where R_{S0} (in Ω) and B_S (in K^{-1}) are constants.

The shunt resistance, R_{SH}, has been similarly reported to decrease with temperature as follows [79]:

$$R_{SH}(T) = R_{SH0} \exp\left(\frac{B_P}{T}\right) \tag{2.20}$$

where R_{SH0} (in Ω) and B_P (in K) are constants. Note that the temperature dependencies of R_S and R_{SH} were found to be negligible for commercial PV cells [80], and will therefore not be considered in the modelling works.

In the future chapters, the temperature effect will be considered in two ways:

1. using an empirical linear correlation for the conversion efficiency, such as the Evans approach [74]
2. using a physics-based approach for calculating $I_0(T)$, using (2.15), and an empirical approach for finding $I_{phot}(T)$ using (2.18).

Chapter 3

Experiment

This chapter details the experimental setup used for collecting data necessary for the model development.

3.1 Experimental Setup

3.1.1 Aleph Experiment

Figure 3-1: A photograph of the Aleph experiment

The Aleph experiment (see Fig. 3-1) was designed by Vincent Bourdin and Anne Migan-Dubois in 2011. It was constructed in the GeePs laboratory in 2012. In July 2013 it was installed at the SIRTA meteorology platform in Palaiseau, France, located at 48.71°N, 2.21°E (see Figs. 1-13 and 1-14).

Element	Size (W × L) in cm	Specification
9 *a*-Si:H modules	26×30	SOLEMS 28/300/260 TD, 5 Wp, tandem
9 *p*-Si modules	30×35	SOLARTEC KS10T, 10 Wp
2 Reflectors (composed of 4 sections each)	192×68	Ordinary 3-mm glass-on-aluminium mirror, specular $\rho \approx 0.95$ in the visible range of wavelengths and at AOI=0°, less for other wavelengths and AOI
28 Temperature probes	-	Pt-100 Class A
Temperature probe	-	Pt-100 Stainless Steel
4 Reference cells	-	RG-100
Instrumentation	-	Keithley 2635A SourceMeter, and a Keithley Multiplexer switch 3706A with two commutation cards, 3720 and 3721 (4T sensing)

Table 3.1: Technical details of the experiment

Holding the experiment together is a steel platform, 2 metres wide in the East-West direction and 4 metres long in the North-South direction. The platform was designed with flexibility in mind, allowing for geometrical modifications to the system (inclination of the mirrors or PV panels, length of the mirrors, etc.) without going outside the $2m \times 4m$ frame. An addition of a fourth row of modules is also an option.

The experiment currently consists of three rows of six PV modules[1]. Each row is comprised of modules of two technologies: amorphous silicon (*a*-Si:H) and polycrystalline silicon (*p*-Si) (see Table 3.1) for technical details).

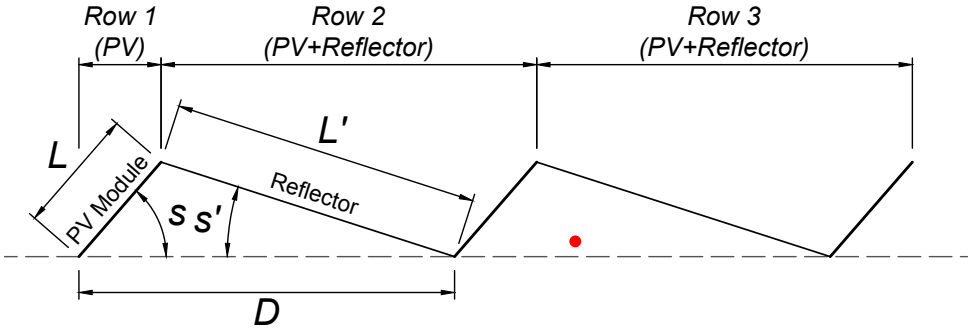

Figure 3-2: Schematic of the experiment showing the geometry of the system. The red dot represents the position of the temperature probe within the back cavity (5 cm off the ground).

The modules are south-facing[2] (γ_0=0) and are inclined with an angle of $s = 49°$ (roughly

[1]All the 18 modules are a donation from the SOLEMS company

[2]South was determined using shadows of vertical poles at solar noon.

equal to the latitude). The rows are spaced apart with a spacing $D/L = 3/1$ (see Fig. 3-2), which eliminates most of winter shading. The two rear rows are equipped with planar reflectors consisting of low-cost mirrors of 3 mm thickness (see Table 3.1 for details). The PV modules are orientated as portrait or landscape to allow the study of the impact of module orientation on system performance.

The set is instrumented to acquire data continuously from sunrise to sunset. The *I-V* characteristic is measured using a Keithley 2635A SourceMeter, and a Keithley Multiplexers switch 3706A with the communication card 3721. The measurement is performed using 4-terminal sensing to guarantee maximum precision. The operating temperature of the PV modules is measured at the rear of each module using platinum probes, Pt-100 Class A. The irradiance in the plane of array is measured with reference solar cells SOLEMS RG-100[3]. The latter two measurements were gathered using the communication card 3720. The positions of the temperature probes and reference solar cells relative to the modules are shown in Fig. 3-3. A stainless steel temperature probe was also placed within the back cavity to measure the interior air temperature (see Fig. 3-2 for position). It was suspended in air parallel to the ground, at a height of 5 cm, and centred in the East-West direction.

3.1.2 SIRTA Instruments

Since 2003, SIRTA has been continuously measuring a large number of atmospheric variables, including global irradiance, diffuse irradiance, direct (beam) irradiance, local albedo, ambient temperature and humidity, wind speed and direction at various altitudes, and others. The fact that the experiment was located at the heart of SIRTA made it relevant to exploit the applicable SIRTA measurements.

Table 3.2 summarises the specification of the instruments used for measuring certain atmospheric variables.

Table 3.2: Technical details of the instruments for measuring atmospheric variables

Element	**Specification**	**Measurement**
Pyrheliometer	Kipp and Zonen, CH1	Direct solar radiation
Pyranometer	Kipp and Zonen, CMP22	Diffuse solar radiation
Pyranometer	Kipp and Zonen, CMP22	Global solar radiation
Anemometer	A100R	Wind speed
Weather vane	W200P	Wind direction
Temperature probe	CS215	Ambient temperature

[3]Since the reference cells were added very recently, there was insufficient time to consider the respective measurements. The plane-of-array irradiances are therefore deduced from SIRTA's solar radiation measurements. Note that the reference cells consider a narrower integration range (equivalent to the reference cell spectral response, 350 nm to 1150 nm) compared to the SIRTA instruments that integrate solar flux from 200 to 4000 nm.

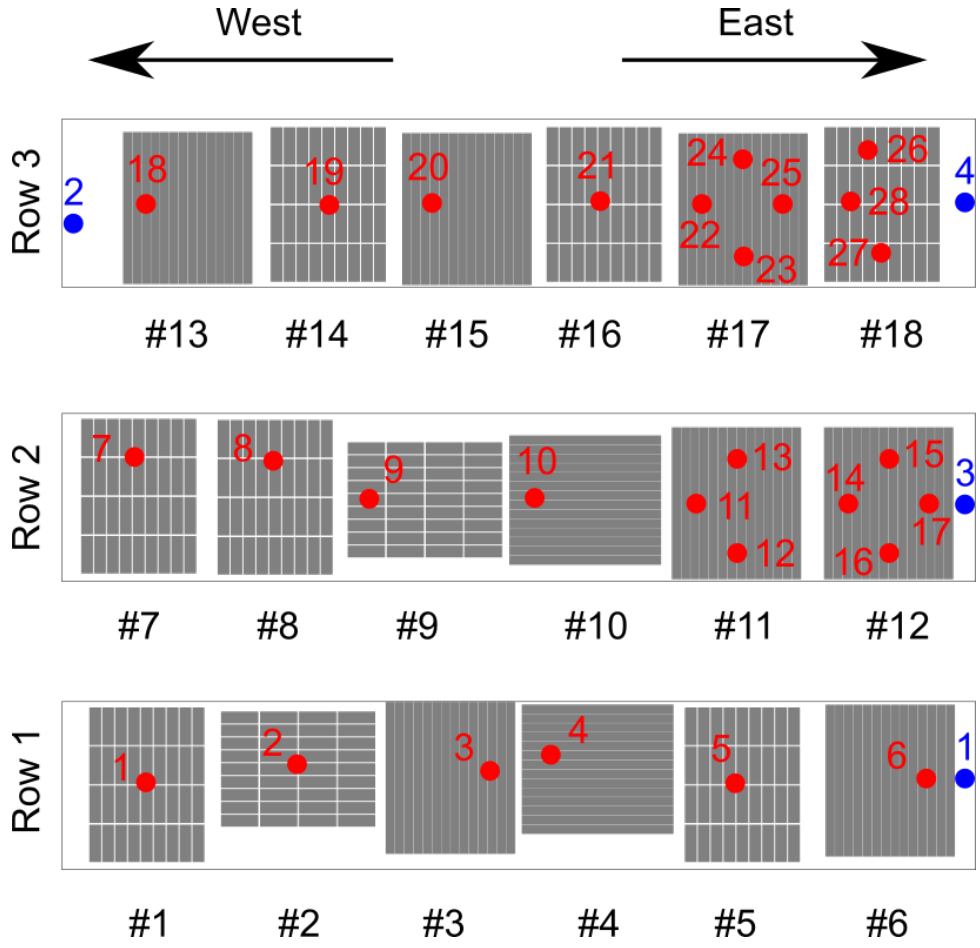

Figure 3-3: Positions and labelling of: (gray) 18 PV modules amongst the three rows; (red) 28 temperature probes Pt-100, attached to the backsheets of the modules; (blue) 4 reference cells RG-100.

The following two sections present the experimental data collected by different equipments, quality control performed on the data, and the interpretation of the data.

3.2 Experimental Data: *I-V* Measurements

Figures 3-4 and 3-5 illustrate the measured *I-V* data for frontal and reflector-equipped modules of *a*-Si:H and *p*-Si technologies, respectively. As times passes from sunrise to solar noon, the amount of solar irradiance on the modules increases, resulting in a larger photo-generated current and hence a larger module short-circuit current, I_{SC}. The increased irradiance also contributes to heating the modules, resulting in higher operating temperatures. This has a negative impact on the module open-circuit voltage, V_{OC}, which is more pronounced for reflector-equipped modules than for frontal ones.

One can note that certain *I-V* curves have the first two points that are not measured correctly. This is a result of a glitch in the measurement process, which could not be resolved. Since a large number of curves have the first two points misread, filtering

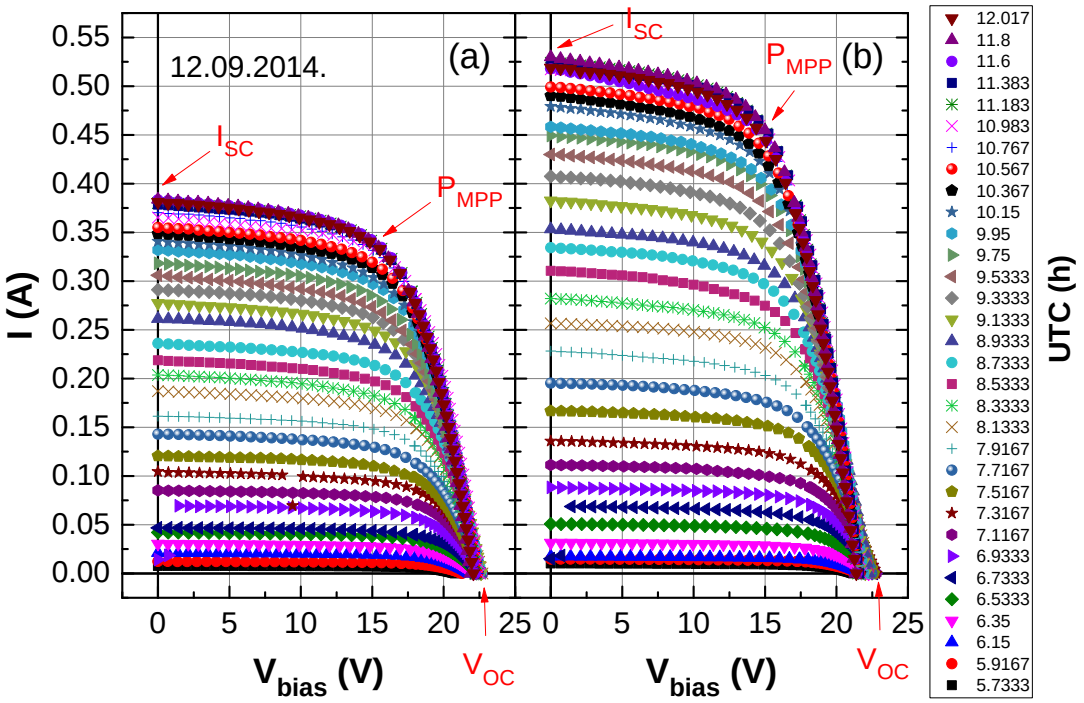

Figure 3-4: A morning of I-V curves measured on a sunny day for (a) a frontal a-Si:H module (module 6), and (b) a reflector-equipped a-Si:H module (module 15).

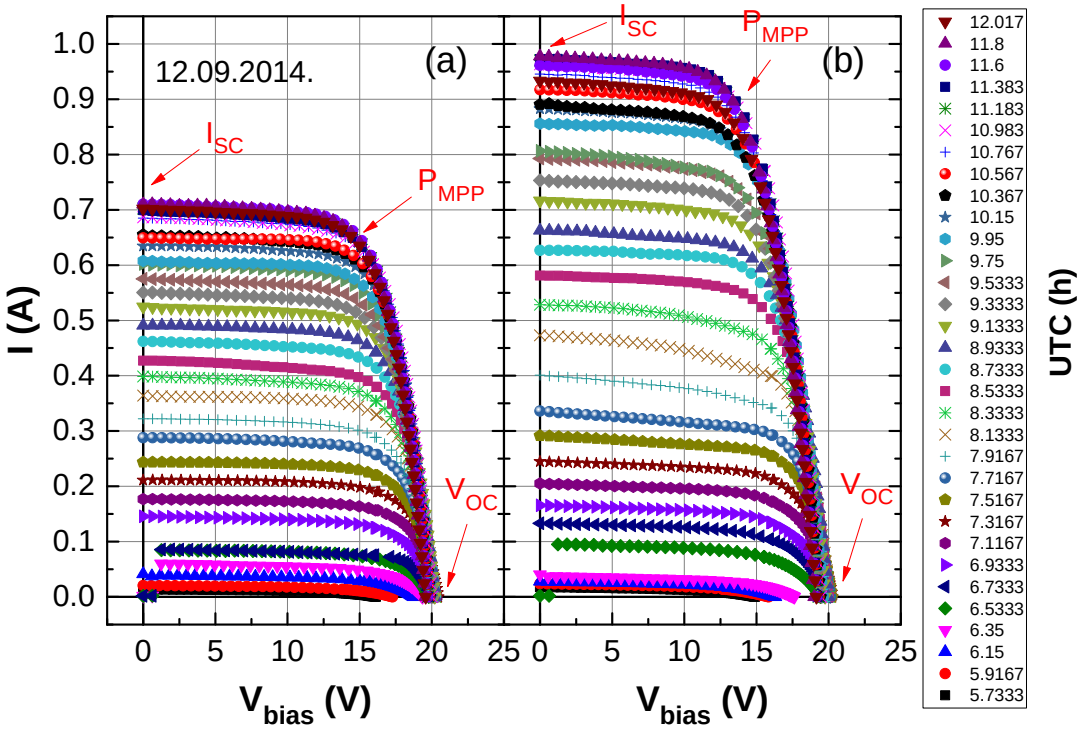

Figure 3-5: A morning of I-V curves measured on a sunny day for (a) a frontal p-Si module (module 5), and (b) a reflector-equipped p-Si module (module 16).

them out would result in a big reduction in the dataset. For this reason, and since the real I_{SC} was not of a particular interest for the model validation, the corresponding I-V measurements were kept. In turn, during the quality check and the electrical parameter

calibration stages, the first two points were ignored for all I-V curves.

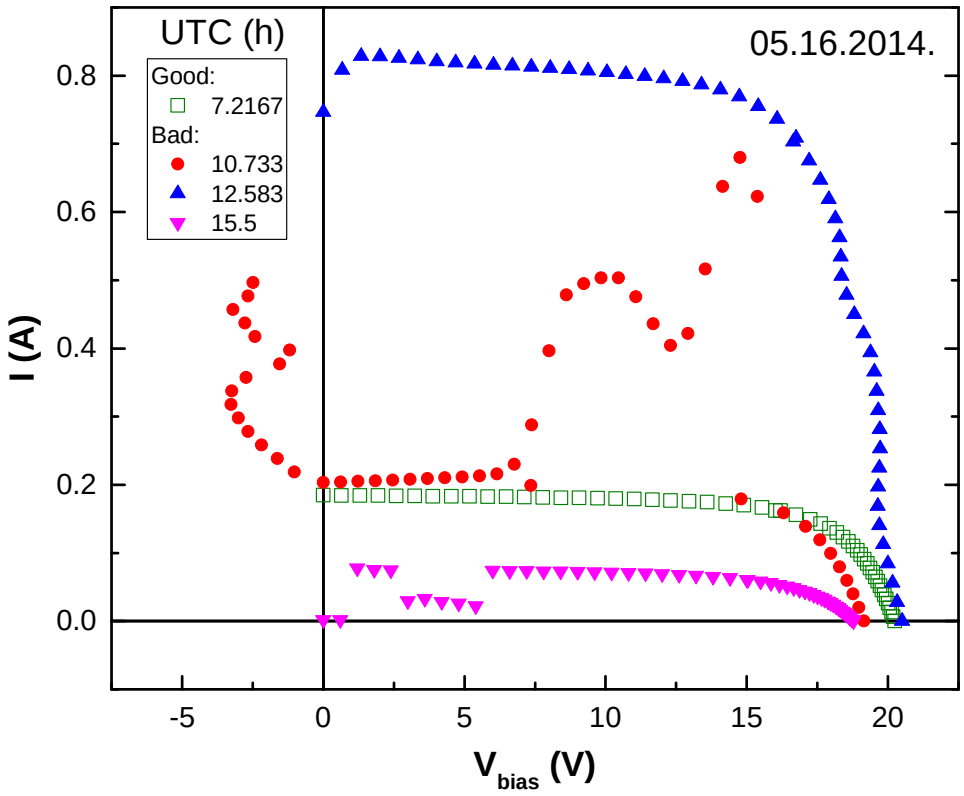

Figure 3-6: Examples of good and bad I-V measurements (module 5). Bad I-V curves are to be eliminated through quality control.

Going through the entire dataset of I-V measurements visually, one can conclude that a certain proportion of I-V curves is faulty (see Fig. 3-6 for example). The phenomenon was observed for all modules in the experiment, and although unpredictable in nature, it was found to be more probable during cloudy conditions. This is likely due to the frequent fluctuations in global irradiance during these periods, which may have a destabilising effect on the measurement. The faulty I-V curves must be flagged in a systematic way to make use of the I-V data when a certain measurement quality is necessary. The following section presents the developed quality check.

3.2.1 Quality Check

A quality check phase has been designed to flag I-V curve measurements based on certain quality criteria.

As seen in Fig. 3-6, many faulty I-V curves share the property of increasing somewhere along the voltage axis ($dI/dV > 0$). A filter based on maximum slope removed most of the faulty I-V curves (see Figs. 3-7 and 3-8, red).

Several faulty measurements that passed the above filter deviated significantly from the regular shape of I-V curves. For this reason, reference curves were constructed using

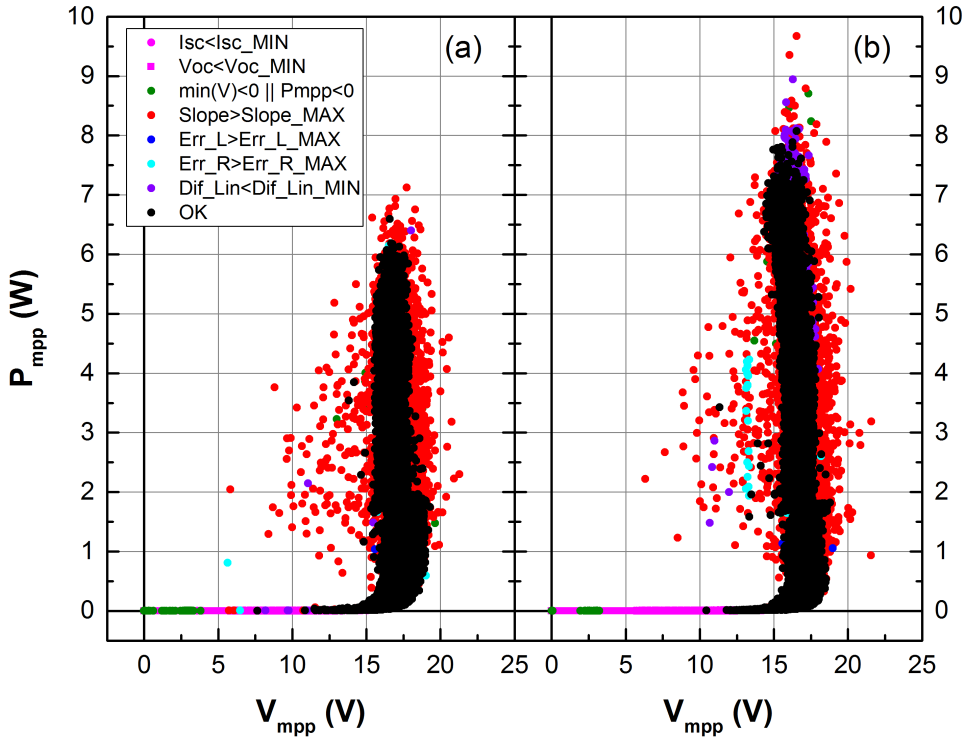

Figure 3-7: Visualisation of the filters as applied to almost two years of measurements (31.03.2014 - 07.03.2016), for (a) module 6 (a frontal *a*-Si:H module), and (b) module 15 (a reflector-equipped *a*-Si:H module).

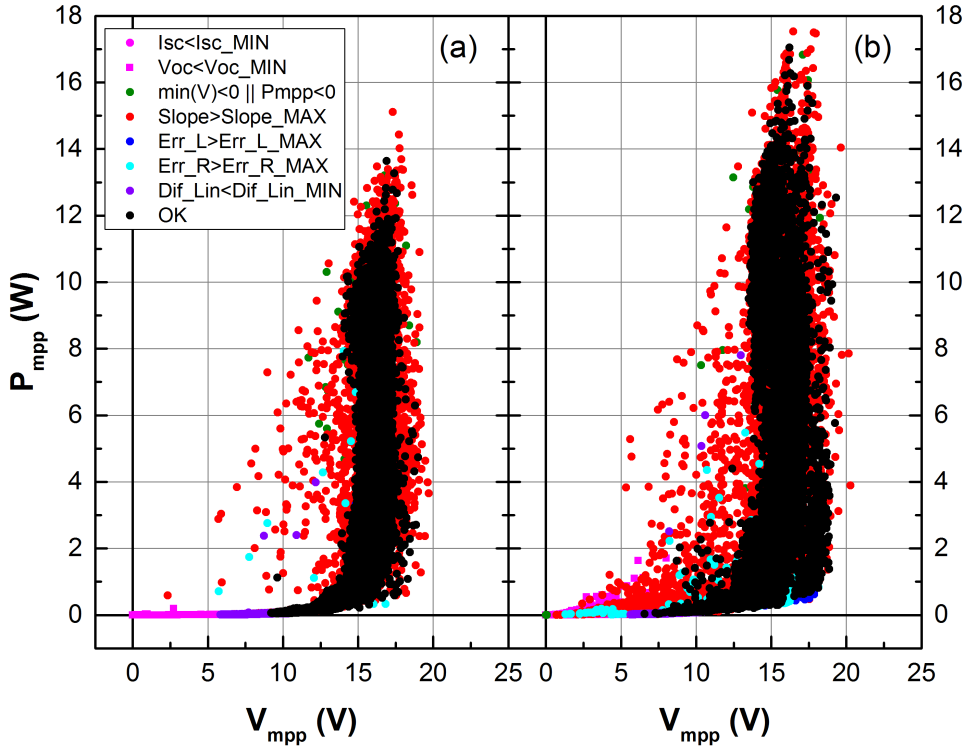

Figure 3-8: Visualisation of the filters as applied to almost two years of measurements (31.03.2014 - 07.03.2016), for (a) module 5 (a frontal *p*-Si module), and (b) module 16 (a reflector-equipped *p*-Si module).

three points: (I_{SC},0),(I_{MPP},V_{MPP}) and (0,V_{OC}). The interpolation was done using the Piecewise Cubic Hermite Interpolating Polynomial (PCHIP), existing as a part of the MATLAB package, which proved better for this purpose compared to using the cubic spline interpolation. The resulting reference curve was composed of the left segment [(I_{SC},V_0),(I_{MPP},V_{MPP})] and the right segment [(I_{MPP},V_{MPP}),(I_0,V_{OC})]. Two filters were established as a result:

- maximum deviation in current of points to the *left* of the MPP compared to the *left* segment of the reference curve (see Figs. 3-7 and 3-8, dark blue)
- maximum deviation in current of points to the *right* of the MPP compared to the *right* segment (see Figs. 3-7 and 3-8, light blue)

There were still several faulty *I-V* curves that passed all the above filters: they were entirely linear from I_{SC} to V_{OC}. To filter these linear *I-V* curves, a filter was based on the minimum deviation from linearity (see Figs. 3-7 and 3-8, purple).

Finally, two more flags were developed aimed at detecting measurements under extremely low irradiance: one is applied when $I_{SC} < I_{SC,MIN}$, and the other when $V_{OC} < V_{OC,MIN}$ (see Figs. 3-7 and 3-8, magenta). These measurements are not always considered bad, but are avoided for certain purposes (e.g. calibration of electrical parameters).

The filters are summarised in Table 3.3.

Table 3.3: Filter summary

Filter Number	Rule	Limit
1	$I_{SC} < I_{SC,MIN}$	$I_{SC,MIN} = 0.001A$
2	$V_{OC} < V_{OC,MIN}$	$V_{OC,MIN} = 10V$
3	$min(V) < 0V \| \| P_{MPP} < 0W$	0
4	$Slope > Slope_{MAX}$	$Slope_{MAX} = 0.001A/V$
5	$Err_L > Err_{L,MAX}$	$Err_{L,MAX} = 0.20$
6	$Err_R > Err_{R,MAX}$	$Err_{R,MAX} = 0.65$
7	$Dif_{Lin} < Dif_{Lin,MIN}$	$Dif_{Lin,MIN} = 0.73$

For visualising the effect of the *I-V* curve filters on a large part of the total dataset, the corresponding P_{MPP} values are plotted against corresponding V_{MPP} values (see Figs. 3-7 and 3-8). Note that when the modules are producing more power, the corresponding V_{MPP} decreases. This is because the moments of high production are often associated with high operating temperatures, which negatively affect V_{OC} and V_{MPP}. In turn, a temperature decrease in the winter months results in an increase in the V_{MPP} in the lower-right part of the cloud of black points.

3.2.2 Observed Gains

The collected data demonstrate the interest of this system. Fig. 3-9 presents the gain in the daily and monthly produced energy achieved by *a*-Si:H and *p*-Si PV modules under

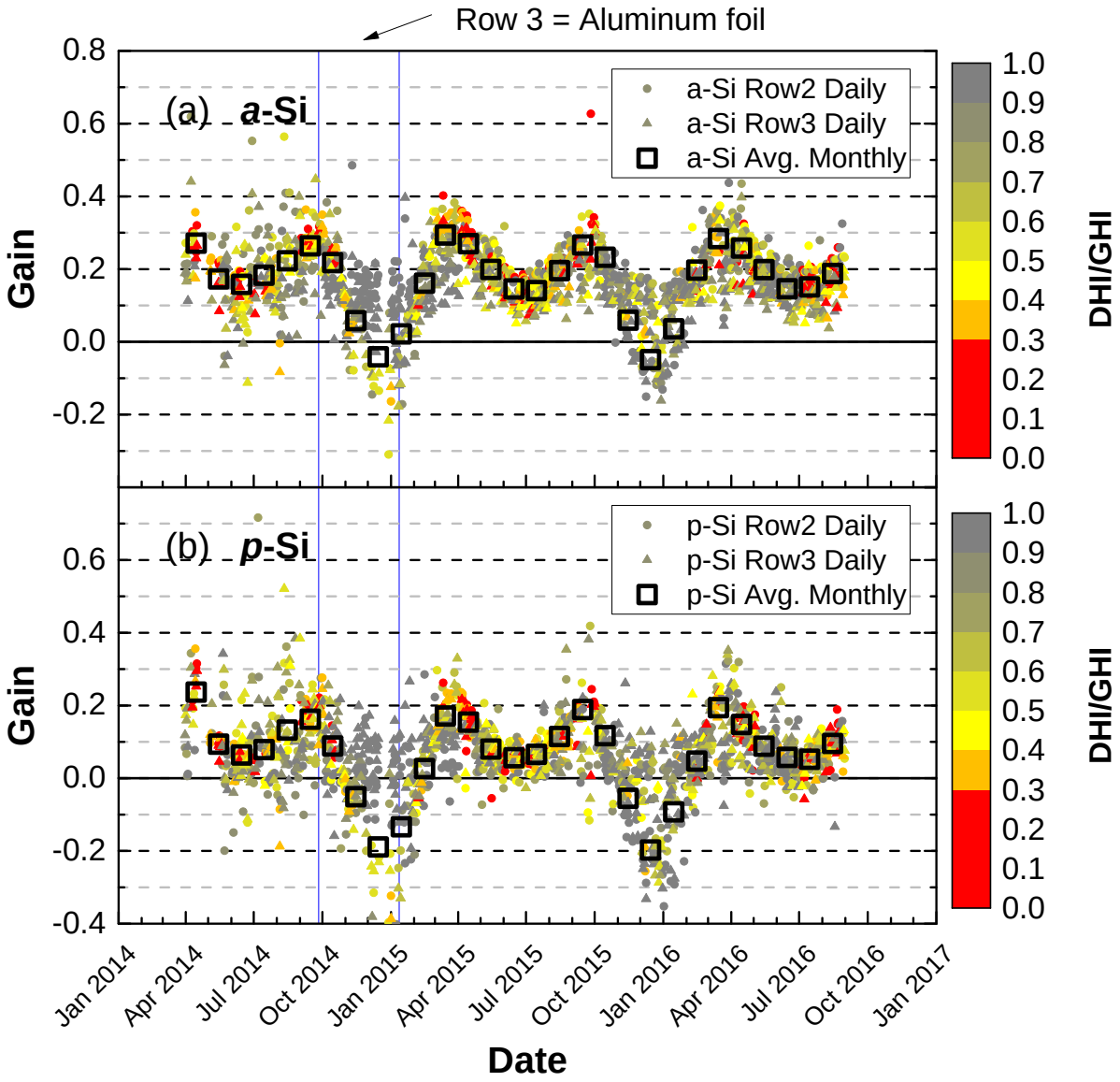

Figure 3-9: Experimental data: gain in daily and monthly produced energy resulting from concentration for (a) *a*-Si:H modules and (b) *p*-Si modules. From September 26 to January 12, 2014, the third row was equipped with aluminium foil as reflector. The color scale represents the daily ratio of diffuse to global irradiation. Negative values are due to isolated spikes of high illumination during the measurement of a particular PV module in an otherwise very cloudy day. Small shadow zones are present in the winter months, contributing to unfavourable gains.

concentration compared to the control modules (with the same orientation and tilt). Note that the days with less than 30% of the *I-V* curves being valid (passing all the quality check filters) are not shown, while in the kept days the bad *I-V* curves were not deleted. This approach in filtering proved to be the most efficient in reducing the scatter of the daily gains while having a negligible impact on the monthly gains.

The modules under concentration represented here are situated in the middle of rows 2 and 3, and are therefore not subject to severe edge effects (see Section 3.2.3.

The monthly gain is highest in the spring and fall, and reaches 29% for *a*-Si:H modules and 20% for *p*-Si modules. The daily gain reaches 40% and 30% for *a*-Si:H and *p*-Si modules, respectively. The average gains in produced energy over a two-year dataset are 19.2% and 8.58% for *a*-Si:H and *p*-Si modules, respectively.

From September 26 to January 12, 2014, the third row was equipped with aluminium foil as reflector. Comparable gains were observed for both reflector types (ordinary mirror and aluminium foil), though in theory the gains with bare aluminum should be slightly higher due to the absence of glass absorption. Perhaps the foil was not perfectly flat (as it is in mirrors), resulting in certain photons being reflected above the modules, and therefore negating the gains from removing the glass. Note that bare aluminum is not a suitable reflector as it is highly susceptible to weathering.

The difference in gains between the two PV module technologies can be largely attributed to two effects, both favouring *a*-Si:H modules. Firstly, the two technologies of PV cell experience different degrees of spectral mismatch losses between the reflected wavelengths and the material spectral response. This effect is further described in Sec. 5.2.2. Secondly, the two technologies of PV module experience different string mismatch losses (limitation of current by the lowest-illuminated cell) due to non-uniform illumination of cells. Modules often receive non-uniform concentration from the reflectors, which is most commonly a horizontal band starting at the bottom of the modules and extending to a certain height. *a*-Si:H modules in portrait orientation contain cells extending along the total height of the module (see Fig. 3-10a), meaning that non-uniform concentrations in the form of horizontal bands result in equal average illuminations of all cells. As a result, the string mismatch losses are minimal. On the other hand, *p*-Si modules have a more intricate cell interconnection (see Fig. 3-10b). Even with the presence of two bypass diodes (forming two strings of series-connected cells), they are much more prone to heterogeneous illuminations of cells and hence mismatch losses. For example, a concentration zone affecting only the bottom half of the lower string results in negligible gains in power production, since the cells in the upper half of the string limit the current to the case of no concentration.

Since all the modules are measured with the same source-meter, simultaneous continuous measurements are not feasible and a time lag exists between the determinations of the P_{MPP} of each module. Therefore, measurements made during periods of highly varying solar irradiation (e.g. during the presence of clouds) may suggest unfavourable ratios of energy production.

Unfavourable monthly ratios of energy production in the winter months, as suggested by Fig. 3-9, can be largely attributed to the above-mentioned data acquisition limitation when taking measurements during periods of intermittent solar resource. This becomes clear when one notes a rather constant gain in daily produced energy during overcast

(a) *a*-Si:H (b) *p*-Si

Figure 3-10: Module electrical interconnections: a) *a*-Si:H module: 14 tandem *a*-Si:H cells connected in series. No bypass diodes are installed; b) *p*-Si module: 2 strings of 18 cells connected in series with a bypass diode across each string.

days (days with high daily average DHI/GHI, shown in gray), and a seemingly variable gain during intermittent days (shown in yellow). A secondary factor contributing to unfavourable ratios of energy production in the winter period is the presence of shadows on reflector-equipped modules during early morning and late evening periods of winter days. This shadow does not appear on the frontal modules used as control, resulting in an apparent loss of energy for the second and third rows. However, the shadow effect would be identical for the two systems (PV+Reflector and classical installation) constructed with the same inter-row spacing. For these reasons and contrary to what the data suggests, no losses of energy should be expected with the addition of inter-row planar reflectors.

It is interesting to note that the shadow has a different effect on the two technologies, having a greater impact on the performance of *p*-Si modules. This is because the resulting heterogeneous illumination produces a more severe string mismatch effect for the *p*-Si compared to the *a*-Si:H modules.

3.2.3 Edge Effect

Since the experiment is built such that the reflectors are of roughly the same length in the East-West direction as the PV modules, the reflected rays affect certain PV modules differently than others in the morning and evening periods.

For example, consider a period of time from sunrise to solar noon (see Fig. 3-11). The Sun rises from the East and move towards the West, making the concentration zone, as projected onto the plane of the modules (parallelogram-shaped), move from West to East. Therefore, the far east-edge modules (12, 18) see a contribution of the reflector later in the morning than the non-edge (central) modules (8-11, 14-17). Similarly, the far west-edge modules (7, 13) are the first ones to experience the end of concentration in the afternoon. In both cases, the concentration of edge-modules is heterogeneous at certain periods of the day, potentially giving way to power losses due to string mismatch. These consequences result in somewhat smaller gains brought by the reflector compared

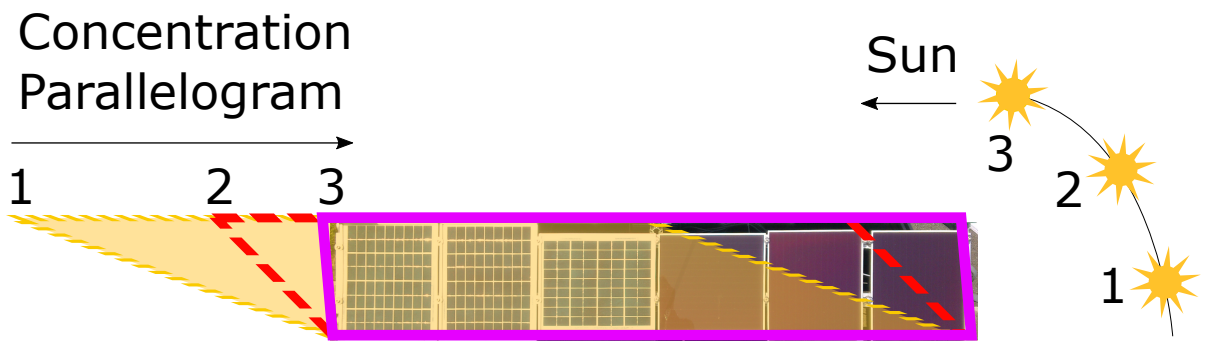

Figure 3-11: Edge effect sketch, showing the eastward movement of the concentration zone in the plane of the second row PV modules throughout the morning period. The edge effect is the most severe for the far-edge modules.

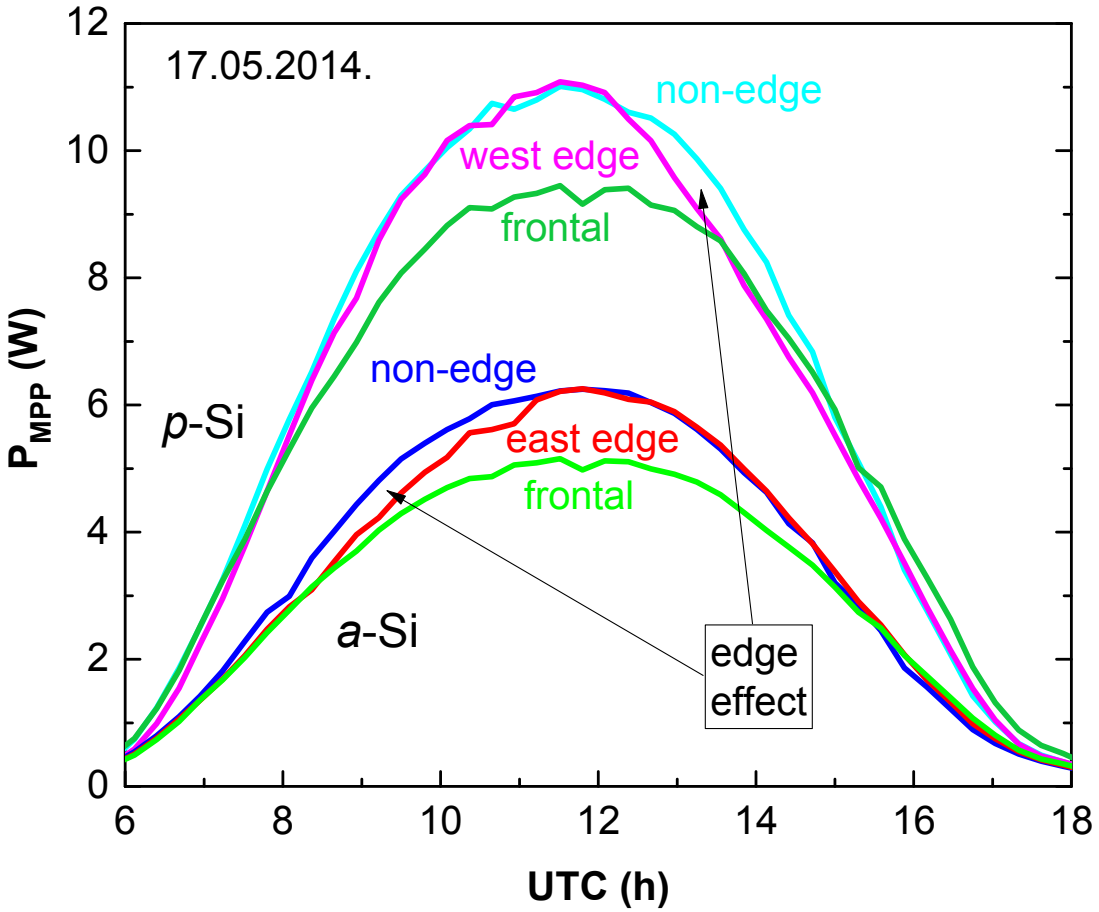

Figure 3-12: Experimental data taken on May 17th, 2014, showing an increased power production of non-edge and edge reflector-equipped modules compared to frontal modules. The edge effect is a result of the finite length of the reflector in the East-West direction, and is the most pronounced on modules closest to the row edges.

to non-edge modules. These phenomena are referred to in further text as the edge effect. The edge effect decreases with distance from the edge and becomes negligible after several module widths away from the edge.

Figure 3-12 shows the edge effect observed by modules 7 and 12 (west- and east-edge modules) on a relatively clear day in May. On this day, the following gains in produced

energy were achieved: 14.7% and 11.5% for central and edge *a*-Si:H modules, and 9.4% and 5.7% for the central and edge *p*-Si modules.

3.3 Experimental Data: Temperature and Other Measurements

Figures 3-13 and 3-14 present various measurements taken on a cloudy day (August 28th, 2014) and a clear day (September 12th, 2014), respectively.

Figure 3-13 presents a day of various measurements taken on August 28th, 2014, a very cloudy day with isolated bursts of high beam irradiance. The figure includes temperature measurements of ambient air (green), back-cavity interior (black), two probes situated on the backs of *p*-Si modules (blue symbols), and two probes attached to *a*-Si:H modules (red symbols). The considered modules are far from the edges and next to each other, and in theory receive a similar amount of concentration. Also shown are the diffuse horizontal and beam normal irradiances (cyan and red), as well as the wind speed and direction (blue and gray).

On this overcast day, the temperature rise of PV modules compared to the ambient temperature is mostly correlated with the DHI profile. One can also note that the temperature of the PV modules and the cavity increases rapidly during bursts of high BNI. The burst of BNI between 17:30 and 18:00 did not increase the cavity and module temperatures because the Sun was behind the modules, effectively not contributing to in-plane irradiance. Note that *p*-Si modules experience a higher degree of heating compared to *a*-Si:H. Due to the relatively large thickness of *p*-Si cells, the non-converted photons in the near infra-red region get largely absorbed as heat. In the *a*-Si:H case the non-converted photons get partially reflected in this range (as evident in Fig. 5-1, page 56). In this case, certain non-absorbed photons traverse the cell, get reflected by the substrate, traverse the cell again, and finally escape the cell without being absorbed as heat.

It is also interesting to note that the increased wind between 22:30 and 00:00 in the westward direction contributed to the mixing of air in the cavity, equating cavity and module temperatures with that of ambient air.

Figure 3-14 presents various measurements taken on September 12th, 2014, a clear day. Measurements related to row 1 are shown in blue, row 2 in red, and row 3 in black. The data show that the modules equipped with reflectors (those in rows 2 and 3) on average experience significantly higher operating temperatures than frontal modules. On this day, row 3 modules were up to 14 °C hotter than row 1 modules. Over the entire dataset, this difference due to heating was observed to rise to as much as 20 °C. It can be noted that row 2 modules are on average cooler than row 3 by about 2 °C.

This can be explained by the fact that the mirrors cast a shadow on the ground below row 2 modules, making it cooler than if it were illuminated. Therefore, row 2 modules experience thermal exchanges with a cooler shaded ground while row 3 modules exchange heat with an illuminated ground (in both cases a concrete surface).

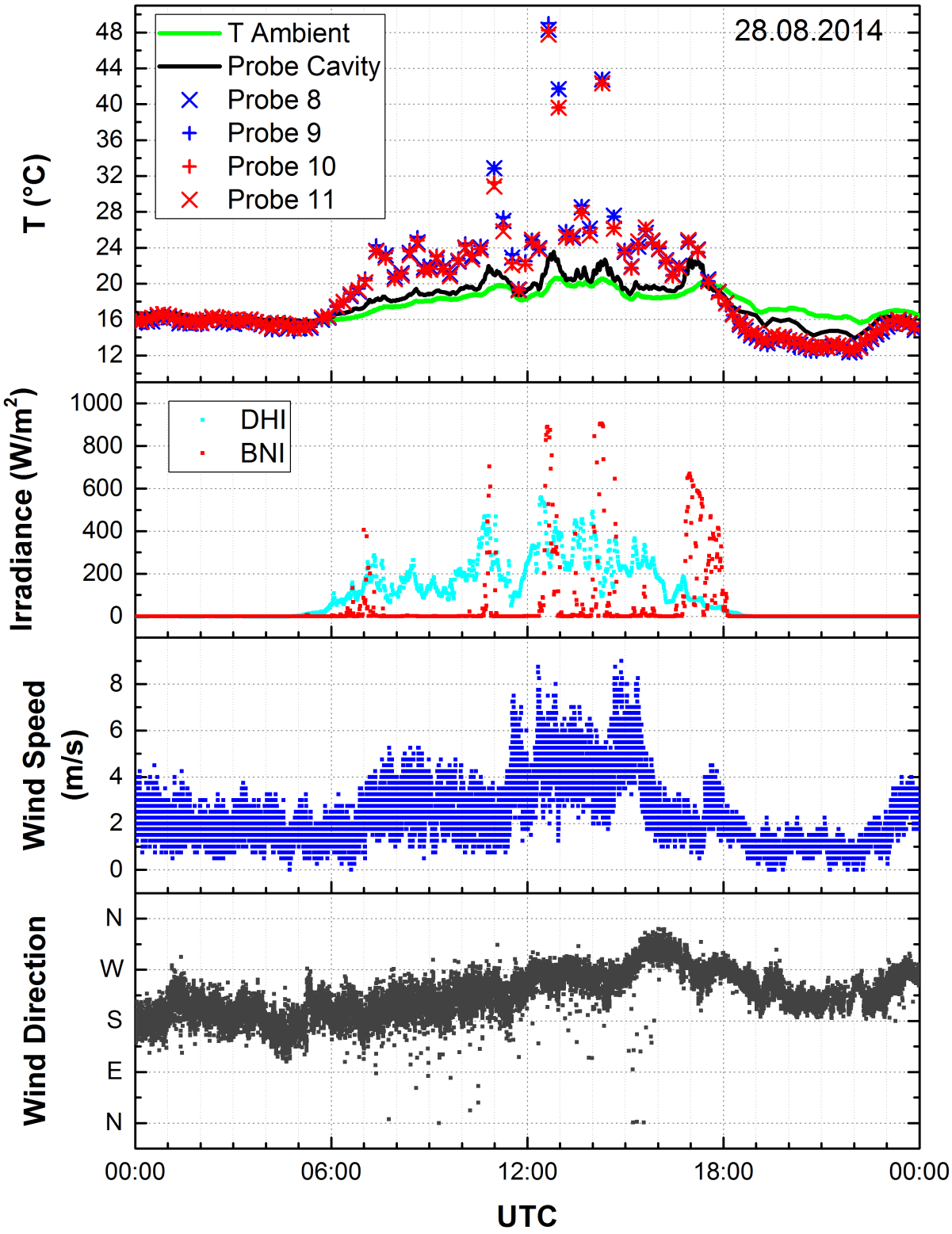

Figure 3-13: Experimental data taken on August 28th, 2014, a cloudy day. (Top graph) Green line: ambient temperature probe; black line: probe situated inside the back triangular cavity; blue symbols: probes on *p*-Si modules; red symbols: probes on *a*-Si:H modules. (Lower graphs) Cyan and red: diffuse horizontal and beam normal irradiances, respectively; blue and gray: wind speed and direction, respectively.

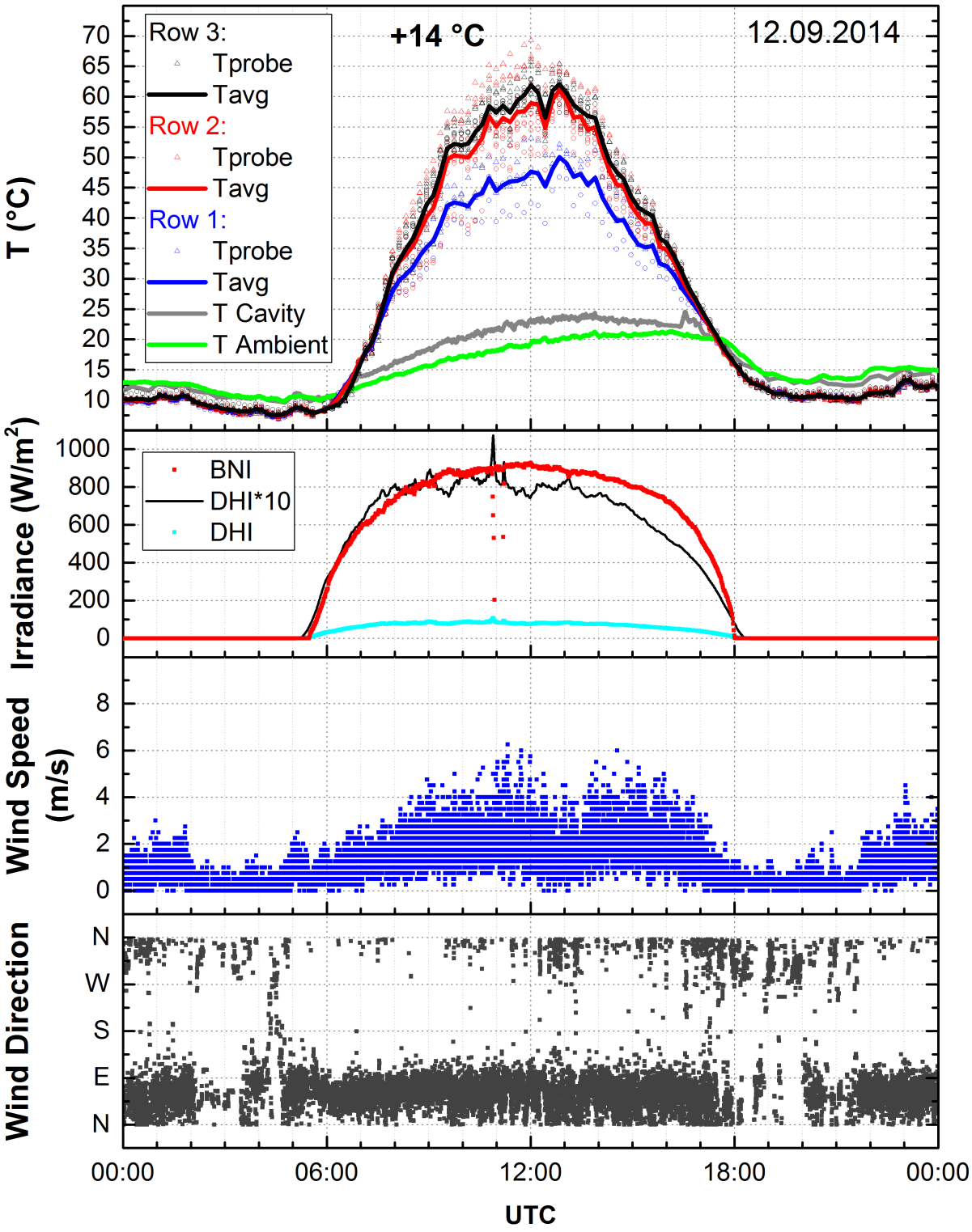

Figure 3-14: Experimental data taken on September 12th, 2014, a clear day. (Top graph) Green line: ambient temperature probe; gray line: probe situated inside the back triangular cavity; blue, red, and black symbols: row 1, row 2, and row 3 modules' probe measurements (circles=*a*-Si:H, triangles=*p*-Si) ; Blue, red, and black lines: row 1, row 2, and row 3 average module temperatures. The difference in temperatures, reaching 14 °C on this day, is caused by an increased illumination of reflector-equipped modules brought by the reflectors. (Lower graphs) Cyan and red: diffuse horizontal and beam normal irradiances, respectively, indicative of a clear day; blue and gray: wind speed and direction, respectively.

Even though the day was clear, certain oscillations of PV module temperatures are observable. Given all probe measurements follow the same trend, the oscillations are likely due to rapid changes in diffuse irradiance (solar and intermediate infra-red from the celestial vault) and wind characteristics.

3.4 Limitations

The data acquisition system of the Aleph experiment is associated with certain limitations. For instance, the process for measuring the module I-V characteristic results in relatively high measurement intervals and systematically incorrect timestamps.

The I-V measurement of a given module is repeatedly taken until a stable measurement is detected (unchanged from previous). This prolongs the time necessary to take measurements for all 18 modules. Furthermore, a common timestamp is recorded for all taken measurements at the end of each cycle, resulting in a somewhat systematic temporal error compared to the actual time of acquisition, and making it impossible to know the exact times the individual measurements were taken. See Fig. 3-15 for a visualisation of measurement intervals of measurements taken in 2014 and 2015.

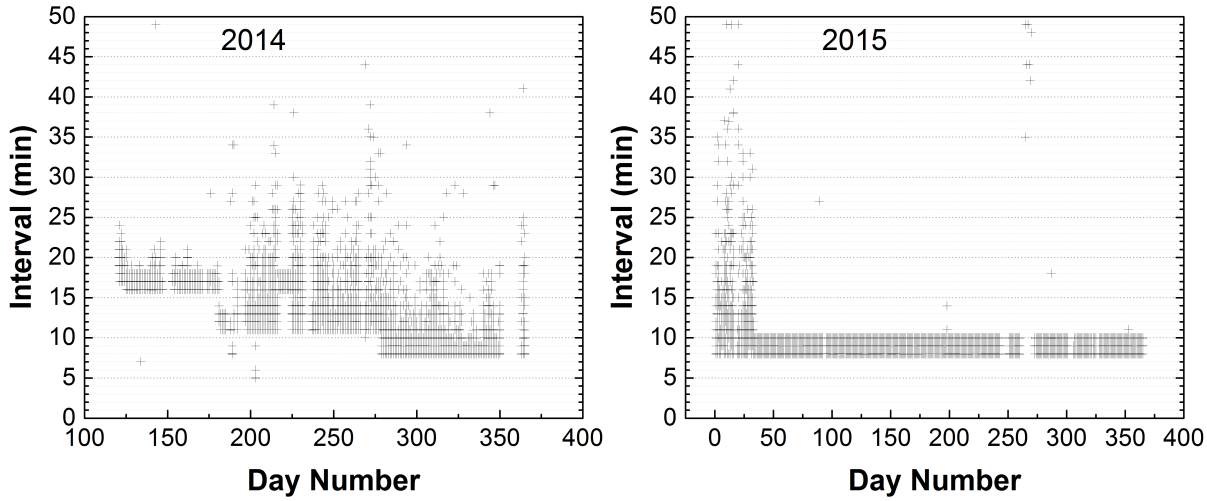

(a) 2014 measurement intervals

(b) 2015 measurement intervals

Figure 3-15: Measurement intervals for (a) 2014, and (b) 2015.

3.5 Conclusion

The Aleph experiment is designed to provide as much insight as possible into the factors affecting the performance of the planar reflector-equipped PV system. It is situated at the heart of SIRTA meteorological station, allowing the exploitation of their high quality irradiance and environmental measurements. Two PV technologies are tested with ALEPH: amorphous silicon and polycrystalline silicon. Frequent I-V measurements

of reflector-equipped and control modules reveal significant gains in produced energy brought by the reflectors (19.2% and 8.58% annual gain for *a*-Si:H and *p*-Si modules, respectively). Filters were developed to flag *I*-*V* measurements based on their shape and values of key points (e.g. V_{OC}). When comparing the performance of central and edge reflector-equipped modules, a considerable edge effect is observable. This shows the importance of reflector overhangs to maximise production. Finally, certain temperature measurements are shown together with environmental variables, highlighting the coupling of several heat transfer phenomena: radiation, conduction and convection. *p*-Si modules experience a higher degree of heating than *a*-Si:H due to the higher absorption as heat of near infra-red radiation. The increased irradiance on the PV modules due to reflectors can increase their operating temperatures by as much as 14 °C, with peak temperatures of up to 70 °C, possibly reducing their lifetime. A PV cell cooling mechanism such as water spray or forced convection can be implemented to help avoid such high temperatures while increasing electricity production.

Chapter 4

Solar Resource Modelling

This chapter describes the part of the solar resource model concerning the position of the Sun and the ground-level irradiance values. The actual representation of the beam and diffuse solar flux in 3-D changes based on the implementation of the optical models, described in Chapter 5. For example, in the analytical model the beam irradiance is considered to come from a point source, while in the ray-tracing model the sun disk or the sunshape is sampled with a certain probability.

4.1 State of the Art

The solar resource has been studied extensively by the scientific community. A state of the art solar position algorithm was proposed by Reda and Andreas (NREL) [81], valid for the years in the range [-2000, 6000], and resulting in uncertainties in solar zenith and azimuth angles of $\pm 0.00003°$.

Perez et al. [82, 83] have studied the incident diffuse irradiance on a tilted plane, taking into account the horizon and circumsolar effects. Buie et al. [84–86] and Eissa et al. [87] have studied the direct irradiance and in particular investigated the influence of sunshape, described by the circumsolar ratio. Blanc et al. [88] give an excellent review of the current state of the art regarding the circumsolar effect, including key definitions and practical aspects.

Several classification methods of sky conditions with respect to the composition of the solar resource have been proposed in the literature. The clearness index compares the global horizontal ground-level irradiance (GHI) to the extra-terrestrial flux. The clear-sky index compares the actual GHI to the hypothetical (modelled) clear-sky GHI, as shown by Marty and Philipona [89]. The diffuse fraction measures the the ratio of diffuse to global horizontal irradiance (DHI/GHI), as shown by Bortolini et al. [90]. Kang and Tam [91] propose a classification method based on the clearness index and the probability of persistence.

4.2 Position of the Sun

The position of the Sun relative to a given point on Earth was described primarily using equations given by Duffie and Beckman [69], which were summarised in Section 2.1. In addition, empirical correlations for the solar declination (Eq. (2.2)) and the equation of time (Eq. (2.6)) proposed by Bourdin [71] were implemented.

4.3 Surface Irradiance: Clear-Sky

Geometrical optimisation of PV systems for a given location is generally performed taking into account several years of local meteorological data. However, a clear-sky model can be of great importance when comparing several competing systems. For example, if clear-sky conditions are imposed and the performance of classical and reflector-equipped installations are evaluated over the course of a year, the effect of reflectors becomes apparent.

There are numerous empirical models for global horizontal irradiance under clear sky [92,93], which work well since quantities such as the extra-terrestrial irradiance (throughout the year) and the optical properties of the atmosphere are well understood. However, the most commonly used variables in solar resource modelling for photovoltaic applications are the beam normal and diffuse horizontal irradiances (BNI and DHI). The decomposition of the global irradiance into its beam and diffuse components is a more delicate task, and is often done with one of two types of models: 1) physics-based models, and 2) empirical models.

The decomposition is a result of the following process. Solar irradiance arrives to Earth as direct irradiance. At the top of the atmosphere (TOA), its mean value is 1366.1 W/m^2 (according to the ASTM Standard Extraterrestrial Spectrum Reference E-490-00), varying slightly based on the Earth-Sun distance (1412.5 W/m^2 at the Perihelion, 1321.7 W/m^2 at the Aphelion). A part of it is reflected by the atmosphere and the clouds back to space. Another part is scattered by the aerosols in the atmosphere (by the process of Rayleigh scattering), resulting in the diffuse component of the ground-level irradiance. The direct irradiance which is neither reflected nor scattered is partially attenuated by the atmosphere. The degree of attenuation depends on 1) the amount of atmosphere traversed, referred to as the optical air mass (AM), itself depending on the solar elevation angle, and 2) the aerosol optical depth (AOD), depending on the presence of urban haze, smoke particles, desert dust, etc.. Note that both attenuation factors have a non-uniform impact across the spectrum of wavelengths (see Fig. 4-1).

While it is relatively easy to calculate the TOA irradiance, as well as the AM [94] at a given moment, modelling the level of attenuation and scattering is not an obvious task. The atmosphere does not have a constant transparency, resulting in a non-linear

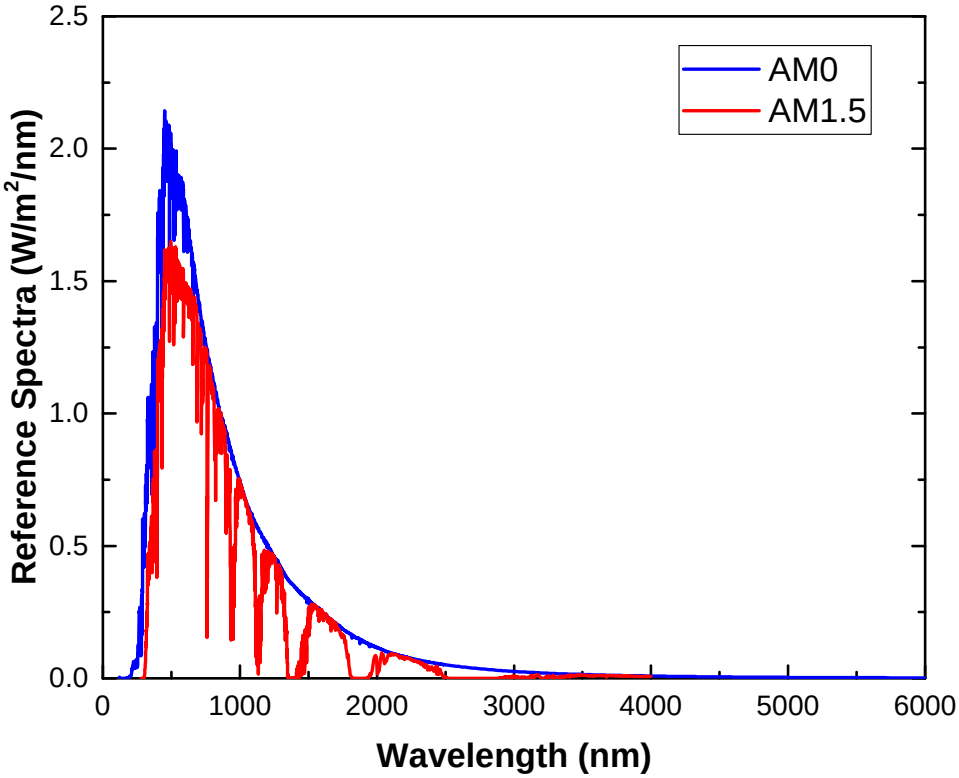

Figure 4-1: Reference spectra AM0 (TOA) and AM1.5, according to the standards ASTM E-490-00 and ASTM G-173-03, respectively. The difference between the two curves is due to the atmospheric attenuation of certain wavelengths.

dependence with AM. Furthermore, the AOD is difficult to predict with high accuracy, as it depends on unpredictable events like wind characteristics, presence of urban haze, and even volcanic eruptions. In other words, the clear-sky irradiance is best modelled with a physics-based model, such as McClear [95].

McClear clear-sky surface irradiance model [95] is a free web service developed by MINES ParisTech and Transvalor Dpt SoDa, which estimates clear-sky surface irradiance data during both clear and non-clear periods. It is based on a radiation transfer model called libRadtran, and uses many input parameters such as:

- Latitude, longitude and elevation above mean sea level of the site of interest
- Total column content of ozone and water vapour
- Standard atmospheric profile
- Aerosol optical depth (AOD) at 550nm, Angstrom coefficient, and aerosol type (urban, continental clean, continental polluted, continental average maritime clean, maritime polluted, maritime tropical, antarctic, and desert)
- Ground albedo

The result is up to 1-minute resolution time-series data of ground-level direct and diffuse components of clear-sky irradiance, with worldwide coverage. Figure 4-2 shows the beam normal and diffuse horizontal irradiances on 16. August 2013, as measured at

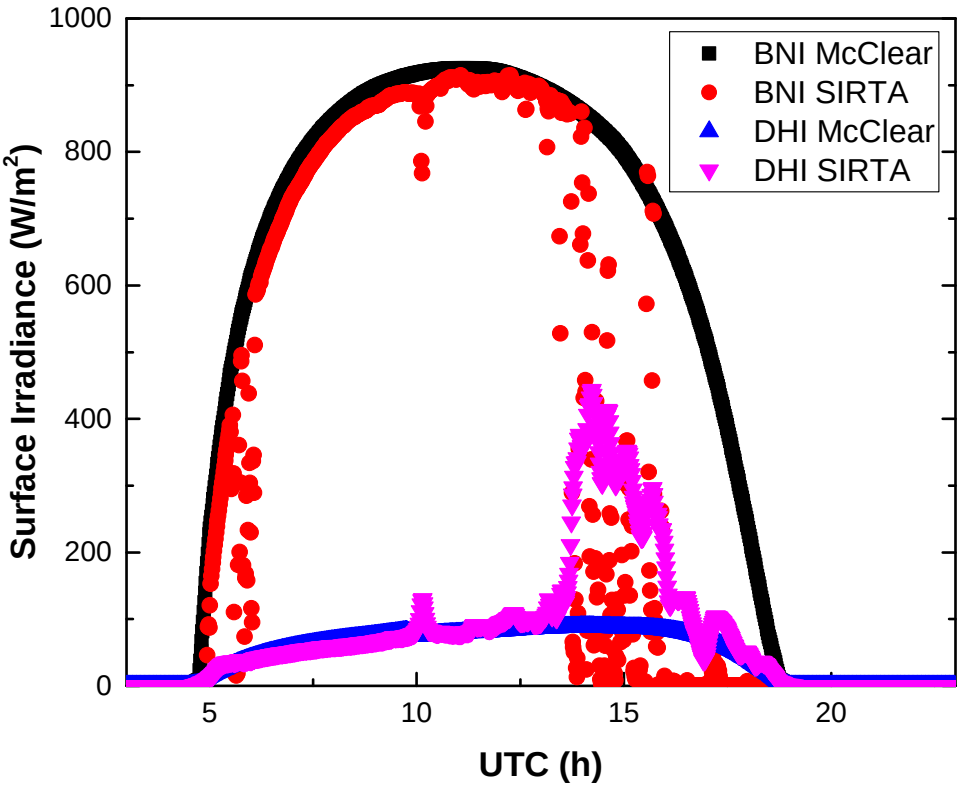

Figure 4-2: Measured and McClear-estimated surface irradiance on 16. August 2013. The day was relatively clear in the morning, and cloudy in the evening.

SIRTA, as well as estimated by McClear for the location of SIRTA. The day was relatively clear in the morning, and cloudy to overcast in the afternoon. McClear model extrapolates the clear-sky condition to the non-clear periods. As seen in the figure, McClear predicts with acceptable accuracy the direct and diffuse components in true clear-sky conditions (in the morning).

4.3.1 Curve Fitting

It is often useful to have models of the clear-sky irradiance in the form of mathematical equations. For example, this allows for an easy implementation into existing codes while eliminating the need to store the irradiance data on the disk. Furthermore, the use of continuous equations guarantees a smooth evolution of the irradiance components, which is not guaranteed with McClear[1]. Dazhi et al. [96] compared several clear-sky models, and concluded that the Adnot model is the best performer despite its simplicity. The Adnot model is an empirical model for the global horizontal irradiance often cited in the literature [92]:

$$GHI_{ClearSky} = a\cos(\theta_Z)^b \tag{4.1}$$

[1]Due to the live recalibration of the McClear model (for example, with newly available clear-sky irradiance measurements), the resulting data occasionaly include a slight jump or drop in irradiance

where θ_Z is the solar azimuth angle, and a and b are empirically derived coefficients. Adnot proposes the values a and b of 951.39 W/m^2 and 1.15, respectively. Dazhi et al. show that the Adnot coefficients a and b have to be adjusted for every location. As a result of the internship of Gwennaëlle Le Bars in LMD in 2014, the b coefficient was found to equal 1.2 for the Palaiseau location. Using 4 years of McClear data (2011-2014), *ideal* values of a were found for each day using the Levenberg-Marquardt optimisation algorithm. When plotted against the day number (J), a was observed to vary sinusoidally throughout the year. For this reason, the following correlation is proposed to be fitted through McClear data:

$$GHI_{ClearSky} = G_{day}[\sin(\alpha)]^{1.2} \quad , \alpha \geq 0 \tag{4.2}$$

where G_{day} is a constant that depends on the day number and α is the solar altitude. Using the same algorithm, the dependence of G_{day} on J was fitted as follows:

$$G_{day} = G_1 \sin(2\pi/365.24 \times J + G_2) + G_3 \tag{4.3}$$

yielding coefficients summarised in Table 4.1.

The decomposition of GHI is often represented with the diffuse fraction coefficient:

$$k_d = \frac{DHI}{GHI} \tag{4.4}$$

The diffuse fraction coefficient is then proposed to be described with the following correlation (inspired by Hottel [97], who developed an empirical model of the atmospheric transmittance with respect to direct flux):

$$k_d = R_{day} + S_{day} * \exp\left[\frac{-T_{day}}{\sin(\alpha)}\right] \quad , \alpha > 0 \tag{4.5}$$

where R_{day}, S_{day}, and T_{day} are constants that depend on the day number, and α is the solar altitude.

Similarly to the case of G_{day}, the *ideal* values of R_{day}, S_{day}, and T_{day} were found to evolve sinusoidally throughout the year, resulting in the following fits:

$$R_{day} = R_1 \sin(2\pi/365.24 \times J + R_2) + R_3 \tag{4.6}$$

$$S_{day} = S_1 \sin(2\pi/365.24 \times J + S_2) + S_3 \tag{4.7}$$

$$T_{day} = T_1 \sin(2\pi/365.24 \times J + T_2) + T_3 \tag{4.8}$$

and yielding coefficients summarised in Table 4.1.

With the knowledge of GHI and k_d, the values of DHI, BHI, and BNI can be calculated

Table 4.1: McClear fitting parameters

GHI Parameters		k_d **Parameters**	
G_1	85.51527	R_1	-0.00522
G_2	20.08476	R_2	0.91013
G_3	1105.36539	R_3	0.927
		S_1	0.01912
		S_2	0.61116
		S_3	-0.84682
		T_1	0.01627
		T_2	-1.13162
		T_3	0.11283

as follows:

$$DHI = GHI \times k_d \tag{4.9}$$

$$BHI = GHI \times (1 - k_d) \tag{4.10}$$

$$\begin{aligned} BNI &= \frac{BHI}{\sin(\alpha)} \\ &= \frac{GHI \times (1 - k_d)}{\sin(\alpha)} \end{aligned} \tag{4.11}$$

Note that (4.2) evaluates to 0 as $\alpha = 0$, while in reality the DHI and GHI are positive for a short time before sunrise and after sunset. However, the values of DHI when $\alpha \leq 0$ are relatively small, and the addition of an extra term to correct this discrepancy proved to have no impact on the model performance. Note also that (4.9) produces a DHI curve symmetrical about the solar noon, while the McClear model for DHI produces slightly higher irradiance values in the afternoon (see Fig. 4-2).

Figure 4-3 presents the performance of the two fitting functions, against the same 4 years used to calibrate it. Both fitting functions show a high performance, shown by the close proximity of red squares (representing high bin counts) to the $y = x$ line. The RMSE is on the order of 30 W/m^2

In Fig. 4-3d, one can note that the model sometimes underestimates the periods of high DHI suggested by McClear. As aerosol measurements are used to predict hypothetical clear-sky conditions, the McClear DHI values are most likely elevated due to a high aerosol concentration. In that regard, the proposed fit represents irradiance values associated with an average concentration of aerosols.

This methodology can be employed to extract the McClear fitting parameters at locations other than Palaiseau.

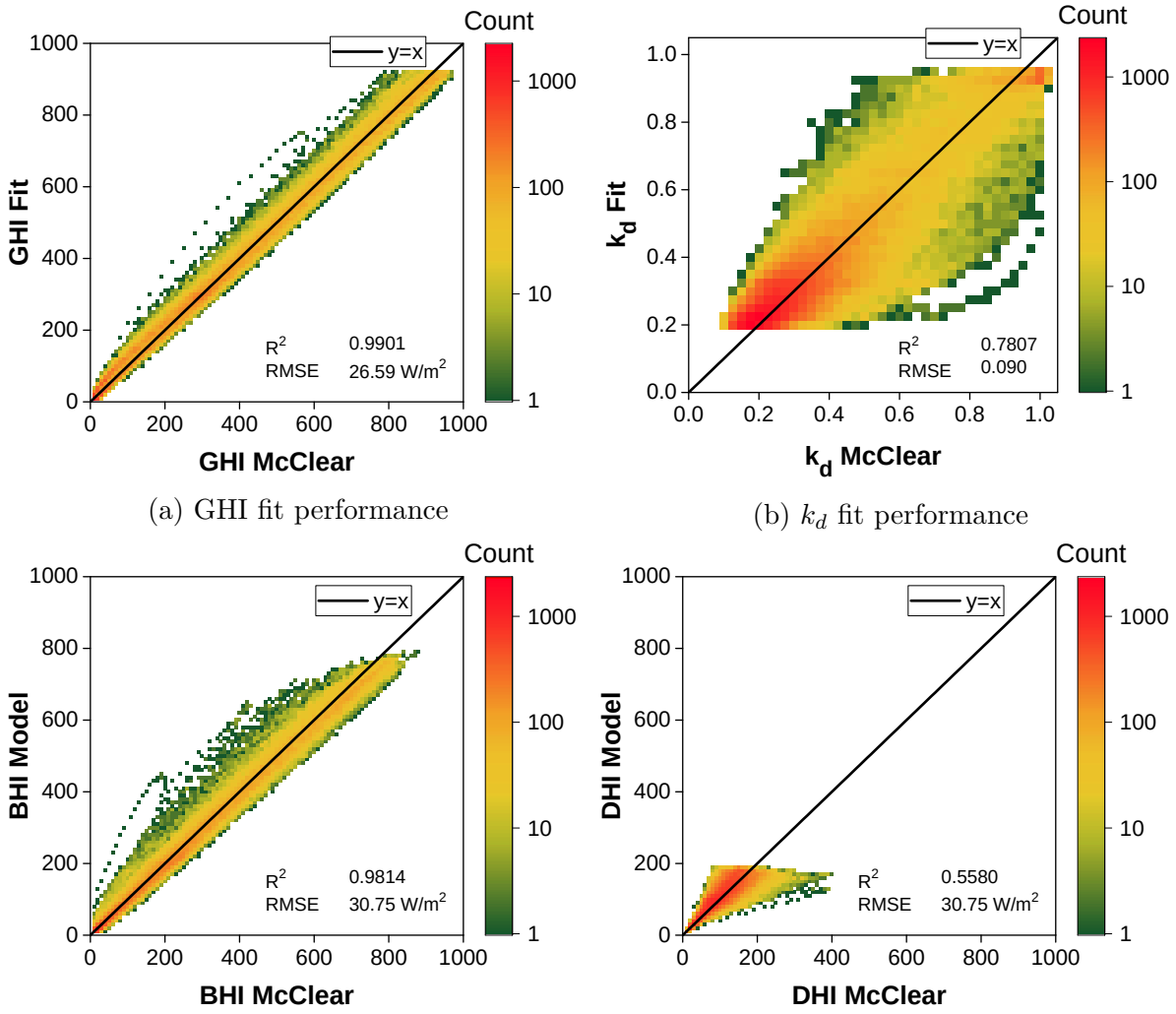

(a) GHI fit performance

(b) k_d fit performance

(c) BNI fit performance

(d) DHI fit performance

Figure 4-3: 2D histograms representing the performance of the fitting functions for (a) GHI, (b) k_d, (c) BHI, and (d) DHI, against the same 4 years of data. Figures (c) and (d) were reproduced using the McClear GHI and modelled k_d. The fitting functions show a high performance, indicated by the close proximity of red squares (representing high bin counts) to the $y = x$ line.

4.4 Surface Irradiance: Satellite Imagery Estimates

The clear-sky model described previously is useful for certain tasks. However, real surface irradiance data for a wide range of locations are necessary for the following tasks:

- geometrical optimisation of PV systems at different locations (subjected to different climates)
- comparing the interest of the PV+Reflector system in different locations

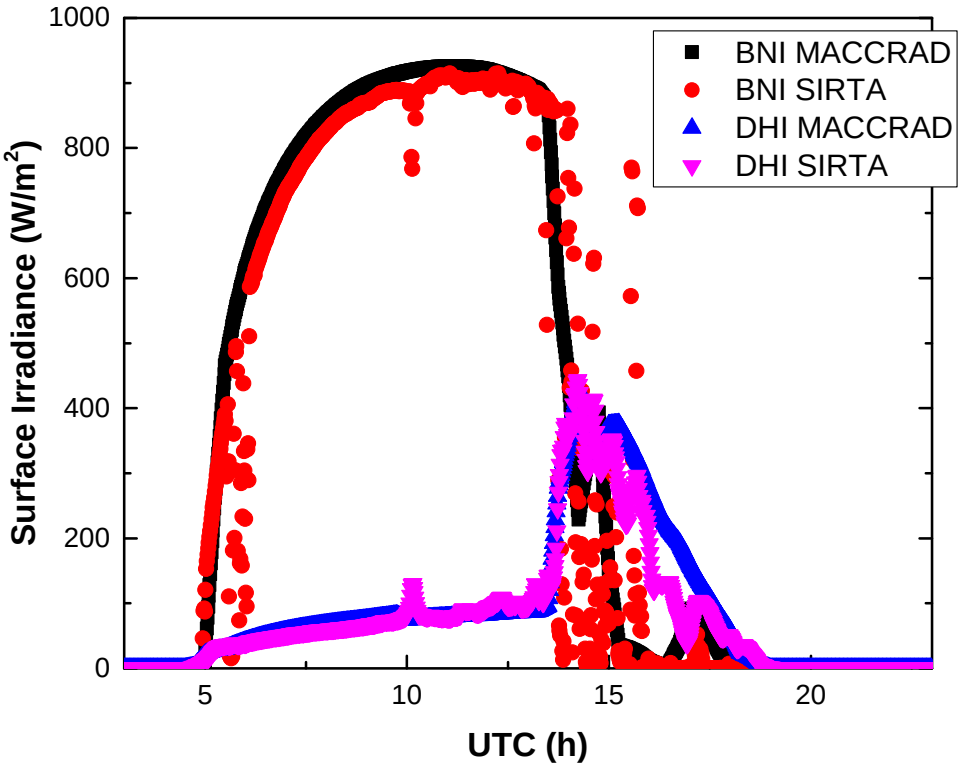

Figure 4-4: Measured and MACC-RAD-estimated surface irradiance on 16. August 2013.

One approach is to seek publicly available ground irradiance measurements. The following issues arise with this approach:

- the quality of the measurements is highly questionable (maintenance, alignment of the shading ball...)
- metadata (e.g. type of measurement apparatus, spectral range being integrated, time reference...) is often not provided, and hard to deduce from the data alone
- the availability of data for a particular location of interest is not guaranteed

One publicly available[2] database of surface irradiance data is the Baseline Surface Radiation Network (BSRN) maintained by the World Radiation Monitoring Center (WRMC). The data is voluntarily contributed by the BSRN stations (e.g. SIRTA station), which measure various components of surface irradiance meeting strict quality criteria for measurements and storage of data. However, the BSRN stations are geographically fairly scarce.

For this reason, the MACC-RAD surface irradiance model [98] was used. Like McClear, it is a free web service developed by MINES ParisTech and Transvalor (Department SoDa). The model uses the previously described McClear model along with MSG satellite measurements to estimate surface irradiance data. As the satellite images are available every 15 minutes, the result is 15-minute time-series data of ground-level direct and diffuse components. The geographical coverage is equal to the view of the MSG (MeteoSat

[2]for R&D purposes

Second Generation) satellite (Europe, Africa, parts of North and South Americas, and a part of Asia). Note that due to the limited satellite view of the northern-most parts of Europe, parts of Scandinavian countries are not covered.

Figure 4-4 shows the beam normal and diffuse horizontal irradiances on 16. August 2013, as measured at SIRTA, as well as estimated by MACC-RAD for the location of SIRTA. It can be noted that the increase in the diffuse component with the presence of clouds is well predicted. One can also note that the rapid fluctuations in the beam irradiance are not reproduced by MACC-RAD, which is expected due to a 15-minute resolution of satellite images. The MACC-RAD model was further tested for validity in Fig. 9-1 of Sec. 9.1.1, using a 4-year dataset of MACC-RAD and SIRTA irradiances and comparing the weekly gains in transmitted energy.

4.5 Discussion

The Sun's position was described using established equations and fitted empirical correlations. The model for clear-sky and actual ground irradiances depends uniquely on the data provided by SoDa through their McClear and MACC-RAD web services.

The advantage of McClear and MACC-RAD models is twofold: 1) the estimated irradiances are based on a validated physics model, giving it a certain degree of reliability, and 2) the ground coverage is very large (whole world for McClear and the view of the MSG satellite for MACC-RAD), allowing for a relative comparison of different climates.

A fit of the McClear data for Palaiseau was performed, relying on modelling the decomposition of global irradiance into direct and diffuse parts. The advantages of having a fit through McClear data are that it:

- provides smooth direct and diffuse irradiance profiles compared to the raw McClear data, which have discontinuities due to real-time model calibration performed by SoDa
- represents an average concentration of aerosols, allowing for a correct accounting of the seasonal aerosol impact without the need to run the model on several years of data (otherwise necessary to avoid a bias caused by rare aerosol fluctuations)
- eliminates the need of text files containing the McClear-calculated irradiances, facilitating implementation and execution

In the next chapters, McClear will be used each time clear-sky irradiance is sought for, and MACC-RAD will be used for obtaining ground-level irradiance values for sites other than Palaiseau.

THIS PAGE INTENTIONALLY LEFT BLANK

Chapter 5

Optical Modelling

As photovoltaics is the direct conversion of light into electricity, precise PV system modelling requires the understanding of the path of photons from the Sun's surface to the PV cell. The previous chapter details some modelling techniques for estimating ground irradiance values. This chapter presents the experimental and modelling works regarding the optical aspects on a system level.

Section 5.2 presents the experimental measurements carried out at the GeePs laboratory to test the reflector and PV module front glass optical properties, as well as typical spectral responses. Section 5.3 details the modelling of angular optical losses as the solar irradiance interacts with two multi-layer interfaces: reflector and PV modules.

As a first approximation, an analytical optical model with an infinite-row assumption (IRM) of the system was developed in C++ to evaluate the approximate gain in produced electricity over the typical PV power plant installation. The model was validated with experimental measurements, and used to highlight the advantages of the reflector-equipped system over the classical installation as well as the PV tracker. The IRM is discussed in Section 5.4.

As described later, the IRM had certain limitations such as the lack of flexibility to change the system setup (e.g. addition of supplementary mirrors, or different geometry), and the disability to accurately describe the spatial distribution of the diffuse module irradiance accounting the impact of the reflector. This called for the development of a more flexible and more precise optical model, employing ray-tracing and the Monte Carlo method. The EDStaR Environment was used to evaluate the distribution of solar flux arriving on the PV module due to direct and diffuse solar radiations, given the characteristics of the system (e.g. geometry, optical properties) and the characteristics of the solar resource (e.g. position of the Sun). EDStaR is further discussed in Section 5.5.

5.1 State of the Art

Optical aspects of PV modules and reflectors has been studied extensively in the literature [8,10,20,34,99–112]. Most authors studied the fate of photons when encountering specular surfaces, though the impact of surface roughness on the mirror reflectance performance has been studied in the past [20, 99–101, 104]. When evaluating various optical losses occurring at multi-layer interfaces, several authors propose the application of Snell's law using different materials' optical properties (e.g. refractive index) [101, 102, 106, 108, 109, 111]. Polyanskiy [113] provides a refractive index database for common materials.

5.2 Laboratory Measurements

Laboratory measurements are an important step in PV systems modelling, reducing the modelling uncertainty and eliminating the need for an additional parameter to be calibrated with outdoor measurements. This section presents the reflectance and spectral response measurements performed in the GeePs laboratory on 18 December 2014, with the help of Alexandre Jaffré.

5.2.1 Optical Characterisation

The following optical characterisation measurements were desirable, but due to various reasons not possible to be performed:

- reflectance and transmittance properties of the *p*-Si module front glass, due to its unavailability
- transmittance properties of the *a*-Si:H module front glass, due to its unavailability. A module sample was available, but the glass could not be separated to perform the test.
- *angular* spectral reflectances and transmittances of all samples, due to the unavailability of adequate equipment[1].

The following samples were available for laboratory testing:

- two reflector samples, one of which was attached to the experiment during a 2-week period to represent soiling effects
- two *a*-Si:H module samples, which were cut from real modules and therefore include all the layers on top of the PV cell

[1]Tests were performed in the GeePs laboratory with the Perkin Elmer Lambda 950 and the Universal Reflectance Accessory (URA), and yielded strange angular reflectance data. For example, as the incidence angle was increased, the specular reflectance of a mirror sample seemed to decrease. This is contrary to the prediction of Snell's law, which predicts total reflection as the angle approaches 90°. Due to the significant thickness of the glass layer, a possible explanation is that the beam traverses a significant path before exiting the sample, and as the incidence angle is increased, the reflected beam misses the detector by an increasing margin.

Due to the opaque nature of these samples, reflectance measurements are the only ones applicable.

For a given wavelength, the global reflectance is composed of two components:

$$R_{global} = R_{specular} + R_{diffuse} \tag{5.1}$$

where $R_{specular}$ is the specular reflectance (beam is reflected at an angle equal and opposite to the angle of incidence), and $R_{diffuse}$ is the diffuse reflectance (beam is diffused in all directions). $R_{diffuse}$ is correlated with material roughness, and is usually very low for smooth surfaces like mirrors.

Reflectance measurements were performed using the Perkin Elmer Lambda 950 spectrometer in GeePs. To acquire both the global and diffuse reflectances of the samples, the integrating sphere attachment of 150 mm diameter was introduced in the spectrometer. The angle of incidence was set to 8°, and the wavelength of the incident beam was varied from 250 to 1300 nm with a step of 5 nm.

The following two measurements were performed on each of the samples:

1. diffuse spectral reflectance, where the specularly reflected beam was allowed to exit the sphere through a small hole
2. global spectral reflectance, where the exiting hole was closed

Note that during the diffuse reflectance measurements, the hole used to let the specular beam exit lets escape a small fraction of the diffused light. The resulting underestimation of diffuse reflectance was estimated by Perkin Elmer to be less than 2% [114], which is acceptable for our purposes.

Figure 5-1 presents the results for the *a*-Si:H module samples. One can note oscillations in the curve for certain wavelengths. This is likely due to the interferances between photons relfected from the first layer and those reflected from lower layers of the *a*-Si:H PV cell. The global reflectance is less than 12% in the visible and UV ranges. Compared to untreated silicon surface [115], the reflectance characteristic is indicative of the application of a certain anti-reflection coating (ARC). Note that the reflectance of wavelengths in the near-infrared reaches 36%. This will not reduce the *a*-Si:H module conversion efficiency due to its narrow spectral response centred around 560 nm (see Fig. 5-3). In fact, it has a potential in increasing the efficiency by reducing the heating of cells.

Figure 5-2 presents the results for the reflector samples. One can note a more regular response compared to the *a*-Si:H samples, reflecting up to 95% of the rays in the range of 500-600 nm, about 78% in the range of 1000-1200 nm, and a negligible amount for wavelengths below 350 nm. Note that the reflector sample R1 was cleaned before the test, while the sample R2 was exposed to outdoor conditions for two weeks without being cleaned. The sample had visible dirt on its surface. As seen in the figure, this resulted in about 2% of light being diffused across most wavelengths, and in very minor impact

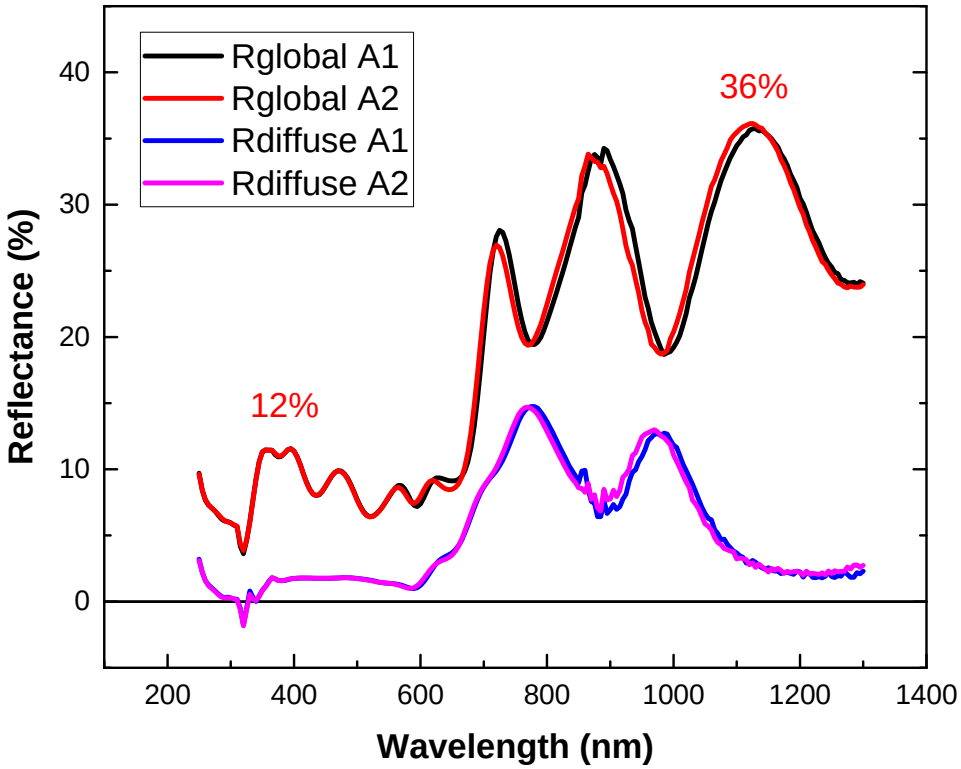

Figure 5-1: Laboratory measurements of total and diffuse reflectance as a function of wavelength for two *a*-Si:H samples.

on total reflectance.

Negative reflectances in Fig. 5-1 could be a sign of a problem of calibration or the equipment in general. At the time of writing, this problem could not be resolved.

5.2.2 Spectral Response

Due to technical and administrative constraints, the tandem-cell *a*-Si:H modules and *p*-Si modules in the experiment, respectively, could not be characterised for spectral response. Nevertheless, spectral response measurements have been carried out in GeePs for similar materials: a typical single junction *a*-Si:H cell and a typical *c*-Si cell (courtesy of Christophe Longeaud). Fig. 5-3 shows the result of the characterisation, with the AM1.5 spectrum given as a reference. The curves give the information about the energy gap of each material, being 1.63 and 1.13 eV for the *a*-Si:H and *p*-Si cells, respectively. Photons with energies lower than the material energy gap do not contribute to electricity production (indicated with red and blue hatch), and instead heat the module. Note that the *c*-Si cell absorbs a wider range of the solar spectrum. Furthermore, within the common range of active wavelengths the *c*-Si cell produces a higher current per Watt of light of a given wavelength compared to the *a*-Si:H cell. These two factors result in the *c*-Si module having a higher overall conversion efficiency than that of the *a*-Si:H cell under the spectrum AM1.5.

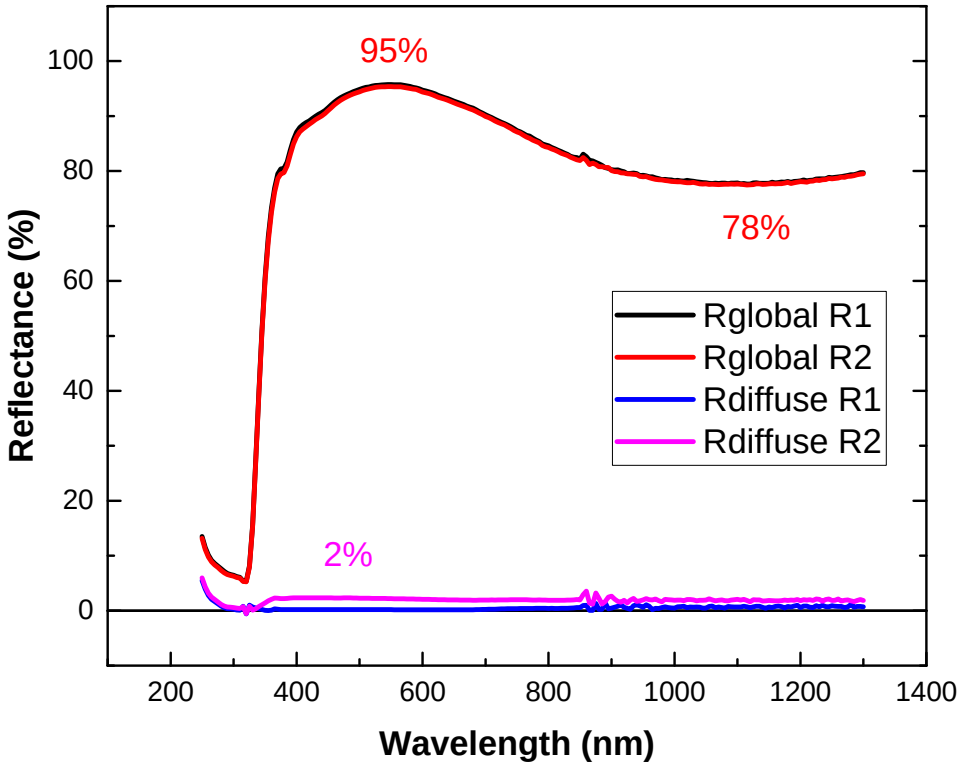

Figure 5-2: Laboratory measurements of global and diffuse reflectance as a function of wavelength for two reflector samples. Reflector sample R1 was cleaned before the measurement was taken. Reflector sample R2 was left in exterior conditions for two weeks, with visible dust on the surface, resulting up to 2% of incident flux being diffused.

Figure 5-3 also shows the measured spectral reflectance of the reflector (black curve). The reflector seems well adapted for reflecting the short wavelengths, which contribute most to electricity production. Visually, the reflectance curve corresponds better to the spectral response curve of the *a*-Si:H cell compared to *c*-Si since the peak of the *a*-Si:H SR is aligned with the peak of reflectance, while the peak of the *c*-Si SR is aligned with the valley. To quantify this difference, the *effective* spectral reflectance can be evaluated for each PV technology which takes into account the mirror reflectance, the PV module front glass transmittance, the solar spectrum (normalised) and the spectral responses of each PV cell (normalised):

$$\rho_{Ref,Effective}(\theta', \lambda) = SS_N(\lambda) \times \rho_{Ref}(\theta', \lambda) \times \tau_{PVGlass}(\theta", \lambda) \times SR_N(\lambda) \qquad (5.2)$$

where SS_N is the normalised solar spectrum, ρ_{Ref} is the mirror spectral reflectance, $\tau_{PVGlass}$ is the PV front glass spectral transmittance, SR_N is the normalised spectral response of a given PV technology, θ' is the incidence angle on the reflector, θ" is the incidence angle of the reflected beam on the PV module, and λ is the wavelength.

Figure 5-4 presents the application of (5.2) with the following inputs:

- solar spectrum AM1.5

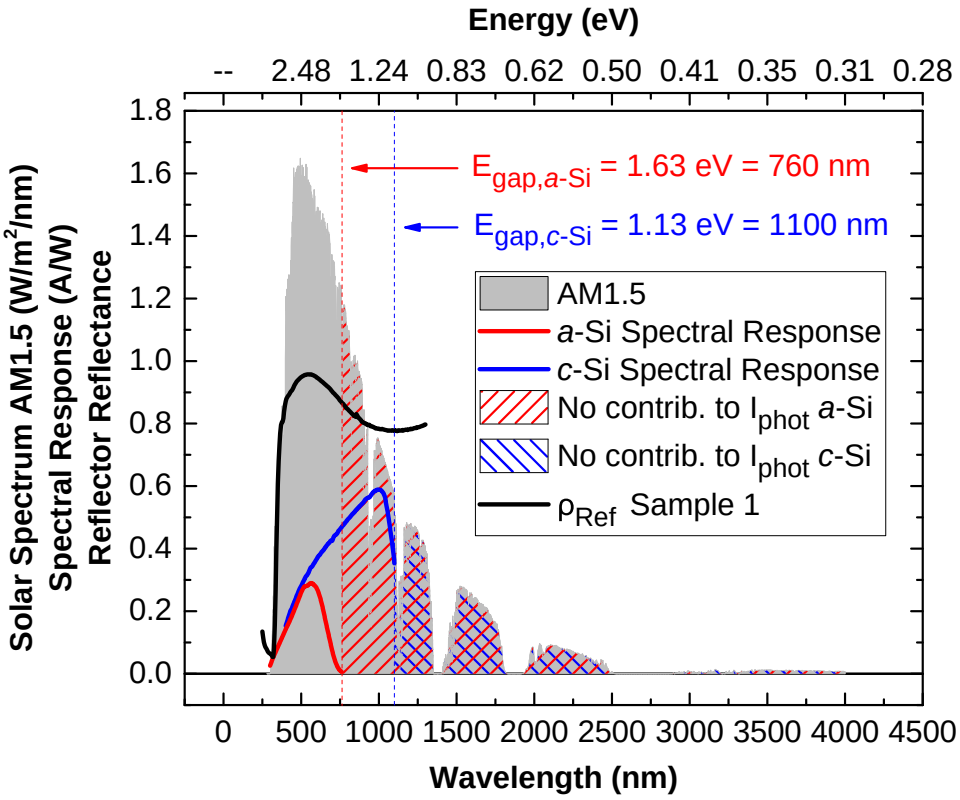

Figure 5-3: Measured spectral response of typical *a*-Si:H and *c*-Si modules (not the ones in the experiment). The AM1.5 spectrum and the reflector reflectance are given as a reference.

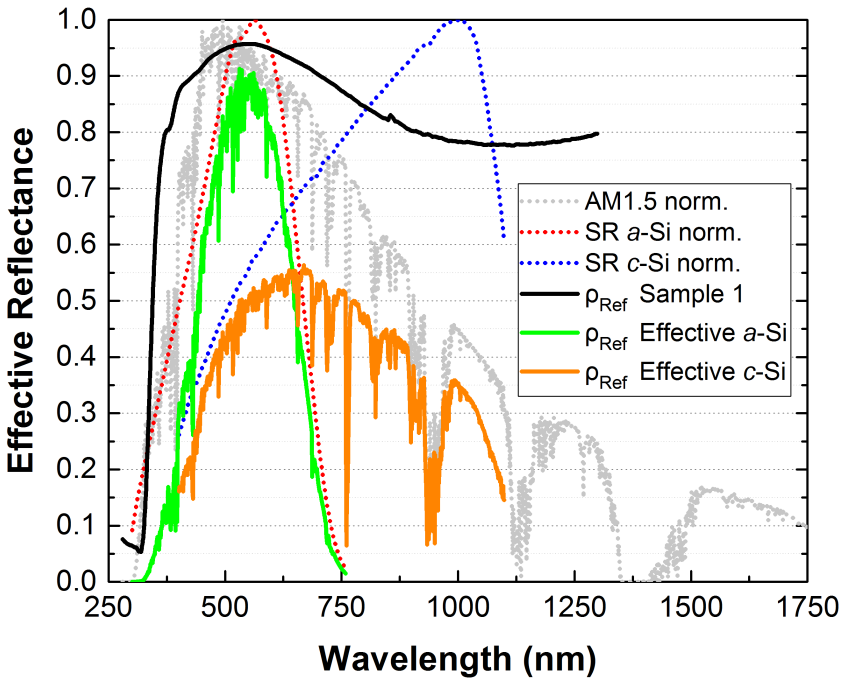

Figure 5-4: Calculated effective reflector reflectances for *a*-Si:H cells (green) and *c*-Si cells (orange), taking into account their spectral responses and the solar spectrum AM1.5. The effect of spectral transmittance is not incorporated here.

- measured reflectance at 8° incidence
- measured spectral response of each cell

while the PV glass transmittance was not taken into account due to the unavailability of data. The effective reflectance for *a*-Si:H peaks at 91%, while the equivalent for *c*-Si is at 56%. The average value of effective reflectance (across all applicable wavelengths) is obtained by integrating these curves and dividing by the domain size, giving 44% and 39% for *a*-Si:H and *c*-Si, respectively. Therefore, higher gains are expected for the *a*-Si:H compared to *c*-Si. Since the *a*-Si:H and *c*-Si spectral response measurements used here are believed to be similar to the cells in the experiment, the reflector is expected to produce higher gains for the *a*-Si:H modules in the experiment compared to the *p*-Si modules. Note that had the transmittance been incorporated, the difference in effective reflectance would further increase. Since the transmittance of most industrial glass is the highest in the visible range and commonly drops in the near infra-red [116], *a*-Si:H modules are favoured compared to *c*-Si.

An improved reflector for LCPV applications would:

- have a higher reflectance in the active wavelengths (contributing to electricity production)
- not reflect the low energy wavelengths (specifically, the ones corresponding to energies below the energy gap of the semiconductor), to reduce the adverse heating of the module

5.3 Snell's Law

Snell's law (also known as the Snell–Descartes law and the law of refraction) is a law describing the way light gets refracted when passing from one medium to another (see Fig. 5-5). It states that the ratio of sines of the angles of incidence and refraction is equal to the ratio of phase velocities in the two media, or equivalently to the reciprocal of the ratio of the indices of refraction:

$$\frac{\sin\theta_1}{\sin\theta_2} = \frac{v_1}{v_2} = \frac{\lambda_1}{\lambda_2} = \frac{n_2}{n_1} \tag{5.3}$$

Figure 5-6 presents the different material layers that photons interact with. Note that there are additional layers beneath the shown structures (e.g. mirror backsheet, metalic contacts, tedlar...) which do not interact with photons. Regarding the interaction with photons, the reflector is composed of a sheet of aluminum, covered with a layer of glass. The *a*-Si:H module is composed of a thin sheet of amorphous silicon, a SnO_2 layer, and glass. The *p*-Si module is composed of a sheet of polycrystalline silicon, an anti-reflection coating, the EVA encapsulant, and glass.

Snell's law was used to describe the behaviour of light when striking a reflector or a

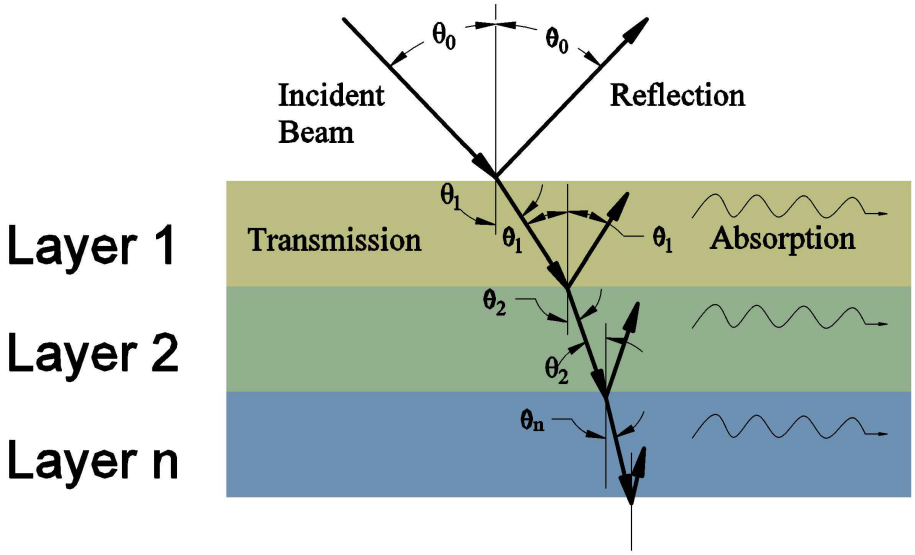

Figure 5-5: Snell's law: light is refracted as it passes into a medium with a different refraction index.

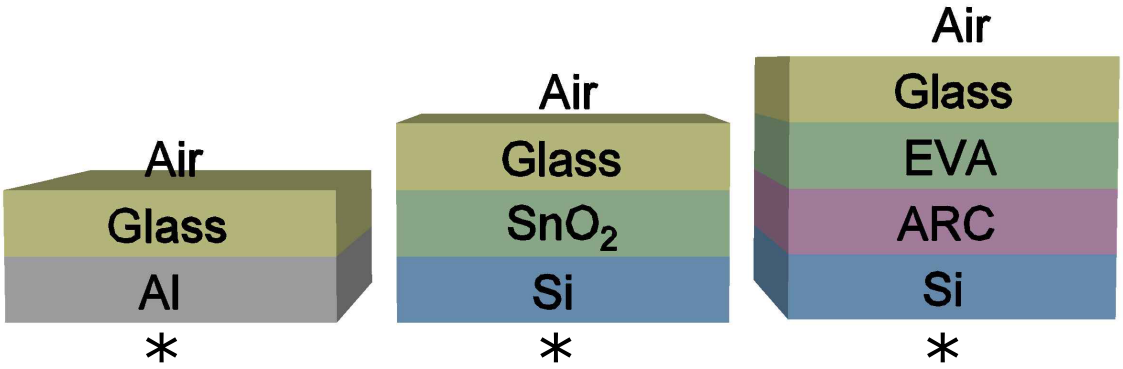

Figure 5-6: Principal material layers that photos interact with, present on the reflector (left), *a*-Si:H module (center), and *p*-Si module (right). Note that there are additional layers (not shown) below the presented structure, which do not interact with photons. The layer thicknesses are not to scale.

given PV module surface as a function of the angle of incidence. The optical properties of the media involved were found in the Polyanskiy refractive index database [113]. The reflector and the *p*-Si module were considered to have a better performance front glass than the *a*-Si:H module (with higher transmittances and lower absorption coefficients). The two types of glass were parametrised using manufacturer data corresponding to two variants of glass made by Saint Gobain: "SGG Diamant" (better-performing) and "SGG Planiclear" (worse-performing). The parameters are summarised in Table 5.1.

The absorption was considered to occur only in the glass layer, and was integrated for three principal reflections. The optical performances (absorptance, transmittance and reflectance) of the reflector, *a*-Si:H module and *p*-Si module interfaces were evaluated for all angles of incidence, θ, with a step of 0.5°. The results of the simulation are shown in

Table 5.1: Inputs for the optical interface model based on Snell's law. Thicknesses and absorption coefficients are only shown for the glass layers where absorption losses were evaluated as a function of distance traversed by the photons.

Layer	n	**Thickness**	**Absorption Coefficient**
Air	1.0003	-	-
Glass SGG Diamant	1.520	3 mm	0.00376 mm^{-1}
Glass SGG Planiclear	1.527	3 mm	0.0237 mm^{-1}
Al	1.097	-	-
SnO_2	2.045	-	-
EVA	1.482	-	-
ARC	2.1	-	-
Si	3.690	-	-

Figs. 5-7, 5-8, and 5-9 for the reflector, *a*-Si:H, and *p*-Si interfaces, respectively.

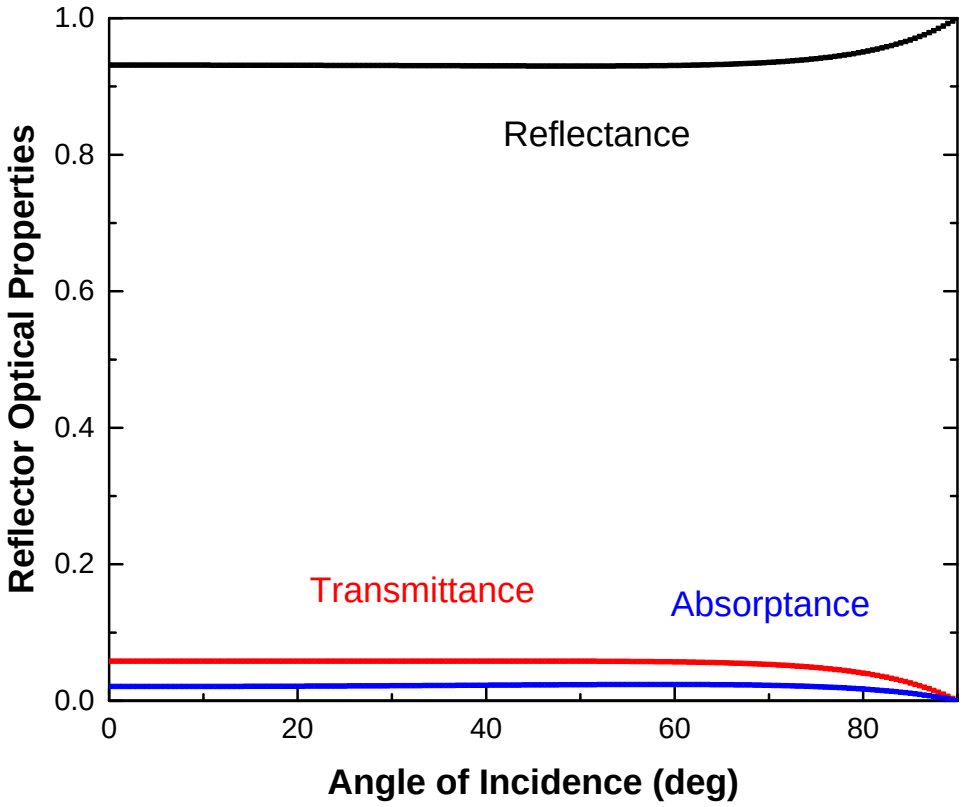

Figure 5-7: Modelled optical performance of the reflector.

All three samples exhibit little change in optical behaviour for angles of incidence between 0 and 45°. Similarly, total reflection is observed for all three samples when the angle of incidence approaches 90°. As expected, the better performing front glass on *p*-Si modules compared to *a*-Si:H modules results in a higher transmittance across all the angles of incidence.

To avoid the application of Snell's during future simulations, it has been decided to fit polynomials through certain simulation results. To keep the fitted curves flat at

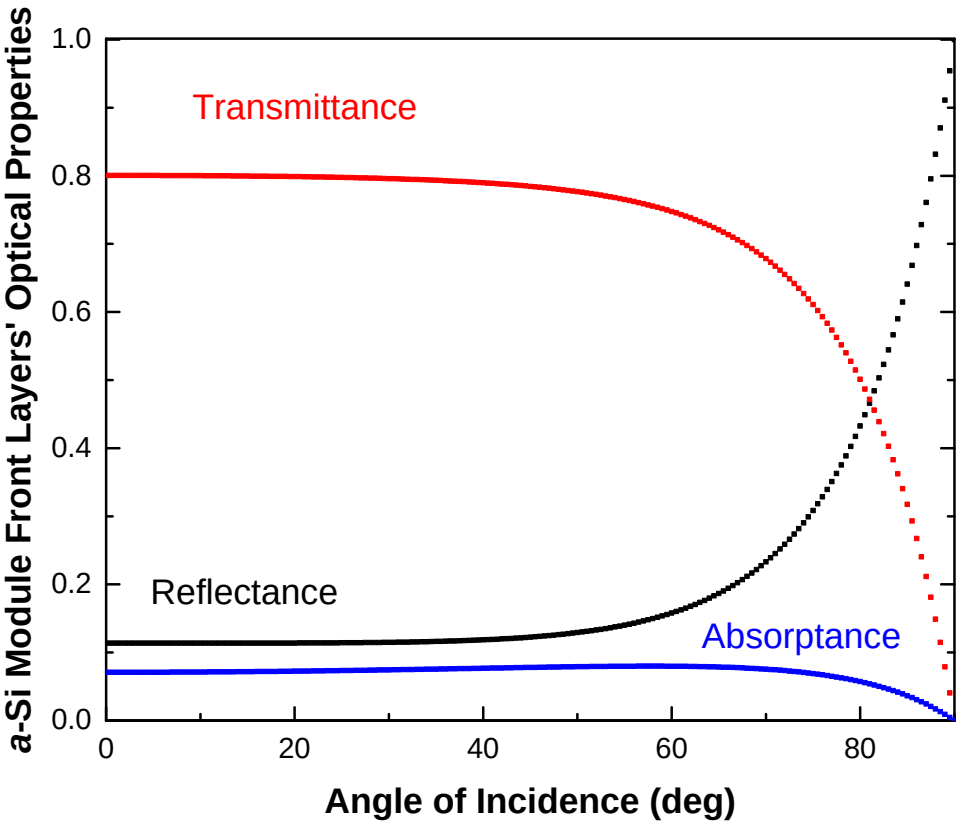

Figure 5-8: Modelled optical performance of the *a*-Si:H module front layers.

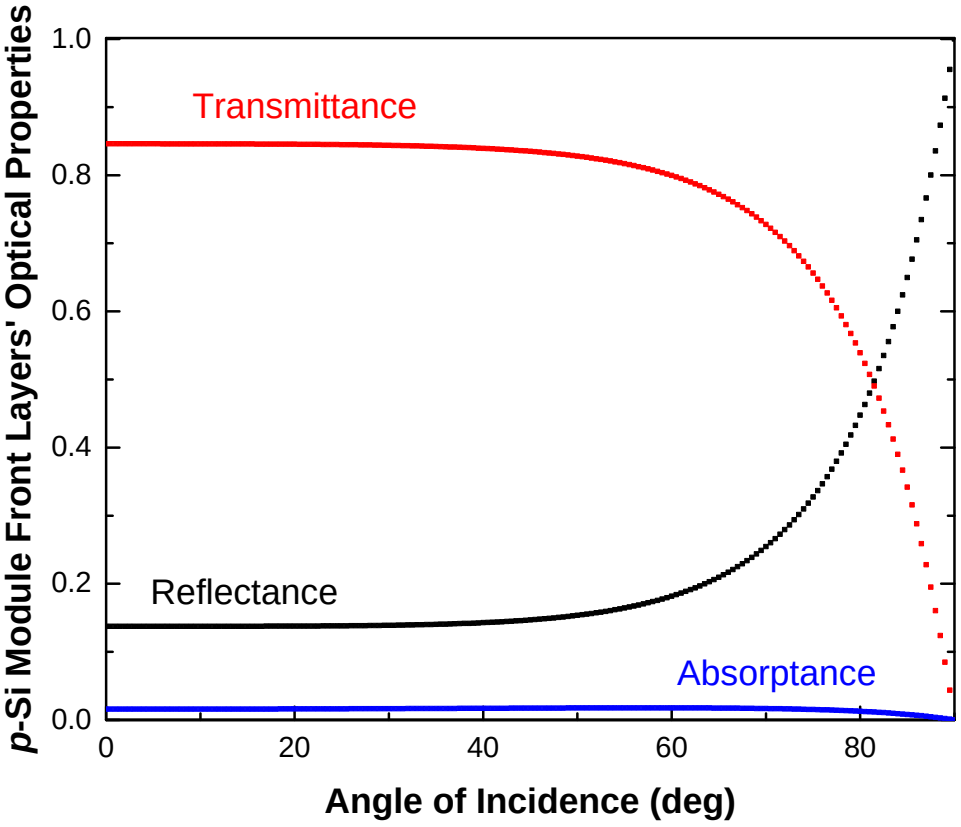

Figure 5-9: Modelled optical performance of the *p*-Si module front layers.

low incidence angles, high-order polynomials were necessary. For example, fifth order polynomials were fitted through the modelling results of the mirror angular reflectance (Fig. 5-7), yielding Equation (5.4) and an R^2 of 9.984×10^{-1}.

$$\begin{aligned}\rho_{Ref}(\theta) = {} & 1.789 \times 10^{-10}\theta^5 - 3.087 \times 10^{-8}\theta^4 + 1.941 \times 10^{-6}\theta^3 - 5.253 \times 10^{-5}\theta^2 \\ & + 5.225 \times 10^{-4}\theta + 9.300 \times 10^{-1}\end{aligned} \tag{5.4}$$

where θ is the angle of incidence in degrees.

Similarly, sixth order polynomials were fitted through the modelling results of the *a*-Si:H and *p*-Si module angular transmittances (Figs. 5-8 and 5-9), yielding Equations (5.5) and (5.6) and an R^2 of 9.999×10^{-1}. In these equations, θ is the angle of incidence in degrees.

$$\begin{aligned}\tau_{a-Si:H}(\theta) = {} & -2.894 \times 10^{-11}\theta^6 + 6.169 \times 10^{-9}\theta^5 - 5.140 \times 10^{-7}\theta^4 + 2.013 \times 10^{-5}\theta^3 \\ & - 3.731 \times 10^{-4}\theta^2 + 2.670 \times 10^{-3}\theta + 7.961 \times 10^{-1}\end{aligned} \tag{5.5}$$

$$\begin{aligned}\tau_{p-Si}(\theta) = {} & -3.118 \times 10^{-11}\theta^6 + 6.641 \times 10^{-9}\theta^5 - 5.533 \times 10^{-7}\theta^4 + 2.166 \times 10^{-5}\theta^3 \\ & - 3.983 \times 10^{-4}\theta^2 + 2.873 \times 10^{-3}\theta + 8.413 \times 10^{-1}\end{aligned} \tag{5.6}$$

The resulting polynomials yield an efficient way to evaluate the optical behaviour of the reflector and the module front layers, avoiding the direct application of Snell's law.

5.4 Analytical Optical Model

This section describes the simple analytical model developed for describing PV+Reflector systems.

5.4.1 Algorithm

The first approach in modelling the in plane irradiance resulting from the influence of reflectors was to develop an analytical model based on Cartesian geometry and the assumption of specular reflectors. To simplify the derivation of the equations, the rows of the PV-modules and reflectors were assumed to be infinitely long. The consequence of this is that any light reflected in the azimuthal direction is considered to contribute to the incident flux on the module. This assumption may be valid for real rooftop or field installations where the rows can be considered long. Since the rows in the experiment are finite and rather short, the assumption of infinite rows may overestimate the impact of reflectors in the morning and evening periods. Nevertheless, the model was decided to

be developed to serve as a reference for more detailed models.

Three principal cases of the system behaviour have been identified (see Fig. 5-10). s and s' are respectively the PV module and reflector inclinations in the meridian plane. α and γ_S are the solar elevation and solar azimuth angles. θ is the angle of incidence (AOI) of non-reflected beams with the PV module, θ' is the AOI of non-reflected beams with the reflector, and θ" is the AOI of reflected beams with the PV module. D is the inter-row spacing. b is the (vertical) distance between the ground and the upper edge of the module. y is the distance between the ground and the boundary between shaded and unshaded regions. z is the distance between the ground and the boundary between concentrated and unconcentrated regions. Similarly, w represents the distance between the ground and and the boundary separating useful from useless reflector regions (the part that is not useful reflects the photons *above* the PV module).

Let $\overrightarrow{\omega_0}$ and $\overrightarrow{\omega_1}$ represent the incoming and reflected rays, respectively. Let North, East, and up represent the positive x, y, and z directions, respectively. The x, y, and z components of $\overrightarrow{\omega_0}$ and $\overrightarrow{\omega_1}$ can be expressed as follows (considering a north-facing mirror inclined at an angle s'):

$$\begin{aligned}
\omega_{0x} &= \cos(\gamma_s)\cos(\alpha) \\
\omega_{0y} &= \sin(\gamma_s)\cos(\alpha) \\
\omega_{0z} &= -\sin(\alpha) \\
\omega_{1x} &= \cos(\alpha)\cos(\gamma_s)\cos(2s') + \sin(\alpha)\sin(2s') \\
\omega_{1y} &= \omega_{0y} = \sin(\gamma_s)\cos(\alpha) \\
\omega_{1z} &= \sin(\alpha)\cos(2s') - \cos(\alpha)\cos(\gamma_s)\sin(2s')
\end{aligned} \tag{5.7}$$

In the case of a sufficiently low solar altitude, α, partial or full shading of the PV module occurs according to the value of y/b, representing the shading fraction (see Fig. 5-10a). The ratio of shaded to total PV module surface is described with (5.8):

$$\frac{A_{shaded}}{A_{total}} = \frac{y}{b} = \frac{\sin(s)\left[\omega_{0z}\cot(s') + \omega_{0x}\right]}{\omega_{0x}\sin(s) - \omega_{0z}\cos(s)} \quad , \quad 0 \leq \frac{y}{b} \leq 1 \tag{5.8}$$

In the case of heterogeneous concentration (see Fig. 5-10b), the ratio of the highlighted to total PV module surface is given by (5.9):

$$\frac{A_{highlighted}}{A_{total}} = \frac{z}{b} = \frac{\sin(s)\left[\omega_{1z}\cot(s') + \omega_{1x}\right]}{\omega_{1x}\sin(s) - \omega_{1z}\cos(s)} \quad , \quad 0 \leq \frac{z}{b} \leq 1 \tag{5.9}$$

The localised and average concentration factors are given by (5.10) and (5.11):

$$C_{loc} = 1 + \frac{\rho_{Ref}(\theta')\sin(s)\cos(\theta')\tau(\theta")}{\sin(s')\cos(\theta)\tau(\theta)(z/b)} \quad , \quad C_{loc} \geq 1 \tag{5.10}$$

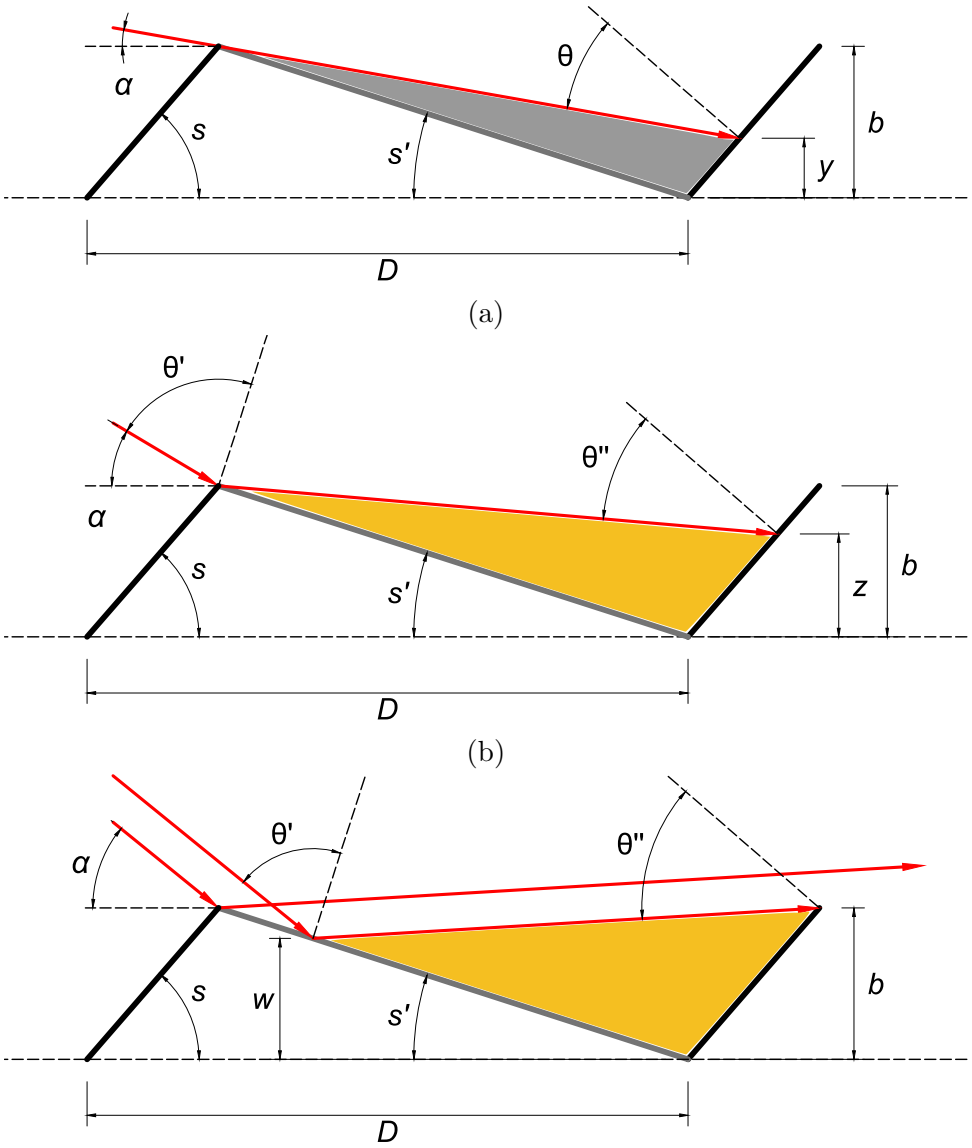

Figure 5-10: Three principal cases of the system behaviour: a) partial or total shading of the PV module, b) heterogeneous concentration and c) homogeneous concentration with a varying degree of utility of the reflector. The PV modules are denoted with thick black lines, the reflectors are denoted with thick gray lines, and the beam irradiance is denoted in red. The schematic is in the meridian plane.

$$C_{avg} = 1 + \frac{\rho_{Ref}(\theta')\sin(s)\cos(\theta')\tau(\theta")}{\sin(s')\cos(\theta)\tau(\theta)} \quad , \quad C_{avg} \geq 1 \tag{5.11}$$

where θ" is the angle of incidence of the reflected ray with PV module obtained with (5.12), $\rho_{Ref}(\theta')$ is the mirror reflectance as a function of angle of incidence, and $\tau(\theta)$ and $\tau(\theta")$ are the PV front glass transmittances as a function of the angle of incidence with the non-reflected and reflected rays, respectively.

$$\cos(\theta") = \cos(\gamma_s)\cos(\alpha)\sin(2s' + s) - \sin(\alpha)\cos(2s' + s) \tag{5.12}$$

Finally, in the case of homogeneous concentration (see Fig. 5-10c), indicated by a value of z/b greater than 1, the utility of the reflector can be found using (5.13):

$$\frac{A_{useful}}{A_{total}} = \frac{w}{b} = \frac{\omega_{1x} - \omega_{1z}\cot(s)}{\omega_{1z}\cot(s') + \omega_{1x}} \quad , \quad 0 \leq \frac{w}{b} \leq 1 \tag{5.13}$$

and the resulting concentration factor is given by (5.14):

$$C_{avg} = 1 + \frac{\rho_{Ref}(\theta')\sin(s)\cos(\theta')\tau(\theta")(w/b)}{\sin(s')\cos(\theta)\tau(\theta)} \quad , \quad C_{avg} \geq 1 \tag{5.14}$$

The diffuse irradiance was modelled using the isotropic sky model [117]. The total diffuse flux transmitted to cells of a PV+Reflector installation was evaluated by the means of view factors (see (5.15) and Fig. 5-11a).

$$\begin{aligned} \phi_{D,Trans,PV+R} &= celestial\ vault + reflector \\ &= \tau_D(D/L)DHI(F_{Sky-PV} + F_{Sky-Ref}\ \rho_{Ref,D}\ F_{Ref-PV}) \end{aligned} \tag{5.15}$$

where τ_D is the average PV front layers transmittance of the diffuse flux, taken as a constant; D/L is the inter-row distance to module height ratio, DHI is the diffuse horizontal irradiance, $\rho_{Ref,D}$ is the average reflector reflectance of the diffuse flux, taken as a constant; F_{Sky-PV} is the view factor from the sky to the PV module (see (5.16)); $F_{Sky-Ref}$ is the view factor from the sky to the reflector (see (5.17)); and F_{Ref-PV} is the view factor from the reflector to the PV module (see (5.18)).

$$F_{Sky-PV} = \frac{1 + (L/D) - \sqrt{1 + (L/D)^2 - 2(L/D)\cos(s)}}{2} \tag{5.16}$$

$$F_{Sky-Ref} = \frac{1 + (L/D)(\sin(s)/\sin(s')) - (L/D)}{2} \tag{5.17}$$

$$F_{Ref-PV} = \frac{\frac{\sin(s)}{\sin(s')} + 1 - (D/L)}{2\frac{\sin(s)}{\sin(s')}} \tag{5.18}$$

5.4.1.1 Classical Installation Modules

A model for classical installations is certainly useful for optimising classical solar farms (consisting of rows of PV arrays without reflectors), but it can be extremely useful for comparing with reflector-equipped installations. For example, given a classical and a reflector-equipped installation that are both geometrically optimised to maximise a certain objective (e.g. annual electricity production), what is the gain brought by the reflectors? Does the gain change if the surface area is limited or costly? To answer these questions, the model was developed as follows.

The direct irradiance of PV modules of a classical installation is calculated similarly to a reflector-equipped installations. Shading is evaluated with (5.8).

The diffuse flux transmitted to cells of a classical PV installation was evaluated by the means of view factors (Figs. 5-11b and 5-11c). This yielded the following components:

- Direct contribution of the sky (Fig. 5-11b):
  $\tau_D(D/L)DHIF_{Sky-PV}$
- contribution of the back of the PV module of the row in front of it (Fig. 5-11b):
  $\tau_D(D/L)DHI[F_{Sky-Back}\ \rho_{Back}(F_{Back-PV} + F_{Back-Grnd}\ \rho_{Grnd}\ F_{Grnd-PV})]$
- contribution of the ground, illuminated by diffuse irradiance (Fig. 5-11b):
  $\tau_D(D/L)DHIF_{Sky-Grnd}\ \rho_{Grnd}\ F_{Grnd-PV}$
- contribution of the ground, illuminated by direct irradiance (ground is considered diffusive) (Fig. 5-11c).
  $\tau_D(D/L)BNI(O/D)\sin(\alpha)\rho_{Grnd}(F_{O-PV} + F_{O-Back}F_{Back-PV})$
  Note that this component must be recalculated at every time step.

The total diffuse flux transmitted to cells is obtained by summing these four components, yielding Equation (5.19).

$$\begin{aligned}\phi_{D,Trans,Clas} = \tau_D(D/L)\{ & \\ & DHI[\\ & F_{Sky-PV} \\ & + F_{Sky-Back}\ \rho_{Back}\ (F_{Back-PV} + F_{Back-Grnd}\rho_{Grnd}F_{Grnd-PV}) \\ & + F_{Sky-Grnd}\ \rho_{Grnd}\ F_{Grnd-PV} \\ &] \\ & + BNI(O/D)\sin(\alpha)\rho_{Grnd}(F_{O-PV} + F_{O-Back}F_{Back-PV}) \\ & \}\end{aligned} \tag{5.19}$$

$$F_{Sky-Back} = \frac{1 + (L/D) - \sqrt{(L/D)[(L/D) + 2\cos(s)] + 1}}{2} \tag{5.20}$$

$$F_{Back-PV} = 1 - (D/L)(F_{Sky-Back} + F_{Sky-PV}) \tag{5.21}$$

$$\begin{aligned}F_{Back-Grnd} &= F_{PV-Sky} \text{ (by symmetry)} \\ &= F_{Sky-PV}(D/L) \text{ (since } F_{PV-Sky}L = F_{Sky-PV}D)\end{aligned} \tag{5.22}$$

$$F_{Sky-Grnd} = 1 - F_{Sky-PV} - F_{Sky-Back} \tag{5.23}$$

$$F_{Grnd-PV} = F_{Sky-Back} \text{ (by symmetry)} \tag{5.24}$$

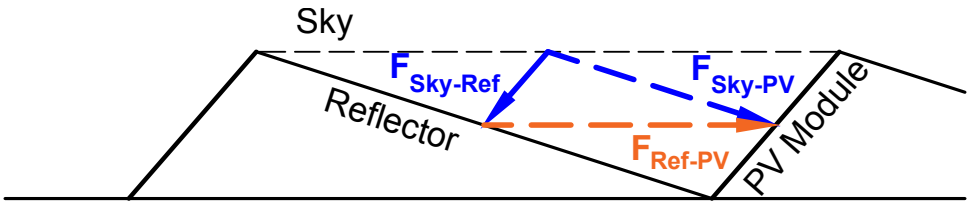

(a) View factors for reflector-equipped installations

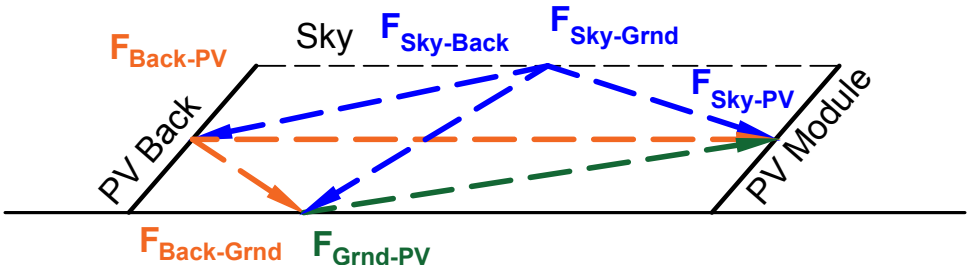

(b) View factors for classical installations, part 1

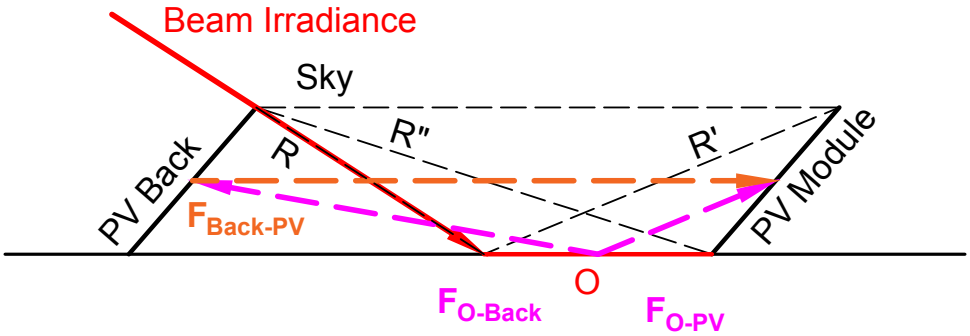

(c) View factors for classical installations, part 2

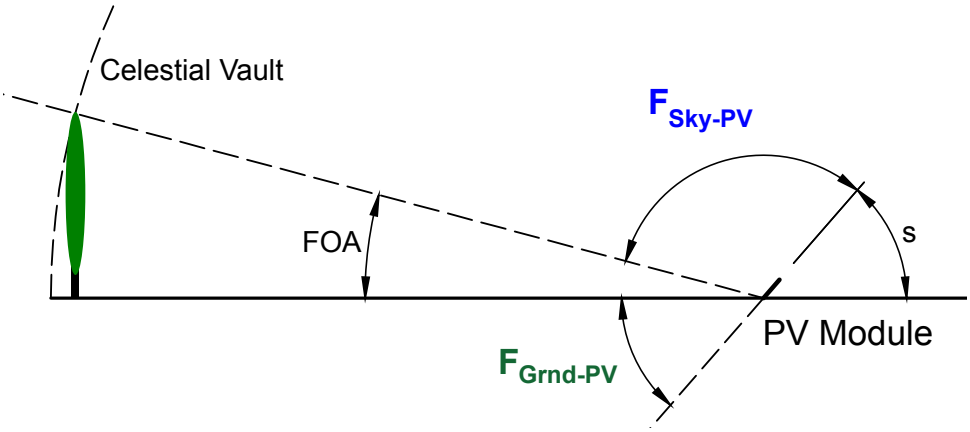

(d) View factors for frontal modules

Figure 5-11: Schematic illustrating the diffuse flux view factors for reflector-equipped installations, classical installations, and frontal modules.

$$(O/D) = 1 - (L/D)\sqrt{[\cos(\gamma_S)]^2 + [\sin(\gamma_S)]^2 * [\cos(s)]^2}\ \frac{\sin(\alpha + u)}{\sin(\alpha)} \tag{5.25}$$

where u is the PV-module inclination angle in the vertical plane containing the sun beam.

$$F_{O-PV} = \frac{(O/D) + (L/D) - (R'/D)}{2} \tag{5.26}$$

$$(R'/D) = \sqrt{(L/D)^2 + (O/D)^2 + 2(L/D)\cos(s)(O/D)} \tag{5.27}$$

$$F_{O-Back} = \frac{(O/D) + (R/D) - (R"/D)}{2(O/D)} \tag{5.28}$$

$$(R/D) = \sqrt{(L/D)^2 + (O/D)^2 - 2(L/D)\cos(s) + 2(L/D)\cos(s)(O/D) - 2(O/D) + 1} \tag{5.29}$$

$$(R"/D) = \sqrt{(L/D)^2 + 1 - 2(L/D)\cos(s)} \tag{5.30}$$

Note that the model for classical installations cannot be validated by experimental measurements, as the experiment does not provide two adjacent rows of PV modules without an inter-row reflector.

5.4.1.2 Frontal Modules

Since every installation has a frontal row of PV modules, it is important to have a model for it. One can expect the front row modules to have a different optimal inclination than the rest of the modules. Since there are no reflected rays favouring a steeper inclination, the optimal inclination is expected to be less steep than for the case of reflector-equipped modules, with the goals of:

1. reducing the angular and reflection losses of the direct irradiance, and
2. increasing the view factor from the module to the sky, for maximising the collection of diffuse irradiance

The direct irradiance of frontal modules was modelled similarly to a classical installation PV module, except that the shadow was assumed not to play a role. It was however still necessary to verify the Sun was in view of the PV cells (i.e. not behind them). Reflection losses were applied as outlined in Section 5.3.

The transmitted diffuse irradiance on frontal modules is given by Equation (5.31):

$$\begin{aligned}\phi_{D,Trans,Frnt} &= celestial\ vault + ground \\ &= \tau_D\{ \\ &DHI\left[\frac{1+\cos(s+FOA)}{2}\right] \\ &+ [DHI + BNI\sin(\alpha)]\,\rho_{Grnd}\frac{1-\cos(s)}{2}\}\end{aligned} \tag{5.31}$$

where:

- FOA is the frontal obstruction angle (see Fig. 5-11d). FOA represents the average altitude angle of the horizon objects in view of the frontal row. For the site of the experiment, FOA was estimated to be about 5 degrees due to the presence of tall trees on the campus of Ecole Polytechnique.
- ρ_{Grnd} is the average reflectance of the ground surface in view of the modules. Since the experiment is surrounded primarily by grass fields, a ρ_{Grnd} value of 0.1 was assumed.

Note that for the purposes of comparing to the stochastic model (see Section 5.5.2), this analytical method used for modelling front row PV modules may in further text and figures be referred to as IRM, even though no infinite-row assumption had to be made for frontal modules.

5.4.2 Validation

Since the experiment was not equipped with irradiance sensors (until the very end of the thesis), it was not possible to calibrate the optical model directly. The analytical optical model IRM was validated indirectly in the following way. A coupled model was assembled, consisting of the IRM, the Evans electrical model, and the measured values of operating temperature. The Evans model parameters and the relevant optical parameters were then adjusted such that the modelled P_{MPP} values matched the P_{MPP} measurements[2]. In the case of heterogeneous illumination, the average flux on the module was used, neglecting the influence of the current mismatch between the PV module cells. This assumption may contribute to the overestimation of power production (or underestimation of power loss under partial shading) even if the total incident irradiance is well calculated.

The model was validated for performance on a clear and an overcast day near the summer solstice (Fig. 5-12 (a, b)) and near the autumnal equinox (Fig. 5-12 (c, d)), by comparing the numerical and experimental values of P_{MPP}. For each of the two technologies, two PV-modules were considered: a module of the front row (control module) and a non-edge module of the third row (module experiencing gains due to concentration

[2]For a detailed calibration and performance test of the Evans model, see Section 6.1, page 95

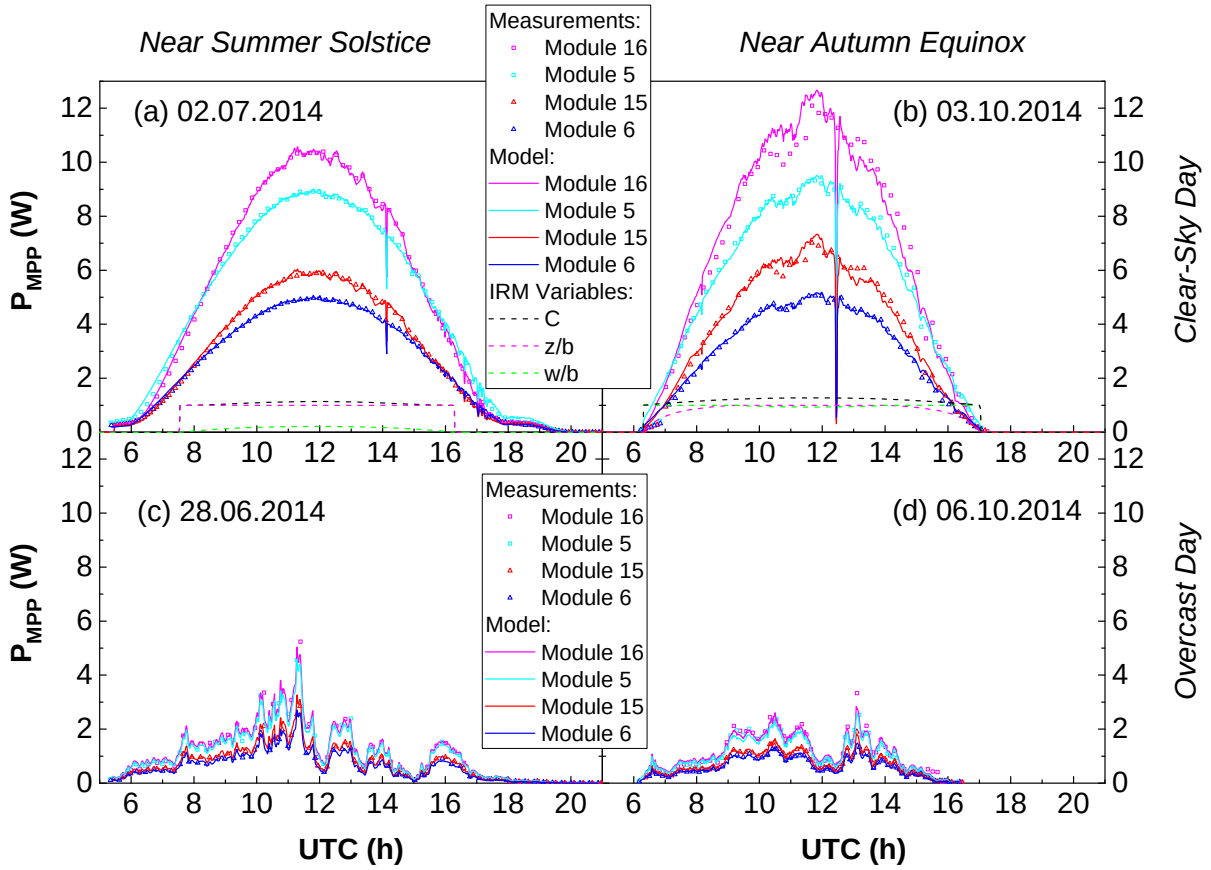

Figure 5-12: Analytical optical model validation (indirectly through P_{MPP} measurements and predictions) on a clear-sky and an overcast day near the summer solstice (a, c), and near the autumnal equinox (b, d). Modules 6 and 15 are row 1 and row 3 a-Si:H modules, while modules 5 and 16 are row 1 and row 3 p-Si modules. Variables C, z/b, and w/b are respectively the average concentration factor, the fraction of module being highlighted, and the fraction of useful reflector. The underperformance of PV modules from 6 to 7h in (b) is due to shading by a bungalow on site, situated south-east from the experiment.

with the smallest degree of edge effect). Modules 6 and 15 are row 1 and row 3 a-Si:H modules, while modules 5 and 16 are row 1 and row 3 p-Si modules. Table 5.2 summarises the differences in modelled and measured daily produced energies for each module and for each day.

Figsures 5-12a and 5-12b present the two clear days near the summer solstice and near the automn equinox. Good model performance is observed throughout the day for the frontal modules of both technologies (modules 5 and 6), and the reflector-equipped modules (15 and 16) are well reproduced throughout the most of the day. The discrepancy between the modelled and the measured performance of the modules under concentration from 10 to 14h is likely due to considerable fluctuations in the solar flux (which in the data is given as 1-minute average). In most cases, the relative error in daily production is on the order of 2%.

Note the difference in the optical model variables z/b (fraction of module being high-

Table 5.2: Relative error between numerical and experimental daily produced energies shown in Fig. 5-12.

Module #	**02.07.2014** (clear)	**03.10.2014** (clear)	**28.06.2014** (overcast)	**06.10.2014** (overcast)
16 (p-Si + Ref.)	0.05%	0.6%	-0.8%	2.0%
5 (p-Si)	0.5%	-0.8%	-1.5%	-1.2%
15 (a-Si:H + Ref.)	-0.2%	-0.1%	-0.9%	1.8%
6 (a-Si:H)	-0.2%	1.3%	-3.6%	-2.4%

lighted, shown in magenta), and w/b (fraction of useful reflector, shown in green) between the two clear days (see Sec. 5.4.1 for schematic). Near the summer solstice (Fig. 5-12a), the activation of the mirror is triggered by the solar azimuth (the mirror is activated when $\cos(\gamma_s) > 0$ - in other words when the sun is located South compared to the system). The ratio w/b rises gradually from 0 (total overshoot) in the morning to about 0.22 (78% overshoot) at solar noon. The ratio z/b is equal to unity throughout this period, indicative of uniform concentration. The concentration factor is kept low in the morning and evening periods due to the cosines related to θ' and θ". Near the equinoxes (Fig. 5-12b), the activation of the mirror is triggered by the solar elevation angle (the mirror is activated when $\cos(\theta') > 0$ - that is, as soon as the solar elevation angle is high enough for the mirror to be lit by direct irradiance). Once the Sun is in view of the mirror, a localised concentration zone is formed in the plane of the modules ($0 < z/b < 1$), with the reflector being 100% useful ($w/b = 1$). The highlighted fraction increases with time, reaching uniform illumination around solar noon. Note that the under-performance of PV modules from 6 to 7h in Fig. 5-12b is due to shading by a bungalow on site, situated south-east from the experiment.

Bollentin and Wilk [32] study the edge effect error resulting from the infinite reflector-width assumption, and propose a method to correct it. Due to a lack of time, a finite-row optical model was not developed.

Figs. 5-12c and 5-12d show the model performance in evaluating the transmitted diffuse flux. Both the figures and the error values in Table 5.2 relating to these figures indicate a good performance. This validates the view-factor approach in modelling the transmitted diffuse irradiance.

5.4.3 Examples

Consider an example of the developed analytical optical model.

Three systems were compared for the best fit to the French electricity demand: the dual-axis tracking system, the classical installation, and the reflector-equipped installation. As a first approach, the comparison was done under clear-sky conditions using

McClear data [95]. This is useful for better visualising the differences between the systems.

The tracker was assumed to be dual-axis, orienting itself towards the sun at all times, and that it never gets shadowed. Diffuse flux shape factors were evaluated similarly to the case of frontal modules. The classical and PV+Reflector installations were considered as infinite-row installations. Assuming the tracker is already geometrically optimised (permanently following the Sun), the PV+Reflector and the classical installations were geometrically optimised for maximising the annual energy transmitted to the cells (see Fig. 5-13). Figure 5-14 presents the simulated annual performance of the three systems under clear-sky conditions.

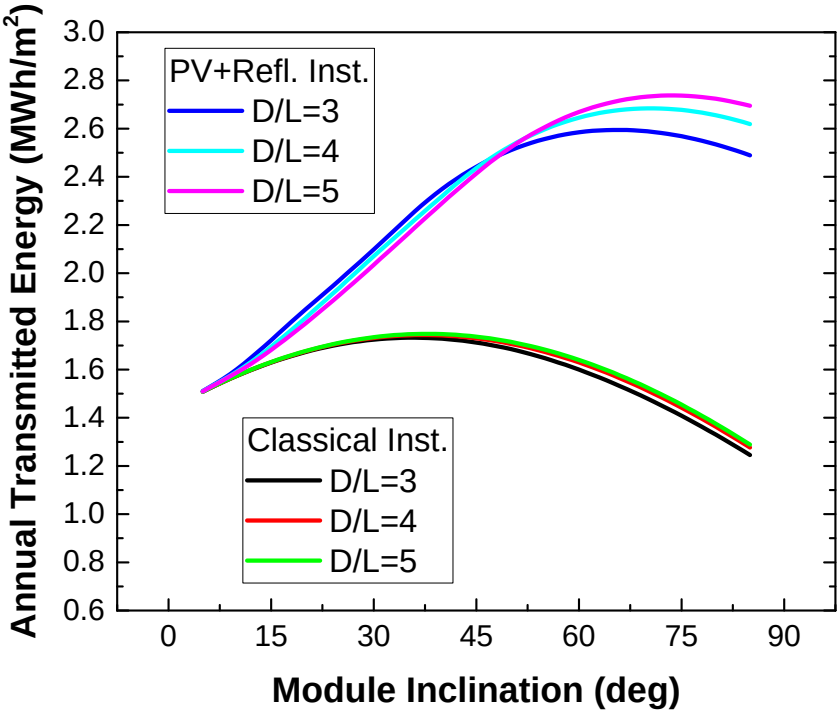

Figure 5-13: Results of geometrical optimisations of infinitely-long PV+Reflector and Classical installations for D/L values of 3, 4, and 5, for maximising the annual transmitted energy under clear-sky conditions.

Under clear sky the weekly global horizontal irradiation is the highest in the summer, which is associated with highest solar elevation angles and hence lowest atmospheric absorption losses. An asymmetrical annual distribution of the diffuse fraction (see Fig. 5-15) results in an asymmetry in the transmitted irradiation curves of the three systems compared. Higher aerosol concentrations in the spring contribute to the diffusion of beam irradiance, increasing DHI at the expense of BHI. This compromise results in lower overall optical losses compared to the fall for all three systems.

The amount of global horizontal irradiation is the main factor driving the transmitted irradiation curves of the tracker and the classical installation. The two systems receive the highest quantities of energy around the summer solstice. The optical losses of the

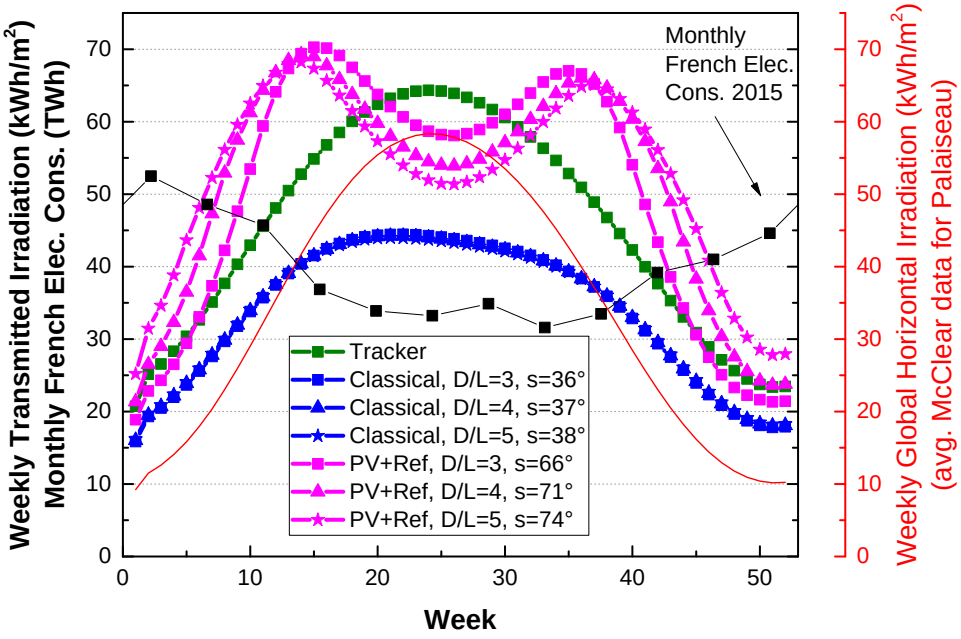

Figure 5-14: Total weekly transmitted irradiation under *clear-sky conditions* for a PV tracker, an infinite classical installation and an infinite PV+Reflector installation, the latter two being optimised for annual transmitted energy at three different values of spacing D/L.

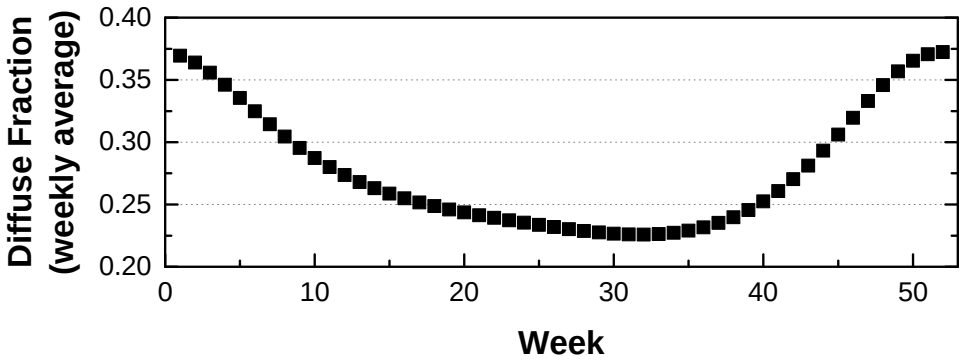

Figure 5-15: The annual distribution of weekly average diffuse fraction under clear sky (using McClear data for Palaiseau). A higher concentration of aerosols in the spring period results in a slightly higher diffuse fraction in spring compared to the fall.

tracker are smaller than the ones of the classical installation due to smaller angular and transmission losses. This results in more energy being transmitted to the PV tracker throughout the year.

In the case of the PV+Reflector installation, the amount of transmitted energy depends on the role of reflectors throughout the year. Near the equinoxes, the reflector utility (variable w/b of the optical model) is maximized (e.g. no overshoot of reflected rays) while the combined optical losses are minimal (e.g. favourable incidence angles of reflected and non-reflected rays, small angular losses). In the summer, the gain brought by the reflector is lower compared to near the equinoxes. This is a result of a reduced

reflector utility (i.e. overshoot) due to higher solar elevation angles, and angular losses. In the winter, the concentration of beam irradiance is heavily reduced due to large angular losses, while the diffuse irradiance remains approximately equally concentrated all year long. This means that the winter gains compared to the classical installation increase with diffuse fraction, and are therefore lower under clear sky compared to cloudy conditions (see Fig. 5-17 for a comparison).

As can be also seen in Fig. 5-14, the PV+Reflector system optical performance better matches the French electricity demand than the classical installation or the PV tracker. For example, when its yield is the highest (near equinoxes), the electrical energy demand is significant. Furthermore, by increasing the spacing D/L (and optimising for annual transmitted flux), the optical gains in the early spring and late fall are significantly improved, creating an even better correspondence to the national electricity demand.

Figure 5-16 presents the result of the same study under measured ground irradiance data. The optimal inclinations for both systems are lower than the ones for clear-sky conditions, which results in a better collection of diffuse flux. One can note that due to frequent cloudy conditions in Palaiseau, less irradiation is transmitted to the cells under real conditions compared to clear sky.

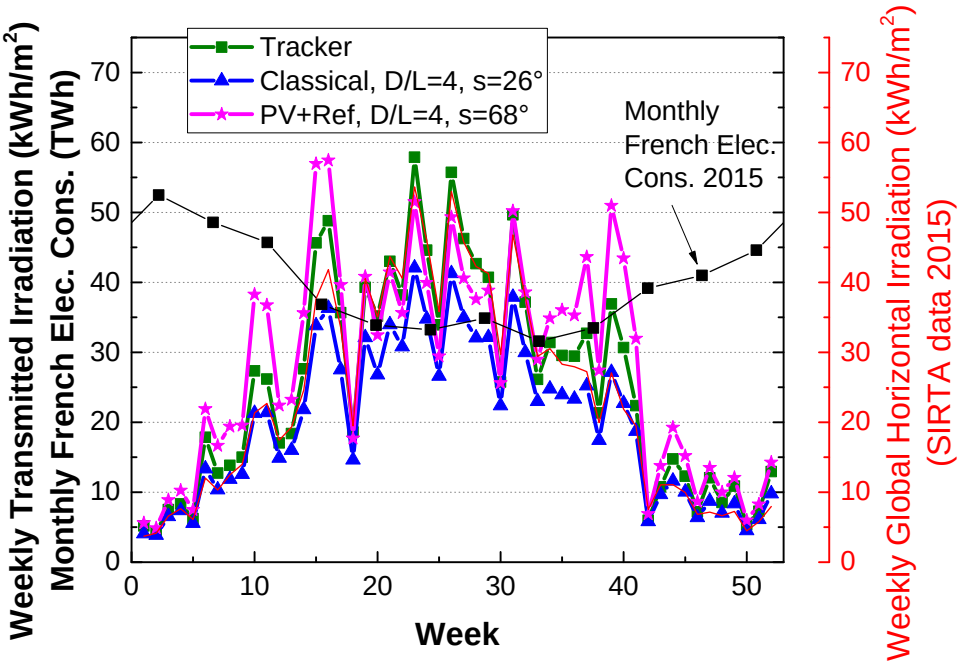

Figure 5-16: Total weekly transmitted irradiation under *measured irradiance data* (2015) for a PV tracker, an infinite classical installation and an infinite PV+Reflector installation, the latter two being optimised for annual transmitted energy at three different values of spacing D/L.

Figure 5-17 presents the relative gains in weekly transmitted irradiation of Aleph compared to the classical installation, under both clear-sky and real conditions. One can note similar shapes of the gains under clear-sky and real conditions. Cloudy winters in

Palaiseau result in higher gains compared to the clear-sky case, as during those periods the geometrical concentration factor is negligible for direct irradiance but remains significant for the diffuse. In the summer when the factor of concentration is much higher for direct compared to diffuse irradiance, the gain under real conditions is lower than under clear-sky conditions due to a lower fraction of direct irradiance.

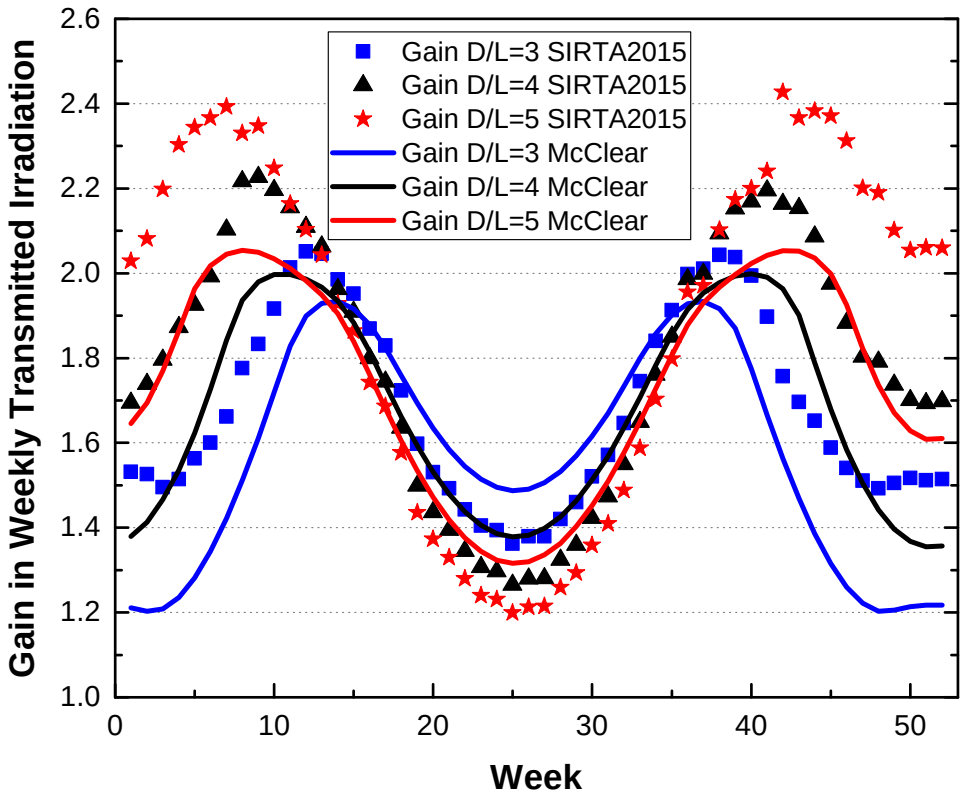

Figure 5-17: Weekly relative gains in transmitted irradiation of an optimised infinite PV+Reflector installation compared to an optimised infinite classical installation, under clear-sky (solid lines) and 2015 measured irradiance data (symbols). The two systems were optimised for annual transmitted energy at three different values of spacing D/L.

It should be noted that, while the gains in the average transmitted flux can give an idea of the overall gains in produced energy, the PV+Reflector system experiences higher operating temperatures and a higher degree of string mismatch than the other two systems. Therefore, the gains in *produced* energy compared to other systems will be lower than suggested by this comparison of *transmitted* energies.

5.5 Ray-Tracing Optical Model

As seen previously, the analytical optical model has several drawbacks due to its simplicity. For example, the incident diffuse flux is considered constant for reflector-equipped modules while it is expected to be higher along the bottom where the module and mirror meet. Furthermore, it does not provide the flexibility for testing other module-mirror

configurations. For this reason, a 3-D ray tracing solution was developed and is presented below.

5.5.1 State of the Art

The tools presented in this chapter are based on the Monte Carlo method. The method has been developed by Nicholas Metropolis in 1949 [118], and allows for a numerical calculation of integrals using random sampling. As the price of computing power decreased over the decades, the stochastic method has found its use across many disciplines. A recent book by Dunn and Shultis [119] gives an excellent overview of the method, including several applications. When applied to radiative transfer, the method allows for the calculation of the fate of photons, from their origins (e.g. Sun or sky), through the interaction with objects (e.g. reflectors or obstacles), to the receivers of interest (e.g. solar collector or PV module). In this case, the method is referred to as Monte Carlo ray-tracing.

A literature review shows that ray-tracing has been used previously to simulate various reflector-receiver geometries [110, 112, 120–122]. For example, Wong et al. [110] used ray-tracing to study the impact of the circumsolar ratio (CSR) on the performance of a concentrator PV system consisting of 194 facet mirrors. There exist numerous codes and software which can be used for ray-tracing, such as SolTrace [123], SolFast [124], Tonatiuh [125], COMSOL Multiphysics (www.comsol.com), POV-Ray (www.povray.org), FRED (www.photonengr.com), and EDStaR [126].

EDStaR was chosen as the simulation tool since its source code is free for research purposes, and has been recently demonstrated for solar energy applications (e.g. thesis of Emeric Tapachez on modelling a linear Fresnel concentrator system [112]).

5.5.2 EDStaR: Overview

EDStaR (Environnement de Développement Statistique Radiative) was developed by the research group STARWest (http://www.starwest.ups-tlse.fr/), with the goal of allowing easy access to simulating particle transport phenomena, in particular the radiative transfer. It is centered on the Monte Carlo method, in view of exploring the sensitivity of a complex system by varying parameters within statistical constraints. EDStaR was written in C++, and parallilised (with MPI) for a faster execution.

The goal of simulations in EDStaR is to obtain the PV module irradiance distribution maps (further referred to as flux maps) for every possible daytime position of the Sun relative to the system. This section briefly describes the different inputs and information necessary for running Monte Carlo simulations in EDStaR, namely pre-generated uniformly-distributed numbers, number of histories, 3-D geometry file, and most importantly, the C++ algorithm of a single Monte Carlo history. Figure 5-18 illustrates the

major inputs and outputs of EDStaR, detailed in the following sections.

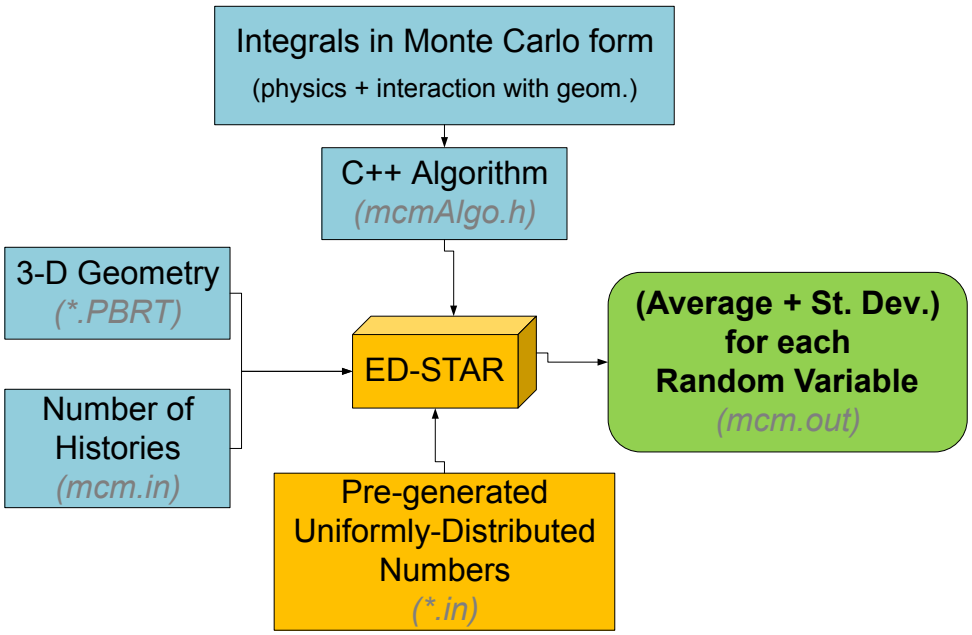

Figure 5-18: Major inputs and outputs of EDStaR. The items in orange were developed by StarWEST, the items in blue are inputs prepared by the user for each Monte Carlo simulation, and the items in green are the outputs.

5.5.2.1 Pre-Generated Uniformly-Distributed Numbers

As described later, the algorithm involves the calls of functions for retrieving uniformly-distributed random numbers. For the purpose of increasing the simulation speed, these numbers were pre-generated by the StarWEST team with trusted methods to guarantee a high degree of uniformity, and stored in a form of input text files. In our case, the uniformly-distributed random numbers are used for performing:

- a uniform sampling of points of the PV module surface, so that after a large number of histories the entire surface is tested for the degree of illumination (or shading)
- a uniform sampling of points of the reflector surface, to quantify the contribution of the reflector to the total flux on the module
- a sampling of the surface of the Sun (or sunshape), for modelling the direct flux
- a sampling of the celestial vault, for modelling the diffuse flux

5.5.2.2 Number of Histories

The file mcm.in is used for indicating the number of histories demanded, N, which is the number of times the Monte Carlo algorithm will be executed. In general, the error is reduced with a higher number of histories at the expense of a higher computation time. The relationship between the standard deviation and the number of histories is

non-linear:

$$\sigma \propto \frac{1}{\sqrt{N}} \tag{5.32}$$

where σ is the standard deviation and N is the number of histories. This relationship means that, for example, to cut the standard deviation in half, one needs to increase the number of histories by a factor of 4. Generally, 10,000,000 histories were demanded for each simulation, which represented a good balance between accuracy and computation cost. As described later, the receiver was discretised to a grid of 48x288 pixels or 13,824 variables, meaning that each variable had on average about 723 histories. With this many variables, N of 10,000,000 was also very close to the upper limit concerning the physical memory limits of the computers used.

5.5.2.3 3-D Geometry

The geometry of the system is described in a separate file with the PBRT (Physically-based Rendering Toolkit) framework syntax. By convention, the file is given the extension .PBRT. The geometry of the system was defined as a south-facing inclined receiver surface, and a north-facing inclined reflector surface. The receiver surface was defined as the virtual surface in the plane of the PV cells, encompassing all the PV modules in the experiment. Within the algorithm header file, this virtual receiver surface was subdivided into a grid of "pixels" (see next section for more details). In this case, each pixel was treated as a random variable, and resulted in an average value and a standard deviation.

Note that the developers of the PBRT framework released its source code for free (which is why it was used in EDStaR) but decided to sell the manual for the product. Therefore, to master the capabilities of PBRT and get the most out of EDStaR, one should purchase and study the official PBRT user manual.

5.5.2.4 C++ Algorithm of a Monte Carlo History

For modelling radiative transfer using EDStaR, the most important input is the algorithm of a single Monte Carlo history. The algorithm contains the following key pieces of information:

1. position of the light source relative to the geometry
2. choice of random variables to be evaluated, including the potential splitting of certain surfaces into a grid of pixels
3. physics of the radiative process including the interaction with geometry (e.g. light comes from the surface of the Sun towards the system, light is reflected by reflectors, etc.)

The following sections detail the development process of applicable C++ algorithms.

Position of the Light Source

To describe the position of a light source within the PBRT framework (defined in the algorithm header file), one must use classical vector notation. However, the physical limits of the positions of the Sun are often expressed with geometrical variables (e.g. solar elevation angle, solar azimuth) or indirectly through astronomical variables (e.g. solar declination angle and solar hour angle). Therefore there are two possibilities for defining the physical Sun position space:

1. Using the solar elevation angle and solar azimuth (e.g. Sun path chart)
2. Using the solar declination angle and solar hour angle (using Duffie and Beckman [69] equations).

Since Monte Carlo simulations are computationally expensive to carry out, a strategy needed to be developed to run simulations at a specific grid of physical Sun positions, in view of interpolating the result for an arbitrary, physical Sun position.

A common way to visually describe the Sun's position for all hours of the day of all months is using a Sun path diagram (see figure 5-19 for an example).

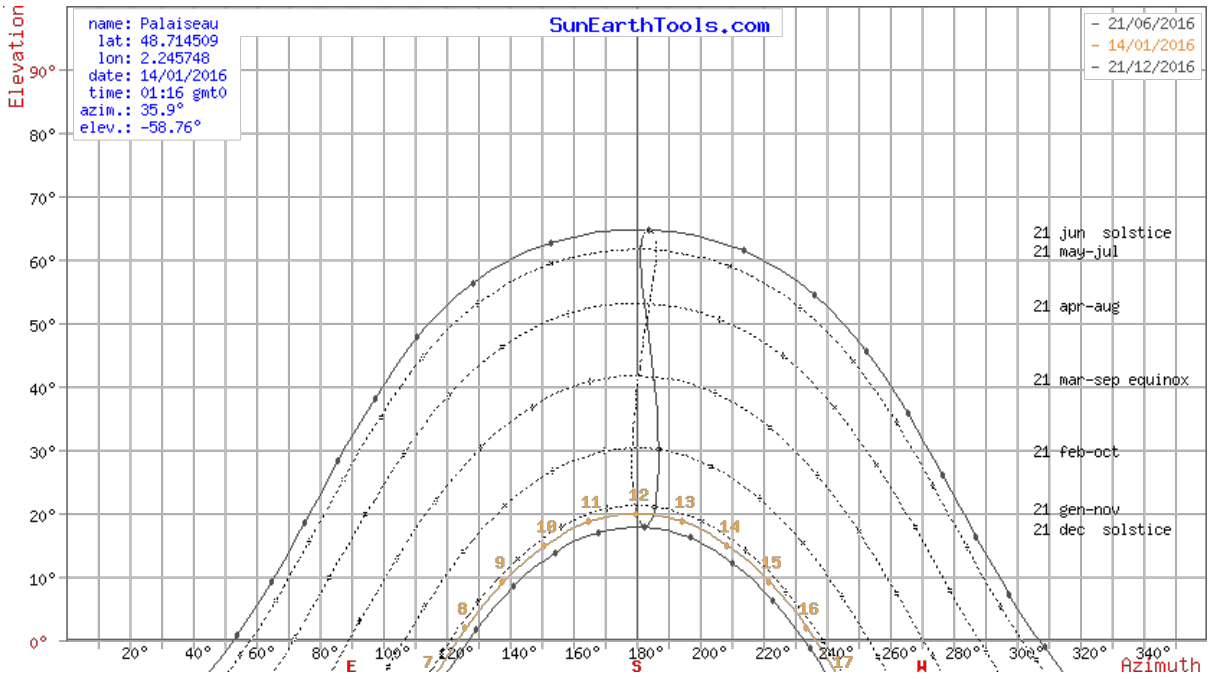

Figure 5-19: Sun path diagram for Palaiseau. Downloaded from *www.sunearthtools.com*

As can be seen in the figure above, the Sun path diagram shows the solar elevation angle as a function of its azimuth. The chart includes data for the summer and winter solstices, spring and fall equinoxes (overlapping curves), and several curves representing a range of days.

The solar elevation angle – azimuth space corresponds to method 1 in the numbered list above. This diagram can serve as a pedagogical tool, or for certain hand calculations such as finding the minimal inter-row spacing to avoid winter shading. However, it was

decided that this representation was not a good approach if interpolation was to be performed afterwards. Due to the non-rectangular nature of the space, the selection of grid points seemed ambiguous.

The solution to the aforementioned limitation was to represent the Sun's position in a space defined by the solar declination angle (δ) and the solar hour angle (ω). See Fig. 5-20 for a visualisation of the $\delta - \omega$ space.

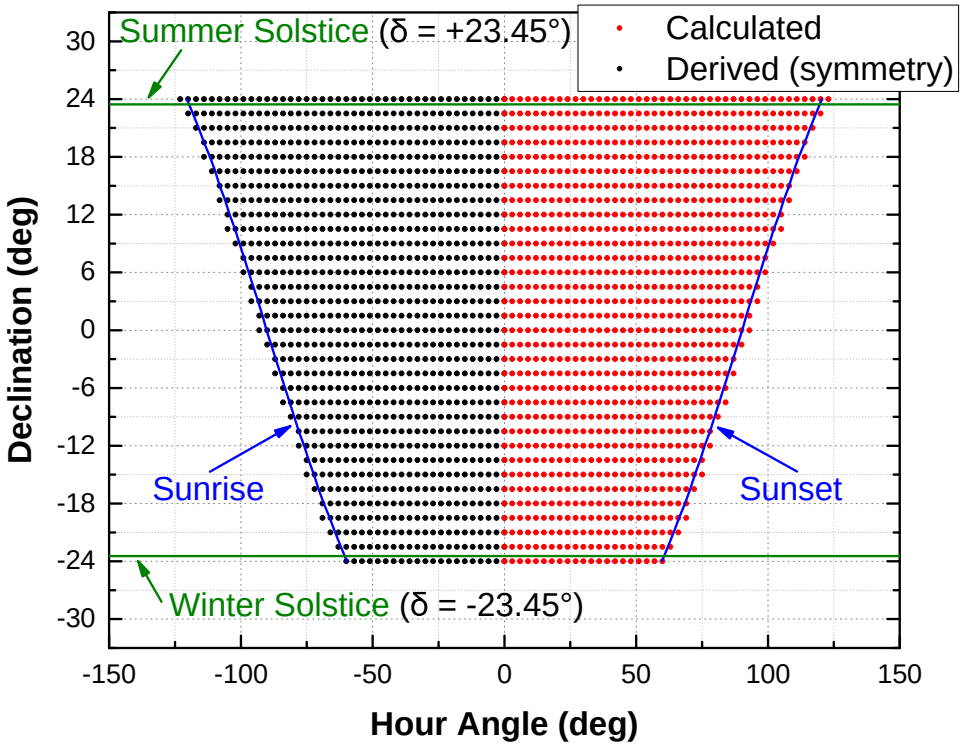

Figure 5-20: $\delta - \omega$ space, showing the $\delta - \omega$ pairs for which flux maps are calculated ($\omega \geq 0$), and derived ($\omega < 0$). Morning flux maps are derived from afternoon ones due to symmetry.

On the ω axis, the limits of the space are defined by the hour angles associated with sunrises and sunsets. On the δ axis, the limits are defined by the summer and winter solstices (where zero declination represents the equinoxes).

The $\delta - \omega$ space is much more regular than the elevation-azimuth space, making it much more suited for interpolation. For example, it is close to rectangular in the equatorial regions (with small inter-seasonal differences in the daylight lengths), and trapezoidal in mid-latitude regions (with a bigger inter-seasonal difference in daylight length).

Once the boundaries of the $\delta - \omega$ space were defined, the space has been divided into a grid, with the resolution in delta of 1.5 degrees and the resolution in omega of 3.0 degrees (corresponding to a 12-minute resolution). As the system is symmetrical in the east-west direction, the flux map in the morning is symmetrical with the one in the afternoon. Recognising this, it is necessary to simulate only one half of the $\delta - \omega$ space, for example

when $\omega \geq 0$, in view of reconstructing the other half of the space during post-treatment.

Choice of Random Variables - Domain Discretisation

Monte Carlo simulations are used to calculate the mean and standard deviation values of a choice of random variables. In the simplest case, the integral of flux on a given surface can be evaluated, represented as a single random variable. To develop the 2-D flux maps on the receiver, it needed to be subdivided into a grid of pixels, each being represented as a random variable. The resolution in pixels of each dimension of the surface was decided as follows. The size of the virtual surface encompassing all the modules was measured on site, and was found to be 1923 mm wide by 353 mm tall. Due to memory constraints of the in-house clusters, it was not feasible to have each pixel representing a mm^2. For this reason, a coarser resolution was necessary, with the following constraints:

- the total number of pixels should not present a memory problem
- the sides of the pixels should not be larger than the respective dimensions of the PV cells (preferably having multiple pixels per dimension)

and the following objectives:

- the resulting pixels should be as close to square as possible, demanding the ratio $Resolution_X/Resultion_Y$ be close to $1923/353 \approx 5.45$
- the resolutions along X and Y should if possible be even numbers, for the ease of splitting it into even segments if necessary

The proposed resolution is 288 px $\times$ 48 px, resulting in each pixel being 6.677 mm wide and 7.354 mm tall. Given the sizes of *a*-Si:H and *p*-Si cells (of which the width of the *a*-Si:H cells is the smallest), this pixel size ensures that there are at least 2 px per side of each PV cell. This resolution results in a total of $288 \times 48 = 13824$ variables to be estimated.

Other random variables can be of interest to be saved, such as the various incidence angles (e.g. incident rays on the receiver, incident rays on the reflector, and reflected rays on the receiver), allowing for the application of optical losses post-calculation.

Physics of the Radiative Process

The description of the physics of the radiative process is centred around the random variable being estimated. By definition, the Monte Carlo method of estimating a random variable involves the evaluation of a carefully designed integral through statistical means (a classic example is that of the estimation of π). An example of integral development is given below.

Consider a system of one specular mirror surface, M_1, and one receiver surface R_2. Consider that the system is illuminated with beam irradiance coming uniformly from the Sun's disk. The total direct flux transmitted to the receiver is the sum of two integrals:

1. the transmitted flux disregarding the reflector contribution, but including a shadow check ($\Phi_{R_2,NM}$ given in (5.33)), and
2. the reflector contribution to the transmitted flux, with a shadow check ($\Phi_{R_2,CM}$ given in (5.34))

Figure 5-21 illustrates the vectors used in the following integrals.

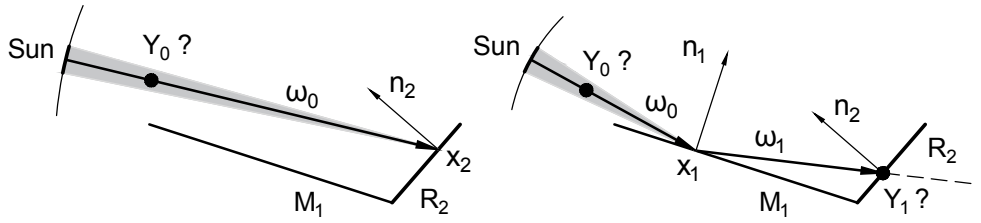

Figure 5-21: Illustration of vectors used in Equations (5.33) through (5.38)

$$\Phi_{R_2,NM} = \int_{R_2} d\ \overrightarrow{x_2} \int_{Sun} d\ (\overrightarrow{-\omega_0})\ |\overrightarrow{-\omega_0} \cdot \overrightarrow{n_2}(\overrightarrow{x_2})|\ Lsol \times \begin{cases} H(\overrightarrow{Y_0} \in (M_1\ U\ R_2)) \times 0 \\ +H(\overrightarrow{Y_0} \notin (M_1\ U\ R_2)) \times \tau_{R_2} \end{cases} \tag{5.33}$$

$$\Phi_{R_2,CM} = \int_{M_1} d\ \overrightarrow{x_1} \int_{Sun} d\ (\overrightarrow{-\omega_0})\ |\overrightarrow{-\omega_0} \cdot \overrightarrow{n_1}(\overrightarrow{x_1})|\ Lsol \times \begin{cases} H(\overrightarrow{Y_0} \in (M_1\ U\ R_2)) \times 0 \\ +H(\overrightarrow{Y_0} \notin (M_1\ U\ R_2)) \times \rho_{M_1} \times \begin{cases} H(\overrightarrow{Y_1} \notin (M_1\ U\ R_2)) \times 0 \\ +H(\overrightarrow{Y_0} \in (M_1\ U\ R_2)) \times \begin{cases} H(\overrightarrow{Y_1} \notin (R_2)) \times 0 \\ +H(\overrightarrow{Y_0} \in (R_2)) \times \tau_{R_2} \end{cases} \end{cases} \end{cases} \tag{5.34}$$

where $H(condition)$ returns 1 if the condition is true, and 0 if it is false. In view of transforming these integrals into the Monte Carlo form ($PDF \times weight$), we multiply the inside of each integral by $\frac{domain\ size}{domain\ size}$, respectively:

$$\Phi_{R_2,NM} = \int_{R_2} \frac{R_2}{R_2}\ d\ \overrightarrow{x_2} \int_{Sun} \frac{2\pi(1-\cos\theta_{sol})}{2\pi(1-\cos\theta_{sol})}\ d\ (\overrightarrow{-\omega_0})\ |\overrightarrow{-\omega_0} \cdot \overrightarrow{n_2}(\overrightarrow{x_2})|\ Lsol \times \begin{cases} H(\overrightarrow{Y_0} \in (M_1\ U\ R_2)) \times 0 \\ +H(\overrightarrow{Y_0} \notin (M_1\ U\ R_2)) \times \tau_{R_2} \end{cases} \tag{5.35}$$

$$\Phi_{R_2,CM} = \int_{M_1} \frac{M_1}{M_1}\, d\,\overrightarrow{x_1} \int_{Sun} \frac{2\pi(1-\cos\theta_{sol})}{2\pi(1-\cos\theta_{sol})}\, d\,(\overrightarrow{-\omega_0})\, |\overrightarrow{-\omega_0}\cdot\overrightarrow{n_1}(\overrightarrow{x_1})|\; Lsol$$
$$\times \begin{cases} H(\overrightarrow{Y_0} \in (M_1\ U\ R_2)) \times 0 \\ +H(\overrightarrow{Y_0} \notin (M_1\ U\ R_2)) \times \rho_{M_1} \times \begin{cases} H(\overrightarrow{Y_1} \notin (M_1\ U\ R_2)) \times 0 \\ +H(\overrightarrow{Y_0} \in (M_1\ U\ R_2)) \times \begin{cases} H(\overrightarrow{Y_1} \notin (R_2)) \times 0 \\ +H(\overrightarrow{Y_0} \in (R_2)) \times \tau_{R_2} \end{cases} \end{cases} \end{cases} \tag{5.36}$$

Integrating the solar luminance over the solar cone to yield ϕ_{BNI} and rearranging, we obtain:

$$\Phi_{R_2,NM} = \int_{R_2} \frac{1}{R_2}\, d\,\overrightarrow{x_2} \int_{Sun} \frac{1}{2\pi(1-\cos\theta_{sol})}\, d\,(\overrightarrow{-\omega_0})\, |\overrightarrow{-\omega_0}\cdot\overrightarrow{n_2}(\overrightarrow{x_2})|\; R_2\; \phi_{BNI}$$
$$\times \begin{cases} H(\overrightarrow{Y_0} \in (M_1\ U\ R_2)) \times 0 \\ +H(\overrightarrow{Y_0} \notin (M_1\ U\ R_2)) \times \tau_{R_2} \end{cases} \tag{5.37}$$

$$\Phi_{R_2,CM} = \int_{M_1} \frac{1}{M_1}\, d\,\overrightarrow{x_1} \int_{Sun} \frac{1}{2\pi(1-\cos\theta_{sol})}\, d\,(\overrightarrow{-\omega_0})\, |\overrightarrow{-\omega_0}\cdot\overrightarrow{n_1}(\overrightarrow{x_1})|\; M_1\; \phi_{BNI}$$
$$\times \begin{cases} H(\overrightarrow{Y_0} \in (M_1\ U\ R_2)) \times 0 \\ +H(\overrightarrow{Y_0} \notin (M_1\ U\ R_2)) \times \rho_{M_1} \times \begin{cases} H(\overrightarrow{Y_1} \notin (M_1\ U\ R_2)) \times 0 \\ +H(\overrightarrow{Y_1} \in (M_1\ U\ R_2)) \times \begin{cases} H(\overrightarrow{Y_1} \notin (R_2)) \times 0 \\ +H(\overrightarrow{Y_1} \in (R_2)) \times \tau_{R_2} \end{cases} \end{cases} \end{cases} \tag{5.38}$$

where the probability density functions corresponding to uniform sampling are denoted in blue, while the weights are denoted in green. These integrals yield the pseudo-codes presented in Algorithms 1 and 2.

$\overrightarrow{x_2} \leftarrow$ Uniformly sample surface R_2;
$\overrightarrow{n_2} \leftarrow$ Calculate the normal at the point $\overrightarrow{x_2}$;
$\overrightarrow{-\omega_0} \leftarrow$ Uniformly sample solar disk;
Launch a photon from $\overrightarrow{x_2}$ towards $\overrightarrow{-\omega_0}$;
$\overrightarrow{Y_0} \leftarrow$ Calculate the intersection with the world;
if $\overrightarrow{Y_0} \notin (M_1\ U\ R_2)$ **then**
  $\hat{w} = |\overrightarrow{-\omega_0}\cdot\overrightarrow{n_2}(\overrightarrow{x_2})| \times R_2 \times \phi_{BNI} \times \tau_{R_2}$;
else
  $\hat{w} = 0$;
end

Algorithm 1: Monte Carlo method pseudo-code for evaluating (5.37)

$\overrightarrow{x_1} \leftarrow$ Uniformly sample surface M_1;
$\overrightarrow{n_1} \leftarrow$ Calculate the normal at the point $\overrightarrow{x_1}$;
$\overrightarrow{-\omega_0} \leftarrow$ Uniformly sample solar disk;
Launch a photon from $\overrightarrow{x_1}$ towards $\overrightarrow{-\omega_0}$;
$\overrightarrow{Y_0} \leftarrow$ Calculate the intersection with the world;
if $\overrightarrow{Y_0} \notin (M_1 \ U \ R_2)$ **then**
  $\overrightarrow{\omega_1} = 2\ |\overrightarrow{-\omega_0} \cdot \overrightarrow{n_1}(\overrightarrow{x_2})|\ \overrightarrow{n_1} + \overrightarrow{\omega_0}$;
  Launch a photon from $\overrightarrow{x_1}$ towards $\overrightarrow{\omega_1}$;
  $\overrightarrow{Y_1} \leftarrow$ Calculate the intersection with the world;
  if $\overrightarrow{Y_1} \in (M_1 \ U \ R_2)$ **then**
    if $\overrightarrow{Y_1} \in (R_2)$ **then**
      $\hat{w} = |\overrightarrow{-\omega_0} \cdot \overrightarrow{n_1}(\overrightarrow{x_2})| \times M_1 \times \phi_{BNI} \times \rho_{M_1} \times \tau_{R_2}$;
    else
      $\hat{w} = 0$;
    end
  else
    $\hat{w} = 0$;
  end
else
  $\hat{w} = 0$;
end

Algorithm 2: Monte Carlo method pseudo-code for evaluating (5.38)

A given pseudo-code is then transformed into a C++ code (in the form of a header file), representing the algorithm for one history. This C++ algorithm sums up the radiative process physics, including the position of the light source, the target, and the eventual interaction of light with geometry (e.g. a specular reflector will reflect a ray at an angle equal and opposite to the angle of incidence).

5.5.3 Calculation of Flux Maps

The goal of calculating shape factor maps is to allow one to impose arbitrary irradiance values (e.g. DHI, BNI) and obtain corresponding flux maps on the receiver *post-calculation*. This is useful for simulating the given geometry under arbitrary climatic conditions and for arbitrary positions of the Sun (e.g. for forecasting electricity production), without the need of running additional Monte Carlo simulations.

We are interested in two kinds of shape factor maps: direct flux shape factor maps (flux maps when BNI is set to 1), and diffuse flux shape factor maps (flux maps when DHI is set to 1). The following sections detail the simulations used for obtaining direct and diffuse flux maps.

Direct Flux Shape Factor Maps

To describe the behaviour of the direct flux, the Pill-Box [111] model of the Sun chosen as a first approach due to its simplicity of implementation. This model makes the following assumptions:

- The totality of the direct flux is assumed to come from the Sun disk. In reality, BNI is measured with a certain opening half-angle (often 2.5 °), which includes a region around the Sun referred to as the circumsolar region. A part of the measured BNI therefore comes from this region, ranging from 0 to over 80 %. The proportion of circumsolar irradiance to the total beam irradiance is referred to as the circumsolar ratio (CSR). CSR depends on the physical characteristics of aerosols and thin clouds, most particularly cirrus clouds [88]
- The distribution of the radiance across the Sun disk is considered as uniform. In reality, the flux is the strongest in the center of the disk, and the weakest at the perimeter [88, 127]. The phenomenon is referred to as limb darkening and varies with wavelength. For example, at 1000 nm the radiance at the edge of the solar disk is approximately 55% while it is around 20% at 370 nm [88].

If the variation in the angle of incidence for a given $\delta - \omega$ pair can be considered as negligible, this simulation can be split into two separate simulations where reflection and transmission losses are not calculated at each history:

(A) a shape factor map of non-reflected light incident on the receiver (0=shadow, (0,1]=light), saving the average angle of incidence, and

(B) a shape factor map of the reflected light incident on the receiver (0=reflector does not contribute, (0,1]=reflector contributes), saving the average angle of incidence on the reflector, and the average incidence angle of the reflected beam on the receiver.

Note that the Lambert cosine law is still applied at each history, yielding values *between* 0 and 1.

The receiver surface was subdivided into a grid of 388 × 48 pixels. Reflector behaviour was defined as perfectly specular. For each version of the algorithm (A and B) and each of the 1040 $\delta - \omega$ pairs, a Monte Carlo simulation was launched with 10,000,000 histories, which was found to have a good balance between calculation time and standard deviation. The pixel standard deviation is in the range [0.0240, 0.0285], resulting from performing 10 million histories.

The result of these simulations are the maps listed in Table 5.3, and Fig. 5-22 gives examples of the resulting flux maps.

Proceeding in this way provides the flexibility of calculating and applying the reflectivity and transmissivity losses post-calculation. For example, it opens the door to:

- the calibration of optical constants of materials in the experiment (specular reflectance of the reflector, transmittance properties of the front glass)

Table 5.3: Maps of the two components of the incident direct flux on the receiver: (A) light/shadow on the receiver, (B) contribution of the reflector.

Ver.	Irradiance	Type	Res. (px)	Maps
A	Direct flux	Shape factor maps of light on receiver	288 × 48	1040
A	Direct flux	Corresponding std. deviation maps	288 × 48	1040
B	Direct flux	Shape factor maps of reflector contribution	288 × 48	1040
B	Direct flux	Corresponding std. deviation maps	288 × 48	1040

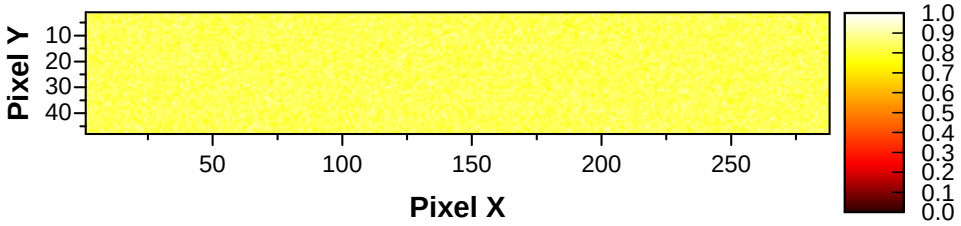

(a) Map A: Direct light on the *frontal* receiver

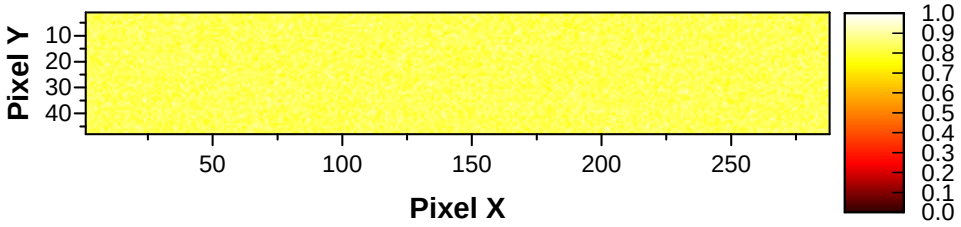

(b) Map A: Partial direct light on the *reflector-equipped* receiver - equal to (a) due to no shadows being present in this case

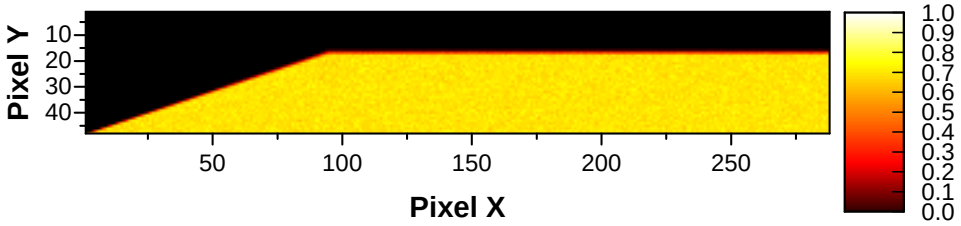

(c) Map B: Reflector contribution to the direct light on the reflector-equipped receiver

Figure 5-22: Incident direct flux shape factor maps: (a) incident light on the frontal receiver (no shadows), (b) incident light due to potential shading cast by the reflector, (c) reflector contribution to the light on the receiver. $\delta = -9°$, $\omega = 33°$.

- simulating different reflector technologies (having different reflection properties) or their degradation over time
- simulating different front glass designs (e.g. different protective layers and anti-reflective coatings) or its degradation
- various other sensitivity analyses

During the integrated model simulations, maps A and B are multiplied by the appropriate irradiance values, optical losses are individually applied to them, and the two components are summed.

Diffuse Flux Shape Factor Maps

To describe the behaviour of the diffuse flux, the Uniform-Sky model [117] model of the sky was chosen as a first approach. This model makes the assumption that the strength of the diffuse flux coming from different parts of the sky is uniform. In reality [82], diffuse flux is slightly stronger near the Sun disk, and also near the horizon due to a phenomenon called *horizon brightening*. The algorithm was set up to randomly sample different positions of the sky with a uniform probability. Note that the Lambert cosine law was not applied at each history.

Since the Uniform-Sky model was used, the position of the Sun had no influence on the shape factors. Therefore, a single pair of simulations was performed for obtaining year-round shape factor maps A and B described on page 86. Similarly to the direct flux, the maps A and B are combined post-calculation.

The result of these simulations is summarised in Table 5.4, and the maps are shown in Fig. 5-23.

Table 5.4: Maps of the two components of the incident diffuse flux on the receiver: (A) light/shadow on the receiver, (B) contribution of the reflector.

Ver.	Irradiance	Type	Res. (px)	Maps
A	Diffuse flux	Shape factor maps of light on receiver	288×48	1
A	Diffuse flux	Corresponding std. deviation maps	288×48	1
B	Diffuse flux	Shape factor maps of reflector contribution	288×48	1
B	Diffuse flux	Corresponding std. deviation maps	288×48	1

As can be seen in Fig. 5-23b, the shading effect of the mirror is the most pronounced in the lower part of the receiver, and slightly more in the center compared to the edges. Figure 5-23c shows the reflector contribution to the incident flux, which is the highest in the lower part of the receiver and decreases towards the top. Note that the contribution is lowest in the top left and right corners of the receiver. Since a larger solid angle is being sampled compared to the case of direct flux (i.e. whole sky vs. sun disk/sunshape), a larger distribution of values is obtained throughout the simulation. This increases the standard deviation of each pixel value, and is reflected as noise in the figure.

5.5.4 Calculation of Flux by Cell

The maps developed previously were pixelated images used for calculating direct and diffuse flux distributions on the imaginary PV cell planes. The goal is to use the obtained

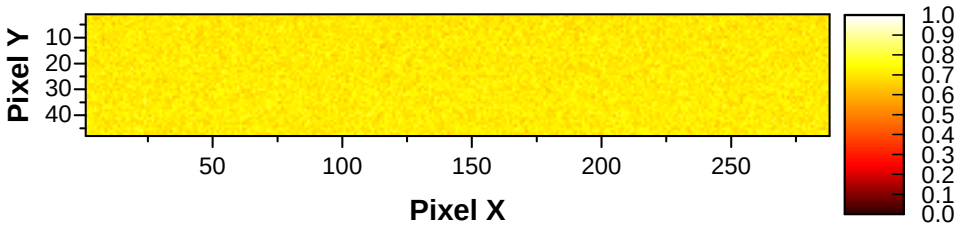

(a) Map A: Diffuse light on the *frontal* receiver

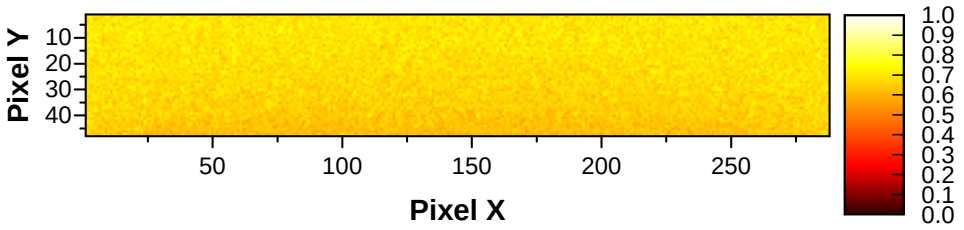

(b) Map A: Partial diffuse light on the *reflector-equipped* receiver. Note the reduced view of the sky along the bottom, due to the presence of the obstacle (mirror)

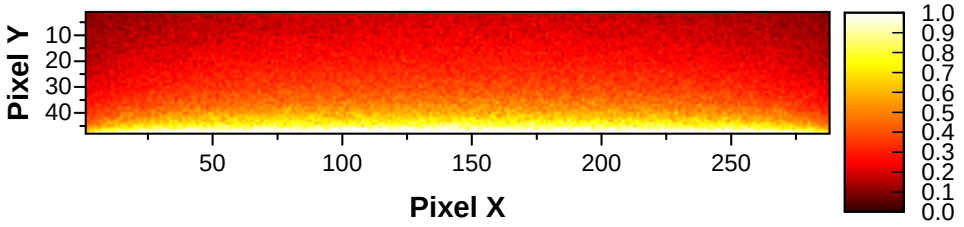

(c) Map B: Reflector contribution to the diffuse light on the reflector-equipped receiver

Figure 5-23: Incident diffuse flux shape factor maps: (a) incident light on the frontal receiver (homogeneous light with a reduced view of the sky), (b) incident light due to shading cast by the reflector (smallest along the bottom), (c) reflector contribution to the light on the receiver (highest along the bottom)

maps to calculate the total transmitted flux to each cell of each module. In other words, the flux maps needed to be attributed to and averaged for the different cells, as a function of their physical position in the experiment/system.

Datasheets of either technology PV module did not provide precise dimensions and positions of individual cells within the module. Therefore, an efficient strategy was necessary for accurately describing the physical positions and sizes of different cells. Furthermore, a systematic method was highly preferable, for an easy adaptation to potential changes (e.g. physical rearrangement of modules, change in pixel resolutions of flux maps).

The immediate idea was to take a photograph, and use image processing to define the positions and sizes of different cells (using the RGB data of the photograph). This proved to be rather challenging in its raw form, due to the following reasons:

- The image is skewed due to perspective effects

- In terms of RGB (Red-Green-Blue) values, the cells were not identically coloured
- bus bars on the *a*-Si:H modules (separating individual cells) are very thin and barely visible in a photograph, making it difficult to identify individual cells

To go around these limitations, a series of steps were carried out in a commercial image processing software (a publicly available software would suffice for these operations):

1. The canvas was set up with pixel dimensions proportional to mm dimensions of the virtual plane (measured on site to be 1923 x 353 mm). To allow for a precise definition of PV cell borders (including the drawing of thin *a*-Si:H bus bars), the canvas was made quite large: the amount of pixels in each dimension was set to 10 times the number of mm in each dimension, resulting in a precision of 0.1 mm per pixel.
2. The image was imported and the perspective effects were eliminated, removing the skew in the virtual plane
3. The resulting image was cropped to isolate the virtual plane, and stretched to fit the canvas
4. The grids of non-cell surface surrounding the cells (e.g. bus bars) were uniformly coloured with pure green (RGB=(0,255,0)) or black (RGB=(0,0,0)) paints, which were decided not to be used for labelling cells
5. The different cells were then coloured manually, using unique RGB colours for labelling the different cells

This procedure resulted in RGB matrices (visualised as images) for the three rows of the experiment, shown in Fig. 5-24. While it may not be obvious, all the cells in a given row have unique RGB colours associated with them.

MATLAB was then used to transform the pixelated shape factor maps (separately for direct and diffuse maps) into the corresponding shape factors by cell. The images shown in Fig. 5-24 were imported into MATLAB as 3-D arrays, holding the R, G, and B components of the images. An algorithm was made where, for each PV cell (identified by its RGB value), the contribution of each pixel of the different maps was evaluated. This allows for a systematic conversion of shape factor maps, calculated in EDStaR, to average shape factors by cell, to be used for calculating the transmitted flux to each cell.

Fig. 5-25 illustrates the mapping algorithm. Note that the isolated concentration zone manifests itself differently on the modules depending on the cell topology and the distance from the edge. This results in varying degrees of illumination heterogeneity of serially-connected cells, and hence string mismatch losses. It can be noted that *a*-Si:H module topology is less prone to string mismatch effects compared to *p*-Si modules regardless of the presence of 2 by-pass diodes in the *p*-Si modules. Furthermore, the *a*-Si:H modules in portrait orientation (with cells stretching the entire height of the module) and far enough from the edges should experience negligible mismatch losses.

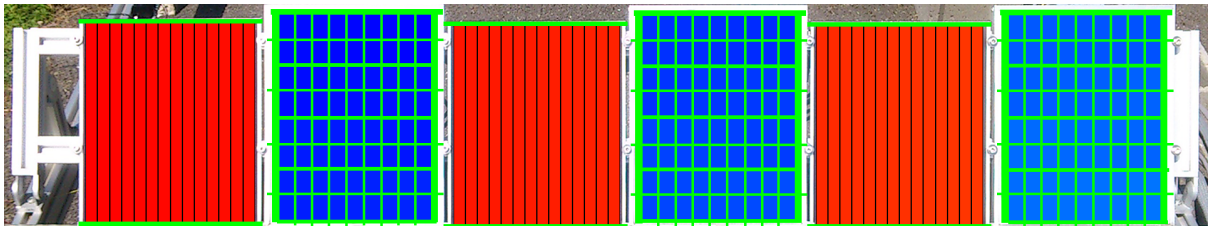

(a) Row 3

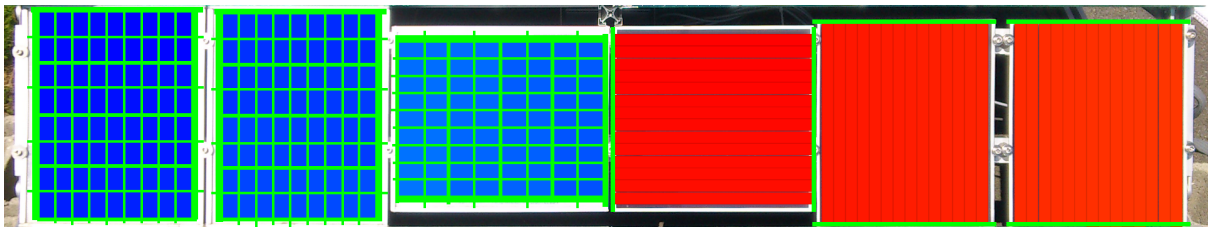

(b) Row 2

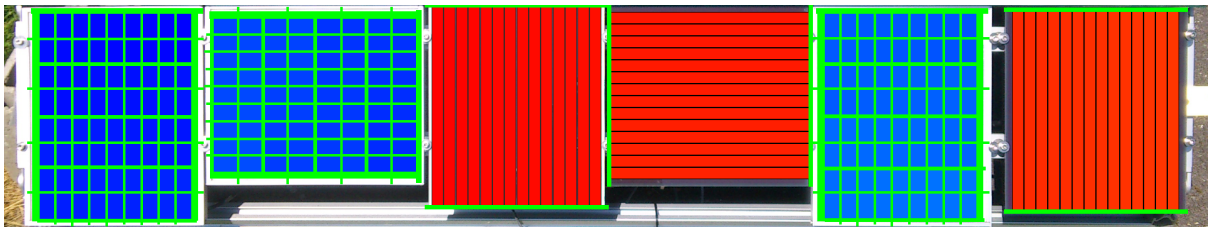

(c) Row 1

Figure 5-24: RGB mapping of PV cells in Rows 3, 2, and 1 of the experiment. Each cell in a given row is uniquely coloured.

For the direct flux shape factors by cell, each minute of daylight of the year was considered in MATLAB to:

- interpolate the shape factor map from maps of 4 nearest $\delta - \omega$ pairs, and
- calculate the shape factors by cell with the mapping algorithm.

For the diffuse flux shape factors by cell, the mapping algorithm was applied only once due to the use of the Uniform-Sky model.

Both direct and diffuse shape factors by cell were stored in text files, and further read as inputs by the main application. They are multiplied by irradiance values and adjusted for optical losses to obtain the values of transmitted flux by cell.

5.5.5 Example

An example application of EDStaR is a geometrical optimisation of a given reflector-receiver setup. Typically, it is in the designer's interest to maximise the amount of annual solar radiation incident on the module or transmitted to the cells. A simulation aimed at maximising the annual *direct* radiation was set up as follows.

A look-up table corresponding to a time series of BNI measured at the SIRTA in 2015 was loaded into the program. This temporal domain of one year was sampled with a uniform probability until a non-zero value of BNI was found. Each such moment picked

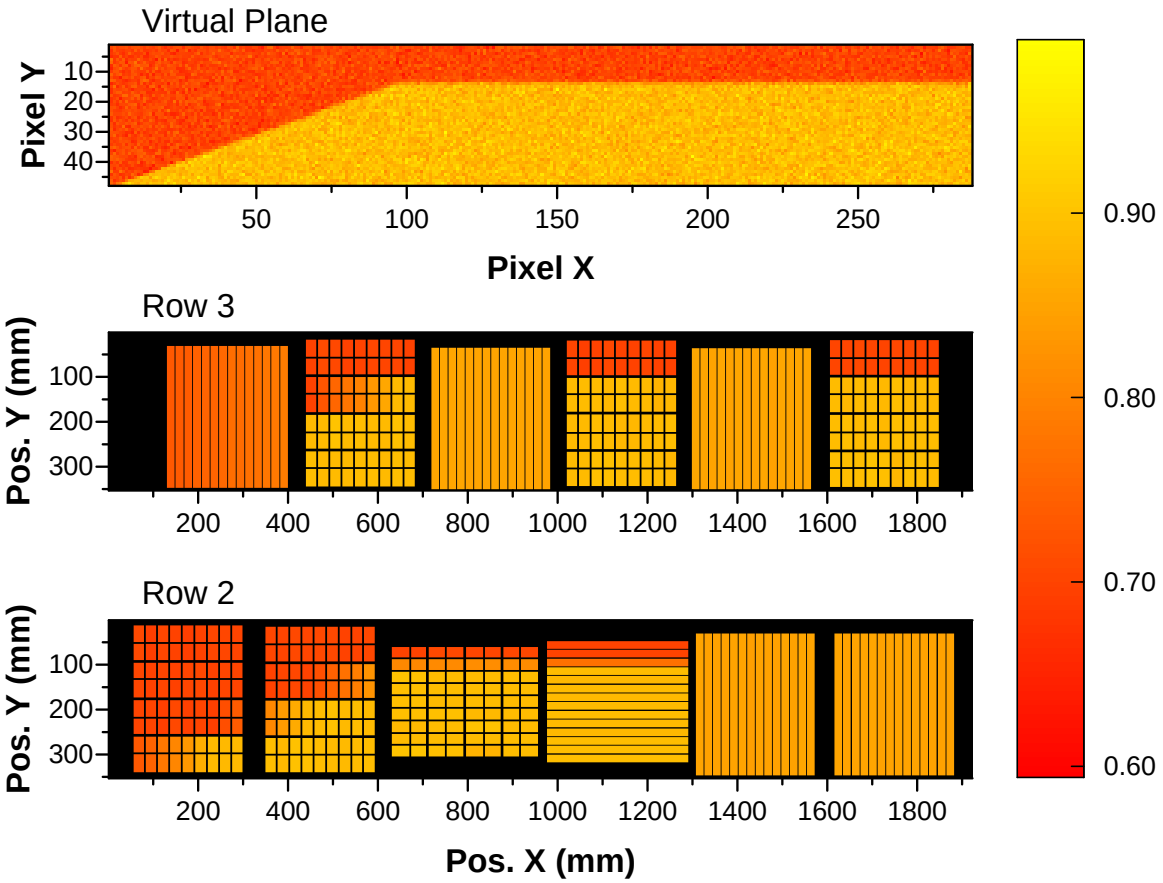

Figure 5-25: Result of the mapping algorithm, calculating the average shape factor by cell from several flux maps (in this case from *a*-Si:H and *p*-Si direct flux shape factor maps on October 15, 2014 at 13:50 UTC).

at random was equally associated with a position of the Sun (using equations presented earlier), defining the origin of the photons. The receiver and the reflector surfaces were both uniformly sampled for selecting two photon targets. The two photons' fates were calculated as they interacted with the world (mirror as obstacle, mirror as reflector, and the receiver front glass). If the photon reached the receiver, the Monte Carlo weight applied was the BNI value less the applicable optical losses (due to imperfect reflection and transmission). This process resulted in the average annual direct irradiance on the receiver (W/m^2). Another variable calculated in the simulation is the amount of time the receiver was operational (i.e. had received a non-zero radiation). Multiplying the two gives the total annual direct irradiation in Wh/m^2.

A loop was established where this process was executed for a range of geometries, in view of identifying the optimal settings. The width of the installation was set as 20 times the height of the modules, representing a medium-sized installation (the width/PV height ratio of the demonstrator is about 5.47). The parameters varied were the D/L and the receiver inclination, whereby the reflector inclination and dimensions were adapted to fit in the inter-row space of a multi-row system (as in the Aleph experiment). Figs.

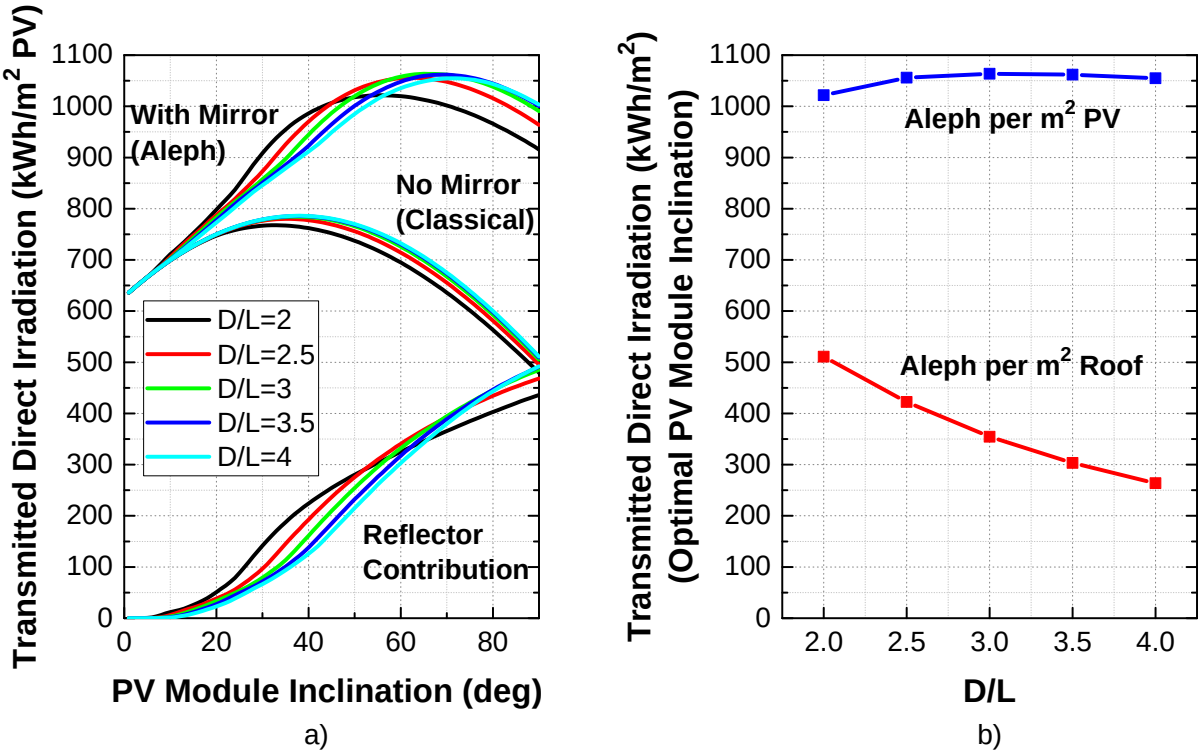

Figure 5-26: Geometrical optimisation of the Aleph system for different inter-row spacings D/L: (a) Transmitted direct irradiation for Aleph and classical installations, along with the associated reflector contribution; (b) Effect of D/L on the transmitted direct irradiation.

5-26a and 5-26b summarise the results.

Due to the increasing reflector contribution with module inclination, an optimal Aleph system demands a higher PV module inclination compared to an optimal classical installation (see Fig. 5-26a). Aleph systems with a higher spacing demand a higher inclination compared to denser systems. As seen in Fig. 5-26b, in the case of Aleph the annual direct radiation per module surface is optimised with the D/L spacing of 3.0, beyond which it begins to decrease. If the objective is to maximise the electricity production per unit area of roof, it is clear that a denser system would be appropriate.

5.6 Discussion

Laboratory measurements such as the reflector spectral reflectance gave insight into the optical performances of the materials in the experiment. The mirror reflects up to 95% of beam irradiance in the visible spectrum, and drops to 78% in the near infra-red due to a more significant absorption in the glass. Spectral response measurements of PV cells similar to the ones in the experiment show that *a*-Si:H cells are the most sensitive in the visible spectrum, while *c*-Si and *p*-Si cells are the most sensitive in the near infra-red. For this reason, *a*-Si:H cells should experience higher gains from the reflector compared

to p-Si cells. Given its relatively low cost and high performance, the glass-on-aluminum mirrors seem like a good choice for the Aleph system.

Two approaches have been taken in calculating the amount of solar irradiance that reaches the PV cells: analytical and statistical (ray-tracing). Both approaches rely on Snell's law to calculate reflection and transmission phenomena of light.

The analytical method was used to calculate the average incident flux on the modules. The solar resource was modelled with a point-source Sun and a uniformly bright sky. This method proved sufficient for modelling frontal modules where the irradiance is uniform across the cells. Since cell-level illuminations are not known, string mismatch losses cannot be calculated under heterogeneous cell illuminations. Nevertheless, the analytical method calculated average module irradiances which proved sufficient for modelling reflector-equipped modules.

Due to the shortcomings of the analytical model, a statistical ray-tracing model was developed to calculate cell-level irradiances. First of all, ray-tracing in three dimensions opens the door to a more accurate modelling of the solar resource. A point-source Sun was replaced with a uniform sampling of the Sun's disk. A view factor-based calculation of diffuse irradiance was replaced by a uniform sampling of the sky. This idea could be extended to describe the influences of non-uniform radiance from the Sun's disk, circumsolar radiance, and non-uniform sky brightness (e.g. horizon brightening effect). Secondly, due to a three-dimensional representation of the reflector, the receiver, and the individual cells, the edge effect is accurately taken into consideration. Once the model is established, it is easily adaptable to include arbitrary configurations of reflective surfaces without the need of deriving equations. The disadvantage of this approach to the analytical one is the high computational cost of the Monte-Carlo simulations. For this reason, a grid of physical Sun positions in the δ-ω space was pre-calculated, allowing for fast interpolation of flux maps at arbitrary Sun positions.

The advantages of the ray-tracing solution outweigh its drawbacks, making it the best candidate for modelling reflector-equipped systems.

Chapter 6

Electrical Modelling

This chapter describes the electrical modelling done throughout the thesis. As a first approach, a simple electrical model proposed by Evans [74] was developed. It is an empirical model for estimating P_{MPP}. The development and some applications are discussed in Section 6.1. The empirical model failed to adequately reproduce certain system behaviours, such as under heterogeneous illumination conditions (e.g. during shading or isolated concentration zones). For this reason, LTSpice was used for developing a more precise electrical model, capable of reproducing entire I-V curves. This electrical model is further discussed in Section 6.2.

6.1 Empirical Electrical Model

This section describes the state of art, and the development of the empirical electrical model.

6.1.1 State of the Art

When modelling the performance of PV modules and arrays, many simple empirical equations exist for estimating the conversion efficiency at the maximum power point (MPP) as a function of environmental variables (e.g. in-plane irradiance, cell operating temperature, wind speed, etc.). The corresponding power output (assumed to operate at the MPP) is obtained by multiplying the instantaneous efficiency by the total irradiance:

$$P_{MPP} = \eta \times I \times A \tag{6.1}$$

where η is the instantaneous efficiency, I is the global in-plane irradiance, and A is the effective solar cell surface area.

Empirical equations are widely used in the industry to estimate the annual array yield. A good review of such equations is given by Skoplaki and Palyvos [128].

For example, a simple yet powerful efficiency correlation is proposed by Evans [74]:

$$\eta = \eta_{T_{ref}}[1 + \beta(T_{cell} - T_{ref}) + \gamma \log_{10} \frac{I}{I_{ref}}] \tag{6.2}$$

where η is the conversion efficiency at arbitrary values of cell temperature, T_{cell} in °C, and in-plane irradiance, I in kW/m^2; $\eta_{T_{ref}}$ is the conversion efficiency at the reference values of cell temperature and in-plane irradiance (T_{ref} = 25 °C, I_{ref} = 1 kW/m^2); β is the temperature coefficient (usually negative, in °C $^{-1}$); and γ is the solar radiation coefficient, used to describe the drop of efficiency at low irradiations.

Other authors attempt to predict the cell temperature as a function of atmospheric variables such as wind speed. For example, CEA [129] proposes the following efficiency correlation:

$$\eta = 0.94 - 0.0043\left[\overline{T_a} + \frac{\overline{G_T}}{22.4 + 8.7\overline{V_w}} - 25\right] \pm 2.6\% \tag{6.3}$$

where η is the conversion efficiency, $\overline{T_a}$ is the daily average air temperature in °C, $\overline{G_T}$ is the total Wh/m^2 received divided by the day length in h, and $\overline{V_w}$ is the daily average wind speed.

Due to their simplicity, certain effects are not accurately taken into account. For example, complex recombination behaviours, such as intrinsic layer recombination in *a*-Si:H cells, are hard to predict. Also, string mismatch due to heterogeneous illumination of PV cells within a module (such as shadows or concentration zones) will not be reproduced. Similarly, behaviour of cells and modules under eventual reverse bias cannot be reproduced. The behaviour of by-pass diodes and their eventual influence on the electricity production cannot be represented. Finally, spectral mismatch effects resulting from the solar spectrum being different from the reference solar spectrum AM 1.5, is often not taken into account.

6.1.2 Implementation

Despite the simplicity and potential drawbacks of empirical electrical models, they can be useful as a basis for comparison for validating more complex models. The model proposed by Evans [74] described in Section 6.1.1 was chosen to be developed and tested for applicability to our problem. The Evans model has the advantage of being simple to implement, and that it can be applied to both *a*-Si:H and *p*-Si modules in its original form. To demonstrate the sensibility of the Evans model, efficiency was calculated for a range of temperature and transmitted flux values, as shown in Fig. 6-1.

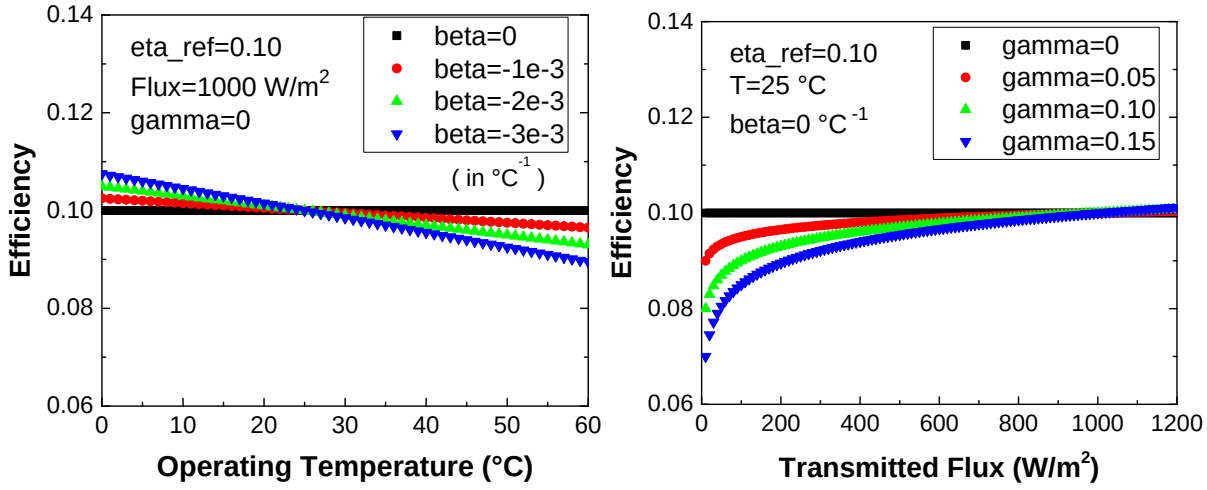

(a) Impact of β (b) Impact of γ

Figure 6-1: Example of the Evans model, showing its impact on the efficiency as a function of varying (a) operating temperature for several β values, and (b) transmitted flux for several γ values.

6.1.3 Calibration and Validation

Since flash tests were not performed on the modules in the experiment, the performance of modules under STC conditions (25 °C, 1000 W/m^2) is unknown. For this reason, experimentally measured irradiance and operating temperature data were decided to be used for calibrating the parameters η_{ref}, β, and γ.

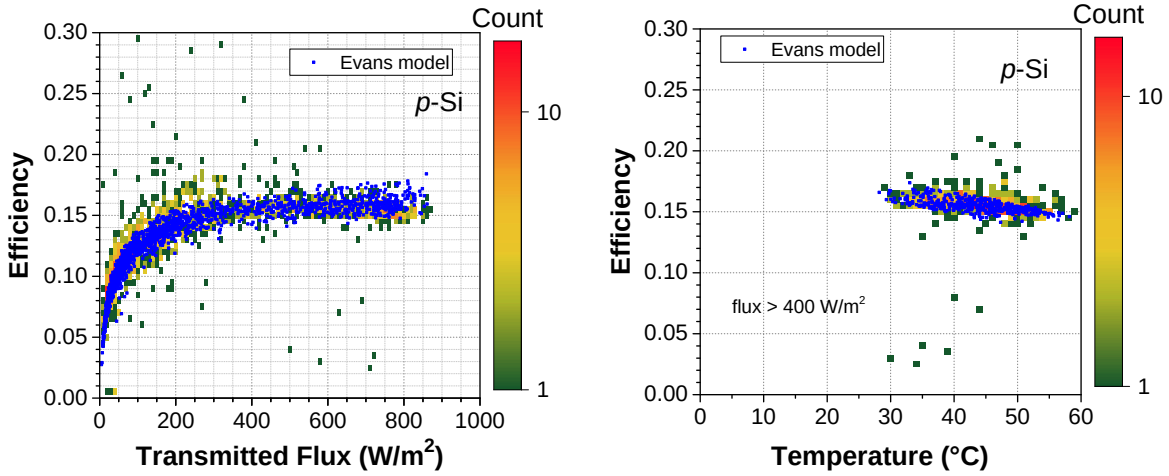

(a) (b)

Figure 6-2: Experimental (colourbar) and numerical (by Evans, in blue) conversion efficiencies for module 5 (frontal p-Si), for the period 17th May - 6th October, 2014. Figure (a) shows the efficiency dependence on transmitted flux, while figure (b) shows the dependence on temperature (only the values corresponding to flux greater than 400 W/m^2 are shown).

A simple coupled model was established as follows. The solar resource equations were

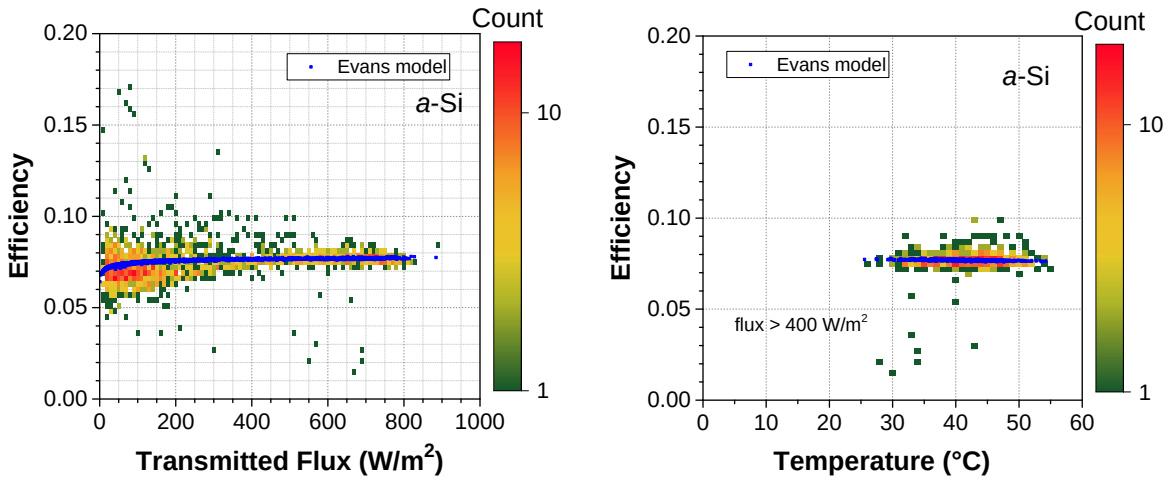

(a) (b)

Figure 6-3: Experimental (colourbar) and numerical (by Evans, in blue) conversion efficiencies for module 6 (frontal *a*-Si:H), for the period 17th May - 6th October, 2014. Figure (a) shows the efficiency dependence on transmitted flux, while figure (b) shows the dependence on temperature (only the values corresponding to flux greater than 400 W/m^2 are shown).

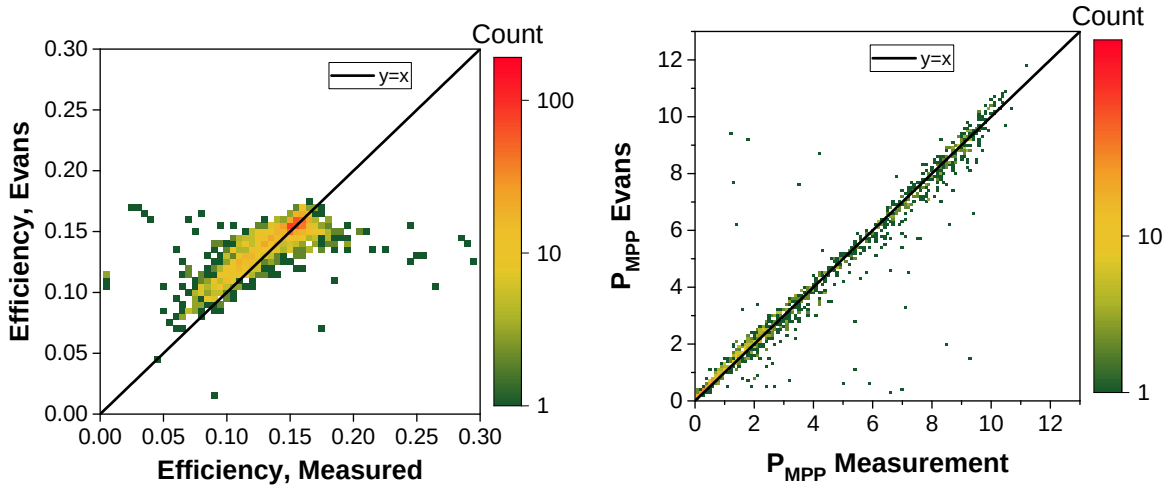

(a) (b)

Figure 6-4: Evans model performance in predicting (a) module conversion efficiency, and (b) the P_{MPP} for module 5 (frontal *p*-Si) and the period 17th May - 6th October, 2014. The analytical optical model was used for calculating irradiances.

used to calculate the angle of incidence of the direct irradiance on the frontal modules of the experiment. Optical losses were calculated for the given angle of incidence. Shape factors were used to define the diffuse flux. Experimentally measured irradiance and operating temperature data were used as input to the electrical model. When needed, the operating temperature values were interpolated. Note that certain *I*-*V* curves were filtered out using shape-based filters and an irradiance stability filter (10% change in GHI was permitted within a preceding two-minute interval). Parameters η_{ref}, β, and γ

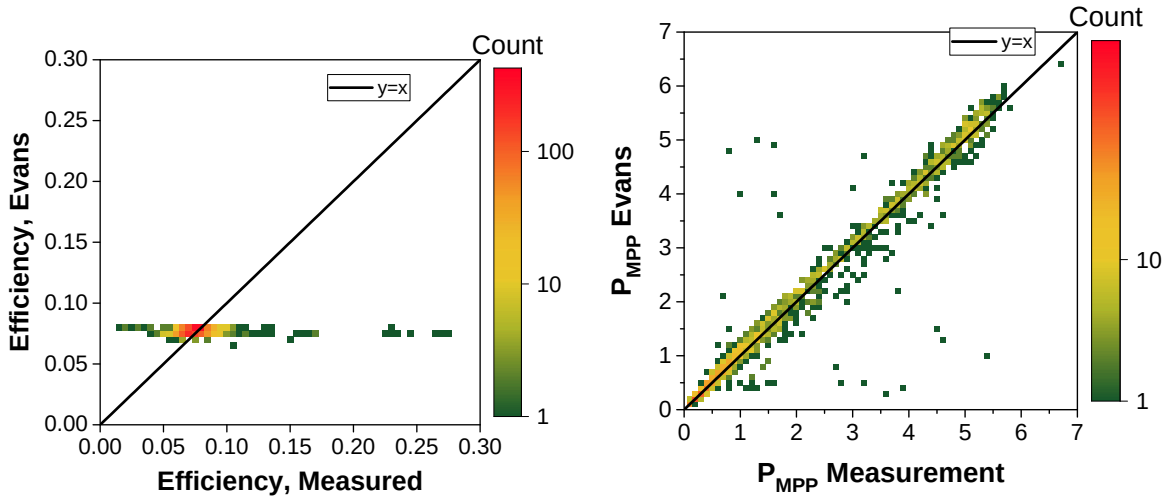

(a) (b)

Figure 6-5: Evans model performance for predicting (a) module conversion efficiency, and (b) the P_{MPP} for module 6 (frontal *a*-Si:H) and the period 17th May - 6th October, 2014. The analytical optical model was used for calculating irradiances.

were varied until the modelled efficiencies matched the measured efficiencies. Note that the "measured" efficiencies still rely on some degree of modelling, for example translating horizontal to plane-of-array diffuse irradiance. The calibration results are summarised in Table 6.1.

Figures 6-2 and 6-3 show the comparison between the experimental and numerical values of efficiency for *p*-Si and *a*-Si:H modules, respectively. Comparing 6-3a and 6-2a, it is evident that *p*-Si modules are more sensitive to low irradiances compared to *a*-Si:H, experiencing higher drops in efficiency during these periods. This explains a higher value of γ for the *p*-Si case. Comparing 6-3b and 6-2b, one can note a higher sensitivity to temperature of *p*-Si modules compared to *a*-Si:H ones, explaining the difference in the values of temperature coefficients, β.

Figures 6-4 and 6-5 show the Evans model performance in predicting the measured efficiency and P_{MPP} values for *p*-Si and *a*-Si:H modules, respectively. In Figs. 6-5a and6-4a one can note an occasional disagreement between experimental and modelled efficiencies. This is particularly pronounced in the case of *a*-Si:H, where the model predicts an almost uniform efficiency for all environmental conditions while the measured efficiency is scattered from almost 0 to almost 30%. This discrepancy is due to the previously described measurement issue during intermittent cloudy conditions, where the measured P_{MPP} values are misaligned with the assumed irradiance values, resulting in unrealistically high or low measured efficiencies. Note that in both graphs the number of points far from the diagonal is very low (marked with low bin counts, in green), while most points (marked with high bin counts, in red) lie very close to the diagonal. For this reason, a good agreement is observed between experimental and numerical values of

P_{MPP}, shown in Figs. 6-4b and 6-5b.

Table 6.1: Evans parameters of *a*-Si:H and *p*-Si modules

Parameter	***p*-Si**	***a*-Si:H**
η_{REF}	0.1856	0.0793
β (°C $^{-1}$)	-5.50×10^{-3}	-9.54×10^{-4}
γ	0.30	0.06

6.2 Equivalent Circuit Electrical Model

6.2.1 State of the Art

Unlike the empirical models for conversion efficiency and P_{MPP} described in the previous section, such as the one proposed by Evans [74], a detailed physics-based model is necessary to explain the PV module behaviour under heterogeneous illumination of cells. In particular, the model must be able to calculate both the cell-level and module-level *I-V* characteristics as a function of radiative and operating temperature inputs.

This section develops the notion of the equivalent circuit model, and details the final model created during this thesis.

6.2.1.1 Ideal Cell Model

The simplest equivalent circuit used to model the photoelectric effect of the PV cells is the ideal cell model. It consists of a circuit with 1) a source of photogenerated current, I_{phot}, proportional to the global irradiance transmitted to the cell, and 2) a diode, representing the dark current resulting from the *p*-*n* junction behaviour of the PV cell.

Figure 6-6 illustrates the resulting equivalent circuit.

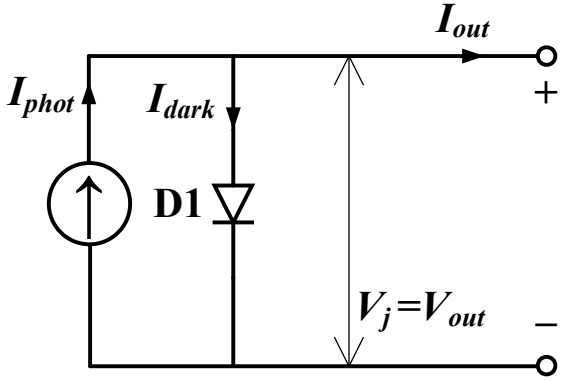

Figure 6-6: Ideal cell model consisting of a source of photogenerated current and an ideal diode ($n = 1$).

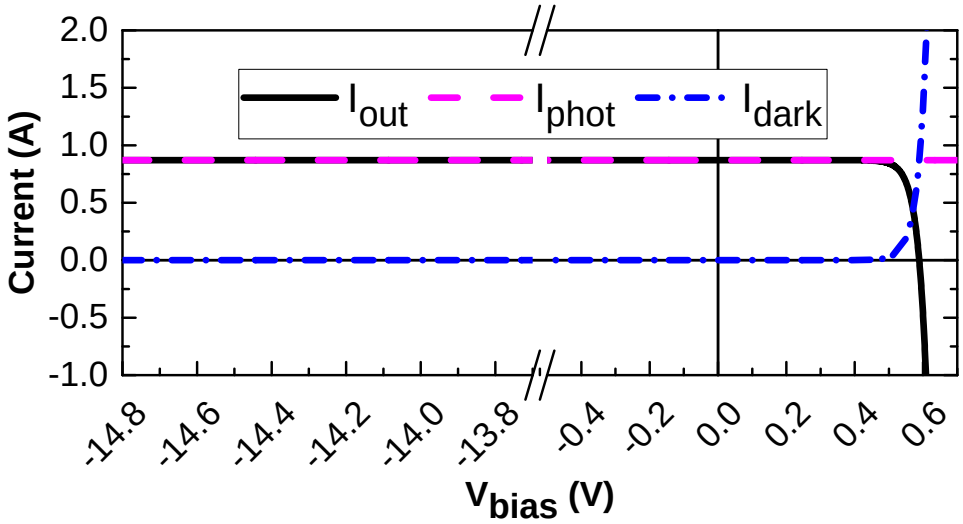

Figure 6-7: The $I-V$ characteristics of each component of the ideal cell model circuit under STC conditions (T=25 °C, G_{POA}=1000 W/m^2). The following parameters were used: I_0=9.8 $\times$ 10^{-11} A, $I_{SC,STC}$=0.871 A. The axis break is shown to demonstrate that the currents stay the same at high negative polarisations.

The circuit in Figure 6-6 results in following equation for I_{out}:

$$I_{out} = I_{phot} - I_0\left[exp\left(\frac{qV_{out}}{nkT}\right) - 1\right] \tag{6.4}$$

where I_{out} is the net current flowing through the diode in A, V_{out} is the output voltage in V, I_{phot} is the photogenerated current in A, I_0 is the dark saturation current (diode leakage current in the absence of light) in A, q is the absolute value of the electron charge (1.602×10^{-19} C or J/V), n is the diode ideality factor, k is the Boltzmann's constant (1.381×10^{-23} J/K), and T is the diode temperature in K. The photogenerated current is generally considered as directly proportional to the incident irradiance, and calculated as follows:

$$I_{phot} = I_{SC,STC}\frac{G_{POA}}{1000\ W/m^2} \tag{6.5}$$

where $I_{SC,STC}$ is the short circuit current at STC conditions (i.e. 1000 W/m^2) in A and G_{POA} is the total plane-of-array irradiance in W/m^2.

To achieve a better model accuracy, an I_{SC} temperature coefficient α can be added to the above definition of I_{phot} to describe the slight increase in I_{SC} with increasing operating temperature:

$$I_{phot} = I_{SC,STC}\frac{G_{POA}}{1000\ W/m^2}[1 + \alpha(T - 25\,°\mathrm{C})] \tag{6.6}$$

where α is the I_{SC} temperature coefficient.

In the ideal case, the ideality factor, n, is set to 1. The resulting circuit is referred to

by the scientific community as the "ideal cell model", partly because of the unity value of n, and partly because of the absence of parasitic effects described in Section 6.2.1.2. The ideal cell model is mostly used for pedagogic purposes.

Figure 6-7 shows the simulated $I-V$ characteristics of each component of the circuit when the cell is exposed to STC conditions.

6.2.1.2 Single Diode Model

A more realistic model is obtained by adding resistances in series and parallel to the circuit, and using a value of n between 1 and 2 to reflect the losses due to junction recombination. The series resistance, R_s, represents the sum of series resistances at the base, emitter, metal grid, contacts and the current collecting bus. The parallel (shunt) resistance, R_{sh}, is used to reflect the leakage current due to localised shunts at the emitter layers, as well as the perimeter shunts along the cell borders. The resulting circuit is referred to by the scientific community as the "single diode model" (see Figure 6-8).

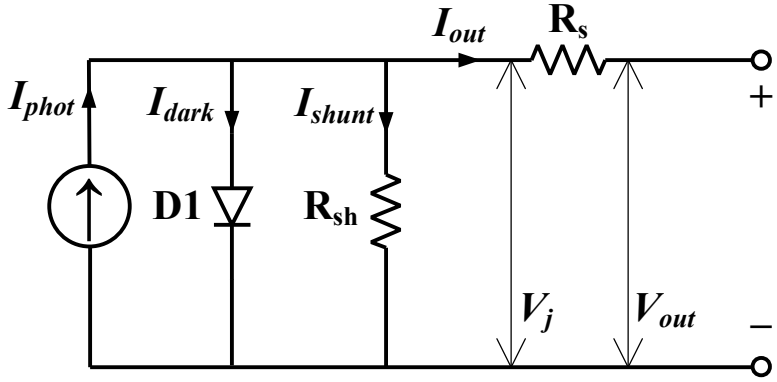

Figure 6-8: Single diode cell model consisting of a source of photogenerated current, a non-ideal diode ($n > 1$), a series resistance, and a parallel (shunt) resistance.

The circuit in Figure 6-8 results in following equation for I_{out}:

$$I_{out} = I_{phot} - I_0\left[exp\left(\frac{q(V_{out}+I_{out}R_s)}{nkT}\right)-1\right] - \frac{V_{out}+I_{out}R_s}{R_{sh}} \tag{6.7}$$

where I_{out}, V_{out}, I_{phot}, I_0, n, q, k, and T were defined in (6.4), R_s and R_{sh} are the cell series and shunt resistances, respectively, in Ω.

Figure 6-9 shows the simulated $I-V$ characteristics of each component of the circuit when the cell is exposed to STC conditions.

Note that this is the most widely used model in the industry, because it is simple and applicable to a variety of PV technologies with an acceptable accuracy. However, due to its simplicity it fails to capture several phenomena such as the recombination at the space charge region (for crystalline silicon devices), the intrinsic layer (i-layer) recombination (for amorphous silicon devices) and the junction breakdown in reverse bias conditions (for

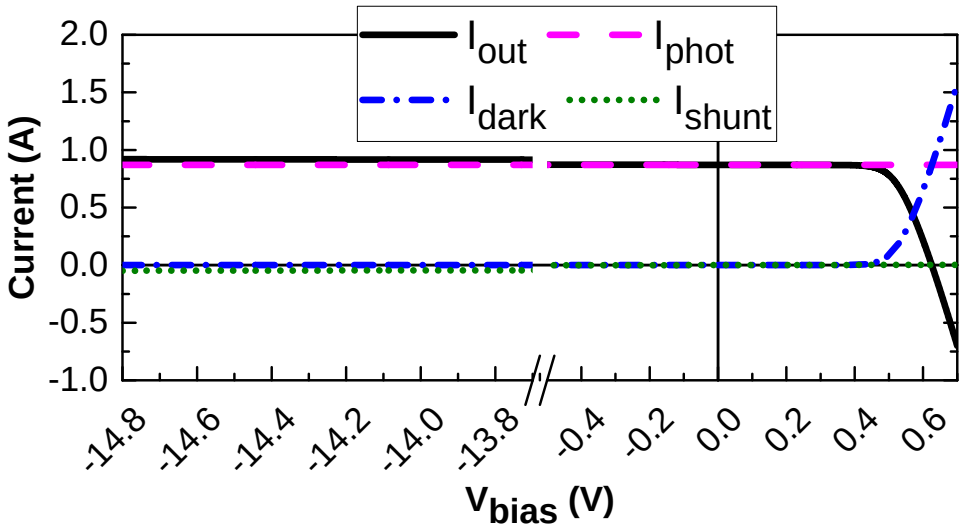

Figure 6-9: The $I - V$ characteristics of each component of the single diode cell model circuit under STC conditions (T=25 °C, G_{POA}=1000 W/m^2). The following parameters were used: I_0=9.8 × 10^{-11} A, $I_{SC,STC}$=0.871 A, R_{sh}=3.0 × 10^2 Ω, R_s=4.2 × 10^{-2} Ω, n=1.000. The axis break is shown to demonstrate the evolution of the shunt current with voltage bias.

both crystalline and amorphous silicon devices). For this reason, this model is commonly expanded, as detailed in the next sections.

6.2.1.3 Double Diode Model

The next improvement in the equivalent circuit model is to attempt to model the recombination at the space charge region, explaining the non-ohmic current paths in parallel with the intrinsic solar cell. This is often done by adding a secondary diode in parallel with the first, where the ideality factor is generally set to a value close to 2.

Figure 6-10 illustrates the resulting equivalent circuit:

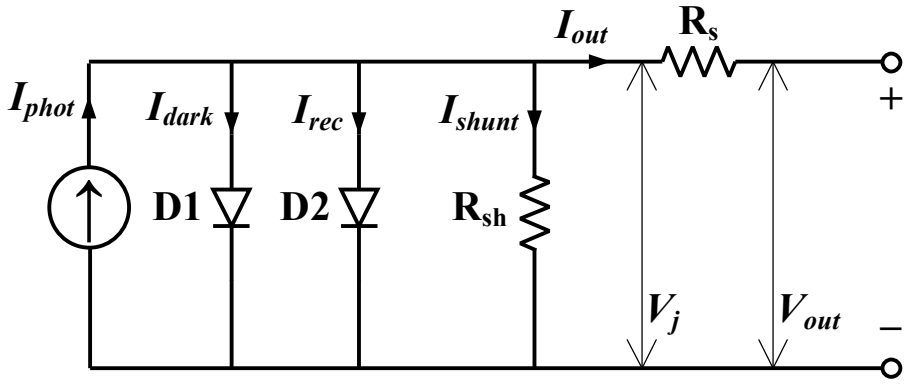

Figure 6-10: Double diode cell model consisting of a source of photogenerated current, a non-ideal diode ($n > 1$), a series resistance, and a parallel (shunt) resistance.

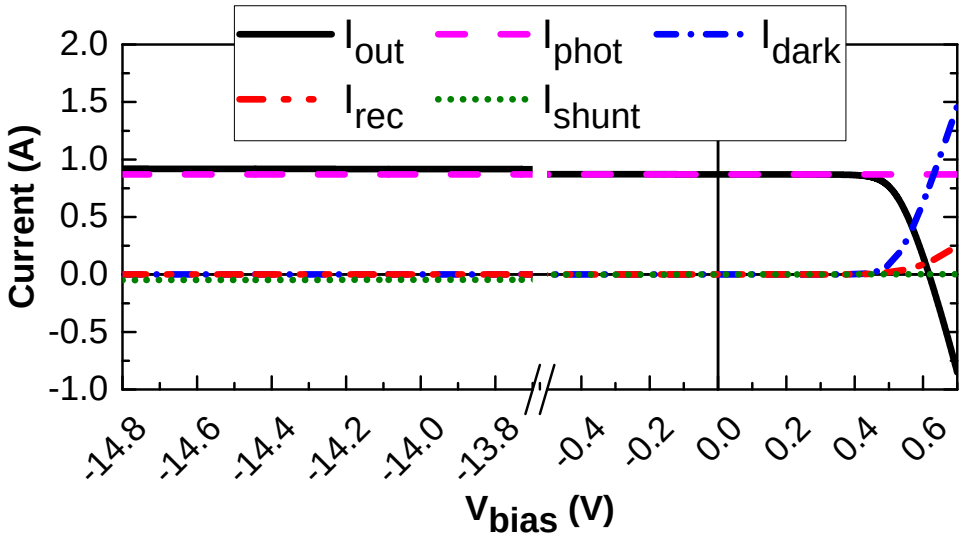

Figure 6-11: The $I-V$ characteristics of each component of the double diode model circuit under STC conditions (T=25 °C, G_{POA}=1000 W/m^2). The following parameters were used: I_{01}=9.8×10^{-11} A, I_{02}=2.2×10^{-7} A, $I_{SC,STC}$=0.871 A, R_{sh}=3.0×10^{2} Ω, R_s=4.2×10^{-2} Ω, n_1=1.000, and n_2=1.819.

The circuit in Figure 6-10 results in following equation for I_{out}:

$$\begin{aligned} I_{out} = & \; I_{phot} \\ & - I_{01}\left[exp\left(\frac{q(V_{out}+I_{out}R_s)}{n_1 kT}\right)-1\right] \\ & - I_{02}\left[exp\left(\frac{q(V_{out}+I_{out}R_s)}{n_2 kT}\right)-1\right] \\ & - \frac{V_{out}+I_{out}R_s}{R_{sh}} \end{aligned} \tag{6.8}$$

where I_{out}, V_{out}, I_{phot}, I_0, q, k, T, R_s and Rsh were defined in (6.7), n_1 and n_2 are the ideality factors for the two diodes, and I_{01} and I_{02} are the dark saturation currents of the two diodes in A.

Figure 6-11 shows the simulated $I-V$ characteristics of each component of the circuit when the cell is exposed to STC conditions.

Note that I_{dark} and I_{rec} currents given by the two diodes differ in behaviour due to the different values of diode parameters (I_0 and n). The fact of having two diodes provides a much greater flexibility in fitting the experimental data with the model.

6.2.1.4 *i*-Layer Recombination in Amorphous Silicon Devices

While a second diode is appropriate for modelling the space charge region recombination in crystalline silicon (c-Si) devices, a better approach exists for amorphous silicon (*a*-Si:H) devices. Since the recombination losses in *a*-Si:H devices are predominantly due to the recombination in the intrinsic layer (*i*-layer), the recombination current has a slightly

different behaviour from a diode. An approach for modelling this behaviour has been proposed by Merten et al. [130], and given in the equation below:

$$I_{rec} = I_{phot} \frac{d_i^2}{(\mu\tau)_{eff}[V_{bi} - (V_{out} + I_{out}R_s)]} \tag{6.9}$$

where I_{rec} is the i-layer recombination current in A, I_{phot} is the photogenerated current in A, d_i is the thickness of the i-layer in cm, $(\mu\tau)_{eff}$ is the effective mobility-lifetime product in cm^2/V, V_{bi} is the built-in voltage in V, and $(V_{out} + I_{out}R_s)$ is the junction voltage in V.

Figure 6-12 illustrates the resulting equivalent circuit:

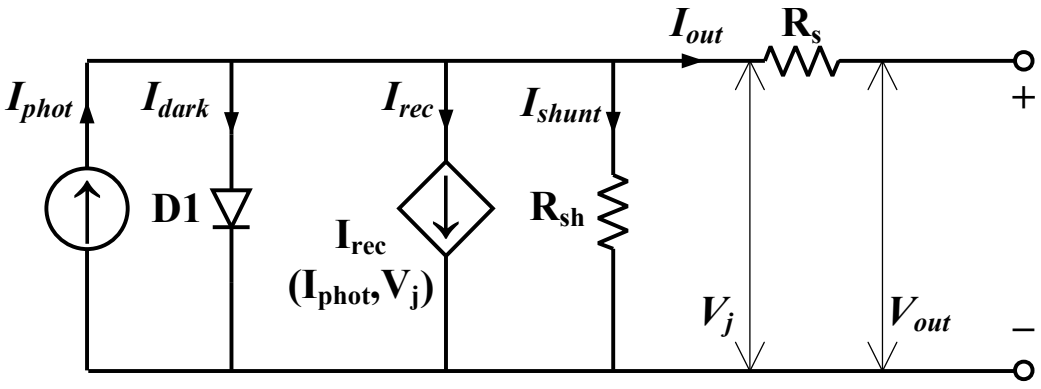

Figure 6-12: Merten cell: single diode cell model with the added Merten term represented by a current sink.

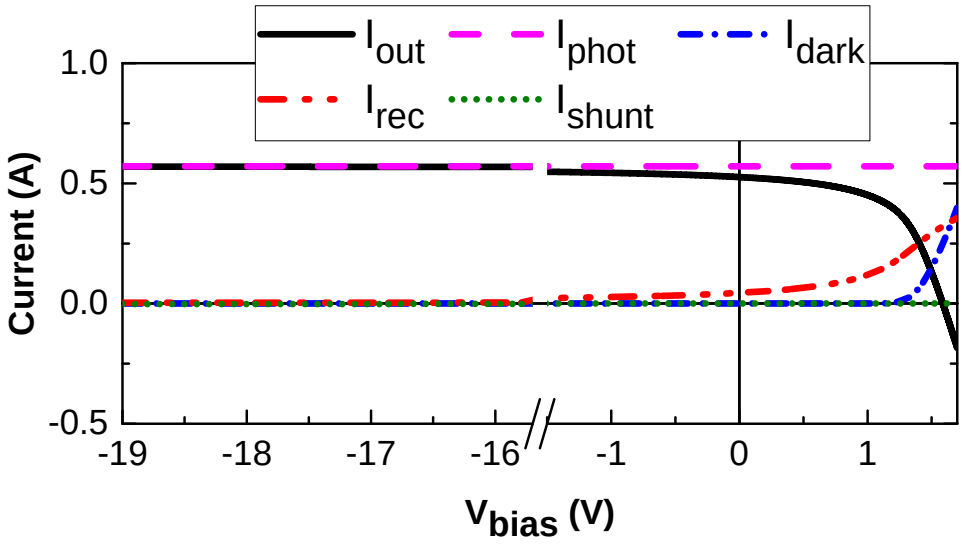

Figure 6-13: The I-V characteristics of each component of the double diode model circuit under STC conditions (T=25 °C, G_{POA}=1000 W/m^2). The following parameters were used: I_0=5.4 × 10^{-17} A, $I_{SC,STC}$=0.571 A, R_{sh}=9.7 × 10^3 Ω, R_s=5.0 × 10^{-1} Ω, and n=1.700.

Figure 6-13 shows the simulated I-V characteristics of each component of the circuit when the cell is exposed to STC conditions.

6.2.1.5 Junction Breakdown

If a given PV cell within a string of series-connected cells is shaded (e.g. by leaves or bird droppings), it can be reverse-biased to voltages up to -15 V depending on the module architecture, and can therefore dissipate the power generated by the neighbouring cells exhibiting full illumination. This power dissipation can lead to hot spots, inducing irreversible damage to PV modules.

All $p-n$ junction devices have a certain value of reverse bias, called breakdown voltage, V_{br}, at which the junction "breaks down" and lets an enormous amount of current pass through the junction. This can be very dangerous for the PV cell, as it can result in excessive heating and permanent damage. This value varies by cell type, and has been reported to range from -7.2 V to -25.2 V [131]. The design of PV modules must take this into account, so that under the worst case of cell reverse bias (e.g. under extreme partial shading of a cell during high irradiances), the cell is not reverse-biased beyond its respective V_{br}. For this reason, bypass diodes are often added to reduce the maximum cell reverse bias under the worst-case scenario, and hence avoid a junction breakdown.

To model this behaviour one can follow the procedure outlined by Bishop [132]. The standard single- and double-diode models describe the leakage current by a parallel resistance, where the current is defined as the junction voltage divided by resistance value. Bishop recommends to modify this term to describe the voltage breakdown:

$$I_{br} = \frac{V_{out} + I_{out}R_s}{R_{sh}} \left[a \left(1 - \frac{V_{out} + I_{out}R_s}{V_{br}} \right)^{-m} \right] \tag{6.10}$$

where I_{br} is the leakage current in the cell reverse characteristic in A, $(V_{out} + I_{out}R_s)$ is the voltage across the junction in V, R_{sh} is the cell shunt resistance in Ω, a is the fraction of ohmic current involved in avalanche breakdown, and m is the avalanche breakdown exponent. The resulting term is a function of junction voltage $(V_{out}+I_{out}R_s)$ and controls the cell reverse characteristic.

The total leakage current becomes:

$$I_{shunt} = \frac{V_{out} + I_{out}R_s}{R_{sh}} \left[1 + a \left(1 - \frac{V_{out} + I_{out}R_s}{V_{br}} \right)^{-m} \right] \tag{6.11}$$

Figure 6-14 illustrates the resulting equivalent circuit.

Figure 6-15 shows the simulated I-V characteristics of each component of the circuit when the cell is exposed to STC conditions.

6.2.2 Implementation

This section details the implementation of the electrical model for the PV modules of two technologies: a-Si:H and p-Si. The strategy is to first model the behaviour of individual

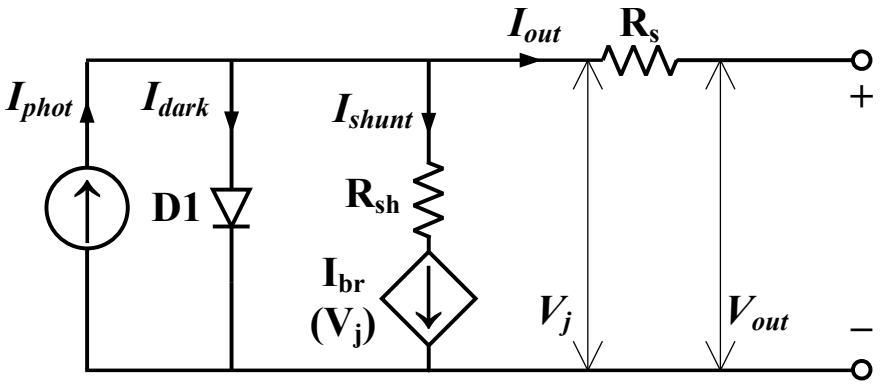

Figure 6-14: Bishop cell: single diode cell model with the added Bishop term represented by a current sink.

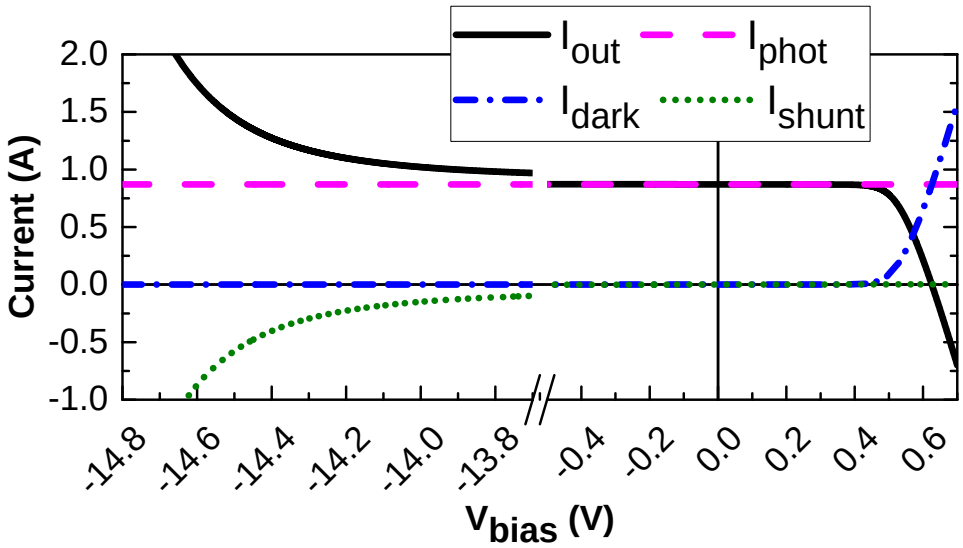

Figure 6-15: The I-V characteristics of each component of the Bishop cell model circuit under STC conditions (T=25 °C, G_{POA}=1000 W/m^2). The following parameters were used: I_0=9.8 × 10^{-11} A, $I_{SC,STC}$=0.871 A, R_{sh}=3.0 × 10^2 Ω, R_s=4.2 × 10^{-2} Ω, n=1, a=2.4 × 10^{-3}, V_{br}=15 V, m=2.57.

cells, and then connect them accordingly. Note that the equations used to describe the output current as a function of voltage bias are transcendental, necessitating an iterative approach for their resolution. This is luckily a built-in feature in most SPICE implementations. In the case of LTSpice, the Newton-Rapson method is implemented.

6.2.2.1 Modelling of PV Cells

Two different electrical circuits are proposed for describing the behaviour of individual a-Si:H and p-Si cells, respectively (see Figs. 6-16 and 6-17).

For the a-Si:H cell (Figure 6-16), a single-diode model is proposed with the addition of the Merten (I_{rec}) and Bishop (I_{br}) terms. For the p-Si cell (Figure 6-17), a double-diode model is proposed with the addition of the Bishop (I_{br}) term. In both cases, the slight increase in short circuit current with temperature was introduced in the photogenerated

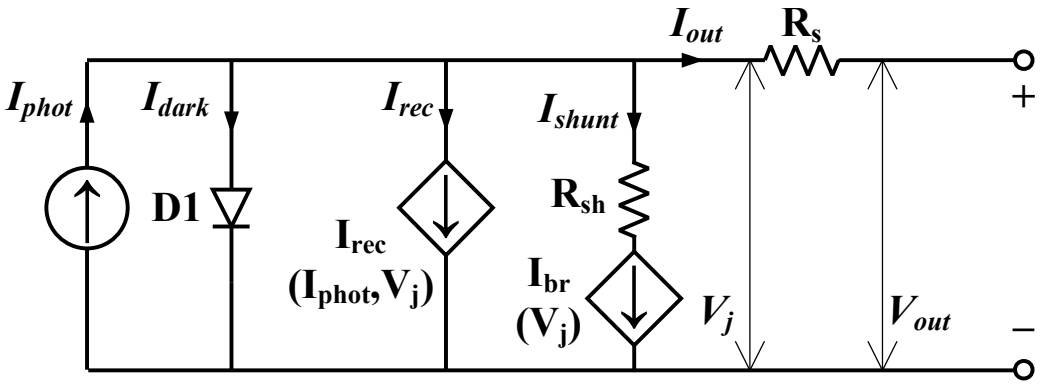

Figure 6-16: *a*-Si:H cell: single diode cell model with the added Bishop and Merten terms, both represented by current sinks.

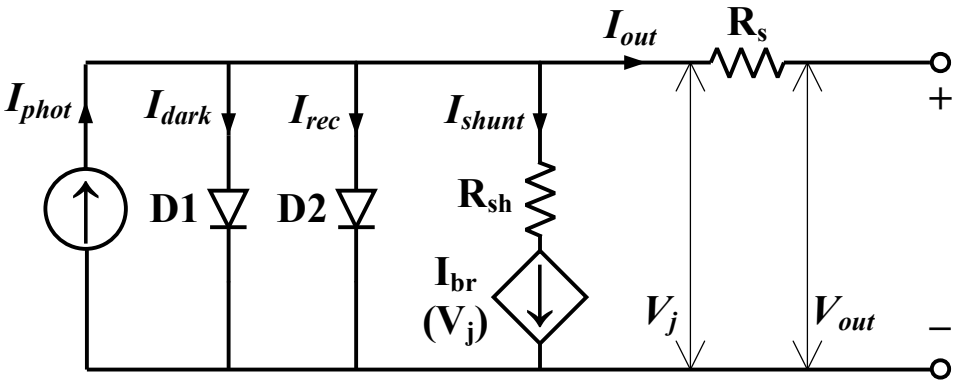

Figure 6-17: *p*-Si cell: double diode cell model with the added Bishop term represented by a current sink.

current source term. The following equations describe the *a*-Si:H circuit:

$$\begin{aligned} I_{out,a-Si:H} = {} & I_{SC,STC}\frac{G_{POA}}{1000W/m^2}[1+\alpha(T-25\,^\circ\mathrm{C})] \\ & - I_{01}\left[exp\left(\frac{q(V_{out}+I_{out}R_s)}{n_1 kT}\right)-1\right] \\ & - I_{phot}\frac{d_i^2}{(\mu\tau)_{eff}[V_{bi}-(V_{out}+I_{out}R_s)]} \\ & - \frac{V_{out}+I_{out}R_s}{R_{sh}}\left[1+a\left(1-\frac{V_{out}+I_{out}R_s}{V_{br}}\right)^{-m}\right] \end{aligned} \tag{6.12}$$

or equivalently

$$\begin{aligned} I_{out,a-Si:H} = {} & I_{SC,STC}\frac{G_{POA}}{1000W/m^2}[1+\alpha(T-25\,^\circ\mathrm{C})]\left\{1-\frac{d_i^2}{(\mu\tau)_{eff}[V_{bi}-(V_{out}+I_{out}R_s)]}\right\} \\ & - I_{01}\left[exp\left(\frac{q(V_{out}+I_{out}R_s)}{n_1 kT}\right)-1\right] \\ & - \frac{V_{out}+I_{out}R_s}{R_{sh}}\left[1+a\left(1-\frac{V_{out}+I_{out}R_s}{V_{br}}\right)^{-m}\right] \end{aligned} \tag{6.13}$$

Similarly to a-Si:H, the following equation describes the I-V characteristic of the p-Si circuit:

$$\begin{aligned} I_{out,p-Si} = I_{SC,STC}\frac{G_{POA}}{1000W/m^2}[1+\alpha(T-25\,^{\circ}\mathrm{C})] \\ - I_{01}\left[exp\left(\frac{q(V_{out}+I_{out}R_s)}{n_1kT}\right)-1\right] \\ - I_{02}\left[exp\left(\frac{q(V_{out}+I_{out}R_s)}{n_2kT}\right)-1\right] \\ - \frac{V_{out}+I_{out}R_s}{R_{sh}}\left[1+a\left(1-\frac{V_{out}+I_{out}R_s}{V_{br}}\right)^{-m}\right] \end{aligned} \tag{6.14}$$

where $I_{SC,STC}$ is the short circuit current at STC conditions in A, G_{POA} is the plane-of-array irradiance in W/m^2, α is the I_{SC} temperature coefficient, and the rest of the terms were defined previously.

Using LTSpice, the two circuits were exposed to STC conditions, and the I-V characteristics of different circuit components were extracted (see Figs. 6-18 and 6-19).

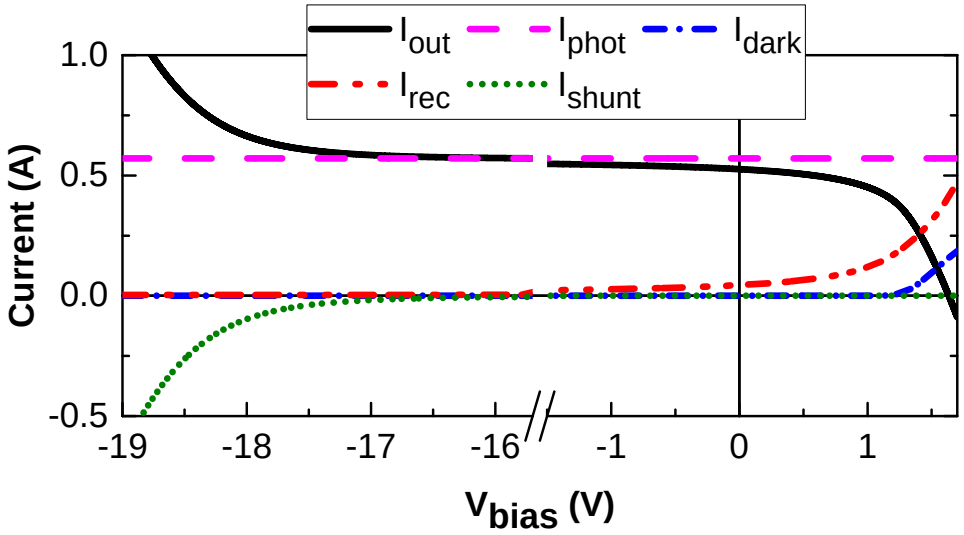

Figure 6-18: Current in each component of the proposed a-Si:H cell model as a function of the applied voltage bias. The cell was parametrised using the values shown in Table 7.1 and subjected to STC conditions.

Figure 6-18 shows the current in each component of the a-Si:H cell equivalent circuit. I_{out} (shown in black) is the output current of the cell, and is equal to I_{phot}-I_{dark}-I_{rec}-I_{shunt}. The photogenerated current (shown in pink), is constant for all values of voltage bias, and is proportional to the total incident flux on the cell. It is set to increase slightly with temperature, according to (6.6). Since STC is applied, I_{phot} is equal to $I_{SC,STC}$ (0.57 A). I_{dark}, the dark saturation current (shown in blue), follows the typical behaviour of a diode, having zero current for negative and slightly positive values of voltage bias, and rising exponentially for voltage bias values grater than the diode built-in voltage

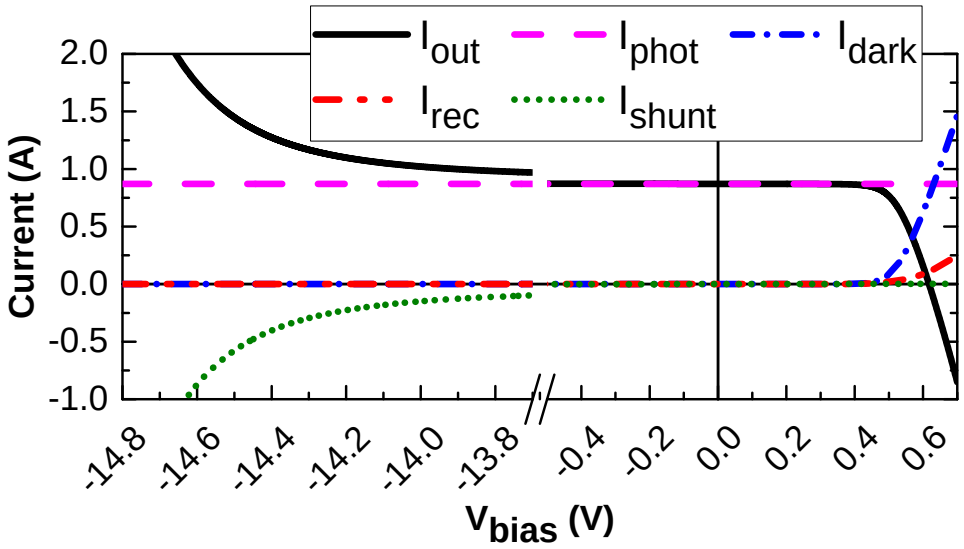

Figure 6-19: Current in each component of the proposed p-Si cell model as a function of the applied voltage bias. The cell was parametrised using the values shown in Table 7.1 and subjected to STC conditions.

(V_{bi}). Typical silicon diodes have a V_{bi} of about 0.7 V. However, as seen in the figure the a-Si:H cell was found to have a V_{bi} greater than 1 V. This is because the cells within the experimental modules are in fact tandem cells composed of two sub-cells stacked vertically. The effective V_{bi} therefore represents the total V_{bi} of the two sub-cells. In this figure and in further modelling, an a-Si:H cell refers to a tandem cell, while an a-Si:H module is considered to have 14 cells connected in series (even though the module specification indicates there are 28 cells in total). I_{rec}, the i-layer recombination current (shown in red), reflects the use of the equation proposed by Merten et al. [130]. Compared with the diode equation, 1) it converges to a small non-zero value as V_{bias} tends to -∞ V, 2) at V_{bias}=0 V, significant recombination current is observed, 3) it is much higher in amplitude in the region $[0, V_{OC}]$, and 4) has a different shape. As seen in the figure, this term is the dominant loss mechanism. I_{shunt}, the shunt current (shown in green), increases gradually with V_{bias} for positive bias values. The slope of the increase depends on the value of R_{sh}. The current is 0 A at V_{bias}=0 V and for slightly negative values of V_{bias}. As V_{bias} approaches the set breakdown voltage of -20 V, I_{shunt} increases rapidly in the negative direction, letting an enormous amount of current pass through the cell.

Figure 6-19 shows the current in each component of the p-Si cell equivalent circuit. Similarly to the a-Si:H cell, the I_{phot} is constant throughout the range of the V_{bias} sweep. As STC conditions were simulated, I_{phot}=$I_{SC,STC}$=0.87 A. I_{dark} (in blue) and I_{rec} (in red) follow diode equations with different sets of parameters, yielding a dark current which is much higher than the recombination current. It is observable that the V_{bi} of both diodes is around 0.7 V, as expected. Finally, I_{shunt} behaves similarly to the case of a-Si:H cells, rising gradually during positive values of V_{bias}, and increasing rapidly in the negative

direction as V_{bias} approaches the breakdown voltage of -15 V.

6.2.2.2 Modelling of PV Modules

After having developed the model of the electrical behaviour of a cell, the next step was to model the behaviour of entire modules. PV modules most commonly consist of PV cells connected in series, with the goal of maximising the open circuit voltage of the module. For example, the *a*-Si:H modules installed in the experiment consist of 14 tandem cells connected in series, while the *p*-Si module consists of 36 cells connected in series (see Figs. 3-10a and 3-10b, page 35). In the case of *p*-Si modules with a large number of cells connected in series, bypass diodes are often added across a certain number of the cells, which are referred to as being in a string. The goal of bypass diodes is to provide an alternate path for current flow during certain configurations of current mismatch, such as during partial shading conditions. The *p*-Si module in the experiment consists of 36 cells in series and two bypass diodes across each of the strings of 18 cells. Bypass diodes are generally not added to *a*-Si:H modules, even if there are many cells connected in series. The main reason for this is that *a*-Si:H cells are generally long (spanning the entire height of the module) making the *a*-Si:H modules less susceptible to partial shading.

Several solutions exist for modelling the PV modules as series-connected cells, such as PVSim [133], Simulink [134] and Spice [135]. Spice analog simulator was chosen as the simulation tool since it is open-source and known to have a great performance. It uses state of the art convergence methods and well-established iterative procedures to calculate the currents and voltages at any part of the circuit. Furthermore, it supports circuits of arbitrary complexities. It is being packaged into a graphical interface by several enterprises, some selling it as a product (e.g. PSpice [136]) while other releasing it for free. Two free alternatives were tested: LTSpice [137] was tested under the Microsoft Windows environment, and ngspice [138] under the Linux environment.

Circuits are defined in files .cir, which can be developed 1) by drawing the schematics using the graphical interface of the software and converting them into a .cir file, or 2) manually (e.g. using an external program). It is desirable to be able to systematically create .cir files of PV modules comprising an arbitrary number of cells and their irradiances and operating temperatures. Therefore, a C++ code has been developed to dynamically generate .cir files as a function of PV technology and module topology.

For additional flexibility and at the same time clarity of the PV module .cir file, the definition of the PV cell circuit was defined in a separate file, conventionally a .lib file. The .lib file is then included in the main .cir file, and the PV cells are easily implemented as subcircuits (see Fig. 6-20).

The C++ code connects a chosen number of PV cells in series by systematically numbering the nodes of each subcircuit (that of an individual cell) within the .cir file. It

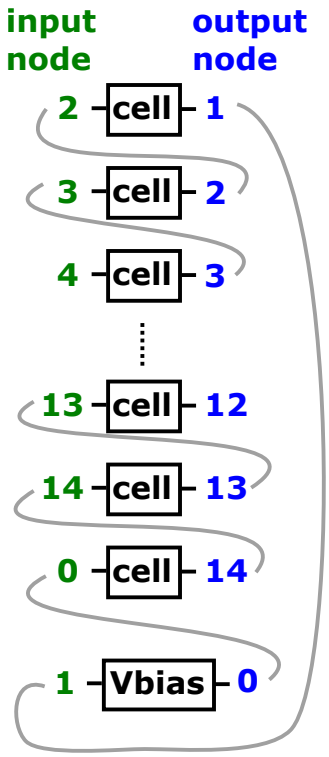

Figure 6-20: Illustration of subcircuit node numbering within the PV module .cir file for connecting PV cells in series. Example given is for a 14-cell module. The system is grounded by numbering one node with 0.

makes sure that the overall circuit is grounded (by adding node 0), and adds a voltage bias between the first and last cells (to be stepped during the simulation). It adds a chosen number of bypass diodes, in our case 0 or 2 for *a*-Si:H and *p*-Si, respectively. It writes modelled or measured irradiance and operating temperature values of each PV cell.

Finally, for the purpose of evaluating the *I*-*V* curve of the assembly, a DC sweep directive is added, varying the voltage bias from 0 V (short circuit conditions) to a point beyond the open circuit conditions (for example 25 V), with a step of 0.01 V.

Both LTSpice and ngspice support the batch mode, where Spice is called externally with the path of the .cir file given as an argument. In this case, the need for a graphic interface is eliminated, and more resources are available for the calculation. Furthermore, this allows one to pilot Spice calculations externally, effectively coupling the electrical model with the rest of the model. As the calculation result was to be imported by the piloting program, Spice needed to be configured to produce ASCII result files (written in .RAW files), as the default is a binary output.

6.2.3 Example: Partial Shading

Partial shading of a PV module (in the worst case, total shading of a single cell) can be of particular danger to its lifetime and performance, as the shaded cell can be reverse-

biased into conditions where it dissipates significant amounts of power. Power dissipation results in significant heat generation within the cell, which can lead to temporary and permanent performance degradation. It is therefore an important design factor for PV modules, and is brought to a minimum by:

- optimising the breakdown voltage of the cell junction thereby reducing the risk of avalanche breakdown, and
- introducing bypass diodes across a certain number of series-connected cells, reducing the worst-case amount of reverse bias

The SPICE electrical model has been used to study the behaviour of partially shaded modules, as described in the following two studies.

6.2.3.1 Study 1: STC vs. Partial Shading

In the first study, a *p*-Si module was simulated under two scenarios:

1. STC conditions (1000 W/m^2, 25 °C) - hence uniform illumination
2. STC conditions with cell 9 shaded by 50%

Figures 6-21, 6-22, 6-23, and 6-24 illustrate cell currents, cell voltages, bypass diode currents, and bypass diode voltages, respectively, as a function of applied voltage bias for the two scenarios.

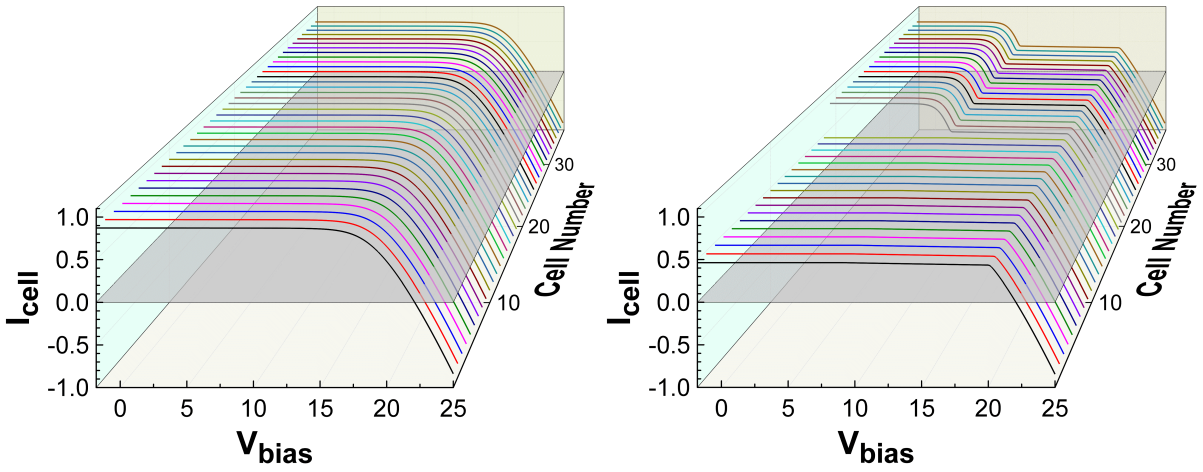

(a) (b)

Figure 6-21: *p*-Si cell currents: (a) at STC, and (b) with cell 9 shaded by 50 %.

Under Scenario 1 (STC conditions, uniform illumination), the cell currents are the same for all 36 cells for a given voltage bias (see Fig. 6-21a). In this case they are around 0.87 A in short circuit conditions. The imposed voltage is uniformly distributed among the cells, resulting in equal voltage across each cell, and increasing linearly with the applied bias (see Fig. 6-22a). For example, if a bias of +18 V is imposed across the module, each cell operates under 18 V / 36 = +0.5 V. Under these conditions, both strings and therefore both bypass diodes are biased to +9 V. Since the bypass diodes

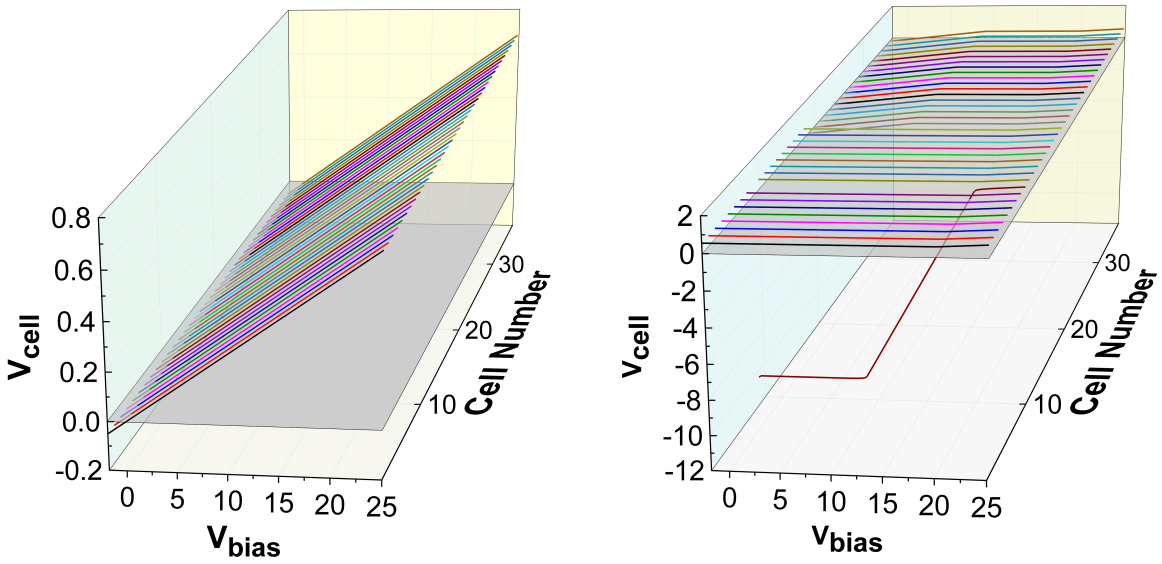

(a) (b)

Figure 6-22: *p*-Si cell voltages: (a) at STC, and (b) with cell 9 shaded by 50 %.

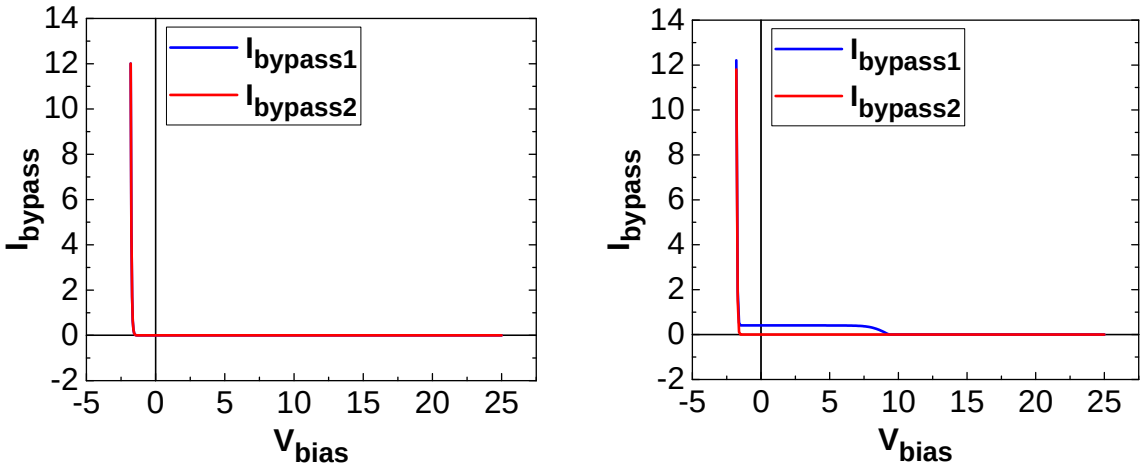

(a) (b)

Figure 6-23: *p*-Si bypass diode currents: (a) at STC, and (b) with cell 9 shaded by 50 %.

only get activated in reverse bias conditions when the string voltage reaches about -0.7 V, they remain off under these conditions (see Figs. 6-23a and 6-24a).

Scenario 2 represents a partial shading condition. When a cell is partially shaded, it is the photocurrent that it is capable of generating which limits the current that flows through the string. For example, a 50% shading results in a short circuit current of 0.46 A (53% compared to unshaded case) for all cells in the affected string (see Fig. 6-21b). This limit in current imposes a constraint on the operating voltage of non-shaded cells in the affected string, ranging between around 0.56 V (corresponding to the limiting current of 0.46 A), and around 0.61 V (the cell-level open-circuit voltage) - see Fig. 6-25.

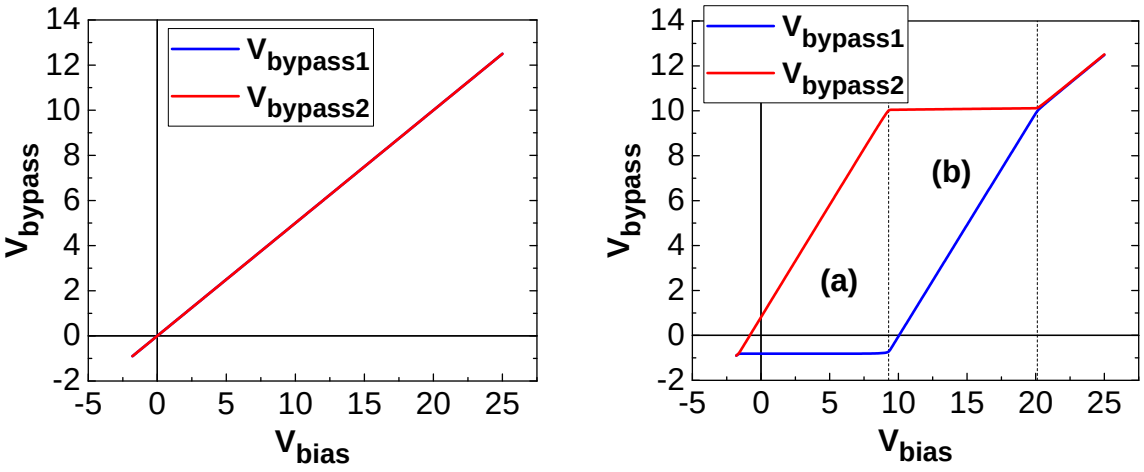

(a) (b)

Figure 6-24: *p*-Si bypass diode currents: (a) at STC, and (b) with cell 9 shaded by 50 %.

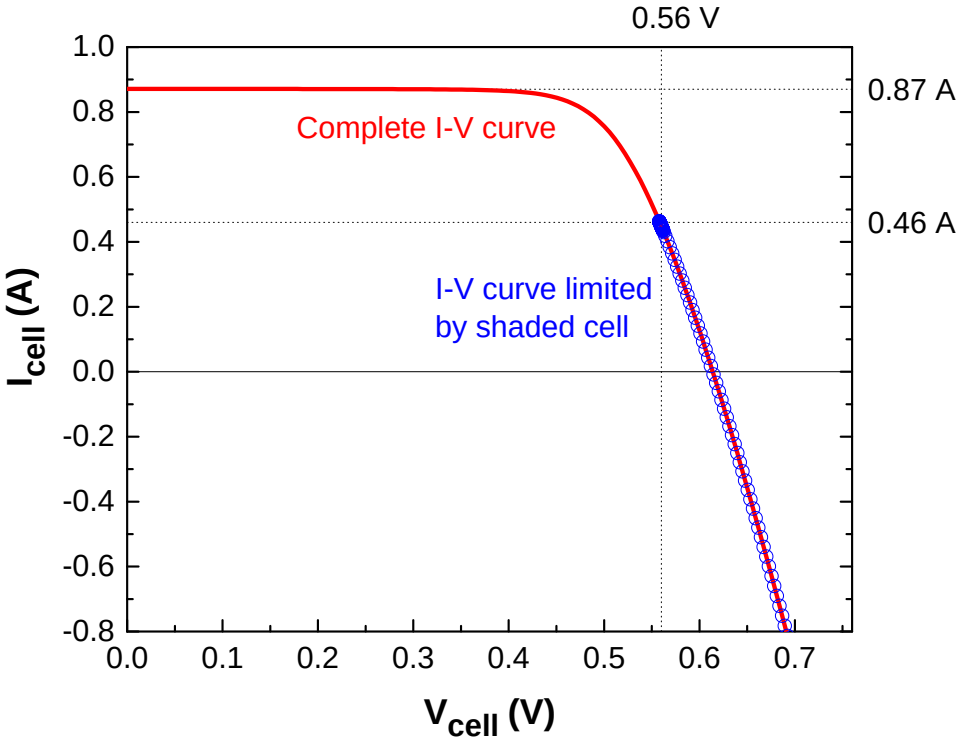

Figure 6-25: Illustration of the operating voltage constraint of non-shaded cells in a string containing a shaded cell.

The resulting mismatch in the short-circuit current between the cells in the string results in the shaded cell being reverse biased for most polarisations (except near the V_{OC}), leading to power dissipation in the cell. At low-enough voltage bias values, the reverse bias becomes high enough to result in the activation of the bypass diode, fixing the voltage across it and across the contained string to around -0.7 V. Consider Fig. 6-24b at zero voltage bias. A voltage of -0.7 V is imposed on the affected string (string 1) by the activated bypass diode encompassing it. String 1 contains 17 cells functioning

at 0.56 V, resulting in the following balance:

$$\begin{aligned} 17 \times 0.56V + Vcell9 &= -0.70V \\ Vcell9 &= -10.22V \end{aligned} \tag{6.15}$$

imposing the operation point of the shaded cell. The number of cells per string can be chosen in this way to ensure the reverse bias does not exceed the cell breakdown voltage. At V_{OC}, the non-shaded string operates at:

$$\begin{aligned} Vbypass2 &= Vbias - Vbypass1 \\ &= +0.70V \end{aligned} \tag{6.16}$$

resulting in each cell operating at 0.70 V / 18 = +0.039 V.

In region (a) of Fig. 6-23b, as the voltage across the module increases, the string 1 (containing the shaded cell) stays at the same operating point with the voltage imposed by the bypass diode. The voltage across string 2 increases linearly. At a certain point (line separating regions (a) and (b)), the cells in string 2 operate at the same voltage as the non-shaded cells of string 1 (0.56 V). It is at this point that string 1 voltage starts increasing linearly, gradually turning off the bypass diode (see Fig. 6-23b). Region (b) is therefore characterised by an increase in string 1 voltage, which manifests itself in a reduction in the shaded cell reverse bias, while the string 2 stays at the same operating point. Region (b) ends at the point where the string 1 voltage reached the one of string 2, beyond which both strings increase linearly with applied voltage (in the same way as under STC conditions).

6.2.3.2 Study 2: Performance vs. Level of Shading

In the second study, a *p*-Si module was simulated under STC conditions, while the level of shading of a single cell (cell 9) was varied from 0 to 100% in 25% increments. The simulation was performed for the cases of zero and two bypass diodes (BPD) being installed. It was assumed that during a given module operation, a maximum power point tracking (MPPT) mechanism controlled the operating point to maximise the module power output.

Fig. 6-26 presents the simulation results - the PV module power output (above) and the shaded cell dissipated power (below) as a function of applied voltage bias. Solid lines represent the case of no BPD, while the dashed lines represent the case with BPD.

In the case of 0% shading, the module maximum power output is 11.0 W, which is evenly distributed among the 36 cells resulting in about 0.3 W of production per cell (not shown).

In the cases of 25 and 50% shading, the module power output drops to 10.0 and 7.1

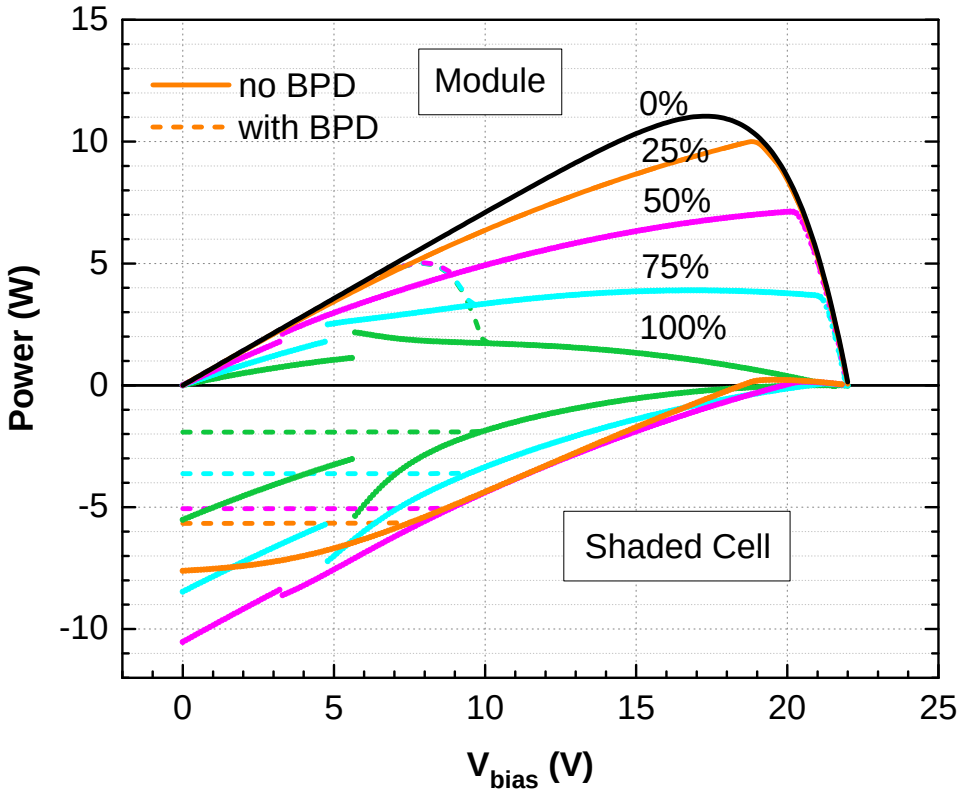

Figure 6-26: P-V characteristics of module output power (above), and shaded cell dissipated power (below), for different levels of shading. The black line represents the case of no shading, while the orange, magenta, blue, and green lines represent the cases of 25, 50, 75, and 100% shading, respectively. The dissipated power values at low V_{bias} for shading rates of 50, 75, and 100% (magenta, blue, and green disconnected segments in the range 0-6 V) are an artefact of Bishop's mathematical formulation of the cell-level avalanche current, which produces incorrect avalanche current values if V_{cell} values greater than Vbr are imposed.

W, respectively, while the V_{MPP} (location of peak) shifts to the right. The associated shaded cell productions reduce to 0.2 and 0.1 W, respectively. In both shading cases, the addition of bypass diodes has no impact on performance. This is because the right-hand peak in module P_{MPP} remains higher than the BPD-resulting left-hand peak, meaning that the point of operation remains unchanged.

Consider the case of 75% shading and no BPD (blue solid lines). The module P_{MPP} drops to 3.9 W, and the V_{MPP} is 16.9 V, lower than in the previous shading cases. At this operating point, the shaded cell is reverse-biased and *absorbs* 0.8 W. The introduction of BPD in this case results in a left-hand peak in module P_{MPP} that is higher than the original right-hand peak. The operating point is therefore shifted to the V_{bias} corresponding to the left peak (i.e. a "turn-over" takes place), with two consequences:

- the module P_{MPP} is increased to 5.0 W (positive impact)
- the shaded cell power dissipation is increased to 3.6 W (negative impact)

Consider the case of 100% shading and no BPD (green solid lines). The module V_{MPP}

is 5.7 V, much lower than in the case of 75% shading. The module power output is 2.2 W, while the shaded cell power dissipation is 5.4 W. Similarly to the previous case, the introduction of BPD results in a dominant peak which in this case shifts the operating point to the right. This has two consequences:

- the module P_{MPP} is increased to 5.0 W (positive impact)
- the shaded cell power dissipation is reduced to 1.9 W (positive impact)

Comparing the results of these shading cases, it is evident that BPD serves the purpose of maximising production in partial shading conditions, while in certain cases negatively impacts the shaded cell dissipation. One can also note that in both "no BPD" and "with BPD" cases, there is a certain value of shading rate where a turn-over takes place due to a change in V_{MPP}. In the case "with BPD" the turn-over is expected between 50 and 75%, while in the case "no BPD" it should occur between 75 and 100%.

To examine the partial shading effect in more detail, the study was repeated for all shading rates of cell 9 (0 to 100% in 1% increments), and several electrical variables were evaluated at the voltage corresponding to the module P_{MPP}. Specifically, the variables saved were the power of the module, the power and voltage of the shaded cell (9), the power and voltage of the unshaded cell in the *unshaded* string (27), and the power of the unshaded cell in the *impacted* string (5). Figs. 6-27a and 6-27b show the results for the case of with and without BPD, respectively.

In both cases, as the shading is increased the module and shaded cell power outputs decrease. Equally, the shaded cell in both cases starts to dissipate power beyond a shading of 63% due to a negative cell voltage.

Consider now the case "with BPD" (Fig. 6-27a). At 65% shading, a turn-over occurs when the BPD turns on. The shaded cell voltage drops to -10.3 V, resulting in a power dissipation of 4.2 W. The cell voltage is not low enough to trigger an avalanche breakdown. As the shading is further increased, the module output power remains the same due to the BPD presence. The shaded cell's voltage continues to decrease slightly as it adapts to the imposed current. The shaded cell power dissipation decreases in magnitude since the cell current decreases faster than its voltage.

Fig. 6-27b presents the case of "no BPD". As the shading is increased beyond 63%, the module power output keeps decreasing. More importantly, the shaded cell voltage continues to decrease resulting in a growing dissipation. At 90% shading, a turn-over occurs since the module V_{MPP} is shifted to a lower polarisation (as it did in Fig. 6-26 when comparing the "75%" and "100%" cases). The turn-over results in the shaded cell voltage being low enough for it to abruptly enter the avalanche mode. The resulting power dissipation is about 6 W and in practice marks the end of the module's life. Therefore, the simulation results beyond the turn-over point have little practical value.

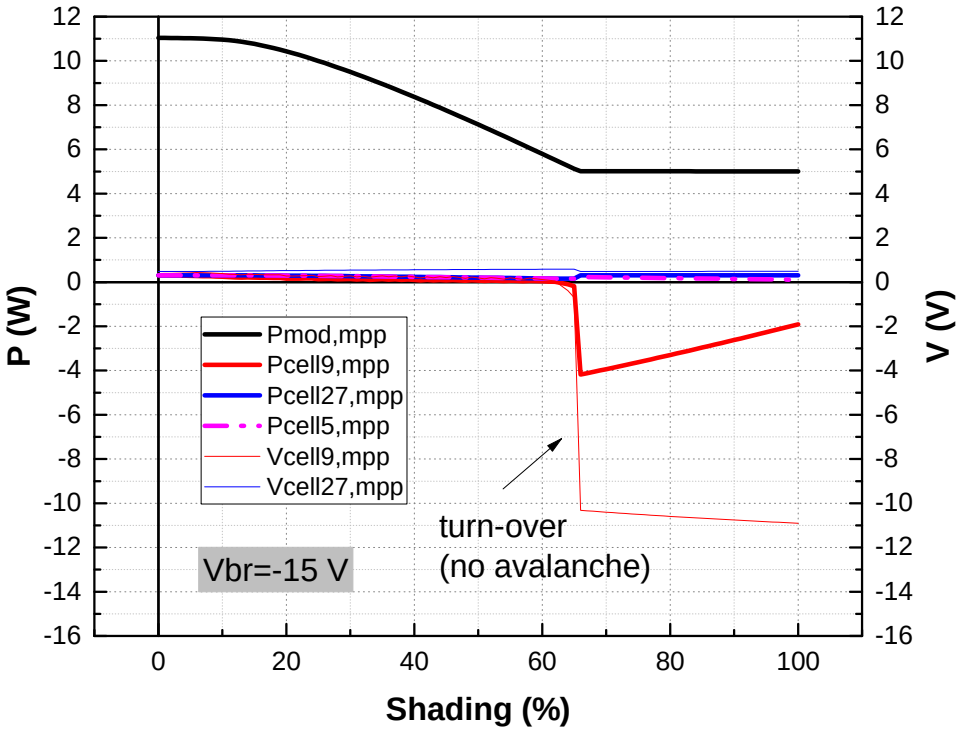

(a) Two bypass diodoes

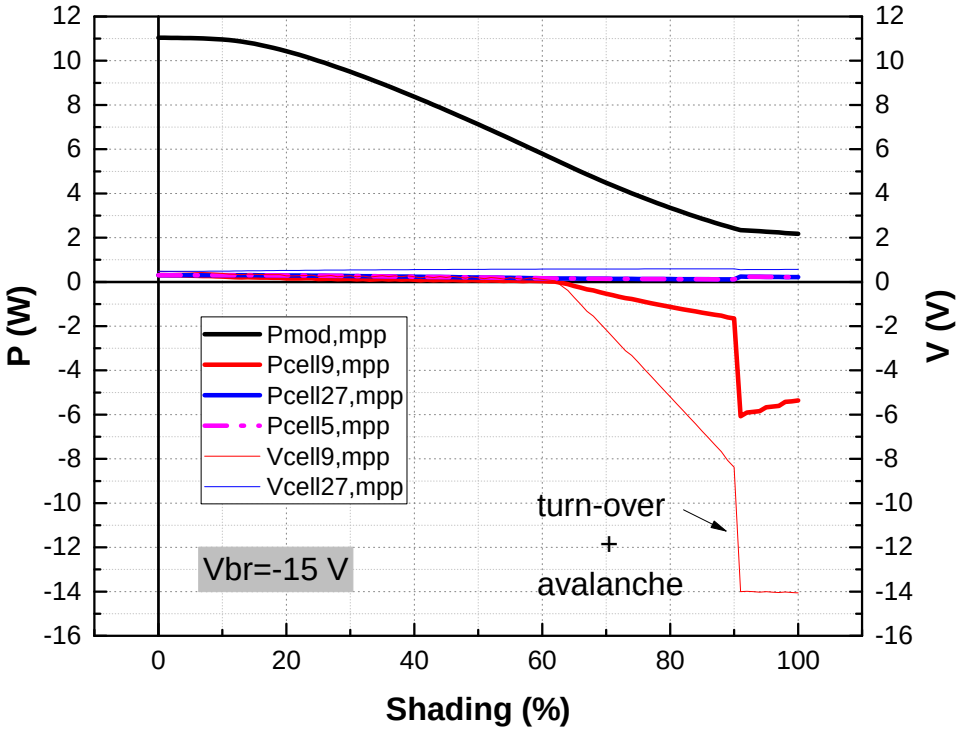

(b) No bypass diodes

Figure 6-27: Evolution of various electrical variables as a function of shading rate of a single PV cell (cell 9, in red) in a *p*-Si module otherwise submitted to STC conditions. Cell 5 (magenta) is a non-shaded cell in the same string as the shaded one. Cell 27 (blue) is a non-shaded cell in a string of non-shaded cells. In (a) the module is equipped with 2 bypass diodes, while in (b) no bypass diodes are installed.

Comparing the two graphs, the following conclusions can be made. The BPD turns on beyond a 65% shading, increasing the module power output compared to "no BPD". In the shading level range of 65 to 90%, the power dissipation in the shaded cell is higher if BPDs are used. Beyond 90% shading the BPDs prevent the avalanche breakdown from occurring. Overall, it is clear that the BPDs are of great importance for modules with many series-connected cells, boosting their production while keeping the cells safe from damage. The results of this study are coherent with results of Fertig et al. [139], who observed the same behaviour of cells and modules as a function of applied shading rate.

6.3 Discussion

Two approaches have been taken in modelling the electrical aspects of the system: empirical and equivalent circuit-based methods.

The Evans empirical model was chosen as the example of an empirical approach due to its simplicity and applicability to several PV technologies. It calculates the effective conversion efficiency and the power output using the average module irradiance and temperature as inputs. When coupled with the analytical model described previously, it proved accurate in describing the power production of frontal modules. The model excelled particularly in predicting power production at low irradiance levels. A disadvantage of this approach is that it assumes a uniform illumination of PV cells, while non-uniform module illuminations are not uncommon due to defined concentration zones and shadows. Calculating and using the average module flux with the Evans model gives way to the underestimation of shadows and similarly the overestimation of the reflector impact.

Due to the shortcomings of the empirical model, a equivalent circuit-based approach was employed to model the photoelectric effect. An *a*-Si:H cell was described with a single diode model, extended to include the phenomena of junction breakdown and *i*-layer recombination. A p-Si cell was similarly described with a double-diode model extended with the junction breakdown term. Modules were assembled with an electrical interconnection of cells, adding bypass diodes to the *p*-Si module. The advantage of the circuit-based approach is that it allows for producing complete $I - V$ characteristics of the cells, including their behaviour under reverse-bias conditions. Furthermore, it allows the study of the influence of bypass diodes, which were shown to prevent junction breakdown in extreme partial shading conditions.

The use of the equivalent-circuit approach is the recommended approach in designing reflector-equipped systems, allowing one to study, anticipate, and design for electrical phenomena that could result in power losses or permanent damage cell damage.

Chapter 7

Calibration and Performance of EDStaR+SPICE

Before validating a given model's performance, it needs to be calibrated with a subset of measured data. The optical and electrical models should ideally be calibrated and validated *independently*. The optical model would use POA irradiance measurements as an input, while the electrical model would need both POA irradiance and operating temperature measurements. The experiment was equipped with temperature probes Pt-100, but *not* with POA irradiance sensors (at the time of writing). Therefore, the optical and electrical models could not be independently calibrated. The solution to this is to calibrate both models together as they work in conjunction to produce I-V curves, which can be compared to corresponding measurements. The use of measured operating temperature would isolate the uncertainty to that of the optical and electrical models.

Note that the parameters related to the reverse I-V characteristic, namely the Bishop parameters (a, m, and V_{br}), cannot be obtained through calibration since the measured I-V characteristics do not contain instances of junction breakdown. A sample cell was unavailable to perform the reverse characteristic measurement in the laboratory. Therefore, the Bishop parameters have been fixed to values found in the literature (a=0.1, m=3.4, Vbr_{a-Si}=-15V, Vbr_{p-Si}=-20V) [131, 132].

7.1 Calibration

The calibration of parameters must be done through trial and error since the governing equations are non-linear and transcendental. The model calibration therefore consists of varying the parameters until the experimental I-V curves are reproduced by the model. The model parameters to be estimated include optical and electrical parameters. The optical parameters to be estimated are:

- the reflector normal reflectance of direct irradiance (at zero angle of incidence)
- the reflector average reflectance of diffuse irradiance
- the PV module front glass normal transmittance of direct irradiance, and

- the PV module front glass average transmittance of diffuse irradiance.

Note that the obtained optical parameters represent *effective* values taking into account the spectral mismatch between the PV cell spectral response and the reflected or transmitted wavelengths. For this reason, the effective reflector properties are found for each PV technology. Similarly, the front glass transmittances must be evaluated independently for each technology due to the difference in their physical properties.

The electrical parameters to be estimated, common to both PV technologies, are J_0, $J_{SC,STC}$, R_s, R_{sh}, α_{Isc}, and n (see Sec. 6.2). The p-Si electrical model has two additional parameters due to a second diode: J_{02} and n_2. The a-Si:H electrical model has three additional parameters due to the Merten term: d_i, $\mu\tau_{eff}$, and V_{bi}.

Note that certain optical and electrical parameters can potentially compensate one another, as their influences on output current are in direct opposition. For example, a high transmittance coefficient of diffuse irradiance can perhaps be compensated by a lower value of $J_{SC,STC}$.

The calibration can be either be done by hand, or by an optimisation technique such as an evolutionary algorithm. Calibration by hand has the advantage of allowing a rapid estimation of parameters that give satisfactory results. An algorithmic approach may not have the advantage of intuition, but with enough time converges to the optimal parameter set (minimising a chosen cost function).

A "teaching-learning based optimisation" (TLBO) algorithm [140] has been developed for the purpose of systematic calibration. It is a general purpose evolutionary algorithm which features easy implementation, good performance (e.g. fast convergence) and robustness (e.g. good resistance to local minimum traps). Furthermore, it allows for a large search space for each parameter without the need to provide an initial estimate of the result. TLBO was modified in two ways compared to the article:

- multiple I-V curves were used as inputs (along with the corresponding transmitted irradiance and operating temperature data), instead of a single one
- the cost function in the article (see (7.1)) was adapted to give a higher weight to I-V points with a higher power (see (7.2)). This was done to ensure a good fit of P_{MPP}.

$$F(X) = \frac{\sum_{k=1}^{p} \left\{ \left[I^{exp}(V_k) - I^{cal}(V_k, X) \right]^2 \right\}}{p} \tag{7.1}$$

$$F(X) = \frac{\sum_{k=1}^{p} \left\{ \left[I^{exp}(V_k) - I^{cal}(V_k, X) \right]^2 I^{exp}(V_k) V_k \right\}}{p} \tag{7.2}$$

where X represents a given parameter set, k is the index of a given I-V point, p is the total number of points in a given I-V curve, and V_k is the voltage at point k.

The input data consisted of many *I-V* curves, representing the targeted model output, and their respective operating temperature, BNI, and DHI measurements. Specifically, a total of 200 *I-V* curves was sampled from ten consecutive days: 17th to 26th of May, 2014. The set contained both clear and cloudy days. The associated daily average diffuse fractions are 0.26, 0.34, 0.25, 0.89, 0.98, 0.68, 0.85, 0.81, 0.70, and 0.89.

The electrical parameters for *p*-Si and *a*-Si:H cells obtained through calibration are outlined in Table 7.1. These parameters correspond to modules 16 and 15, respectively.

Table 7.1: Electrical parameters of *p*-Si and *a*-Si:H cells corresponding to modules 16 and 15, respectively

Parameter	***p*-Si**	***a*-Si:H**
$Area\ (cm^2)$	22.0	65.9
$J_0\ (A/cm^2)$	4.44×10^{-12}	8.24×10^{-19}
$J_{02}\ (A/cm^2)$	1.00×10^{-8}	–
$J_{SC,STC}\ (A/cm^2)$	3.96×10^{-2}	8.66×10^{-3}
$Rs\ (\Omega.cm^2)$	0.932	33.0
$Rsh\ (\Omega.cm^2)$	6.70×10^{3}	6.36×10^{5}
$\alpha_{Isc}\ (1/°C)$	1.041×10^{-3}	1.00×10^{-3}
n_1	1.00	1.70
n_2	1.819	–
a	0.1	0.1
m	3.4	3.4
$V_{br}\ (V)$	-15.0	-20.0
$d_i\ (cm)$	–	3.46×10^{-5}
$\mu\tau_{eff}\ (cm^2/V)$	–	1.00×10^{-8}
$V_{bi}\ (V)$	–	1.80

The thermal model (discussed in the next chapter) has been then calibrated with the calculated irradiances. The subset used for the calibration of the thermal model is 15th May - 31 December, 2014.

7.2 Validation

The performance of the combined model is demonstrated on three levels:

1. individual *I-V* curves
2. daily production profile (P_{MPP} comparison)
3. annual production profile (output power integrated daily)

Figure 7-1 presents the first level comparison for module 6 on May 17th, 2014, a relatively clear day. The *I-V* curves are rather well reproduced throughout the day, especially near the P_{MPP}. As the cost function of the calibration is weighted to favour accuracy near the P_{MPP} at the expense of the accuracy near I_{SC} and V_{OC}, the resulting modelled curves sometimes overestimate the I_{SC} (for example at 12:05), or underestimate the V_{OC} (for example at 06:24).

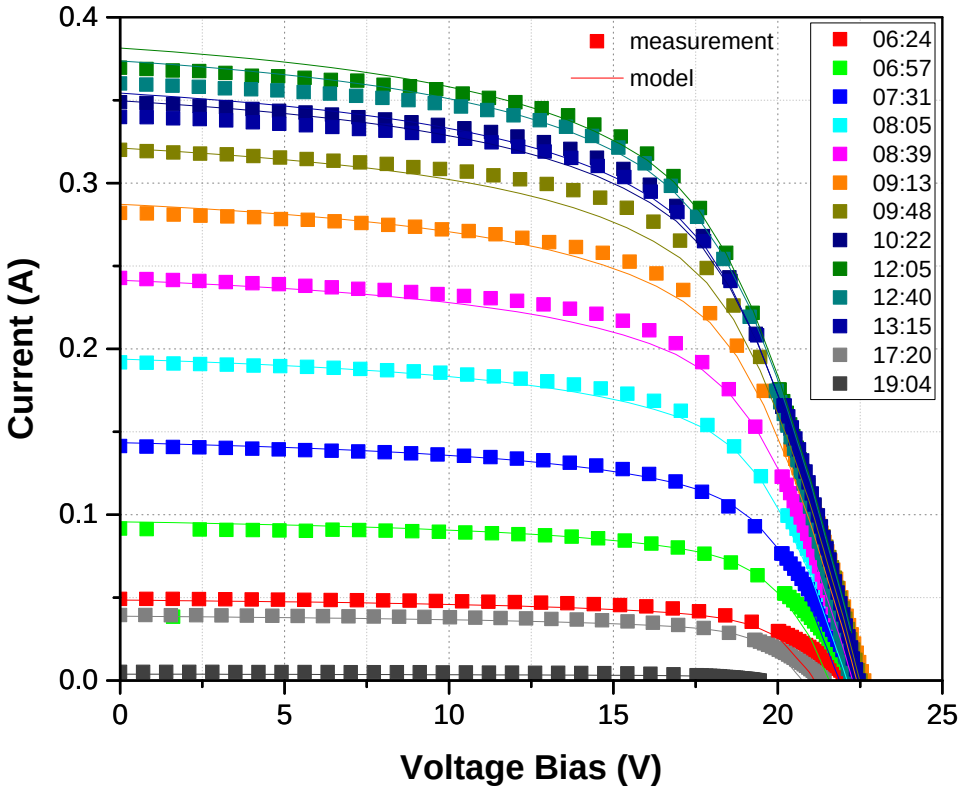

Figure 7-1: Comparison of experimental and numerical I-V curves for module 6 on May 17th, 2014, after a calibration of model parameters. The calibration was performed using 200 I-V curves sampled from 10 consecutive days in May, 2014.

Figure 7-2 presents the experimental and numerical daily production profiles of six modules: frontal, edge and non-edge modules of both a-Si:H and p-Si technologies on May 17th, 2014. The performance of all six modules has been successfully reproduced. Due to the advantages of both the optical and electrical models, the edge effect on production has been successfully reproduced for both technologies as seen in the magenta and black curves.

Figure 7-3 presents the experimental and numerical long term production profiles, integrated daily, for four representative modules: 6, 15, 5, and 16. The temporal range of the I-V and temperature measurement subset used for the calibration of optical and electrical models is highlighted in blue (17th - 26th May, 2014). EDStaR+SPICE was used with appropriate inputs, including the measured operating temperature, to reproduce the daily produced energy until the rest of the year.

The thermal model ETM (discussed in the next chapter) has been then calibrated with the calculated irradiances with the subset of 15th May - 31 December, 2014, highlighted in yellow. The complete model (EDStaR+SPICE+ETM) has been used to reproduce measurements from 1st January, 2015 to 31st August, 2016.

Note that there is a significant amount of holes in the graph, represented by the connecting lines spanning several days. This is due to the absence or the bad quality of

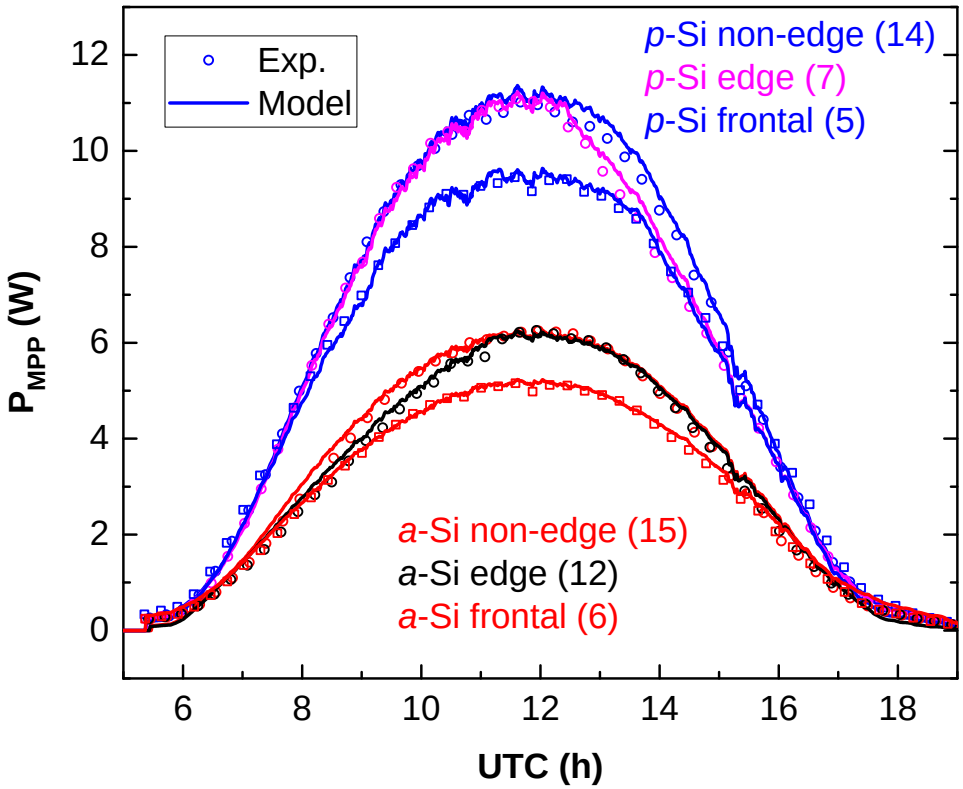

Figure 7-2: Comparison of experimental and numerical daily production profiles for frontal modules (5 and 6), edge modules (7 and 12) and non-edge modules (14 and 15), on May 17th, 2014.

one or more key inputs - I-V characteristic, module temperature, BNI or DHI - in which case the model was not executed and the corresponding measurement is not shown. As seen in the figure, the model shows a good performance in predicting the power output of modules 6, 15, and 5, and 16. The relative errors for modules 6, 15, 5, and 16 are -2.0%, +1.9%, -4.4% and -4.5%, respectively. The biggest discrepancies between experimental and numerical values come from measurement errors during days with an intermittent solar resource. With the same training period, the model seems more accurate for *a*-Si:H modules. This is likely due to the lower uncertainty related to the electrical model of the *a*-Si:H module. For instance, there are no bypass diodes to model, and the mismatch conditions are much less frequent and severe. Note that a longer training period could further decrease the prediction error of the model.

Figures 7-4 and 7-5 present a direct comparison of experimental and numerical P_{MPP} used to compute the daily integrals in Fig. 7-3. A good performance is observed for all four representative modules (frontal and reflector-equipped *a*-Si:H and *p*-Si), with RMSE ranging from 0.43 to 0.87 W. Note the two clouds of outliers in each of the four graphs, where the model seems to severely over- and under-estimate the module power output. This is due to the previously-mentioned error in the I-V curve measurement timestamp, caused by sequentially measuring the 18 modules and saving a single timestamp at the

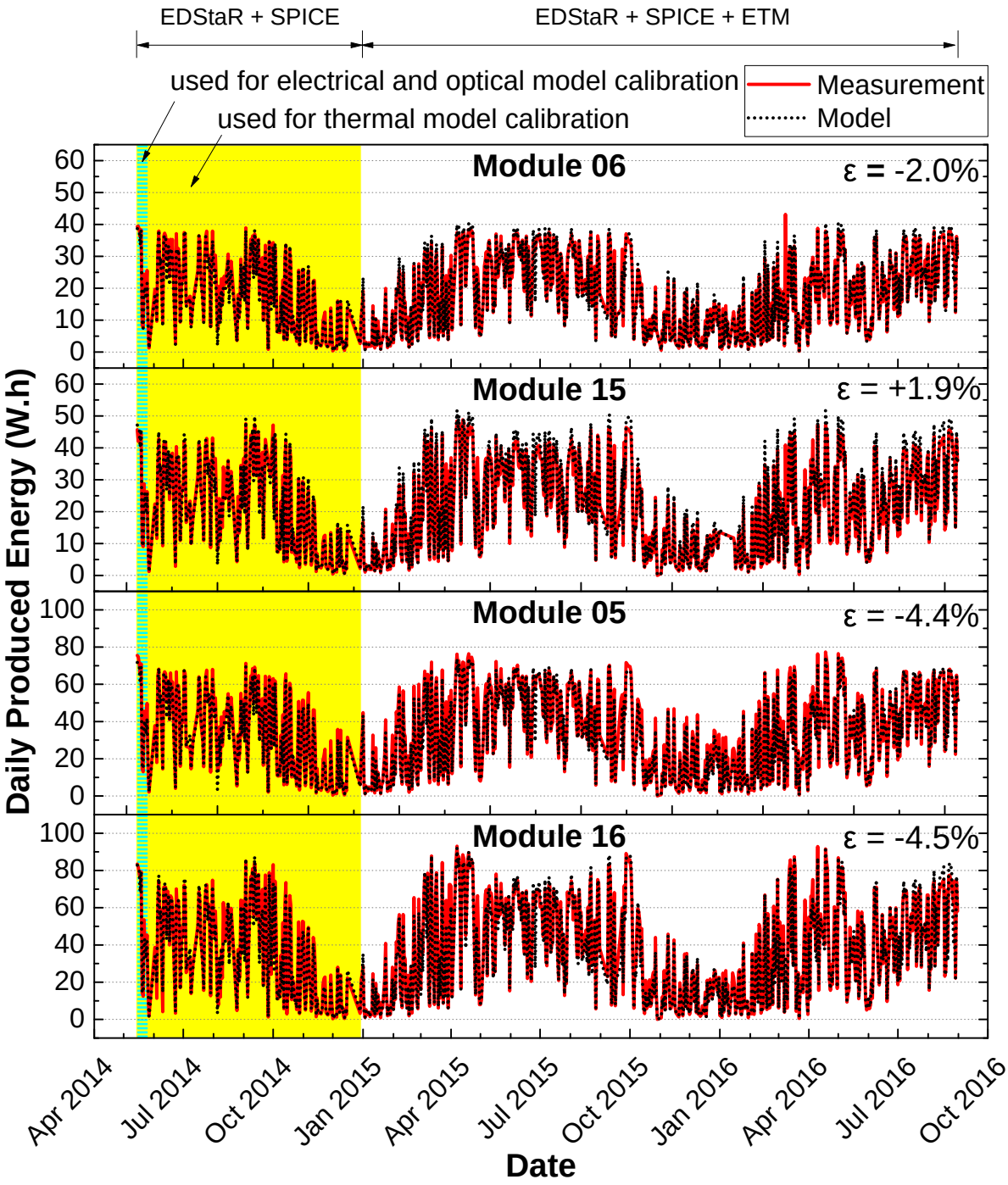

Figure 7-3: Comparison of experimental and numerical values of the annual distribution of the daily produced energy for modules 6, 15, 5, and 16, for the period of 15th May to 31st December, 2014. The temporal range of the I-V and temperature measurement subset used for the calibration of optical and electrical models is highlighted in blue (17th - 26th May, 2014). The subset used for the calibration of the thermal model (discussed in the next chapter) is highlighted in yellow (15th May - 31 December, 2014). ϵ represents the relative difference between the modelled and measured total produced energy (over the range 15th May, 2014 - 31st August, 2016).

end. In highly variable irradiance conditions, several minutes of timestamp error can

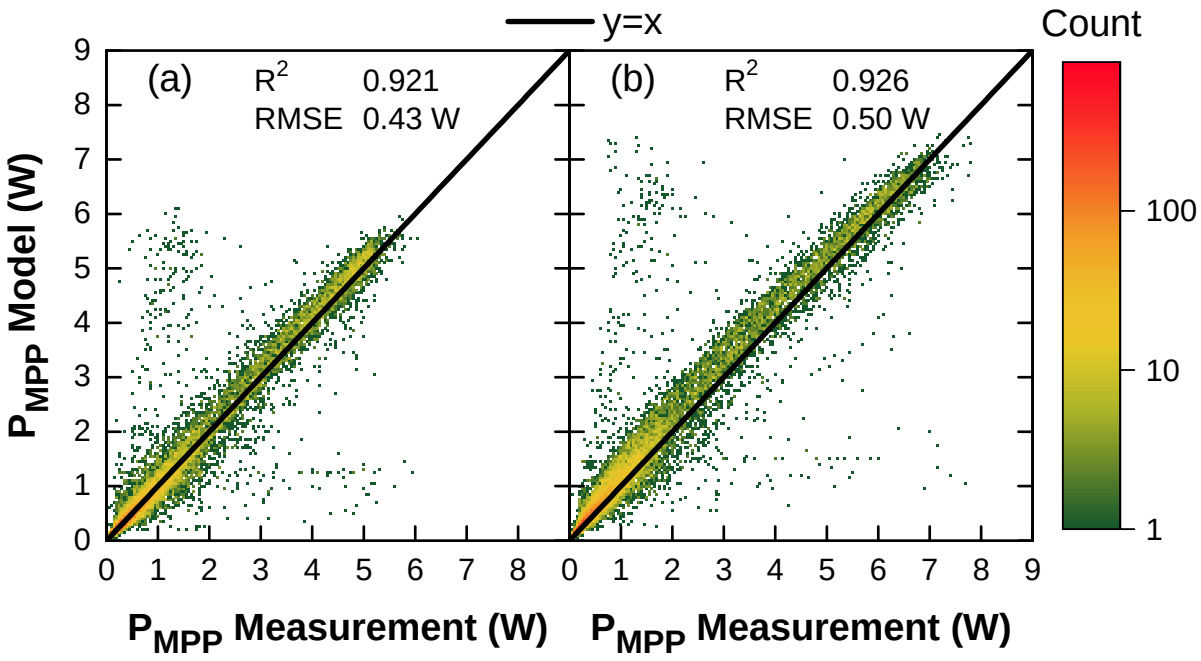

Figure 7-4: Comparison of experimental and numerical P_{MPP} values for (a) module 6 (frontal *a*-Si:H), and (b) module 15 (row 3 *a*-Si:H), for the period of 15th May to 31st August, 2016. The clouds of points far from the diagonal correspond to points with erroneous timestamps taken during periods of variable solar resource. Filter based on irradiance fluctuations was already applied and eliminated most of the points in the clouds. Stricter filters on irradiance fluctuations would be necessary to eliminate these points.

result in it being associated with much different surface irradiance values, resulting in errors. The positive or negative bias at lower P_{MPP} values (0-2 W for *a*-Si:H, 0-4 W for *p*-Si) is due to suboptimal optical parameters concerning diffuse irradiance. As the cost function has been weighted to favour higher P_{MPP} over lower ones, the *I*-*V* curves associated with diffuse irradiance have been by default given less importance. The larger spread in this area is partly due to the timestamp issue, and partly due to the uniform-sky assumption. If the diffuse irradiance source had been modelled in more detail (e.g. taking into account the position of the Sun), a lower spread could have perhaps been achieved in this region.

7.3 Conclusion

As seen in this chapter, the combined EDStaR+SPICE model shows a good performance in reproducing experimental *I*-*V* curves. The model's robustness is demonstrated by its ability to reproduce complete daily production profiles of modules of both technologies, situated in different positions compared to the reflector. Finally, with a learning dataset of just ten days in May, the model succeeded in reproducing the daily electricity production until the end of the year with the measured module temperatures. After a calibration

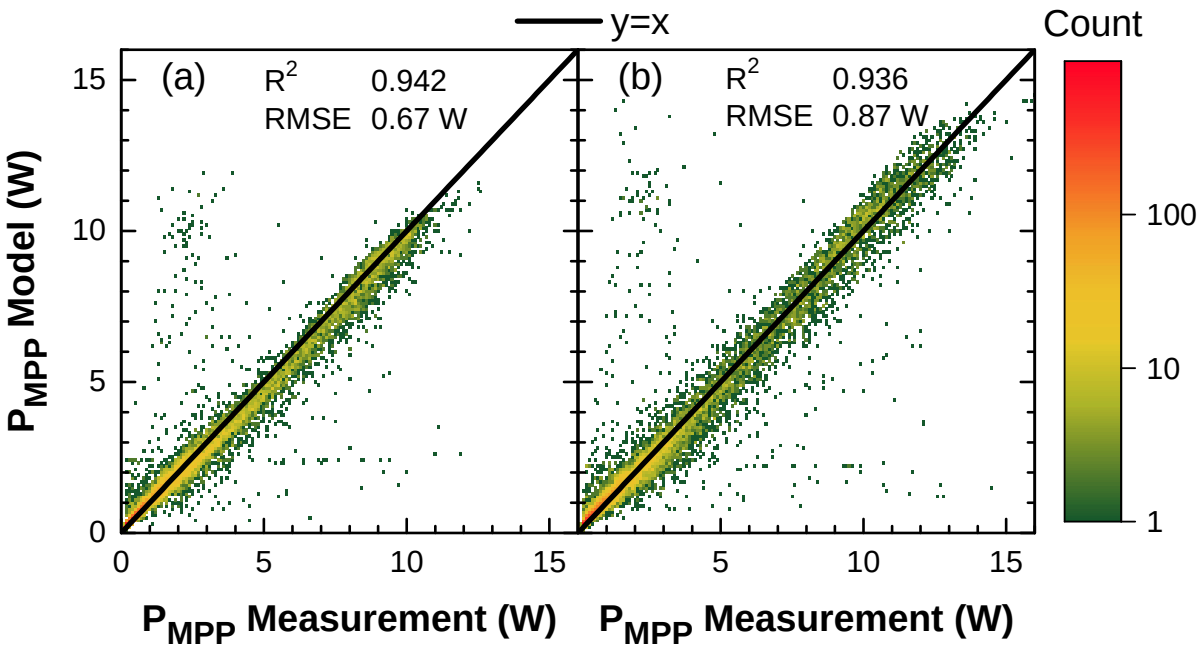

Figure 7-5: Comparison of experimental and numerical P_{MPP} values for (a) module 5 (frontal p-Si), and (b) module 16 (row 3 p-Si), for the period of 15th May to 31st August, 2016. The clouds of points far from the diagonal correspond to points with erroneous timestamps taken during periods of variable solar resource. Filter based on irradiance fluctuations was already applied and eliminated most of the points in the clouds. Stricter filters on irradiance fluctuations would be necessary to eliminate these points.

of the thermal model with about a half a year of measurements, the combined model was able to reproduce over two years of power output, purely based on radiative and environmental variables (i.e. the operating temperature was calculated).

The next chapter details the proposed thermal model able to reproduce the temperature measurements as a function of calculated module irradiances (through SIRTA-measured BNI and DHI) and measured environmental variables (e.g. ambient temperature and wind speed).

Chapter 8

Thermal Modelling

As seen before, the PV cell performance decreases with increasing operating temperature, owing to increased rates of internal carrier recombination caused by increased carrier concentrations. Therefore, an accurate prediction of the PV module performance requires the knowledge (or estimate) of the PV cell operating temperature. Various thermal models exist for predicting the operating temperature, involving basic environmental variables and numerical parameters that are material or system dependent. All of them rely on representing different mechanisms of heat transfer contributing to the final temperature. This chapter presents the thermal modelling performed as a part of the thesis.

8.1 State of The Art

Most of the models proposed in the literature are empirical, meaning that the proposed equations were fitted through a large number of data to yield empirically-derived, system-specific coefficients [74, 102, 128, 129, 141–159].

The most commonly used empirical models (such as the ones proposed by King [141] and Faiman [142]) are instantaneous in nature, meaning that the thermal mass of the PV cells is considered negligible. The consequence of this assumption is that the operating temperature can be 1) severely overestimated during spikes of high irradiance in cloudy periods, and 2) severely underestimated during cloud passages in clear periods. In these scenarios, the change in temperature is assumed instantaneous, while it is in fact gradual and asymptotical in nature.

King et al. [141] (Sandia Labs) propose the following correlation for the module temperature:

$$T_M = T_{amb} + E \times \exp(a + b \times WS) \tag{8.1}$$

where T_M is the back-surface module temperature (°C), T_{amb} is the ambient air temperature (°C), E is the global solar irradiance incident on the module surface (W/m^2), WS is the wind speed measured at 10-m height (m/s), and a and b are empirically-determined coefficients. In the above equation, a establishes the upper limit for module temperature

at zero-wind conditions, for example due to natural convection-driven heat losses. The parameter b represents the rate at which module temperature drops as wind speed increases. The reported RMSE is 5 °C, resulting in a 3% uncertainty in the module power output.

Note that the King model works with incident, rather than transmitted irradiances. This may lead to overestimations at high incidence angles, where a part of the flux is reflected away from the module and does not contribute to heating the modules. Furthermore, the amount of heating is related to the PV cell conversion efficiency, which is not explicitly taken into account by King. As the photons that contributed to the creation of electron-hole pairs are considered to have not heated the cell, the amount of heating is inversely proportional to the conversion efficiency. Wind direction was reported to have a small but noticeable impact on operating temperature, and was finally not included in their model. They also observed a degradation in model performance due to thermal transients caused by the module's heat capacitance, which is inevitable for instantaneous models.

Faiman proposed a more comprehensive correlation, overcoming some of the limitations of the King model:

$$T_M = T_{amb} + \frac{E(\eta_o - \eta_e)}{U_0 + U_1 \times WS} \tag{8.2}$$

where T_M is the back-surface module temperature (°C), T_{amb} is the ambient air temperature (°C), E is the global solar irradiance incident on the module surface (W/m^2), WS is the wind speed measured at 10-m height (m/s), η_o is the optical efficiency (measurement of optical losses), η_e is the conversion efficiency, and U_0 and U_1 are empirically-determined heat loss coefficients similar to a and b in the King model. Note that Faiman considers a constant conversion efficiency, while it in fact varies with temperature. Nevertheless, the model showed a good performance, resulting in a RMSE of 1.85 K. This error was reported to result in 1% uncertainty in power output.

Faiman [142] has measured nighttime inter-cell temperature differences within a given module of up to 0.26 K (RMSE), the difference being non-systematic across the 7 modules tested. The daytime measurements showed that central cells were on average 2 K hotter than corner cells. This information gives an idea of a good empirical model performance, which by definition assumes a uniform temperature across the cells.

There are examples of dynamical empirical models [145, 148, 150, 152, 154, 155], which attempt to represent the PV cell thermal mass to produce a more accurate prediction. This is often done by employing an energy balance approach taking into consideration various heat transfer mechanisms (including radiative), and often using one or more past measurements/results to estimate the current operating temperature.

Several authors propose a time-dependent physics-based thermal model, using a dis-

cretised domain (2-D or 3-D) and applying fundamental laws of physics and numerical methods to model the relevant heat transfers [160–170]. This is of particular importance when heat sinks are relied upon to divert heat (e.g. in HCPV applications), or when natural convection is of particular importance to cool the modules [165–167, 169, 171] (e.g. in building-integrated PV applications). Such models are more computationally-intensive than empirical models, and are therefore rarely included in commercial PV array modelling software such as PVSyst.

8.2 Empirical Thermal Model (ETM)

As a first approach to modelling the operating temperature, an instantaneous empirical model was developed, inspired by the Sandia model [141]:

$$T_M = T_{amb} + (C_0 \times E_B + C_1 \times E_D) \times \exp(C_2 \times WS) \tag{8.3}$$

Compared to the Sandia model, the contribution of direct and diffuse irradiances was separated to reflect the difference in spectral compositions of the two. This is of particular importance since the reflector often results in different concentrations of direct and diffuse irradiances. Furthermore, the parameter a in the Sandia model was removed as limited natural convection-driven heat-losses are expected (the modules are a part of a closed triangular cavity).

As can be seen in Fig. 8-1, the model shows a good performance over the entire range of measurements. The RMSE is below 5 °C for all four modules, which is the same order of magnitude as the original Sandia model. The parameter C_2, corresponding to parameter b in the Sandia model, is consistent with values obtained by King. C_2 was found to vary from -0.0706 to -0.1056, while b was reported by King to vary from -0.0455 to -0.130.

For all modules analysed, C_1 has been found to be about 2.5 times greater than C_0. This means that a Watt of diffuse irradiance heats the PV cells about 2.5 times more than a Watt of beam irradiance. This difference is explained by the difference in the spectral distributions of the two irradiances, since the diffuse irradiance contains a larger fraction of short-wavelength photons.

Furthermore, the similarities and differences in parameter values across different modules are coherent and explainable. Parameters C_0 and C_1 are coherent for modules with a unique PV module technology, which is a result of a unique module front glass and PV cell spectral response. C_0 and C_1 of p-Si modules are higher than a-Si:H modules, which is consistent with the conclusions made in Sec. 3.3.

At the same time, the wind speed coefficient, C_2, is shared by modules of the same row. As wind has a better access to the row 3 modules compared to those of row 1, these

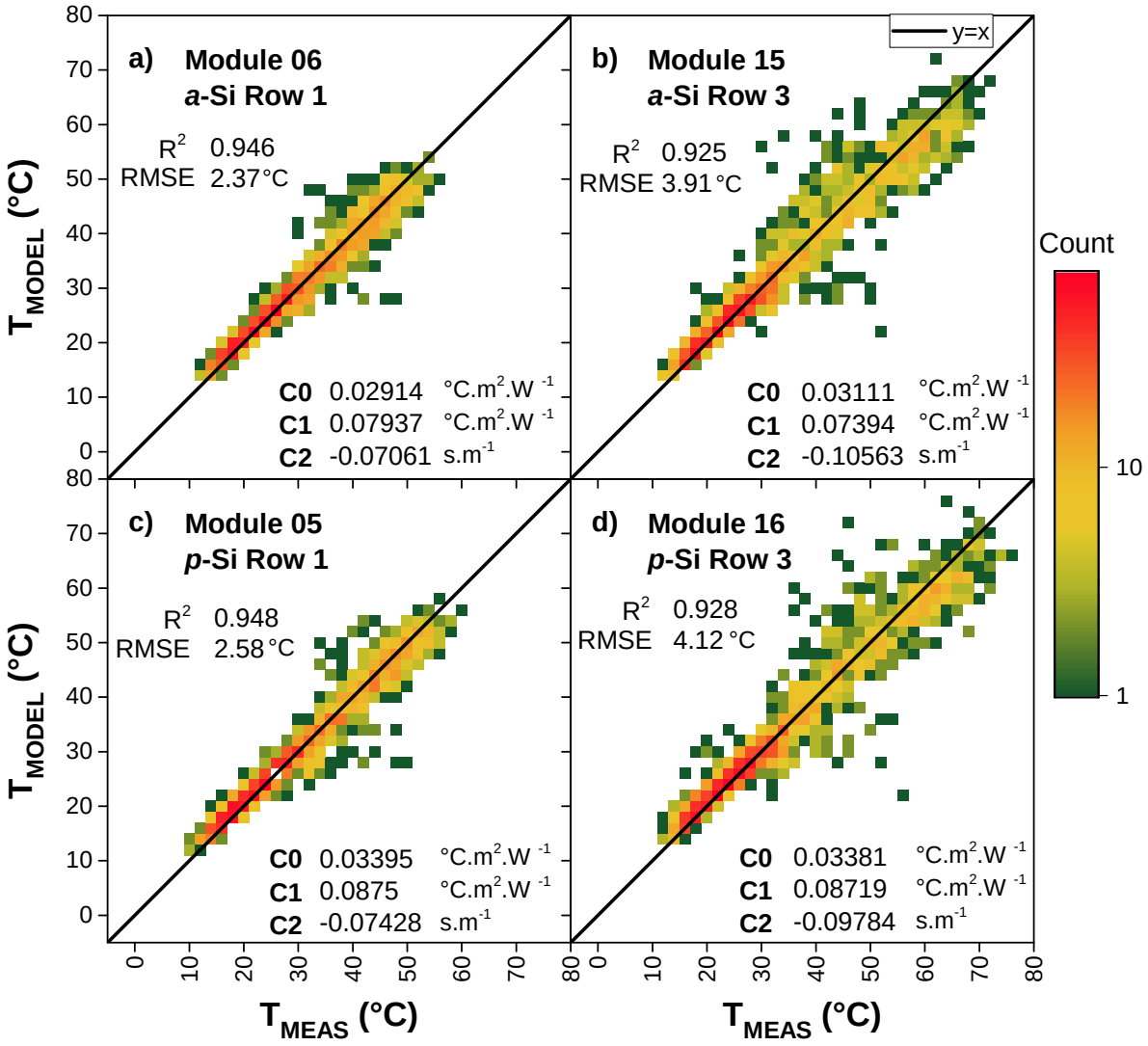

Figure 8-1: Performance of the proposed empirical model, fitted for a) a Row 1 *a*-Si:H module (# 06), b) a Row 3 *a*-Si:H module (# 15), c) a Row 1 *p*-Si module (# 05), and d) a Row 3 *p*-Si module (# 16). The period considered was 15th May - 31st December, 2014.

modules are cooled more per unit of wind speed. This results in a higher (more negative) value of C_2 for row 3 modules compared to row 1 modules.

8.3 Discussion

An empirical operating temperature model was developed in the scope of this thesis, which was an adaptation of the well-known King model. The model calculates the cell operating temperature as a function of instantaneous values of ambiant temperature, direct and diffuse plane-of-array irradiances, and wind speed. After calibration, the model performed with an RMSE smaller than 5 °C for all modules. This accuracy results in an error in power production smaller than 3 %, which is acceptable for most purposes.

The accuracy and the obtained coefficients are consistent with the values found in King's paper [141]. The coefficients obtained through calibration show that diffuse irradiance heats the cells about 2.5 times more than direct irradiance, owing to spectral effects. Nevertheless, direct irradiance is in most cases expected to be the dominant source of heat in absolute terms.

Due to a lack of time, Faiman's model was not tested for performance, but should be explored in future works due to the higher performance reported in the paper (RMSE $<$ 2 °C).

A physics-based, fluid dynamics model was not developed due to the sufficient accuracy of the proposed empirical model. Nevertheless, it could be used to achieve a better model accuracy by more precisely describing the thermal exchanges. For example, when the irradiance increases rapidly, the heat capacity of the modules allows it to remain cool for a certain time, reducing the rate at which efficiency decreases. This effect cannot be explained by the proposed empirical model.

Despite this potential, the development and calibration of such a model would be challenging due to:

- poor availability of bibliographic references for open, differentially-heated triangular cavities with (likely) turbulent interior flow conditions
- lack of sufficient temperature and air velocity sensors inside the cavity

A comprehensive study of the thermal exchanges inside the cavity is therefore left as a perspective.

THIS PAGE INTENTIONALLY LEFT BLANK

Chapter 9

Case Studies

Now that the modelling tools have been developed and validated with measurements, it is time to demonstrate some of their applications. Consider the design process of a large-scale PV installation in a given location. Consider that the designer has the choice of installing either a classical PV installation (rows of PV modules), or an Aleph installation (rows of PV modules equipped with fixed planar reflectors). To arrive at the optimal solution, the designer must (among other things) answer the following questions:

1. From an economical point of view, is the local climate attractive for investing in reflectors? This depends on the achievable optical gains due to the reflectors, as well as the cost of reflectors.
2. What is the optimal geometry of the system? The inter-row spacing is preferably chosen such that shadows on PV cells are avoided throughout the year. If the surface area is a constraint (e.g. in rooftop installations), a denser system may be justified to allow for additional rows of PV modules. The inclination of PV modules must then be optimised to reach a specific objective (commonly maximising the annual electricity production). What is the sensitivity of the maximum production and the optimum geometry to the reflector performance?
3. Should the reflectors be extended at each extreme (East-West) to reduce or eliminate the edge effect (decrease in optical gains of modules situated at row edges)? This is again an economical decision, depending on the possible gains and the added cost of reflectors.
4. What is the best PV cell layout and interconnection among different PV technologies? This depends on the difference in electrical losses, for example due to string mismatch. Of course, having a bypass diode across each cell would optimise production, but this alternative was considered too costly.

The following case studies aim to explore these design questions. Note that an economics model has not been developed due to a lack of time. The results of these optimisations should therefore be taken with care, and complemented with an economics model for the final design.

9.1 Effect of Local Climate on Optimal Geometry

In order to decide whether the local climate is appropriate for the Aleph system, the installation performance should be simulated with several years of local climate data in view of evaluating the benefit of reflectors. In this study, the performance of the Aleph system is evaluated for three cities with similar latitudes but different climates: St. John's (Canada, 47.56 °N, 52.71 °W), Palaiseau (France, 48.71 °N, 2.21 °E) and Bratislava (Slovakia, 48.15 °N, 17.11 °E). The climates are first compared amongst each other, and the effect of local climates was highlighted by comparing it to clear-sky conditions. Then, simulations are run to evaluate the optimal system geometry and achievable gains compared to the classical installation for the three locations.

9.1.1 Comparison of Climates

The two European cities are classified as *Cfb* according to the Köppen-Geiger climate classification [172], meaning that they have a warm temperate humid climate with warm summers. St. John's is classified as *Dfb*, meaning it has a snow humid climate with warm summers. The Köppen-Geiger climate classification suggests that the major difference in climate between the European cities and St. John's is a lower minimum average monthly temperature (i.e. colder winters) in St. John's. However, the performance of PV systems greatly depends on the yearly distribution of the surface solar irradiance, which is not accurately taken into account by the Köppen-Geiger climate classification method.

For the three cities, four years (2011-2014) of surface solar irradiance data were obtained from the MACC-RAD database [98], which estimates the direct and diffuse irradiances at the ground level from satellite imagery. To verify the quality of the obtained data, weekly gain in transmitted energy was calculated with two sets of surface irradiance data: MACC-RAD data and flux measurements obtained locally at SIRTA (see Fig. 9-1). Simulations using the MACC-RAD data resulted in similar gains as the ones done using minute data measured locally. This validated the use of MACC-RAD data in estimating the optimal settings and achievable gains for various cities contained within the database.

Figure 9-2 shows a 4-year average yearly distribution of k_D (defined here as the ratio of diffuse to global irradiations) for the three cities under consideration. It was calculated using two sets of surface irradiance data: 1) MACC-RAD satellite-estimated surface irradiance data (Fig. 9-2, upper part), and 2) McClear clear-sky surface irradiance data (Fig. 9-2, lower part).

As seen in Fig. 9-2 (upper part), St. John's is associated with a much greater value of k_D throughout the year as compared to Palaiseau and Bratislava, and this is due to its close proximity to the Atlantic Ocean, resulting in frequent periods of cloudy conditions. When comparing the value of k_D for the three cities in the summer, one can note that on average Bratislava experiences summers with more clear-sky days than both Palaiseau

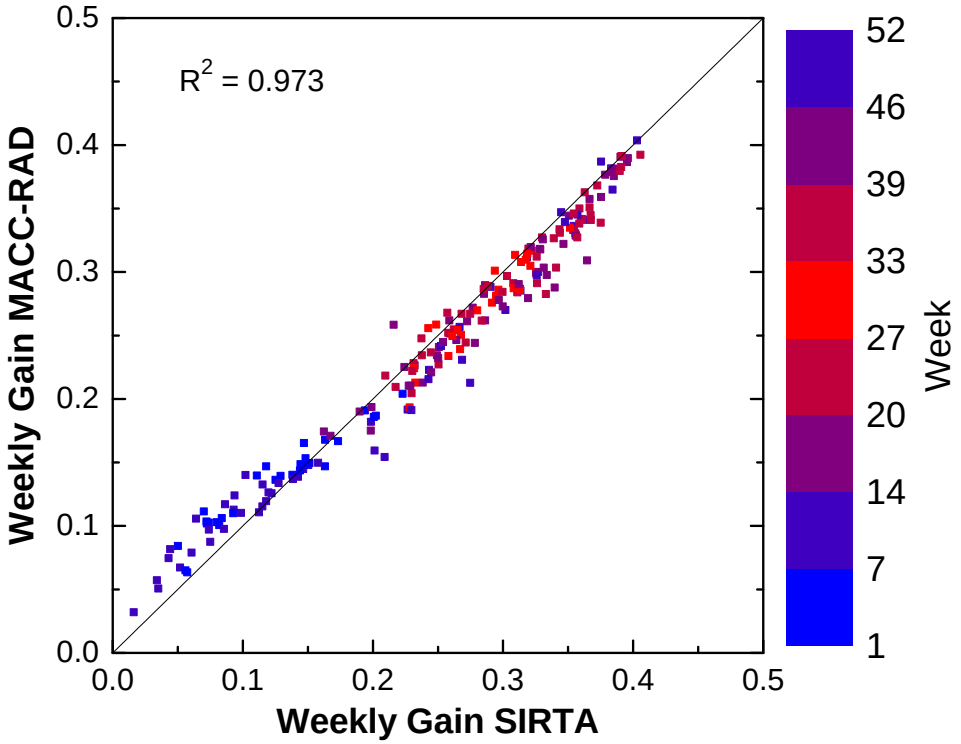

Figure 9-1: Validation of MACC-RAD surface irradiance data. A simulation was run for each year using two sets of data (MACC-RAD and locally measured) to calculate the weekly gain in energy transmitted to the cells. The geometry of both control and reflector-equipped modules were set to match the experiment (module inclination of 49° and D/L of 3.00).

and St. John's.

To compare the cities based on the influence of local aerosols on the yearly distribution of k_D, k_D was evaluated under local clear sky conditions. The corresponding surface irradiances were obtained from the McClear database [95], containing hypothetical all-year clear-sky irradiances that were extrapolated at non-clear periods using actual clear-sky irradiance data and continuous local aerosol measurements. Figure 9-2 (lower part) shows a 4-year average yearly distribution of k_D under local clear-sky conditions for the three cities under consideration. One can note that the average yearly distribution of k_D under clear-sky conditions is very similar, and varies very slightly from city to city. This variation can be attributed to the difference in yearly distributions and severities of local aerosols. For example, one can note that between April and September, Bratislava has a slightly larger value of k_D. It can therefore be said that Bratislava has higher aerosol levels during these months, resulting in more light being diffused compared to the other two cities.

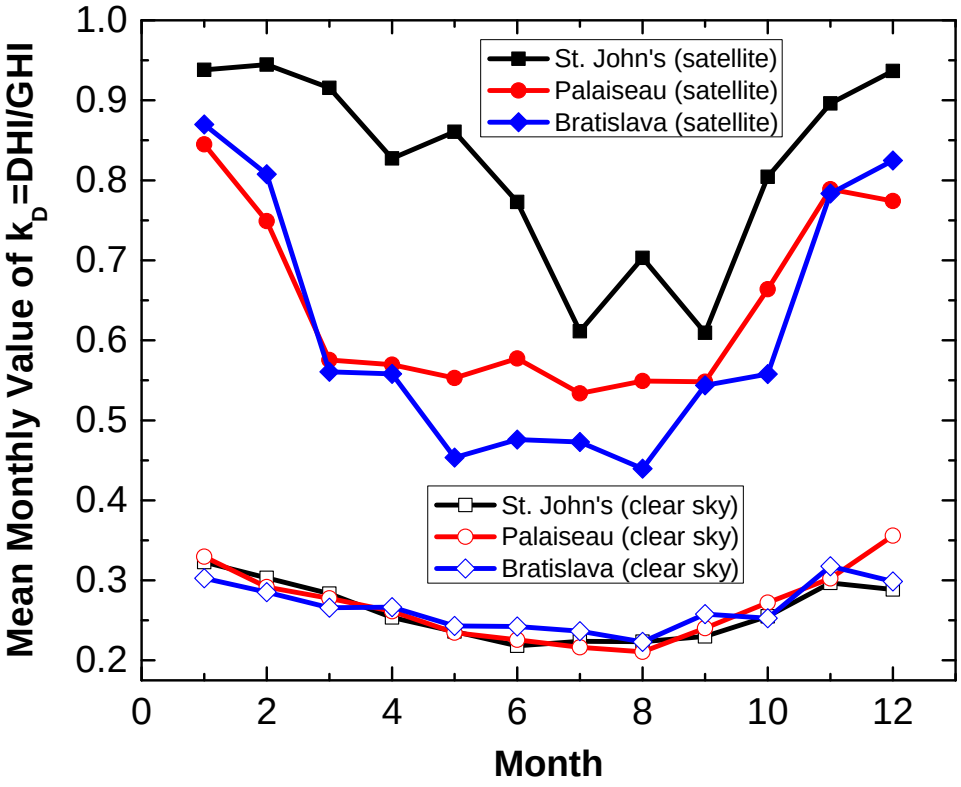

Figure 9-2: Comparison three cities' climates based on the 4-year average mean monthly value of k_D, the diffuse component of the global horizontal irradiance. Filled symbols represent the satellite-estimate surface irradiance, empty symbols represent the local clear-sky surface irradiance [95].

9.1.2 Results and Discussion

To study the impact of climate on the performance of the Aleph system, two simulations were performed for each city. Common to both simulations, the dimensionless inter-row spacing D/L was set to 3.00 and the specular reflectance of the reflectors was set to 0.90.

In the first simulation, summarized in Table 9.1, the cities were simulated under hypothetical local clear-sky surface irradiance using the McClear database [95]. The McClear irradiance data was used with the analytical optical model to find the optimal settings for the two systems (Aleph and classical installation) for maximizing the total energy transmitted to the cells. The annual gains in transmitted energy were evaluated, defined as the ratio of total transmitted energies for the two individually optimized systems:

$$Gain = \frac{\int_{2011}^{2014} \Phi_{TRANS.}^{Aleph\ (OPT.)} dt}{\int_{2011}^{2014} \Phi_{TRANS.}^{PV\ CLASSICAL\ (OPT.)} dt} \tag{9.1}$$

In the second simulation, summarized in Table 9.2, the cities were simulated under a satellite-estimated surface irradiance, using the MACC-RAD database [98]. The integrated model consisted of the analytical optical model, the Evans electrical model, and the developped empirical thermal model. For the purpose of evaluating the operating

Table 9.1: Optimal module inclinations (s_{OPT}) for maximizing the total energy transmitted to the cells and achievable gains, under a local clear-sky climate, for an *a*-Si:H installation with the spacing D/L=3.00 and specular reflectance of 0.90. Due to the similarity in the latitude, the optimal geometries and annual gains are very similar under clear-sky conditions.

Clear Sky	s^a_{OPT}	s^b_{OPT}	*Gain*[c]
St. Johns	36 °	66 °	**32.2 %**
Palaiseau	36 °	66 °	**32.3 %**
Bratislava	36 °	66 °	**32.3 %**

[a] Classical installation

[b] Aleph system

[c] Gain in transmitted energy, Equation 9.1

temperature of the cells (which impacts their efficiency), the monthly average daily distributions of air temperature were obtained from the Weather Network database [173] (for St. John's) and the PVGIS database [174] (for the two European locations). Note that the use of average temperature profiles breaks the coupling between high irradiance and air temperature, which might result in overestimations of efficiency. Due to the unavailability of wind data for all locations, the wind speed was assumed to be constant at 1 m/s. The irradiance data (from the MACC-RAD database) and the environmental data were used with the developed model to find the optimal settings for the two systems (Aleph and classical installation) for maximizing the total energy production. The annual gains in produced energy were evaluated, defined as the ratio of energy productions of the two individually optimized systems:

$$Gain = \frac{\int_{2011}^{2014} P_{MPP}^{Aleph\ (OPT.)} dt}{\int_{2011}^{2014} P_{MPP}^{PV\ CLASSICAL\ (OPT.)} dt} \tag{9.2}$$

Table 9.1 shows the achievable gains (rounded to the nearest per cent) and optimal settings under local clear-sky conditions, taking into account the local aerosol measurements. The optimal settings under clear sky are identical for the three cities for both the Aleph system and the classical installation, since their latitudes are very similar. The achievable gains in transmitted energy are very similar, and are practically equal. However, slight differences in achievable gains in transmitted energy were observed (<1% relative difference in gain) due to the slightly different local annual distributions of the aerosol levels. While in this study the aerosols have a negligible impact on gain, regions with heavy air pollution might experience severe gain reductions.

Table 9.2 presents the results of optimal settings and *energy production gains* under the three cities' respective local climates. Bratislava and Palaiseau climates provide considerably higher gains in produced energy compared to the one of St. John's. This

Table 9.2: Optimal module inclinations (s_{OPT}) for maximizing the total produced energy and achievable annual gains, under a local climate, for a CIGS installation with the spacing D/L=3.00 and a specular reflectance of 0.90. The impact of local climate is apparent.

Local Climate	s^a_{OPT}	s^b_{OPT}	*Gain*^{c}
St. Johns	11 °	56 °	**8.0 %**
Palaiseau	21 °	61 °	**19.0 %**
Bratislava	21 °	63 °	**20.0 %**

[a] Classical installation

[b] Aleph system

[c] Gain in produced energy, equation 9.2

is due to the higher proportion of clear-sky days of the two continental European cities compared to the coastal Canadian one, notably near the equinoxes when the reflectors have the highest influence.

A higher module inclination favours the collection of direct flux due to a smaller resulting angle of incidence, while a lower module inclination favours the collection of diffuse flux due to a higher shape factor from the PV module to the sky. Since St. John's is associated with a highly cloudy climate and a high value of k_D, the optimal PV module inclination is considerably lower compared to the two European cities.

When one compares Tables 9.1 and 9.2, the impact of the local climate becomes apparent. Higher deviations from a clear-sky climate result in lower optimal PV module inclinations, lower annual yields, and lower achievable gains.

It should be noted that the yield and gain estimates were made using a model that assumes the string mismatch has no impact on efficiency. This is approximately true for modules exhibiting minor impacts of non-uniform illumination, such as those situated away from the edges (the case for most modules in large installations), and in which the individual cells span the entire height of the module (common with thin film PV modules). However, mismatch losses can be significant for modules with different cell topologies, or for modules which experience the edge effect (non-uniform concentration). Note also that higher gains are achievable with larger D/L inter-row spacings, as larger reflector surfaces can be installed leading to higher factors of concentration. Naturally, reflectors with a higher reflectance would further boost gains.

9.1.3 Conclusion

The study shows that the addition of inter-row reflectors brings significant gains in the annual produced energy for all three cities considered. Comparing the results of simulations based on clear-sky and local climate irradiances, it is clear that the local climate

has a significant impact on both the achievable gains and the optimal settings. A highly cloudy climate can result in significantly lower achievable gains and demand a lower PV module inclination to maximize production. The annual distribution of aerosols has a slight impact on achievable gains and a negligible impact on optimal settings.

9.2 Reflector Performance Effect on Optimal Geometry

When designing an Aleph installation, a choice of reflector must be made before performing a geometrical optimisation. Since better-performing reflectors (e.g. ones with a higher reflectance) are often more expensive, the most economical design will depend on the sensitivity of the system performance on mirror reflectance. Similarly, the optimal geometry will depend on its sensitivity to the reflector performance.

To explore these sensitivities, the following study was performed. An integrated model was assembled, consisting of the analytical optical model, the proposed thermal model, and the Evans efficiency model [74]. Four years (2011-2014) of atmospheric variables measured at SIRTA (surface irradiance, air temperature and wind speed) were used as inputs. The dimensionless inter-row spacing D/L was set to 3.00. Annual and winter energy productions were evaluated for Palaiseau for a range of PV module inclinations (mirror is assumed to adapt in size to close the triangular cavity), and a range of mirror reflectances. The winter period was assumed to include the months of January, February, November and December.

9.2.1 Results and Discussion

In both annual and winter optimisations of an *a*-Si:H Aleph installation (Figs. 9-3 and 9-4), a similar trend is observed: for an arbitrary module inclination, the production (represented by the colour scale) increases with an increasing reflector performance. By noting the difference in spacing between contour lines in the two graphs (1 kWh/m^2 and 0.01 kWh/m^2 for annual and winter graphs, respectively), and observing the density of contour lines along the optimum line (in white), it is clear that this increase is more rapid in the annual case compared to the winter case. For the same increase in reflector performance (varying ρ_{Ref} from 0.4 to 0.9) and under optimal geometries, the annual production increased by 16.3%, while the winter production increased by 2.2%. This is a result of a better concentration of beam irradiance compared to diffuse. Since a full year has a higher fraction of beam irradiance compared to the winters, the annual production has a higher sensitivity to the reflector performance compared to the winter production.

In the annual optimisation of an *a*-Si:H Aleph installation (Fig. 9-3), one can observe a linear increase in the optimal PV module inclination with respect to ρ_{Ref}. The optimal

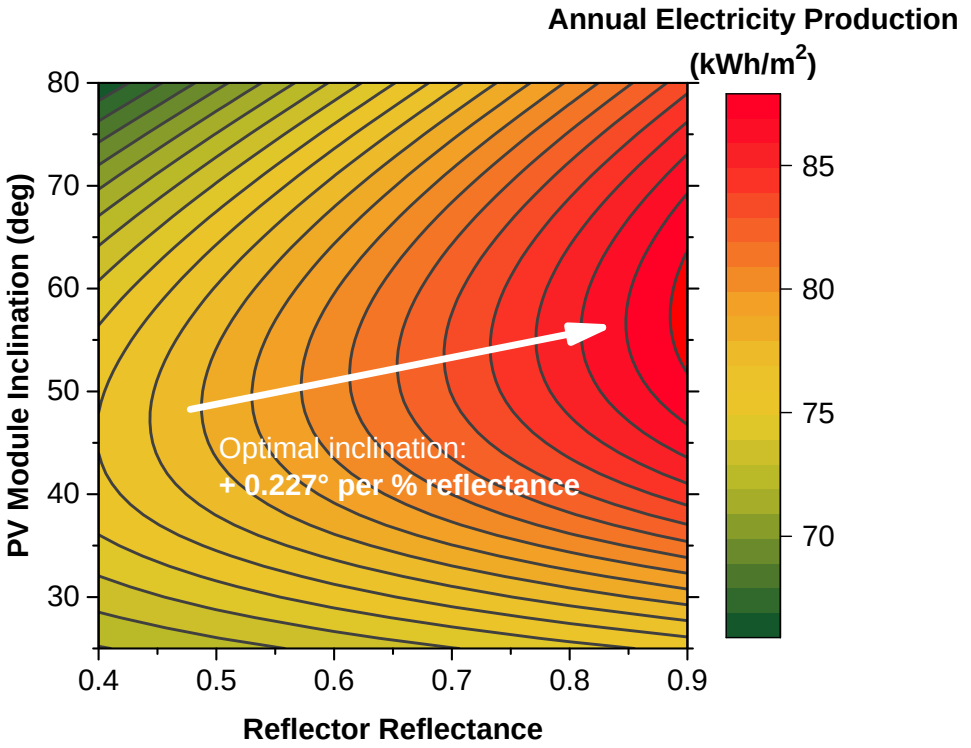

Figure 9-3: Annual energy production of a-Si:H modules equipped with planar reflectors, as a function of PV module inclination and mirror reflectance. Spacing between contour lines: 1 kWh/m^2.

inclination was found to increase by about 0.227° for each per cent of reflectance increase. For example, if a 40% reflective mirror is replaced by a 90% reflective one, the PV module inclination should be increased by about 11° (from 46° to 57°). This increase in the optimal inclination is a result of the reflectors producing a higher gain in direct irradiance compared to diffuse, and because the collection of direct irradiance increases with higher PV module inclinations. Note that the geometrical optima for a given value of reflectance are rather flat. This information indicates the tolerance of error from the optimal PV module inclination during the construction phase, within which negligible losses of production are expected. If significant degradation of reflectance is anticipated, this graph can be used to design the system for the post-deterioration reflectance.

In the winter optimisation (Fig. 9-4), the opposite trend is observed: the optimal inclination decreases with ρ_{Ref}. The optimal inclination was found to decrease by about 0.033° for each per cent of reflectance increase, which is a negligible rate compared to the previous case. Winters in Palaiseau are associated with frequent overcast conditions, resulting in a large diffuse fraction of the ground-level irradiance, k_D. As ρ_{Ref} is increased, the system tends towards a lower inclination angle for a more efficient collection of diffuse irradiance (increasing the view factor from the module to the sky). Note that the optimal PV module inclination for winter production is about 60° for most values of reflectance. This may come as a surprise considering the classical installations often require lower

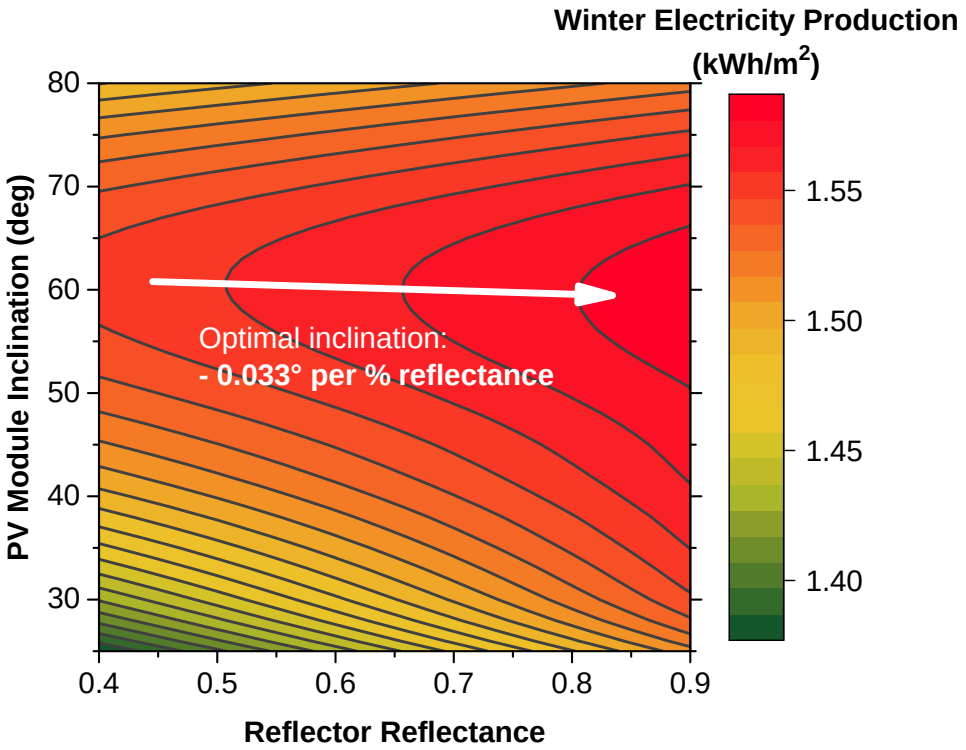

Figure 9-4: Winter energy production of *a*-Si:H modules equipped with planar reflectors, as a function of PV module inclination and mirror reflectance. Spacing between contour lines: 0.01 kWh/m^2.

inclinations for best collecting diffuse light. Such a high optimum is justified by the role of reflectors in collecting diffuse irradiance. In classical installations, higher PV module inclinations present a direct trade-off between improving the collection of beam irradiance (through lower optical losses) and losing a part of the view of the sky (behind it, and due to shading from the row in front of it). The addition of the planar reflector results in a smaller decrease in the overall view factor of the sky as the inclination is increased. This allows for the optimisation of the collection of direct irradiance (reducing optical losses), even if its fraction is low in this period, resulting in a high PV module inclination angle.

9.2.2 Conclusion

The study shows the expected gains in production from replacing worse-performing reflectors by better ones, or inversely the loss of production due to the weathering of reflectors. By upgrading a 40% reflective mirror with a 90% one, a 16.3% increase in annual production is expected. The economical viability of this upgrade depends of course on the cost of the reflectors.

The optimal PV module inclinations of the Aleph system were found to change based on the objective (maximum annual or winter energy productions). Specifically, it was found to increase with reflectance for the annual production and decrease for winter production. Since the amount of ground irradiance is relatively low in the winter period,

the annual optimum is more likely to be used in construction. However, if intra-annual changes in geometry are permitted, the information from a winter optimisation can be used to adapt the system for an optimal winter production.

9.3 Edge Effect

The edge effect has been observed with edge modules in the experiment. These modules receive less reflected radiation in either morning or evening periods depending on their location (East or West), resulting in a lower production compared to equivalent non-edge modules. Beside receiving less reflected radiation, the concentration is more likely to be heterogeneous across the cells. The resulting mismatch effect is more likely to impact *p*-Si modules due to the specific PV cell topology.

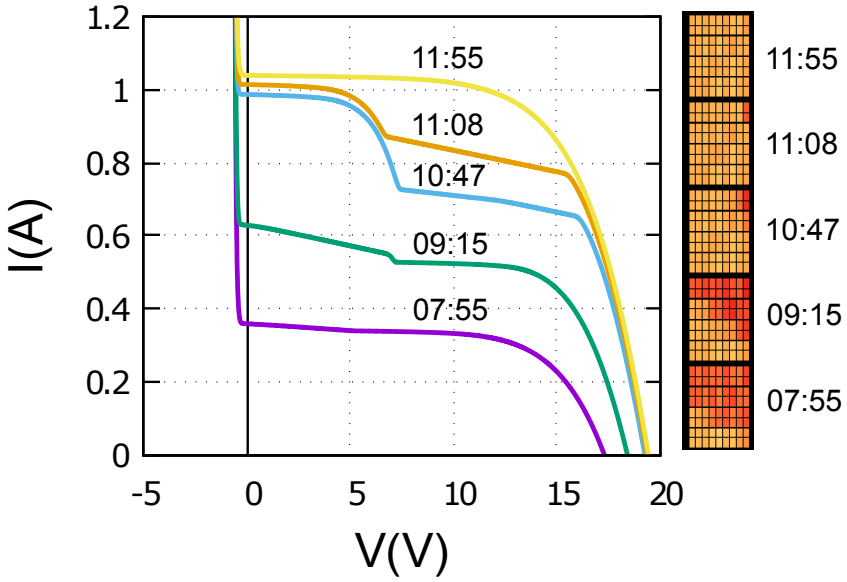

Figure 9-5: Simulated *I-V* characteristic of an edge *p*-Si module, equipped with two bypass diodes, resulting from different distributions of the concentration zone and hence degrees of string mismatch. The bypass diodes are active in mismatch conditions, as well as in reverse bias.

To illustrate the combined impact of the edge effect and the corresponding influence of the bypass diodes on the performance of *p*-Si modules, a simulation was set up as follows. An integrated model was assembled, consisting of the ray-tracing optical model and the SPICE electrical model. The geometry of the system was that of the experiment (D/L=3.00, s=49°). ρ_{Ref} was set to 0.93. The SPICE model of the *p*-Si cells was parametrised according to Table 7.1. The *I-V* characteristic was simulated for an east edge *p*-Si module at various points throughout the morning period, characterized by different distributions of the concentration-shading-transmission factor (see Fig. 9-5). To emphasize the mismatch effect, the beam normal and diffuse horizontal irradiances were

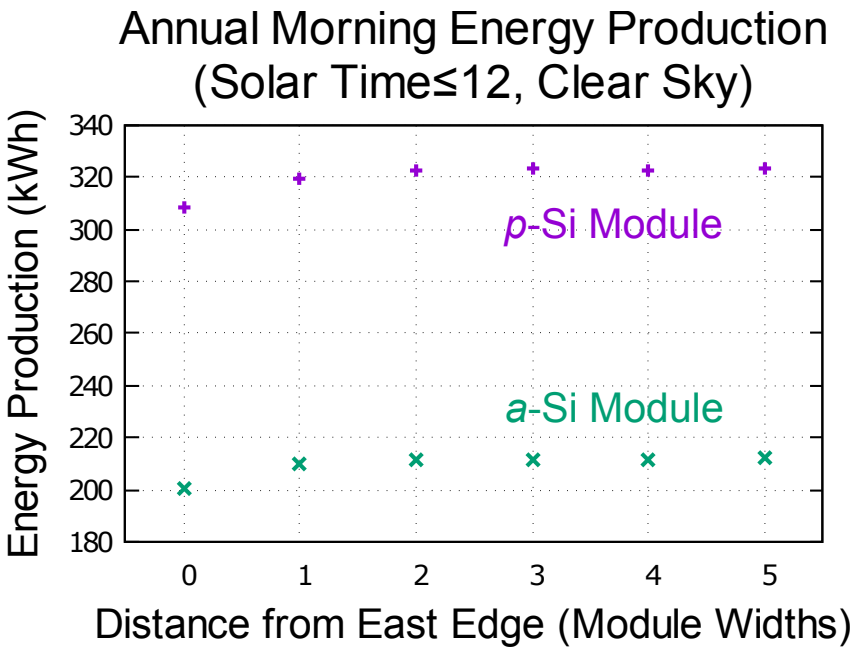

Figure 9-6: Annual morning energy production of *a*-Si:H and *p*-Si modules as a function of distance from the east row edge, evaluated under clear sky conditions [95]. The equivalent energy productions for frontal *a*-Si:H and *p*-Si modules are 183 kWh and 282 kWh, respectively.

set to 800 and 0 W/m^2, respectively. The operating temperature was fixed at 70 °C. The simulation was run for August 16, 2014, at: a) 07:55, b) 09:15, c) 10:47, d) 11:08, and e) 11:55 UTC. It can be seen that in forward bias conditions, the influence of the bypass diodes depends on the degree of mismatch, while in reverse bias (around -0.7 V) they result in a rapid increase in current. Note the difference between 11:08 and 11:55. A lower illumination of the corner cell results in a disproportional loss in power production compared to uniform illumination, despite the presence of bypass diodes.

It is therefore in the designer's interest to eliminate the edge effect if possible, by extending the reflector length in the East-West direction. In view of deciding on the optimal length of reflector overhang, the integrated model was used to evaluate the influence of the distance of a module from the edge of the row on the yield (see Fig. 9-6). To emphasize the edge effect, the annual production of *east* edge modules was considered during *morning* periods (a similar behaviour exists during evening periods for the west edge modules). During these periods, the influence of the reflector varies based on the distance from the edge, favouring the central modules. Furthermore, as the edge and the string mismatch effects are the most influential during clear sky periods, McClear clear-sky model was used to set irradiance values in view of representing the worst case relative losses.

The result of the simulation is summarised in Fig. 9-6. The loss in production of the marginal modules compared to the ones furthest from the edge amount to about 5% for

both technologies. It is clear that the edge effect decreases as the distance from the edge is increased. Furthermore, diminishing returns are observed beyond a certain length of reflector overhang. The result of this study can be used to decide on the optimal length of a reflector overhang to minimise the edge effect and in turn maximise production (in this case, 2-3 module widths of overhang is recommended). Note that in temperate climates where the diffuse component presents a significant portion of the total irradiation, the edge effect will be less influential on the yield.

9.4 Mismatch Effect

Another information that could be useful to the designer is a quantitative analysis of the mismatch losses (losses in power or energy due to the string mismatch effect). This can for example aid in selecting the most favourable cell layout and interconnection. Similarly, it gives insight into the potential gains from optimising the cell layout or interconnection to reduce mismatch losses. The mismatch losses can also give an idea of the energy absorbed by the mismatched cells (ones receiving less irradiation compared to the neighbours).

The study of this effect consisted of contrasting results of two simulations, sharing in common the following setup. An integrated model was assembled consisting of the ray-tracing optical model, the SPICE electrical model, and the empirical thermal model. The inputs consisted of the 2014 measured values of direct and diffuse irradiances, air temperature, and wind speed. The SPICE model was parametrised according to Table 7.1. ρ_{Ref} was set to 0.80 to represent an average quality reflector. The geometry of the system was that of the demonstrator (D/L=3.00, s=49°).

In the first simulation, the cell irradiances calculated by EDStaR were used as inputs in SPICE. In the case of heterogeneous illumination, a certain degree of string mismatch effect was possible. In the second simulation, an average of the cell irradiances was found and imposed on all the cells. In theory, this would eliminate the string mismatch while resulting in the same factor of concentration. Figures 9-7 and 9-8 present the results for the case of the central (non-edge) *p*-Si and *a*-Si:H modules. In all graphs, the colour scale represents the the ratio of diffuse to global in-plane transmitted irradiance.

In the case of *p*-Si (Figs. 9-7a and 9-8a), the mismatch losses are considerable throughout the year. In Fig. 9-7a, it is clear that the non-uniform concentration of diffuse irradiance contributes to mismatch losses. During overcast periods associated with high diffuse fractions and denoted with gray points, the relative power loss due to mismatch is about 5% (reaching 5.6%). In absolute terms (Fig. 9-8a), overcast days bring more mismatch losses in the summer (0.2 W) compared to the winter (0.1 W) due to the difference in summer and winter diffuse irradiations. Fig. 9-7a equally presents the mismatch losses due to direct irradiance. During clear periods dominated by direct irradiances and denoted with red points, the degree of mismatch varies throughout the year. It is minimal

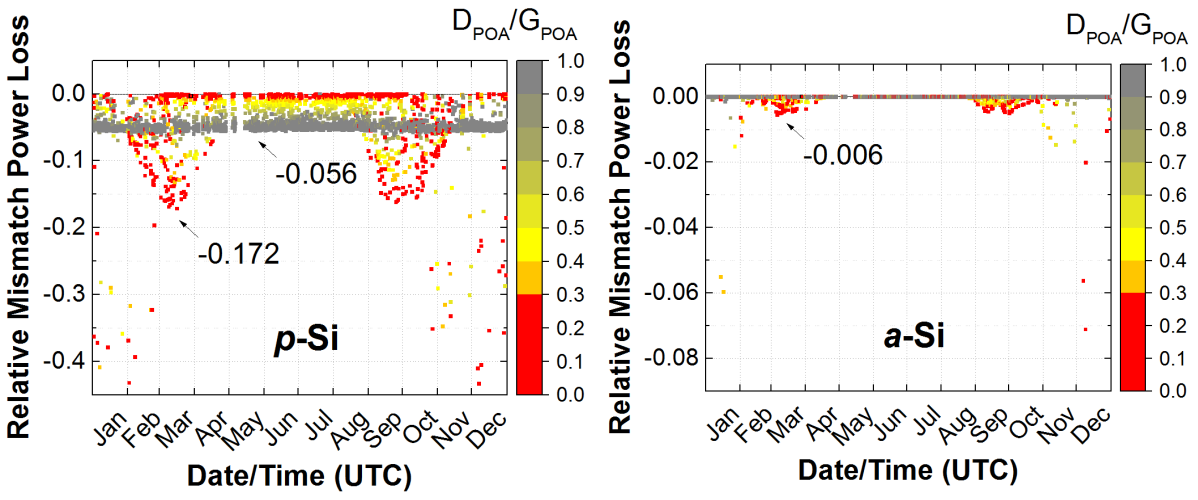

(a) *p*-Si (b) *a*-Si:H

Figure 9-7: Relative power losses due to string mismatch in reflector-equipped modules, for (a) a central *p*-Si module, and (b) a central *a*-Si:H module. The relative losses in the annual produced energy are 2.82% and 0.02% for *p*-Si and *a*-Si:H modules, respectively.

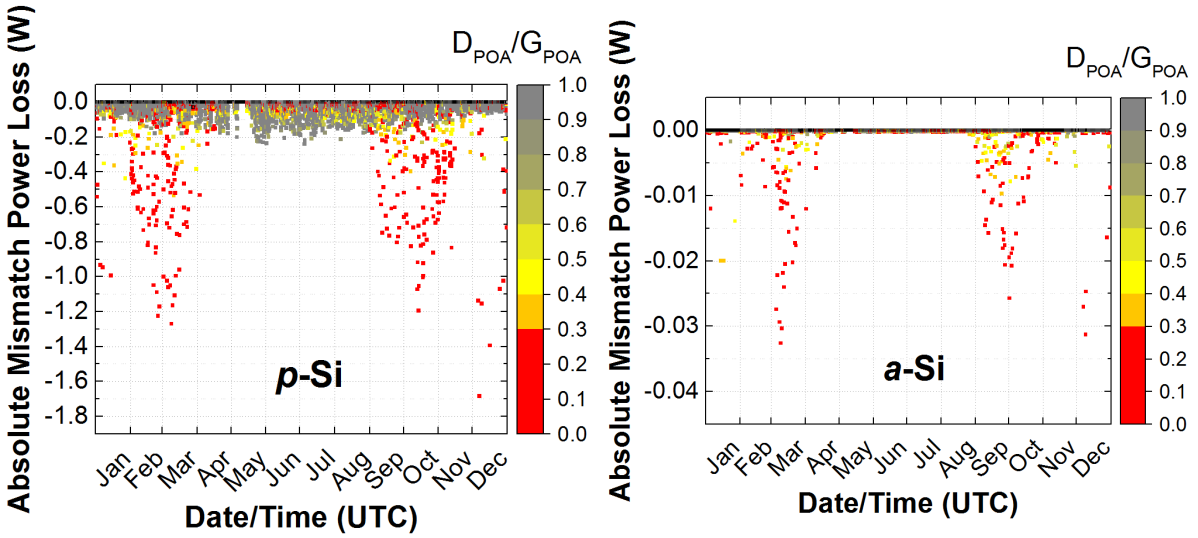

(a) *p*-Si (b) *a*-Si:H

Figure 9-8: Absolute string mismatch power losses in reflector-equipped modules, for (a) a central *p*-Si module, and (b) a central *a*-Si:H module

in the summer months when uniform concentration is achieved across the modules and the edge effect is negligible due to the high solar elevation angle. Significant relative losses are observed near the equinoxes, with peaks on March 15th and September 31st. These losses are due to the heterogeneous flux brought by the edge effect, and reach 17.2%. In the winter months, high relative mismatch losses (up to 43.4 %) are obtained due to the edge effect, highly isolated shadows and similarly narrow concentration bands affecting only the bottom row of cells (cells in the lower half of the bottom string). Note that the high relative losses correspond to periods of low irradiance during morning and evening

periods. To highlight this, Fig. 9-8a presents the absolute mismatch losses. In absolute terms, the mismatch losses reach 1.27 W near the equinoxes, and up to 1.69 W in the winter periods.

In the case of *a*-Si:H (Figs. 9-7b and 9-8b), the mismatch losses are less significant. The heterogeneous concentration of diffuse irradiance does not contribute to heterogeneity of flux among the cells since the diffuse concentration (far from the edges) is symmetrical about the height of the modules and the cells are vertical spanning the entire height of the module. This is noted by the gray points in Figs. 9-7b and 9-8b indicating zero loss in overcast conditions dominated by diffuse irradiance. Similarly to the *p*-Si case, near the equinoxes the direct irradiance contributes to string mismatch losses reaching 0.6% or 0.033 W. This is uniquely due to the edge effect, which in the case of the demonstrator is influential even on central modules. In the winter, the mismatch loss can reach up to 7.1% or 0.031 W.

The relative losses in the annual produced energy are 2.8% and 0.02% for *p*-Si and *a*-Si:H modules, respectively. This observation confirms the advantage of *a*-Si:H cell layout and interconnection (long series-connected cells in portrait orientation) in reducing the string mismatch losses throughout the year. For this reason the recommended module technology for the Aleph system is the one with a vertical cell layout (common with thin film modules). With such a layout, the mismatch losses could be further reduced or eliminated by installing East-West mirror extensions and therefore reducing the edge effect.

Chapter 10

Conclusions

The Aleph platform has been successfully installed in the SIRTA meteorological station, and a data acquisition system has been put in place to perform and store $I - V$ and operating temperature measurements of 18 modules. Today, over two years of outdoor performance data have been gathered. A relatively small budget for performing this study was compensated by using low-cost reflectors, relying on donations of materials (notably PV modules thanks to the SOLEMS company), using a switch to sequentially perform measurements of several modules, and using certain existing SIRTA equipment (notably their computer for data storage).

In addition to 12 reflector-equipped modules, a row of 6 reference modules was used to experimentally evaluate the impact of planar reflectors. Experimental measurements show that *a*-Si modules are more adapted for the Aleph system, experiencing higher gains in daily produced energy compared to *p*-Si modules. The three main reasons for this are 1) a more favourable topology and interconnection of PV cells, 2) a better match of the *a*-Si cell spectral response with the spectral reflectance of the mirror, and 3) smaller thermal losses (smaller sensitivity to temperature). Compared to reference modules, reflector-equipped *a*-Si and *p*-Si modules produced respectively 19.2% and 8.58% more energy annually. Highest gains were measured near the equinoxes, where monthly gains reached 30% and 20% for *a*-Si and *p*-Si modules, respectively. Significant gains were measured in the summers for both technologies: 18% and 8% for *a*-Si and *p*-Si modules. Due to an insufficient inter-row spacing, shadows were present on the reflector-equipped modules during certain periods of the winter. For this reason, sunny winter days resulted in unfavourable gains in daily produced energy compared to unobstructed frontal reference modules. Nevertheless, since the reflector continued to offer a higher albedo in the vicinity of the modules, significant energy gains were observed during overcast days: up to 20% and 10% gain in daily produced energy for *a*-Si and *p*-Si modules, respectively.

Several modelling tools have been developed in the scope of the thesis. As the behaviour of PV modules depends on optical, thermal, and photo-electric phenomena, an integrated model coupling these phenomena was necessary to describe it.

The amount of light reaching the PV modules was calculated analytically and statistically (using EDStaR providing the Monte-Carlo method and ray-tracing in three dimensions). The statistical approach provided a higher flexibility in the modelling of the solar resource and the system geometry. The statistical model was able to provide cell-level irradiances necessary for accurate electrical modelling. Despite a higher calculation cost, the ray-tracing solution is favourable for modelling concentrator PV systems.

The photoelectric conversion has been also modelled in two ways: empirically and using equivalent circuits. The empirical approach seemed adequate for the case of uniform illumination of cells (e.g. for frontal modules), but inadequate for heterogeneous illumination conditions common with reflector-equipped modules (i.e. partial shading conditions or isolated concentration zones). For this reason, equivalent circuits have been employed to model individual PV cells. PV modules have been assembled in the SPICE environment, adding bypass diodes to the *p*-Si modules. Compared to 3 parameters in the empirical model, the SPICE model had 11 and 12 parameters for the *a*-Si and *p*-Si cells, respectively. A solution for a systematic calibration of the parameters has been developed in the form of an evolutionary algorithm.

A calibrated coupled EDStaR and SPICE model, using measured data of module operating temperature, proved accurate in reproducing $I-V$ curve and P_{MPP} measurements. The RMSE of the model in reproducing the P_{MPP} measurements is 0.68 W and 1.26 W for frontal *a*-Si:H and *p*-Si modules, and 0.96 W and 1.87 W for reflector-equipped *a*-Si:H and *p*-Si modules. For reference, these modules produce up to 6, 10, 7 and 12 W, respectively.

Finally, a simple empirical thermal model has been developed, inspired by the famous King model. The model performance was satisfactory, resulting in an RMSE of less than 5 °C and a power error of less than 3%.

Simulations yield that the achievable annual gains and optimal geometry of the Aleph system greatly depend on the local climate, the latitude (best performance in mid-latitude regions), and the reflector performance (more precisely, its adaptation to the PV cell spectral response). The gains are also affected by the PV cell thermal sensitivities, cell topologies (i.e. string mismatch losses), and the modules' distances from the reflector edge (e.g. amount of reflector overhang). Compared to a geometrically-optimised classical installation, the Aleph installation (considering a mirror with a 90% broadband reflectance) is expected to produce up to 19% more electrical energy annually in the Palaiseau region, up to 20% in continental climates like Bratislava, Slovakia, and up to 8% in coastal climates like St. Johns, Canada.

While the use of planar reflectors is a technique of great potential in reducing the cost of PV-generated electricity, its competitiveness over conventional installations will depend on the life-cycle costs of PV modules, mirrors and the ground surface area.

Chapter 11

Perspectives

The first perspective is the consideration of the totality of spectral effects, which were not introduced in the final model despite significant progress of the team on this subject. An attempt was made at modelling the spectral distribution of the solar flux, using SMARTS2. Encouraging results were obtained during clear sky periods, while the diffuse spectra could not be accurately reproduced. Furthermore, while the reflector was characterised for spectral reflectance, spectral responses of actual cells in the experiment were impossible to obtain. These measurements are key in accurately describing the spectral mismatch effect.

Secondly, a fluid dynamics-based thermal model could be developed for a more accurate prediction of thermal transfers within the cavity module-mirror-ground. It could be used to optimise the gaps between modules and mirrors in view of maximising natural convection cooling, or aid in the design of a combined PV+T system (where the heat in the cavity is captured and used for heating the building).

Advances can be made in the analytical optical model, currently based on the infinite-row assumption. A "finite-row" optical model would imply an analytical derivation of the concentration zone shape taking into account the edge effect. This approach should result in similar results obtained by EDStaR, but with a much lower computation cost.

Next, a comprehensive economics model of the system would be of great value. Since the relationship between the costs of PV modules, surface area, and reflectors varies from application to application, this model would help select the most economical configuration.

An environmental model would be a great asset in highlighting the advantage of the Aleph system compared to conventional ones - whether it is due to a decrease in the PV cell surface area, a decrease in the ground area, or the reliance on relatively environmentally benign PV module technologies.

Finally, an simple-to-use executable should be made to allow a non-expert to simulate the behaviour of reflector-equipped PV installations.

THIS PAGE INTENTIONALLY LEFT BLANK

Appendix A

Résumé Substantiel

Le projet « Aleph » a été inspiré par les contraintes des installations photovoltaïques (PV) conventionnelles sur plan horizontal, comme les installations en toiture ou bien les centrales PV sur champ. Dans le cas d'une installation typique, le « ground coverage ratio » (le rapport entre la surface des cellules PV et celle du sol) est limité par le besoin de réduire les périodes d'ombrage le matin et le soir. Le système résultant consiste en rangées de modules PV largement espacées. Cela conduit à une forte illumination de l'espace entre les rangées pendant des périodes de forte irradiance (par exemple vers midi solaire) qui ne contribue pas à la production électrique. Dans le cadre du projet Aleph nous explorons l'intérêt d'ajouter des réflecteurs plans entre les rangées pour maximiser la production électrique, et nous établissons des règles claires permettant l'optimisation géométrique de l'ensemble dans un lieu et sous un climat donnés.

La littérature existante montre que l'emploi des réflecteurs plans est une technique bien établie pour augmenter le flux solaire incident sur un collecteur. Des nombreuses études ont été réalisées pour estimer l'augmentation de l'irradiation d'un système collecteur-réflecteur donné, se basant le plus fréquemment sur les systèmes solaires thermiques. Cependant, peu d'études ont été effectuées sur des systèmes PV équipés de réflecteurs plans. Aucune étude ne comprend à la fois la partie numérique et expérimentale du système en testant plusieurs technologies de modules PV en parallèle.

Ce travail combine l'expérimentation sur la plateforme météorologique SIRTA de modules PV équipés de miroirs, et la modélisation multiphysique du système prenant en compte tous les phénomènes physiques en jeu.

Deux technologies de modules PV sont testées expérimentalement : silicium amorphe hydrogéné (*a*-Si:H) et silicium polycristallin (*p*-Si). Le banc de test consiste en 18 modules PV *a*-Si:H et *p*-Si installés sur trois rangées successives, avec un même angle d'inclinaison de 49° (proche de la latitude de Palaiseau). Les deux rangées arrières sont équipées de réflecteurs en verre aluminisé en face arrière, plans et fixes, et la rangée frontale sans réflecteur sert de référence. Cela permet l'évaluation expérimentale des gains énergétiques apportés par les réflecteurs. Des sondes de température ont été installées en face arrière

des modules PV, permettant, entre autre, la quantification de l'élévation en température des cellules PV due à la concentration du flux solaire. Le banc de test est instrumenté pour mesurer la caractéristique I-V et la température de chacun des modules PV est mesurée séquentiellement depuis le lever jusqu'au coucher du soleil. Nous avons également accès à toutes les mesures faites par le SIRTA, notamment les irradiances solaires directe et diffuse, les caractéristiques du vent, et la température ambiante.

Les mesures *I-V* mettent en évidence des gains énergétiques importants grâce aux réflecteurs, ainsi que des différences entre les deux technologies de module PV. Par exemple, le gain annuel mesuré en énergie produite est de 19% pour les modules *a*-Si:H, et de 9% pour les modules *p*-Si. L'écart de gain vient principalement de la différence des réponses spectrales des deux technologies des cellules PV, ainsi que des topologies et des interconnexions des cellules dans les modules. Pour une technologie donnée, le gain instantané dépend principalement du rapport diffus/globale de l'irradiance au sol et de la période de l'année (gain plus fort en mi-saison). Nous constatons aussi une baisse du rendement sous faible irradiance plus sensible pour les modules *p*-Si que pour les *a*-Si:H.

Les mesures de température des modules montrent que, sous fort éclairement, les modules équipés de miroirs s'échauffent de +20° C par rapport aux modules frontaux sans miroir. Cela conduit à une baisse de rendement de 11% pour le *p*-Si, plus sensible à la température, et de 2% pour l'*a*-Si:H. Pour une rangée donnée, les modules *p*-Si chauffent jusqu'à 5° C de plus que les *a*-Si:H du fait de l'absorption sans conversion d'une partie du spectre solaire (une fraction dans le proche infrarouge). Cela est dû à la différence des propriétés optiques des deux modules PV, ainsi qu'à la différence d'épaisseur des couches de silicium.

L'ensemble des mesures permet le développement et la calibration d'un modèle multiphysique du système. La position du soleil a été modélisée par l'emploi des équations de Duffie et Beckman ainsi que des équations empiriques de l'angle de déclinaison et de l'équation du temps. Les propriétés optiques des interfaces multicouches (modules PV et miroirs) ont été décrites par la loi de Snell-Descartes, en utilisant les indices de réfraction trouvés dans la littérature. Dans un premier temps, le modèle optique a été développé de manière analytique, prenant comme hypothèse simplificatrice des rangées de modules PV et de miroirs de longueur infinie. En l'absence de sondes d'éclairement dans le plan des modules (jusqu'à récemment), ce modèle n'a pas pu être validé de manière directe mais seulement en se basant sur les mesures d'irradiance du SIRTA. Afin de valider ce modèle optique, un modèle électrique empirique du rendement (approche d'Evans) a été utilisé permettant la comparaison des puissances générées expérimentales et calculées numériquement à partir des mesures d'irradiance directe et diffuse sur plan horizontal. L'ensemble de ces deux modèles (optique et électrique) a prouvé sa pertinence en reproduisant le comportement des modules frontaux, ainsi que des modules équipés de miroirs.

Le modèle analytique ne calcule pas les irradiances au niveau de la cellule, nécessaire par exemple pour le calcul des pertes dus au « mismatch ». Au contraire, il suppose un éclairement moyen uniforme due à la présence du miroir, alors que celui-ci est plus élevé à proximité de la ligne de connexion miroir-module PV. Malgré ces limitations, ce modèle optique couplé avec l'approche d'Evans est une technique numériquement peu coûteuse pour simuler le comportement des grandes installations.

Dans un deuxième temps, un modèle optique basé sur le lancer de rayons en 3-D et la méthode de Monte-Carlo a été développé sous l'environnement EDStaR. Cette approche permet, comme la méthode analytique, le calcul précis de la zone de concentration ou ombrage sur le plan des modules. Elle permet aussi une meilleure modélisation de la ressource solaire (tirage statistique du disque solaire, de la région circumsolaire, où bien de la voûte céleste) qui conduit plus simplement à quantifier, l'éclairement des zones de pénombre et l'hétérogénéité de la réflexion du rayonnement diffus par les miroirs. De plus, elle permet la simulation des différentes configurations des miroirs et modules sans le besoin de la réécriture d'équations. Grâce aux cartes de flux sur le plan des modules calculées par EDStaR, le flux moyen de chaque cellule PV à été calculé en fonction de sa position dans l'expérience. Afin de valider ce modèle optique et d'exploiter l'information des flux par cellule, un modèle photoélectrique des modules PV plus détaillé a été développé.

Le modèle photoélectrique avancé des modules PV a été développé sous SPICE, un simulateur performant des circuits électriques. Ce modèle s'appuie sur un modèle du comportement des cellules PV basé sur les circuits équivalents. Les cellules *a*-Si:H et *p*-Si ont été indépendamment modélisées suivant les phénomènes physique en jeu. Par exemple, les pertes de recombinaison ont été décrites par une deuxième diode pour les cellules *p*-Si, et avec un terme Merten pour les *a*-Si:H. Les deux modèles de cellules PV ont été équipés d'un terme Bishop afin de bien représenter le comportement de ces dernières lors la polarisation inverse (ex. déclenchement de l'avalanche). Les modèles des modules PV de deux technologies ont été ensuite construits suivant les interconnexions correspondant des cellules. Deux diodes bypass ont été ajoutées dans le cas des modules *p*-Si.

L'ensemble de ces deux modèles (optique sous EDStaR et photoéléctrique sous SPICE) a été systématiquement calibré avec les données expérimentales en utilisant un algorithme évolutif. Vu que la température des modules dépend du flux transmis aux cellules qui lui dépend des paramètres optiques, cette calibration a été faite avec les températures mesurées des modules. Une fois calibré, le modèle démontre une bonne performance en simulant la puissance générée par les modules en fonction des données atmosphériques et radiatives. Par exemple, l'erreur sur la production électrique annuelle est inférieure à 5%.

Avec les modèles optique et électrique calibrés, la dernière étape de modélisation était le développement du modèle thermique. Pour simplifier, une approche empirique a été employée. Ce modèle empirique prend en compte le fait que la température des cellules dépend de la température ambiante, des flux incidents directs et diffus, et de la vitesse du vent. Une fois calibré, le modèle thermique démontre une bonne performance : RMSE inférieur de 5° C, soit 3% d'erreur sur la puissance. Les coefficients liés à l'échauffement par flux solaire sont consistent pour une technologie donnée quel que soit la rangée. Ils révèlent qu'un watt de flux diffus chauffe 2,5 fois plus qu'un watt de flux direct, ce qui est dû en partie à la différence des distributions spectrales des deux composantes (fraction plus importante des photons de courte longueur d'onde du flux diffus) mais aussi probablement au fait que le flux solaire diffus est accompagné d'un flux infrarouge moyen (vers 10μm) retrodiffusé vers le bas par les aérosols atmosphériques. Les coefficients liés au refroidissement par le vent sont consistent pour une rangée donnée quel que soit la technologie (ex. la rangée arrière, sans miroir à l'arrière des modules, est plus exposée aux échanges convectifs ce qui se traduit par une influence négative du vent sur la température plus importante).

Plusieurs applications du modèle sont exposées sous forme d'études de cas. Grâce au modèle MACC-RAD de l'irradiance au sol (par les images satellite), le comportement du système Aleph et de l'installation classique ont été simulés dans trois villes de même latitude mais de climats différents. Les résultats démontrent que le gain atteignable en énergie produite (en comparent les deux systèmes géométriquement optimisés) varie de 8% pour la ville la moins ensoleillée, à 20% pour celle la plus ensoleillée (plus de rayonnement direct).

L'influence de la réflectance des miroirs sur la géométrie optimale ainsi que sur la production électrique a été étudiée par des simulations, pour le cas des modules *a*-Si:H et le climat de Palaiseau. Nous constatons que l'inclinaison des modules PV optimisant la production annuelle monte de 0.227° par pour cent de réflectance, alors qu'elle décroit de 0.033° par pour cent de réflectance pour la production optimale hivernale. De même, les productions annuelles et hivernales montent de 0.326% et 0.044% par pour cent de réflectance, respectivement.

L'effet de bord (diminution de la production des modules situés aux bords de la rangée) a été étudié numériquement pour les deux technologies de modules PV. Nous constatons que cet effet peut être largement réduit par l'installation de miroirs supplémentaires sur les deux côtés est-ouest. La longueur optimale de ces extensions est de 2 à 3 largeurs des modules PV.

Finalement, l'impact du « string mismatch » a été évalué pour les deux technologies. Prenant les mesures radiatives de l'année 2014, le comportement des systèmes *p*-Si et *a*-Si:H a été simulé d'abord avec des vraies irradiances des cellules, et ensuite avec des

irradiances moyennées. L'écart des deux résultats représente des pertes dues au mismatch. Les pertes relatives en puissance sont les plus importantes en mi-saison, montant jusqu'à 17.2% pour le *p*-Si et 0.6% pour les *a*-Si:H. La perte annuelle en énergie produite est de 2.8% et 0.02% pour *p*-Si et *a*-Si:H, respectivement.

THIS PAGE INTENTIONALLY LEFT BLANK

Appendix B

NREL efficiency chart

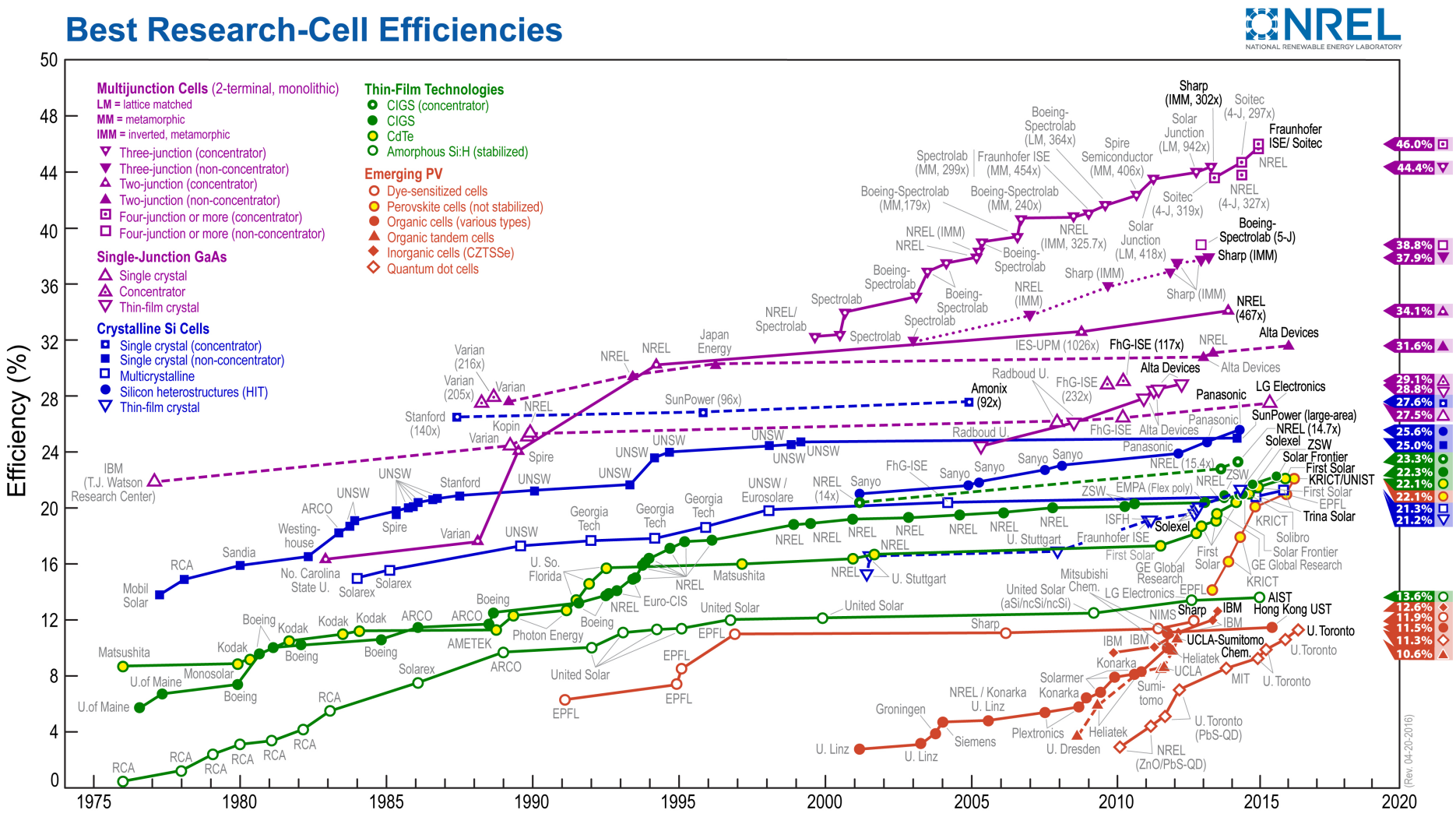

Figure B-1: Best research-cell efficiencies chart, by the United States National Renewable Energy Laboratory (NREL) [16]

Appendix C

Additional Theoretical Background

C.1 Navier-Stokes Equations

The Navier-Stokes equations are the fundamental partial differential equations that describe the motion of fluids. In this section, general Navier-Stokes equations are reduced using the simplifications associated with our problem.

C.1.1 Continuity equation

The continuity equation is another way of referring to the conservation of mass. In a general form, it can be written as:

$$\frac{\partial \rho}{\partial t} + \nabla . \left(\rho \overrightarrow{U} \right) = 0 \tag{C.1}$$

Where ρ is the density, t is the time, and $\overrightarrow{U}$ is the velocity field.

The continuity equation for an incompressible fluid can be simplified to

$$\nabla . \overrightarrow{U} = 0$$

C.1.2 Momentum equation

Three forces act upon a parcel of fluid: viscous force, pressure force and the body force. Let V be the volume of a unit parcel of fluid.

The viscous force for an incompressible Newtonian fluid is $\frac{F_{viscous}}{V} = \mu \nabla^2 \overrightarrow{U}$, where μ is the dynamic viscosity. The pressure force is defined as $\frac{F_{pressure}}{V} = -\nabla \mathrm{p}$, where p is the pressure. The body force, $\frac{F_{body}}{V}$, can be a combination of external forces, the most common for terrestrial applications being the sum of the Archimedes buoyancy and the gravitational body force, $(\rho - \rho_0) g \hat{e}_\mathrm{z}$ (where $\hat{e}_\mathrm{z}$ is the upward unit vector). Adding the three forces and equating them to Newton's law for fluids, $\frac{F}{V} = \rho \frac{\partial \overrightarrow{U}}{\partial t} + \rho \left(\overrightarrow{U} . \nabla \right) \overrightarrow{U}$,

yields

$$\rho\frac{\partial\overrightarrow{U}}{\partial t}+\rho\left(\overrightarrow{U}.\nabla\right)\overrightarrow{U}=(\rho-\rho_0)g\hat{e}_z-\nabla\mathrm{p}+\mu\nabla^2\overrightarrow{U} \tag{C.2}$$

C.1.3 Convection-diffusion Heat equation

The convection-diffusion heat equation is a partial differential equation describing the distribution of heat (i.e. variation in temperature) in a given region over time, resulting from a combination of diffusion and convection processes. Note that viscous dissipation has been neglected in the energy equation, which is a reasonable assumption for the small velocities associated with free convection [175].

Assuming an incompressible flow without viscous dissipation, it reads

$$\frac{\partial T}{\partial t}+\left(\overrightarrow{U}.\nabla\right)T=\alpha\nabla^2T+\Phi$$

where α is the thermal diffusivity (in m^2/s), and Φ represents the sources or sinks of heat (in this formulation in K/s).

Assuming no external fluxes (replicating the conditions in the triangular cavity), the above equation reads

$$\frac{\partial T}{\partial t}+\left(\overrightarrow{U}.\nabla\right)T=\alpha\nabla^2T \tag{C.3}$$

C.2 Heat Transfer

Incropera et al [175] give an excellent and in-depth overview of multiple concepts regarding heat transfer. The following sections introduce the concepts of conduction, boundary layers, convection, flow conditions, and radiation.

C.2.1 Conduction

Conduction is the transport of energy in a medium due to a temperature gradient, the physical mechanism being random atomic or molecular movement that permit exchange of microscopic kinetic energy between particles [175]. Conduction heat transfer is governed by Fourier's law which is phenomenological in nature, meaning it was developed from observed phenomena rather than being derived from first principles.

Consider the steady-state heat conduction experiment (see Figure C-1), comprised of a cylindrical rod of known material, insulated on its lateral surface, with its end faces maintained at different temperatures. The condition $T_1 > T_2$ results in heat transfer in the positive x-direction, since heat is always transferred in the direction of decreasing temperature.

In this case, the direction of the heat flux is normal to the cross-sectional area. More generally, the direction of heat flow will always be normal to a surface of constant temperature, called an isothermal surface. In this manner, the heat flow will follow the temperature gradient, which can take any shape or density.

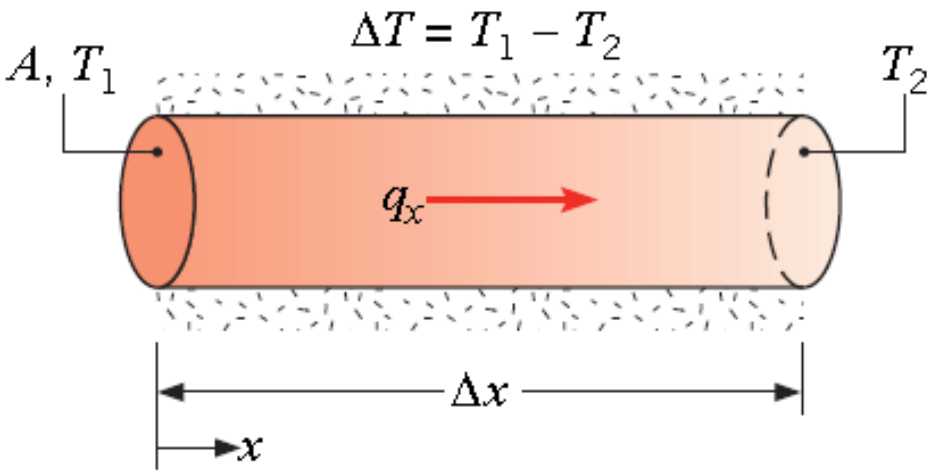

Figure C-1: Steady-state heat conduction experiment. Source: [175]

A general form of the conduction rate equation (Fourier's law) reads

$$q" = -k\nabla T \tag{C.4}$$

where q" is the local surface heat flux (in W/m^2) and k is the thermal conductivity (in W/m.k), a transport property of the material, describing the rate at which energy is transferred by the diffusion process. Thermal conductivity depends on the physical structure of matter (atomic and molecular), where the thermal conductivity of a solid is larger than that of a liquid, which is larger than that of a gas. Note that the total heat flux through a surface A$_s$ is simply $q = \int_{A_s} q"\, dA_s$.

C.2.2 Boundary Layers

Unlike the conductive heat transfer, convection includes energy transfer by both advection (through the bulk fluid motion) and conduction, which has a vast importance near the plate surface. This section introduces the concept of boundary layers, which is central to the understanding of convection heat transfer between a surface and a fluid flowing past it.

C.2.2.1 Velocity Boundary Layer

To illustrate the concept of boundary layers, consider a flow over a flat plate (see Figure C-2).

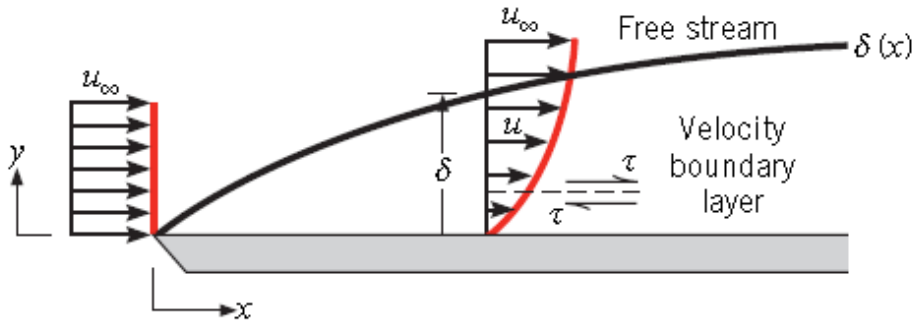

Figure C-2: Velocity boundary layer. Source: [175]

When fluid particles make contact with the plate surface, their velocity is significantly reduced compared to the fluid velocity upstream of the plate. Furthermore, it is for most situations valid to assume that particle velocity is zero at the plate surface. These particles act to retard the motion of particles in the adjoining fluid layer, which retard the motion of the particles in the next layer, and so on until a distance $y = \delta$ from the surface where the effect of the plate is negligible. As a result, a velocity gradient is present in this layer, called the velocity boundary layer. The retardation of one layer onto another can be attributed to shear stresses acting in planes parallel to the fluid velocity. The thickness of the velocity boundary layer, δ, is defined as the value of y where $u = 0.99\ u_\infty$. With increasing distance from the leading edge, the effect of the plate on the flow penetrates further into the free stream, and the velocity boundary layer grows.

C.2.2.2 Thermal Boundary Layer

Similarly to the velocity boundary layer, a thermal boundary layer develops if the fluid free stream and surface temperatures differ (see Figure C-3).

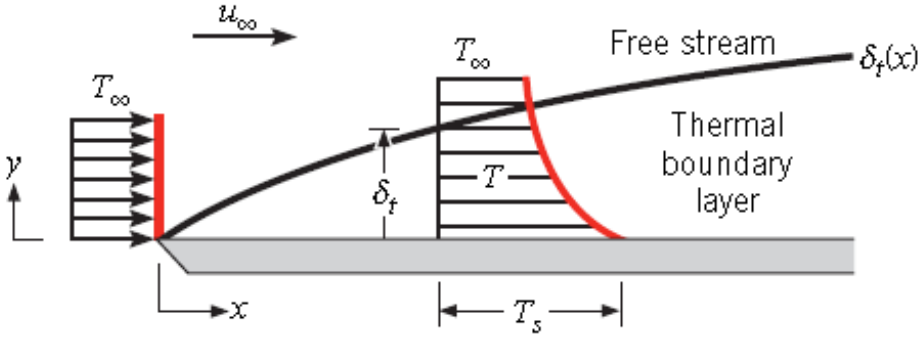

Figure C-3: Thermal boundary layer. Source: [175]

At the leading edge of the plate, the temperature profile is uniform with $T\,(y) = T_\infty$

(there is no temperature gradient). However, when fluid particles achieve contact with the plate, they achieve thermal equilibrium at the plate's surface temperature. Particles in this layer exchange energy with those in the neighbouring layer, and similarly to a velocity boundary layer, a temperature gradient is developed in the fluid. The resulting thermal boundary layer thickness, δ_t is typically defined as the value of y where $[(T_s - T)/(T_s - T_\infty)] = 0.99$. Similarly to the velocity boundary layer, the thermal boundary layer grows with the distance from the leading edge.

An important dimensionless parameter used to characterise a fluid is the Prandtl number, which provides a measure of the relative effectiveness of momentum and energy transport by diffusion in the velocity and thermal boundary layers, respectively [175]. The Prandtl number is defined as the ratio of the kinematic viscosity (also called momentum diffusivity), ν, to the thermal diffusivity, α:

$$Pr = \frac{\nu}{\alpha}$$

The Prandtl number is close to unity for gases, $Pr \ll 1$ for liquid metals, and $Pr \gg 1$ for oils.

For laminar boundary layers, the relationship between the two boundary layers can be written as follows:

$$\frac{\delta}{\delta_t} \approx \mathrm{Pr}^{\mathrm{n}}$$

where Incropera et al. suggest it is for most applications reasonable to assume a value of $n = 1/3$. The equation implies that $\delta_t \approx \delta$ for a gas, $\delta_t \gg \delta$ for a liquid metal, and $\delta_t \ll \delta$ for an oil.

C.2.3 Convective Heat Transfer

Once the concept of boundary layers is well understood, the concept of convective heat transfer can easily be grasped. At the plate surface, there is no fluid motion, and energy transfer occurs only by conduction. Hence, at any distance x from the leading edge, the local surface heat flux, q" may be obtained by applying Fourier's law to the fluid at $y = 0$:

$$q" = -k_f \frac{\partial T}{\partial y} \mid_{y=0} \tag{C.5}$$

where k_f is the thermal conductivity, in $\frac{W}{m.K}$.

Recalling Newton's law of cooling, $q" = h(T_s - T_\infty)$, and combining with Equation C.5, we can solve for the local convective heat transfer coefficient, h:

$$h = \frac{-k_f \frac{\partial T}{\partial y} \mid_{y=0}}{T_s - T_\infty} \tag{C.6}$$

In Equation C.6 it is evident that the rate of heat transfer strongly depends on the

conditions in the thermal boundary layer, particularly the wall temperature gradient, $\frac{\partial T}{\partial y} \mid_{y=0}$. Since $(T_s - T_\infty)$ is a constant (independent of x), while δ_t increases with x, it is clear that temperature gradients in the boundary layer must decrease with increasing x. Accordingly, the magnitude of $\frac{\partial T}{\partial y} \mid_{y=0}$ decreases with increasing x, and q" and h decrease with increasing x.

The total heat transfer rate, q, may be obtained by integrating the local flux over the entire surface:

$$q = \int_{A_s} q" \, dA_s \tag{C.7}$$

or equivalently,

$$q = (T_s - T_\infty) \int_{A_s} h \, dA_s$$

An important dimensionless parameter, Nusselt number, is the ratio of convective to conductive heat transfer across a boundary. Local Nusselt number is defined as

$$Nu_L = \frac{Convective\ heat\ transfer\ coefficient}{Conductive\ heat\ transfer\ coefficient} = \frac{hL}{k_f} \tag{C.8}$$

where h is the local convective heat transfer coefficient, L is the characteristic length, and k_f is the thermal conductivity. The Nusselt number ranges from about 1 for laminar flows, to much more than a hundred for turbulent flows.

C.2.4 Flow Conditions

For treating convection problems, it is essential to determine whether the boundary layer is laminar or turbulent, as the surface friction and the convection transfer rates strongly depend on which of these two conditions exists. Figure C-4 illustrates the formation of the boundary layer, showing both laminar and turbulent flow conditions as they are naturally developed under such conditions.

In the laminar boundary layer, the fluid flow is highly ordered and it is possible to identify streamlines along which fluid particles move. The transition zone is characterized by a conversion from laminar to turbulent conditions, and the flow condition within it alternates over time between being laminar and turbulent. The flow in the turbulent boundary layer is highly irregular and is characterised by random, three-dimensional motion of relatively large parcels of fluid. Due to the interactions of fluid particles, velocity and pressure fluctuations occur at any point within the turbulent boundary layer.

The turbulent boundary layer may further be subdivided along the height. The viscous sub layer is characterised by diffusion transport of fluid particles and a quasi-linear velocity profile. The buffer layer is characterised by both diffusion and turbulent mixing,

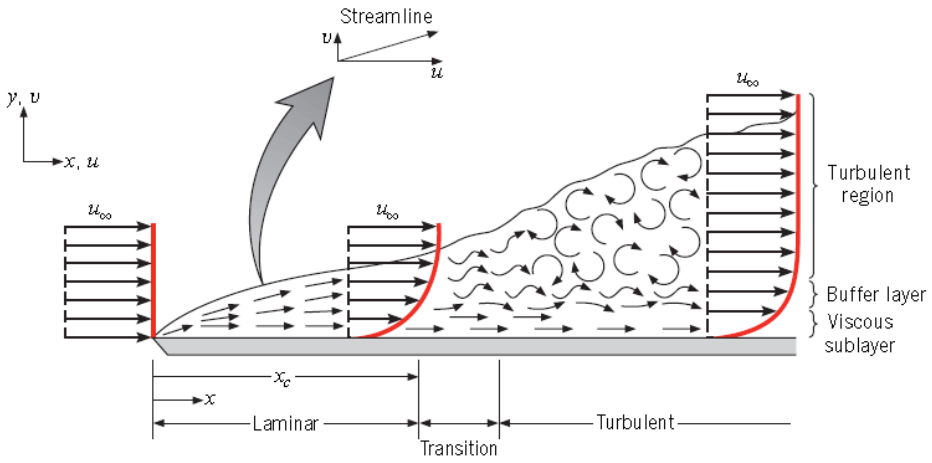

Figure C-4: Velocity boundary layer development on a flat plate. Source: [175]

while in the turbulent zone, the transport is dominated by turbulent mixing.

The transition from laminar to turbulent flow is ultimately due to triggering mechanisms (e.g. interaction of unsteady flow structures, disturbances, etc.). For forced convection (differing from natural convection described later), the transition can be predicted by a dimensionless group of parameters called the Reynolds number:

$$Re_x = \frac{\rho u_\infty \, x}{\mu} \tag{C.9}$$

where Re_x is the Reynolds number with the characteristic length of x (depending on the position on the surface), ρ is the fluid density, u_∞ is the velocity upstream of the plate, and μ is the dynamic viscosity of the fluid.

For example, the location of the transition can be estimated by solving for the critical value of x whereby Re_x is set to its critical value, $e_{x,c}$, a value which depends on topology of the problem (internal/external flows, curvature of the surface, etc.). For a flow over a flat plate it is known to vary from about 10^5 to 3×10^6, and is most often taken as 5×10^5 [175].

The significance of the flow regime can be illustrated by considering its impact on the local heat transfer coefficient, as seen in Figure C-5.

Similarly to the laminar velocity boundary layer, the turbulent region is also characterised by a growth of the thermal boundary layer along the streamwise direction, and a corresponding decrease of the temperature gradient at $y = 0$, resulting in a decreasing heat transfer coefficient. However, the transition region is characterised by a notable increase in the heat transfer coefficient, which can be attributed to the large temperature gradients at $y = 0$ caused by turbulent mixing.

This relationship can be useful in problems where the optimisation of the local heat transfer coefficient is the goal.

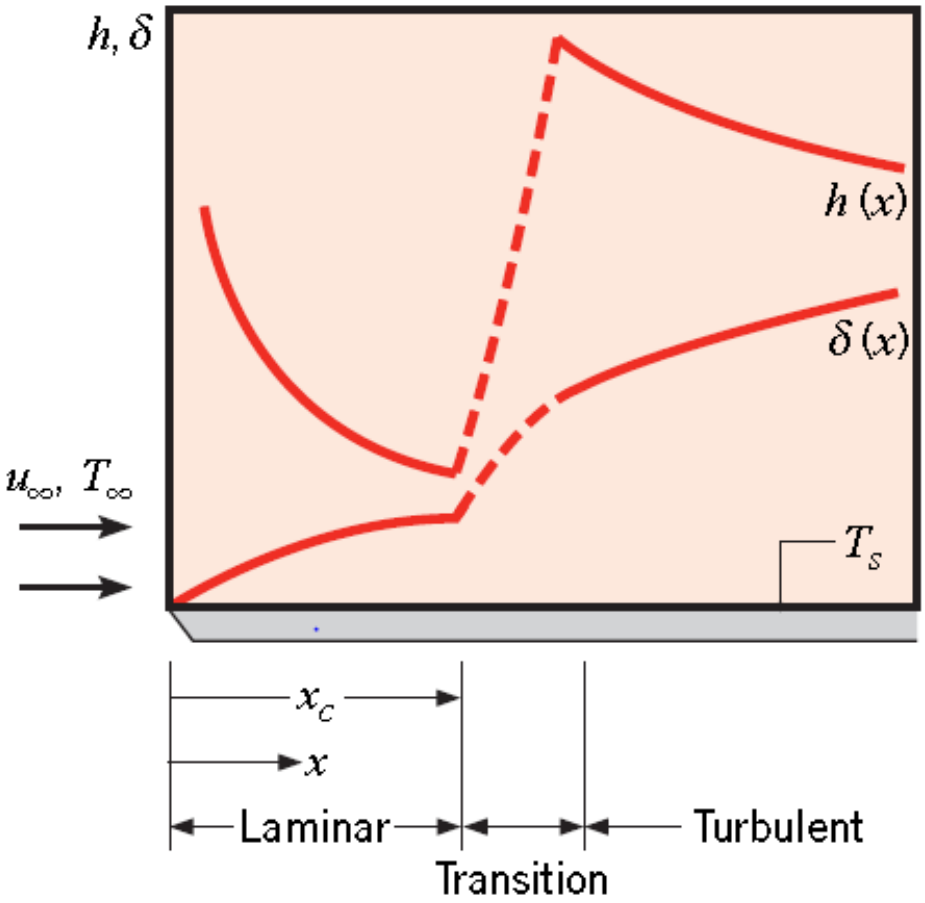

Figure C-5: Variation of velocity boundary layer thickness δ and the local heat transfer coefficient h for flow over an isothermal flat plate. Source: [175]

C.2.5 Free (Natural) Convection

Previously, we have considered convection in fluids that originates from an external forcing condition (e.g. wind or a fan). Free convection encompasses situations for which there is no forced velocity, yet convection currents exist within the fluid. Incropera et al. [175] define free convection as the buoyancy-driven flow, where the buoyancy force is the result of the combined presence of a fluid density gradient and a body force proportional to density. In our case (and in the most common case), the density gradient is caused by a temperature gradient (the fluid density generally decreases with increasing temperature), while the body force is due to the gravitational field. However, the body force can equally be a centrifugal force in rotating fluid machinery, or a Coriolis force in atmospheric and oceanic rotational motions. Natural convection flow in enclosures has many thermal engineering applications in a wide range of scales: from cooling solutions of radioactive waste containers, to crystal growth in liquids.

It should be noted that the presence of a fluid density gradient and a gravitational field

does not ensure the existence of convection currents. Consider Figure C-6, illustrating two cases of fluid enclosed by two large horizontal plates of different temperature. In

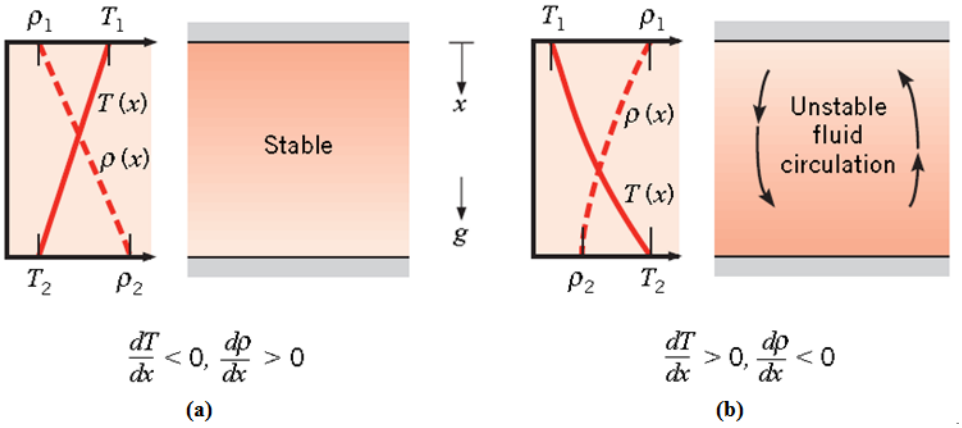

Figure C-6: Conditions in a fluid between large horizontal plates at different temperatures: (a) Stable temperature gradient, (b) Unstable temperature gradient. Source: [175]

case (a), the temperature of the upper plate is higher than the temperature of the lower plate, and the density increases in the direction of the gravitational force. This results in a stable condition, which is not characterised by bulk fluid motion.

In case (b), the temperature of the lower plate is higher than the temperature of the upper plate, and the density decreases in the direction of the gravitational force. If the temperature difference exceeds a critical value, conditions become unstable, and the buoyancy forces are able to overcome the retarding influence of viscous forces. The gravitational force acting on the denser fluid exceeds that of the lighter fluid (in the lower layers), and a circulation pattern forms.

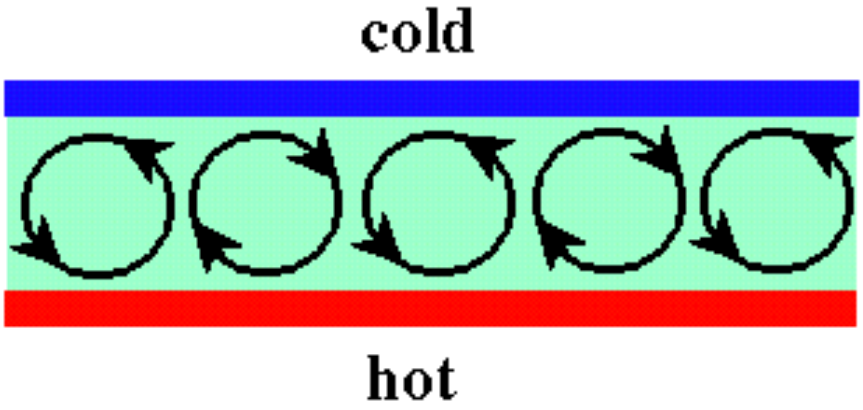

Figure C-7: Schematic of Rayleigh-Bénard convection. Source: [176]

This type of natural convection (occurring in a horizontal layer of fluid heated from below) is called Rayleigh-Bénard convection, and it results in a regular pattern of convective cells developing in the fluid, referred to as Bénard cells (see Figure C-7).

As for forced convection, the equations that describe momentum and energy transfer in free convection originate from the related conservation principles. The main difference between the two flows is that, in free convection, the flow is driven by buoyancy forces.

Consider a laminar boundary layer flow over a vertical plate, which is driven by buoyancy forces (see Figure C-8).

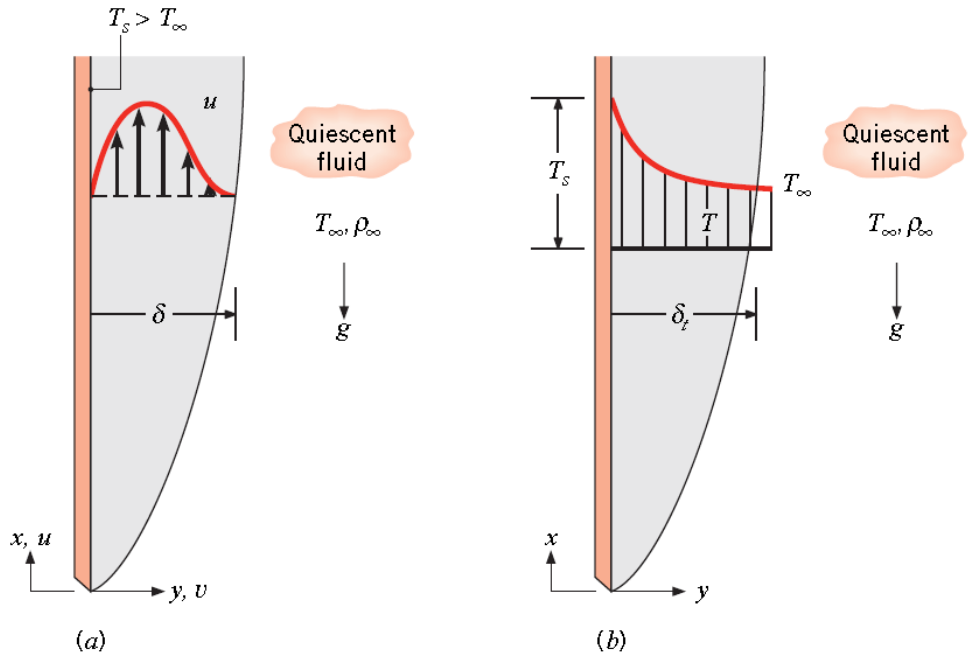

Figure C-8: Boundary layer development on a heated vertical plate: (a) Velocity boundary layer. (b) Thermal boundary layer. Source: [175]

Assume steady, two-dimensional, constant property conditions in which the gravity force acts in the negative-x (downward) direction. Free convection flows can nearly always be treated as if the fluid is incompressible, if an extra term is added to the momentum equation to account for the buoyancy force. Therefore, assume the fluid to be incompressible, while accounting for the effect of variable density only in the buoyancy force, since it is this variation that induces fluid motion. The x-momentum equation is then of the form:

$$u\frac{\partial u}{\partial x}+v\frac{\partial u}{\partial y}=-\frac{1}{\rho}\frac{dp_\infty}{dx}-g+\nu\frac{\partial^2 u}{\partial y^2} \tag{C.10}$$

where $\frac{dp_\infty}{dx}$ is the free stream (outside the boundary layer) pressure gradient. Since in this region $u = 0$, then:

$$\frac{dp_\infty}{dx}=-\rho_\infty\, g \tag{C.11}$$

Substituting Equation C.11 into Equation C.10 gives:

$$u\frac{\partial u}{\partial x}+v\frac{\partial u}{\partial y}=g\left(\frac{\rho_\infty-\rho}{\rho}\right)+\nu\frac{\partial^2 u}{\partial y^2} \tag{C.12}$$

The first term of the right-hand side of the above equation is the buoyancy force per unit mass, and flow originates because the density ρ is a variable. If density variations are due only to temperature variations, the term may be related to a fluid property known as the volumetric thermal expansion coefficient, β:

$$\beta = -\frac{1}{\rho}\left(\frac{\partial \rho}{\partial T}\right) \tag{C.13}$$

This coefficient is a thermodynamic property that provides a measure of density changes in response to a change in temperature (at constant pressure). If it is expressed in the following approximate form,

$$\beta \approx -\frac{1}{\rho}\frac{\rho_\infty - \rho}{T_\infty - T} \tag{C.14}$$

then it follows that

$$(\rho_\infty - \rho) \approx \rho\beta(T - T_\infty) \tag{C.15}$$

This simplification is known as the Boussinesq approximation. This simplification can be employed only in problems where the temperature and density variations are small ($< 2K$ for water, $< 20K$ for air [177]), and where the flow is non-reacting. When substituting Equation C.15 into Equation C.12, the x-momentum equation becomes

$$u\frac{\partial u}{\partial x} + v\frac{\partial u}{\partial y} = g\beta\,(T - T_\infty) + \nu\frac{\partial^2 u}{\partial y^2} \tag{C.16}$$

In summary, the set of governing equations for free convection, employing the Boussinesq approximation, is

$$\frac{\partial u}{\partial x} + \frac{\partial v}{\partial y} = 0 \tag{C.17}$$

$$u\frac{\partial u}{\partial x} + v\frac{\partial u}{\partial y} = g\beta\,(T - T_\infty) + \nu\frac{\partial^2 u}{\partial y^2} \tag{C.18}$$

$$u\frac{\partial T}{\partial x} + v\frac{\partial T}{\partial y} = \alpha\frac{\partial^2 T}{\partial y^2} \tag{C.19}$$

These equations are strongly coupled and must be solved simultaneously. It is important to note that free convection boundary layers are not restricted to laminar flow. As it is the case with forced convection, hydrodynamic instabilities may arise in free convection. In other words, disturbances within the flow may be amplified, leading to the transition from laminar to turbulent flow (see Figure C-9).

In forced convection, Reynolds number (ratio of inertial to viscous forces) is used to predict this transition. However, in free convection this transition depends on the relative magnitude of the buoyancy and viscous forces in the fluid, captured by the dimensionless

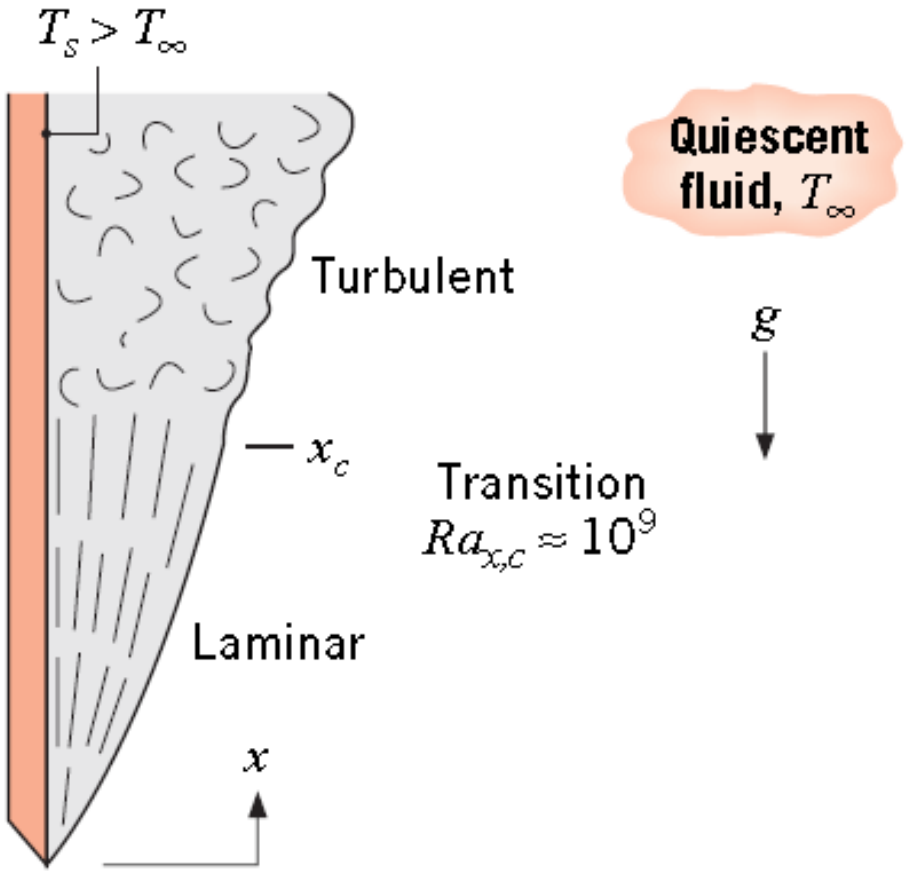

Figure C-9: Free convection boundary layer transition on a vertical plate. Source: [175]

parameter called the Grashof number:

$$Gr_L = \frac{g\beta\,(T_s - T_\infty)\,L^3}{\nu^2} \tag{C.20}$$

In free convection problems, it is customary to consider the Rayleigh number of the fluid, which is simply the product of the Grashof and Prandtl numbers:

$$Ra_L = Gr_L\ Pr = \frac{g\beta}{\nu\alpha}\ (T_s - T_\infty)\,L^3 \tag{C.21}$$

where L is the characteristic length.

Similarly to the forced flow, the location of the transition from laminar to turbulent conditions can be predicted by solving for L after setting Ra_L to its critical value, $Ra_{L,C} \approx 10^9$.

If the Rayleigh number of a system is increased beyond the critical value, a bifurcation is observed whereby multiple asymptotic mirror image solutions can be found, and where only asymmetric solutions are stable. The critical value of the Rayleigh number greatly depends on the geometry and the boundary conditions of the system. Furthermore, several types of bifurcation exist depending on the system geometry and the boundary con-

ditions. For example, there exist a HOPF bifurcation (found in the differentially heated cubic cavities), pitch-fork bifurcation (occurring in Rayleigh-Bénard configurations), etc.

C.2.6 Radiation

While heat transfer by conduction and convection requires the presence of a temperature gradient in some form of matter, heat transfer by thermal radiation requires no matter. Radiation is relevant to many applications, including industrial heating, cooling and drying processes, as well as energy conversion methods such as photovoltaics.

The solid, being at a higher temperature than its surroundings, cools until reaching an equilibrium with the surrounding temperature. The cooling is associated with a reduction in the internal energy stored by the solid and is a consequence of the emission of thermal radiation from the surface. The mechanism of emission is related to energy released as a result of oscillations of electrons that constitute matter. In turn, the surface will intercept and absorb radiation originating from its surroundings.

In fact, four distinct radiation fluxes can be defined at a surface [175] (refer to Figure C-10 for illustration):

1. Emissive power, E
2. Irradiation, G
3. Radiosity, J
4. Net radiative flux, $q_{rad}" = \ J - G$

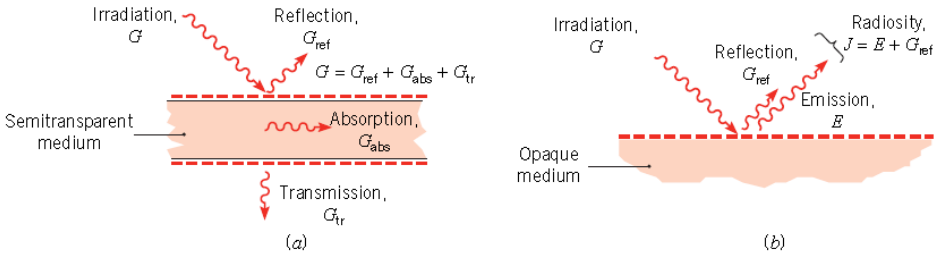

Figure C-10: Radiation at a surface. (a) Reflection, absorption, and transmission of irradiation for a semi-transparent medium. (b) The radiosity for an opaque medium. Source: [175]

The emissive power, E (W/m^2) is the rate at which radiation is emitted from a surface per unit area (over all wavelengths and in all directions). Emissive power can be found through the relation

$$E = \epsilon \sigma T_s^4 \tag{C.22}$$

where ϵ is a surface property known as the emissivity $(0 \leq \epsilon \leq 1)$, σ is the Stephan-Boltzmann constant (equal to $5.670373 \times 10^{-8}\ W/m^2K^4$), and T_s is the absolute temperature (in K).

The irradiation, G (W/m^2) is the rate at which radiation is incident upon the surface per unit area. Note that this radiation can originate from its surroundings (in the case of a temperature difference between the surface and the surroundings), or from an external source such as the sun or a laser.

When radiation is incident upon a semi-transparent medium, portions of the irradiation may be transmitted, absorbed or reflected. Transmission refers to radiation passing through the medium. Absorption occurs when radiation interacts with the medium, causing an increase in the internal thermal energy of the medium. Reflection is the process of incident radiation being redirected away from the surface, having no effect on the medium. If we define:

1. transmissivity τ as the fraction of the irradiation that is transmitted,
2. absorptivity, α as the fraction of the irradiation that is absorbed, and
3. reflectivity, ρ as the fraction of the irradiation that is reflected,

then, $\rho + \alpha + \tau = 1$ (Note, opaque media experience no transmission: $\tau = 0$).

The radiosity, J (W/m^2) of a surface sums up all the radiant energy leaving the surface, which for an opaque surface includes emission and the reflected portion of the irradiation, while for a semi-transparent medium includes the reflected portion of the irradiation, as well as the radiation transmitted through the medium from below (not shown in Figure C-10 above).

Finally, the net radiative flux from a surface, q_{rad}" (W/m^2) is simply the difference between outgoing and incoming radiation. The net radiative flux can be expressed in general form as

$$q_{rad}" = J - G \tag{C.23}$$

and for an opaque surface as

$$q_{rad}" = E + \rho G - G = \epsilon\sigma T_s^4 - \alpha G \tag{C.24}$$

It is important to note that radiation can deeply change the uniformity of the temperature of the PV panel as well as the mirror, having a big impact on the flow conditions within the cavity.

Bibliography

[1] U.S. Energy Information Administration. *Total Primary Energy Consumption*. 2016.

[2] World Resources Institute. *CAIT Climate Data Explorer*. 2015.

[3] *Climate change 2014: mitigation of climate change: Working Group III contribution to the Fifth Assessment Report of the Intergovernmental Panel on Climate Change*. Cambridge University Press, 2014. OCLC: ocn892580682.

[4] SolarPower Europe. Global market outlook for solar power 2016-2020, 2016.

[5] Marc Perez and Richard Perez. Update 2015–a fundamental look at supply side energy reserves for the planet. *IEA-SHCP-Newsletter*, 62, Nov 2015.

[6] REN21. *Renewables 2016 Global Status Report*. 2016.

[7] C. Breyer and A. Gerlach. Global overview on grid-parity event dynamics, 2010.

[8] Rob W. Andrews, Andrew Pollard, and Joshua M. Pearce. *Model of Loss Mechanisms for Low Optical Concentration on Solar Photovoltaic Arrays with Planar Reflectors*, page 0446–0453. Rayleigh NC, 2011.

[9] W. T. Xie, Y. J. Dai, R. Z. Wang, and K. Sumathy. Concentrated solar energy applications using Fresnel lenses: A review. *RENEWABLE & SUSTAINABLE ENERGY REVIEWS*, 15(6):2588–2606, AUG 2011.

[10] Johan Nilsson. *Optical Design and Characterization of Solar Concentrators for Photovoltaics*. 2005.

[11] Daniel Feuermann and Jeffrey M Gordon. High-concentration photovoltaic designs based on miniature parabolic dishes. *Solar Energy*, 70(5):423–430, 2001.

[12] Juan C. Miñano, Juan C. González, and Pablo Benítez. A high-gain, compact, nonimaging concentrator: Rxi. *Applied Optics*, 34(34):7850, Dec 1995.

[13] RALF LEUTZ, AKIO SUZUKI, ATSUSHI AKISAWA, and TAKAO KASHIWAGI. Design of a nonimaging fresnel lens for solar concentrators1. *Solar Energy*, 65(6):379–387, Apr 1999.

[14] Cristina Sierra and Alfonso J. Vazquez. High solar energy concentration with a fresnel lens. *Journal of Materials Science*, 40(6):1339–1343, Mar 2005.

[15] SHARP. Press releases. `http://sharp-world.com/corporate/news/130614.html`, June 2013.

[16] NREL. Best research-cell efficiencies. `http://www.nrel.gov/ncpv/images/efficiency_chart.jpg`, June 2016.

[17] Joe S. Coventry. Performance of a concentrating photovoltaic/thermal solar collector. *Solar Energy*, 78(2):211–222, Feb 2005.

[18] G. Sala, J. C. Arboiro, A. Luque, J. C. Zamorano, J. C. Minano, C. Dramsch, T. Bruton, and D. Cunningham. *The EUCLIDES prototype: An efficient parabolic trough for PV concentration*, page 1207–1210. May 1996.

[19] M. F. Piszczor, M. J. O'Neill, and L. M. Fraas. *A novel space photovoltaic module using a linear Fresnel lens and a line-focus tandem cell receiver*, page 1386–1391. May 1993.

[20] Rob W. Andrews, Andrew Pollard, and Joshua M. Pearce. *Photovoltaic System Performance Enhancement With Non-Tracking Planar Concentrators: Experimental Results and BDRF Based Modelling*, page 0229–0234. IEEE, 2013.

[21] B. Karlsson and G. Wilson. *MaReCo—a large asymmetric CPC for high latitudes*. 1999.

[22] T.K. Mallick, P.C. Eames, T.J. Hyde, and B. Norton. The design and experimental characterisation of an asymmetric compound parabolic photovoltaic concentrator for building façade integration in the uk. *Solar Energy*, 77(3):319–327, Sep 2004.

[23] Hasan Baig, Nabin Sarmah, Keith C. Heasman, and Tapas K. Mallick. Numerical modelling and experimental validation of a low concentrating photovoltaic system. *Solar Energy Materials and Solar Cells*, 113:201–219, Jun 2013.

[24] K. G. T. Hollands. A concentrator for thin-film solar cells. *Solar Energy*, 13(2):149–163, May 1971.

[25] Jeff Freilich and J. M. Gordon. Case study of a central-station grid-intertie photovoltaic system with v-trough concentration. *Solar Energy*, 46(5):267–273, 1991.

[26] Naum Fraidenraich. Analytic solutions for the optical properties of v-trough concentrators. *Applied Optics*, 31(1):131–139, Jan 1992.

[27] M. A. Mosalam Shaltout, A. Ghettas, and M. Sabry. V-trough concentrator on a photovoltaic full tracking system in a hot desert climate. *Renewable Energy*, 6(5–6):527–532, Jul 1995.

[28] N. Fraidenraich. Design procedure of v-trough cavities for photovoltaic systems. *Progress in Photovoltaics: Research and Applications*, 6(1):43–54, Jan 1998.

[29] F. Reis, M.C. Brito, V. Corregidor, J. Wemans, and G. Sorasio. Modeling the performance of low concentration photovoltaic systems. *Solar Energy Materials and Solar Cells*, 94(7):1222–1226, Jul 2010.

[30] G. E. Ahmad and H. M. S. Hussein. Comparative study of pv modules with and without a tilted plane reflector. *Energy conversion and management*, 42(11):1327–1333, 2001.

[31] M. Aziz-ul Huq, M. I. Hossain, and M. M. Rahman. *Effect of flat reflectors on the performance of photovoltaic modules*, volume 1, page 161–168 vol.1. IEEE, 2000.

[32] Joseph W. Bollentin and Richard D. Wilk. Modeling the solar irradiation on flat plate collectors augmented with planar reflectors. *Solar Energy*, 55(5):343–354, Nov 1995.

[33] Lars Broman. *Non-Imaging Solar Concentrators With Flat Mirrors*, volume 0441, page 102–109. 1984.

[34] Kok-Keong Chong, Chee-Woon Wong, Fei-Lu Siaw, and Tiong-Keat Yew. *Solar flux distribution analysis of Non-Imaging Planar Concentrator for the application in concentrator photovoltaic system*, page 003013–003018. Jun 2010.

[35] Miguel García, Luis Marroyo, Eduardo Lorenzo, and Miguel Pérez. Experimental energy yield in $1 \cdot 5 \times$ and $2 \times$ pv concentrators with conventional modules. *Progress in Photovoltaics: Research and Applications*, 16(3):261–270, May 2008.

[36] Stuart L. Grassie and Norman R. Sheridan. The use of planar reflectors for increasing the energy yield of flat-plate collectors. *Solar Energy*, 19(6):663–668, 1977.

[37] D. P. Grimmer, K. G. Zinn, K. C. Herr, and B. E. Wood. Augmented solar energy collection using different types of planar reflective surfaces; theoretical calculations and experimental results. *Solar energy*, 21(6):497–501, 1978.

[38] H. M. S. Hussein, G. E. Ahmad, and M. A. Mohamad. Optimization of operational and design parameters of plane reflector-tilted flat plate solar collector systems. *Energy*, 25(6):529–542, Jun 2000.

[39] Ljiljana T. Kostic and Zoran T. Pavlovic. Optimal position of flat plate reflectors of solar thermal collector. *Energy and Buildings*, 45:161–168, Feb 2012.

[40] D. C. Larson. Optimization of flat-plate collector-flat mirror systems. *Solar Energy*, 24(2):203–207, 1980.

[41] Toshio Matsushima, Tatsuyuki Setaka, and Seiichi Muroyama. Concentrating solar module with horizontal reflectors. *Solar energy materials and solar cells*, 75(3):603–612, 2003.

[42] D. K. McDaniels, D. H. Lowndes, H. Mathew, J. Reynolds, and R. Gray. Enhanced solar energy collection using reflector-solar thermal collector combinations. *Solar Energy*, 17(5):277–283, Nov 1975.

[43] Bengt Perers. *Optical modelling of solar collectors and booster reflectors under non stationary conditions: application for collector testing, system simulation and evaluation*. PhD thesis, Uppsala University, 1995.

[44] Bengt Perers and Björn Karlsson. External reflectors for large solar collector arrays, simulation model and experimental results. *Solar Energy*, 51(5):327–337, 1993.

[45] M. D. J. Pucar and A. R. Despic. The enhancement of energy gain of solar collectors and photovoltaic panels by the reflection of solar beams. *Energy*, 27(3):205–223, 2002.

[46] F. Reis, M.C. Brito, V. Corregidor, J. Wemans, and G. Sorasio. Modeling the performance of low concentration photovoltaic systems. *Solar Energy Materials and Solar Cells*, 94(7):1222–1226, Jul 2010.

[47] M. Ronnelid, B. Karlsson, P. Krohn, and J. Wennerberg. Booster reflectors for pv modules in sweden. *Progress in Photovoltaics: Research and Applications*, 8(3):279–291, May 2000.

[48] Steven C. Seitel. Collector performance enhancement with flat reflectors. *Solar Energy*, 17(5):291–295, Nov 1975.

[49] R. Soler-Bientz, F. Gomez-Castro, and L. Omar-Ricalde. *Preliminary results of a computational tool to model low concentration PV modules*, page 002779–002784. Jun 2010.

[50] H. Tabaei and M. Ameri. The effect of booster reflectors on the photovoltaic water pumping system performance. *Journal of Solar Energy Engineering*, 134(1):014501, 2012.

[51] H. Tabor. Mirror boosters for solar collectors. *Solar Energy*, 10(3):111–118, Jul 1966.

[52] Hiroshi Tanaka. Solar thermal collector augmented by flat plate booster reflector: Optimum inclination of collector and reflector. *Applied Energy*, 88(4):1395–1404, Apr 2011.

[53] Johan Wennerberg, John Kessler, Jonas Hedström, Lars Stolt, Björn Karlsson, and Mats Rönnelid. Thin film pv modules for low-concentrating systems. *Solar Energy*, 69:243–255, 2001.

[54] Roland Winston, Joseph J. O'Gallagher, and Randy C. Gee. *Nonimaging solar concentrator with uniform irradiance*, volume 5529, page 237–239. 2004.

[55] Zoran T. Pavlović and Ljiljana T. Kostić. Variation of reflected radiation from all reflectors of a flat plate solar collector during a year. *Energy*, 80:75–84, Feb 2015.

[56] G.M. Tina and C. Ventura. Energy assessment of enhanced fixed low concentration photovoltaic systems. *Solar Energy*, 119:68–82, Sep 2015.

[57] H. F. Chiam. Stationary reflector-augmented flat-plate collectors. *Solar Energy*, 29(1):65–69, 1982.

[58] D. Faiman and A. Zemel. Low-profile solar water heaters: The mirror booster problem revisited. *Solar Energy*, 40(4):385–390, 1988.

[59] J.I. Rosell, X. Vallverdú, M.A. Lechón, and M. Ibáñez. Design and simulation of a low concentrating photovoltaic/thermal system. *Energy Conversion and Management*, 46(18-19):3034–3046, Nov 2005.

[60] Stefan Hessa and Vic Hanbyb. *Stationary Booster Reflectors for Solar Thermal Process Heat Generation.* 3rd Southern African Solar Energy Conference, South Africa, 11-13 May, 2015., 2015.

[61] tenKsolar. tenksolar home page. http://www.tenksolar.com, 2013.

[62] 3M. 3m films. http://solutions.3m.com/wps/portal/3M/en_US/Renewable/Energy/Product/Films/, 2016.

[63] Spectrolab. *CDO-100 Concentrator Photovoltaic Cell Datasheet*. Apr 2008.

[64] E. Skoplaki and J. A. Palyvos. On the temperature dependence of photovoltaic module electrical performance: A review of efficiency/power correlations. *SOLAR ENERGY*, 83(5):614–624, MAY 2009.

[65] M. Rosa-Clot, R. Rosa-Clot, G. M. Tina, and P. F. Scandura. Submerged photovoltaic solar panel: SP2. *RENEWABLE ENERGY*, 35(8):1862–1865, AUG 2010.

[66] H. Bahaidarah, Abdul Subhan, P. Gandhidasan, and S. Rehman. Performance evaluation of a PV (photovoltaic) module by back surface water cooling for hot climatic conditions. *ENERGY*, 59:445–453, SEP 15 2013.

[67] Erzat Erdil, Mustafa Ilkan, and Fuat Egelioglu. An experimental study on energy generation with a photovoltaic (PV) - solar thermal hybrid system. *ENERGY*, 33(8):1241–1245, AUG 2008.

[68] M Sabry, R Gottschalg, TR Betts, MAM Shaltout, AF Hassan, MM El-Nicklawy, and DG Infield. Optical filtering of solar radiation to increase performance of concentrator systems. In *CONFERENCE RECORD OF THE TWENTY-NINTH IEEE PHOTOVOLTAIC SPECIALISTS CONFERENCE 2002*, pages 1588–1591, 345 E 47TH ST, NEW YORK, NY 10017 USA, 2002. IEEE Electron Devices Soc, IEEE. 29th IEEE Photovoltaic Specialists Conference, NEW ORLEANS, LA, MAY 19-24, 2002.

[69] J. A. Duffie and W. A. Beckman. *Solar Energy Thermal Processes*. John Wiley & Sons, 1974.

[70] P. I. Cooper. The absorption of radiation in solar stills. *Solar Energy*, 12(3):333–346, Jan 1969.

[71] V. Bourdin. Master physique et ingéniérie de l'energie. http://perso.limsi.fr/bourdin/master/Calculs_astronomiques_simples.pdf, 2013.

[72] Bureau des Longitudes. Astronomical data. http://www.imcce.fr/en/presentation/bdl.php, 2013.

[73] Marius Grundmann. *The Physics of Semiconductors*. Graduate Texts in Physics. Springer Berlin Heidelberg, 2010.

[74] D. L. Evans. Simplified method for predicting photovoltaic array output. *Solar energy*, 27(6):555–560, 1981.

[75] Fraunhofer ISE. *Photovoltaics Report 11/03/2016*. Nov 2016.

[76] NREL. Nrel pv cell efficiency chart, May 2016.

[77] V. Perraki. Temperature dependence on the photovoltaic properties of selected thin-film modules. *International Journal of Renewable and Sustainable Energy*, 2(4):140, 2013.

[78] Jinlei Ding, Xiaofang Cheng, and Tairan Fu. Analysis of series resistance and p-t characteristics of the solar cell. *Vacuum*, 77(2):163–167, Jan 2005.

[79] S. Bensalem and M. Chegaar. Thermal behavior of parasitic resistances of polycrystalline silicon solar cells. *Revue des Energies Renouvelables*, 16(1):171–176, 2013.

[80] Nicolas Barth, Raka Jovanovic, Said Ahzi, and Mohammad A. Khaleel. Pv panel single and double diode models: Optimization of the parameters and temperature dependence. *Solar Energy Materials and Solar Cells*, 148:87–98, Apr 2016.

[81] Ibrahim Reda and Afshin Andreas. Solar position algorithm for solar radiation applications. *Solar Energy*, 76(5):577–589, 2004.

[82] Richard Perez, R. Stewart, R. Seals, and T. Guertin. *The development and verification of the Perez diffuse radiation model*. 1988.

[83] Richard Perez, Pierre Ineichen, Robert Seals, Joseph Michalsky, and Ronald Stewart. Modeling daylight availability and irradiance components from direct and global irradiance. *Solar energy*, 44(5):271–289, 1990.

[84] Damien Buie, C. J. Dey, and S. Bosi. The effective size of the solar cone for solar concentrating systems. *Solar Energy*, 74(5):417–427, 2003.

[85] Daniel Buie, A. G. Monger, and C. J. Dey. Sunshape distributions for terrestrial solar simulations. *Solar Energy*, 74(2):113–122, 2003.

[86] D. Buie and A.G. Monger. The effect of circumsolar radiation on a solar concentrating system. *Solar Energy*, 76(1-3):181–185, Jan 2004.

[87] Yehia Eissa, Philippe Blanc, Armel Oumbe, Hosni Ghedira, and Lucien Wald. Estimation of the circumsolar ratio in a turbid atmosphere. *Energy Procedia*, 57:1169–1178, 2014.

[88] P. Blanc, B. Espinar, N. Geuder, C. Gueymard, R. Meyer, R. Pitz-Paal, B. Reinhardt, D. Renné, M. Sengupta, L. Wald, and et al. Direct normal irradiance related definitions and applications: The circumsolar issue. *Solar Energy*, 110:561–577, Dec 2014.

[89] Christoph Marty and Rolf Philipona. The clear-sky index to separate clear-sky from cloudy-sky situations in climate research. *Geophysical Research Letters*, 27(17):2649–2652, Sep 2000.

[90] Marco Bortolini, Mauro Gamberi, Alessandro Graziani, Riccardo Manzini, and Cristina Mora. Multi-location model for the estimation of the horizontal daily diffuse fraction of solar radiation in europe. *Energy Conversion and Management*, 67:208–216, Mar 2013.

[91] Byung O Kang and Kwa-Sur Tam. A new characterization and classification method for daily sky conditions based on ground-based solar irradiance measurement data. *Solar Energy*, 94:102–118, Aug 2013.

[92] J. Adnot, B. Bourges, D. Campana, and R Gicquel. Utilisation des courbes de frequence cumulees pour le calcul des installation solaires. *Analise Statistique des Processus Meteorologiques Appliquee a l'Energie Solaire*, page 9–40, 1979.

[93] Charles N. Long and Thomas P. Ackerman. Identification of clear skies from broadband pyranometer measurements and calculation of downwelling shortwave cloud effects. *Journal of Geophysical Research: Atmospheres*, 105(D12):15609–15626, Jun 2000.

[94] Fritz Kasten and Andrew T. Young. Revised optical air mass tables and approximation formula. *Applied optics*, 28(22):4735–4738, 1989.

[95] M. Lefèvre, A. Oumbe, P. Blanc, B. Espinar, B. Gschwind, Z. Qu, L. Wald, M. Schroedter-Homscheidt, C. Hoyer-Klick, A. Arola, and et al. Mcclear: a new model estimating downwelling solar radiation at ground level in clear-sky conditions. *Atmos. Meas. Tech.*, 6(9):2403–2418, Sep 2013.

[96] Yang Dazhi, Panida Jirutitijaroen, and Wilfred M. Walsh. The estimation of clear sky global horizontal irradiance at the equator. *Energy Procedia*, 25:141–148, 2012.

[97] Hoyt C. Hottel. A simple model for estimating the transmittance of direct solar radiation through clear atmospheres. *Solar Energy*, 18(2):129–134, 1976.

[98] Z. Qu, B. Gschwind, M. Lefevre, and L. Wald. Improving helioclim-3 estimates of surface solar irradiance using the mcclear clear-sky model and recent advances in atmosphere composition. *Atmos. Meas. Tech.*, 7(11):3927–3933, Nov 2014.

[99] Kenneth E. Torrance and Ephraim M. Sparrow. Theory for off-specular reflection from roughened surfaces. *JOSA*, 57(9):1105–1112, 1967.

[100] Xiao D. He, Kenneth E. Torrance, François X. Sillion, and Donald P. Greenberg. *A Comprehensive Physical Model for Light Reflection*, page 175–186. SIGGRAPH '91. ACM, 1991.

[101] C. Schlick. *An inexpensive BRDF model for physically-based rendering*, volume 13. Jan 1994. 13.

[102] S. Krauter and R. Hanitsch. Actual optical and thermal performance of pv-modules. *Solar Energy Materials and Solar Cells*, 41–42:557–574, Jun 1996.

[103] D.L. King, J.A. Kratochvil, and W.E. Boyson. *Measuring solar spectral and angle-of-incidence effects on photovoltaic modules and solar irradiance sensors*, page 1113–1116. Sep 1997.

[104] Kristin J. Dana, Bram van Ginneken, Shree K. Nayar, and Jan J. Koenderink. Reflectance and texture of real-world surfaces. *ACM Trans. Graph.*, 18(1):1–34, Jan 1999.

[105] N. Martin and J. M. Ruiz. Calculation of the pv modules angular losses under field conditions by means of an analytical model. *Solar Energy Materials and Solar Cells*, 70(1):25–38, Dec 2001.

[106] C. E. Kennedy and K. Terwilliger. Optical durability of candidate solar reflectors. *Journal of Solar Energy Engineering*, 127(2):262, 2005.

[107] Rob W. Andrews and Joshua M. Pearce. The effect of spectral albedo on amorphous silicon and crystalline silicon solar photovoltaic device performance. *Solar Energy*, 91:233–241, May 2013.

[108] P. Hoang, V. Bourdin, Q. Liu, G. Caruso, and V. Archambault. Coupling optical and thermal models to accurately predict pv panel electricity production. *Solar Energy Materials and Solar Cells*, 125:325–338, Jun 2014.

[109] Marko Topič, Martin Sever, Benjamin Lipovšek, Andrej Čampa, and Janez Krč. Approaches and challenges in optical modelling and simulation of thin-film solar cells. *Solar Energy Materials and Solar Cells*, Oct 2014.

[110] Chee Woon Wong, Kok-Keong Chong, Ming Hui Tan, Tiong-Keat Yew, and Woei-Chong Tan. *Flux Distribution Analysis of Non-Imaging Planar Concentrator Considering Effects of Circumsolar Radiation and Mirror Slope Error*, page RW4B.2. OSA Technical Digest (online). Optical Society of America, Dec 2014.

[111] I. R. Cole and R. Gottschalg. Optical modelling for concentrating photovoltaic systems: insolation transfer variations with solar source descriptions. *IET Renewable Power Generation*, 9(5):412–419, 2015.

[112] Emeric Tapaches. *Estimation du Potentiel de la Technologie Solaire Thermodynamique à Concentration en Climat Non Désertique - Application à La Réunion.* PhD thesis, Université de La Réunion, Apr 2015.

[113] M. N. Polyanskiy. Refractive index database. 2014.

[114] Jeffrey L. Taylor. Reflectance measurements of materials used in the solar industry. *PerkinElmer Technical Note*, 2009.

[115] Hemant Kumar Raut, V. Anand Ganesh, A. Sreekumaran Nair, and Seeram Ramakrishna. Anti-reflective coatings: A critical, in-depth review. *Energy & Environmental Science*, 4(10):3779, 2011.

[116] David C. Miller, Michael D. Kempe, Cheryl E. Kennedy, and Sarah R. Kurtz. Analysis of transmitted optical spectrum enabling accelerated testing of multijunction concentrating photovoltaic designs. *Optical Engineering*, 50(1):13003–13003–17, 2011.

[117] H. Hottel and B. Woertz. Performance of flat-plate solar-heat collectors. *Trans. ASME (Am. Soc. Mech. Eng.); (United States)*, 64, Jan 1942.

[118] Nicholas Metropolis and S. Ulam. The monte carlo method. *Journal of the American Statistical Association*, 44(247):335–341, Sep 1949.

[119] William L. Dunn and J. Kenneth Shultis. *Exploring Monte Carlo Methods*. Elsevier, 2011.

[120] J. C. Daly. Solar concentrator flux distributions using backward ray tracing. *Applied Optics*, 18(15):2696–2699, 1979.

[121] Gregory J. Ward, Francis M. Rubinstein, and Robert D. Clear. A ray tracing solution for diffuse interreflection. *ACM SIGGRAPH Computer Graphics*, 22(4):85–92, 1988.

[122] Chi-Feng Chen, Chih-Hao Lin, Huang-Tzung Jan, and Yun-Ling Yang. Design of a solar concentrator combining paraboloidal and hyperbolic mirrors using ray tracing method. *Optics Communications*, 282(3):360–366, Feb 2009.

[123] Tim Wendelin. Soltrace: A new optical modeling tool for concentrating solar optics. page 253–260, Jan 2003.

[124] J. P. Roccia, B. Piaud, C. Coustet, C. Caliot, E. Guillot, G. Flamant, and J. Delatorre. Solfast, a ray-tracing monte-carlo software for solar concentrating facilities. *Journal of Physics: Conference Series*, 369(1):12029, 2012.

[125] Manuel J. Blanco. *Tonatiuh: An object oriented, distributed computing, Monte-Carlo ray tracer for the design and simulation of solar concentrating systems*. Citeseer, 2016.

[126] J. Delatorre, G. Baud, J. J. Bézian, S. Blanco, C. Caliot, J. F. Cornet, C. Coustet, J. Dauchet, M. El Hafi, V. Eymet, and et al. Monte carlo advances and concentrated solar applications. *Solar Energy*, 103:653–681, May 2014.

[127] Donald Grether, Jerry Nelson, and Michael Wahlig. *Measurement Of Circumsolar Radiation*, volume 0068, page 41–48. 1976.

[128] E. Skoplaki and J.A. Palyvos. On the temperature dependence of photovoltaic module electrical performance: A review of efficiency/power correlations. *Solar Energy*, 83(5):614–624, May 2009.

[129] CEA. Influence of temperature on photovoltaic module efficiency. page 119, 2004.

[130] Jens Merten, J. M. Asensi, C. Voz, A. V. Shah, R. Platz, and J. Andreu. Improved equivalent circuit and analytical model for amorphous silicon solar cells and modules. *Electron Devices, IEEE Transactions on*, 45(2):423–429, 1998.

[131] W. Herrmann, M. Adrian, W. Wiesner, and TÜV Rheinland. *Operational behaviour of commercial solar cells under reverse biased conditions*, page 2357–2359. Citeseer, 1998.

[132] J. W. Bishop. Computer simulation of the effects of electrical mismatches in photovoltaic cell interconnection circuits. *Solar Cells*, 25(1):73–89, Oct 1988.

[133] D. L. King, J. K. Dudley, and W. E. Boyson. *PVSIMC: a simulation program for photovoltaic cells, modules, and arrays*, page 1295–1297. IEEE, May 1996.

[134] MathWorks. `http://www.mathworks.com/products/simulink/`, 2016.

[135] http://bwrcs.eecs.berkeley.edu/Classes/IcBook/SPICE/, 1972.

[136] http://www.orcad.com/products/orcad-pspice-designer/overview, 2016.

[137] http://cds.linear.com/docs/en/software-and-simulation/LTspiceGettingStartedGuide.pdf, 2016.

[138] http://ngspice.sourceforge.net/, 2016.

[139] F. Fertig, S. Rein, M. C. Schubert, and W. Warta. Impact of junction breakdown in multi-crystalline silicon solar cells on hot spot formation and module performance. *26th European Photovoltaic Solar Energy Conference and Exhibition*, page 1168–1178, Oct 2011.

[140] Sanjaykumar J. Patel, Ashish K. Panchal, and Vipul Kheraj. Extraction of solar cell parameters from a single current–voltage characteristic using teaching learning based optimization algorithm. *Applied Energy*, 119:384–393, Apr 2014.

[141] David L. King, Jay A. Kratochvil, and William Earl Boyson. *Photovoltaic array performance model*. United States. Department of Energy, 2004.

[142] David Faiman. Assessing the outdoor operating temperature of photovoltaic modules. *Progress in Photovoltaics: Research and Applications*, 16(4):307–315, Jun 2008.

[143] A. Virtuani, D. Pavanello, and G. Friesen. *Overview of temperature coefficients of different thin film photovoltaic technologies*, page 6–10. 2010.

[144] David L. King, Jay A. Kratochvil, and William E. Boyson. *Temperature coefficients for PV modules and arrays: measurement methods, difficulties, and results*, page 1183–1186. IEEE, 1997.

[145] Pankaj Yadav, Brijesh Tripathi, Kavita Pandey, and Manoj Kumar. Effect of varying concentration and temperature on steady and dynamic parameters of low concentration photovoltaic energy system. *International Journal of Electrical Power & Energy Systems*, 61:101–110, Oct 2014.

[146] T. Nordmann and L. Clavadetscher. *Understanding temperature effects on PV system performance*, volume 3, page 2243–2246 Vol.3. May 2003.

[147] Subhash Chander, A. Purohit, Anshu Sharma, Arvind, S. P. Nehra, and M. S. Dhaka. A study on photovoltaic parameters of mono-crystalline silicon solar cell with cell temperature. *Energy Reports*, 1:104–109, Nov 2015.

[148] Giuseppina Ciulla, Valerio Lo Brano, and Edoardo Moreci. Forecasting the cell temperature of pv modules with an adaptive system. *International Journal of Photoenergy*, 2013:1–10, 2013.

[149] C. Schwingshackl, M. Petitta, J.E. Wagner, G. Belluardo, D. Moser, M. Castelli, M. Zebisch, and A. Tetzlaff. Wind effect on pv module temperature: Analysis of different techniques for an accurate estimation. *Energy Procedia*, 40:77–86, 2013.

[150] Diego Torres-Lobera and Seppo Valkealahti. Inclusive dynamic thermal and electric simulation model of solar pv systems under varying atmospheric conditions. *Solar Energy*, 105:632–647, Jul 2014.

[151] Wagner Teixeira da Costa, Jussara Farias Fardin, Lauro de Vilhena B. Machado Neto, and Domingos Sávio Lyrio Simonetti. Estimation of irradiance and temperature using photovoltaic modules. *Solar Energy*, 110:132–138, Dec 2014.

[152] Tuza A. Olukan and Mahieddine Emziane. A comparative analysis of pv module temperature models. *Energy Procedia*, 62:694–703, 2014.

[153] Jurij Kurnik, Marko Jankovec, Kristijan Brecl, and Marko Topic. Outdoor testing of pv module temperature and performance under different mounting and operational conditions. *Solar Energy Materials and Solar Cells*, 95(1):373–376, Jan 2011.

[154] Diego Torres Lobera and Seppo Valkealahti. Dynamic thermal model of solar pv systems under varying climatic conditions. *Solar Energy*, 93:183–194, Jul 2013.

[155] Sharif Z. Aljoaba, Aaron M. Cramer, and Bruce L. Walcott. Thermoelectrical modeling of wavelength effects on photovoltaic module performance 2014;part i: Model. *IEEE Journal of Photovoltaics*, 3(3):1027–1033, Jul 2013.

[156] M. Mattei, G. Notton, C. Cristofari, M. Muselli, and P. Poggi. Calculation of the polycrystalline pv module temperature using a simple method of energy balance. *Renewable Energy*, 31(4):553–567, Apr 2006.

[157] E. Kaplani and S. Kaplanis. Thermal modelling and experimental assessment of the dependence of pv module temperature on wind velocity and direction, module orientation and inclination. *Solar Energy*, 107:443–460, Sep 2014.

[158] John K. Kaldellis, Marina Kapsali, and Kosmas A. Kavadias. Temperature and wind speed impact on the efficiency of pv installations. experience obtained from outdoor measurements in greece. *Renewable Energy*, 66:612–624, Jun 2014.

[159] Hui-Feng Tsai and Huan-Liang Tsai. Implementation and verification of integrated thermal and electrical models for commercial pv modules. *Solar Energy*, 86(1):654–665, Jan 2012.

[160] Malte R. Vogt, Hendrik Holst, Matthias Winter, Rolf Brendel, and Pietro P. Altermatt. Numerical modeling of c-si pv modules by coupling the semiconductor with the thermal conduction, convection and radiation equations. *Energy Procedia*, 77:215–224, Aug 2015.

[161] Yixian Lee and Andrew A.O. Tay. Finite element thermal analysis of a solar photovoltaic module. *Energy Procedia*, 15:413–420, 2012.

[162] Jicheng Zhou, Qiang Yi, Yunyun Wang, and Zhibin Ye. Temperature distribution of photovoltaic module based on finite element simulation. *Solar Energy*, 111:97–103, Jan 2015.

[163] G. Notton, C. Cristofari, M. Mattei, and P. Poggi. Modelling of a double-glass photovoltaic module using finite differences. *Applied Thermal Engineering*, 25(17–18):2854–2877, Dec 2005.

[164] A. D. Jones and C. P. Underwood. A thermal model for photovoltaic systems. *Solar energy*, 70(4):349–359, 2001.

[165] M. Montiel-Gonzalez, J.F. Hinojosa, H.I. Villafan-Vidales, A. Bautista-Orozco, and C.A. Estrada. Theoretical and experimental study of natural convection with surface thermal radiation in a side open cavity. *Applied Thermal Engineering*, 75:1176–1186, Jan 2015.

[166] Ionut-Razvan Caluianu and Florin Baltaretu. Thermal modelling of a photovoltaic module under variable free convection conditions. *Applied Thermal Engineering*, 33–34:86–91, Feb 2012.

[167] O.A. Tkachenko, V. Timchenko, S. Giroux-Julien, C. Ménézo, G.H. Yeoh, J.A. Reizes, E. Sanvicente, and M. Fossa. Numerical and experimental investigation of unsteady natural convection in a non-uniformly heated vertical open-ended channel. *International Journal of Thermal Sciences*, 99:9–25, Jan 2016.

[168] Jong Pil Kim, Ho Lim, Ju Hun Song, Young June Chang, and Chung Hwan Jeon. Numerical analysis on the thermal characteristics of photovoltaic module with ambient temperature variation. *Solar Energy Materials and Solar Cells*, 95(1):404–407, Jan 2011.

[169] S. Saravanan and C. Sivaraj. Coupled thermal radiation and natural convection heat transfer in a cavity with a heated plate inside. *International Journal of Heat and Fluid Flow*, 40:54–64, Apr 2013.

[170] M. Usama Siddiqui, A.F.M. Arif, Leah Kelley, and Steven Dubowsky. Three-dimensional thermal modeling of a photovoltaic module under varying conditions. *Solar Energy*, 86(9):2620–2631, Sep 2012.

[171] B. Moshfegh and M. Sandberg. Flow and heat transfer in the air gap behind photovoltaic panels. *Renewable and Sustainable Energy Reviews*, 2(3):287–301, Sep 1998.

[172] Markus Kottek, Jürgen Grieser, Christoph Beck, Bruno Rudolf, and Franz Rubel. World map of the köppen-geiger climate classification updated. *Meteorologische Zeitschrift*, 15(3):259–263, Jun 2006.

[173] The Weather Network. Statistics, 2015.

[174] Thomas A. Huld, Marcel Šúri, Ewan D. Dunlop, and Fabio Micale. Estimating average daytime and daily temperature profiles within europe. *Environmental Modelling and Software*, 21(12):1650–1661, Dec 2006.

[175] F. Incropera, D. Dewitt, T. Bergman, and A. Lavine. *Fundamentals of Heat and Mass Transfer, Seventh Edition*. John Wiley & Sons, 2011.

[176] University of Toronto Dept. of Physics. Rayleigh-bénard and bénard-marangoni convection. `http://www.physics.utoronto.ca/~nonlin/thermal.html`, 2013.

[177] Donald D. Gray and Aldo Giorgini. The validity of the boussinesq approximation for liquids and gases. *International Journal of Heat and Mass Transfer*, 19(5):545 – 551, 1976.

ÉCOLE DOCTORALE
Sciences mécaniques et énergétiques, matériaux et géosciences (SMEMAG)

Titre : Modélisation numérique du couplage thermique-photoélectrique pour des modules photovoltaïques sous faible concentration

Mots clés : modules photovoltaïques, faible concentration, réflecteurs plans, modélisation multiphysique, silicium amorphe, silicium polycristallin

Résumé : La faible exploitation de l'irradiation inter-rangée limite la production des modules photovoltaïques (PV). Le projet "Aleph" explore l'intérêt d'ajouter des réflecteurs plans entre les rangées pour augmenter la production, et dégage des règles claires permettant l'optimisation géométrique de l'ensemble.

Ce travail presente une modélisation multiphysique du système, des simulations numériques de son comportement, et la comparaison avec des données expérimentales. Deux technologies de module PV sont considérées : silicium amorphe (a-Si:H) et silicium polycristallin (p-Si). Les mesures montrent des gains énergétiques importants grâce aux réflecteurs. Les gains sont plus importants pour les modules a-Si:H que p-Si. La modélisation associe un modèle optique de lancers de rayons par méthode Monté-Carlo sous EDStaR, un modèle photoélectrique sous SPICE, et un modèle thermique empirique. Le modèle complet est calibré avec des données expérimentales en utilisant un algorithme évolutif. Une fois calibré, le modèle démontre une bonne performance en simulant la puissance générée par les modules en fonction des données atmosphériques et radiatives.

Title : Numerical modelling of the coupling of thermal and photoelectric effects for the photovoltaic modules under low concentration

Keywords : photovoltaic modules, low concentration, planar reflectors, multiphysics modelling, amorphous silicon, polycrystalline silicon

Abstract : The poor utilisation of the inter-row irradiation limits the production of photovoltaic (PV) modules. The "Aleph" project explores the potential of adding inter-row planar reflectors to increase the system yield, and defines clear rules for optimal settings of such systems in a given location and under a given climate.

This work presents a multiphysics model of the system, numerical simulations of its behaviour, and the comparison with experimental data. Two PV module technologies are tested: amorphous silicon (a-Si:H) and polycrystalline silicon (p-Si). The experimental data show significant gains in produced energy brought by the reflectors. The gains are higher for a-Si:H modules compared to p-Si. The modelling work combines a Monte-Carlo ray-tracing optical model (EDStaR), a photo-electric model (SPICE), and an empirical thermal model. The complete model is calibrated with measurements using an evolutionary algorithm. Once calibrated, the model demonstrates good performance in predicting the module power output as a function of atmospheric and irradiance data.

Université Paris-Saclay
Espace Technologique / Immeuble Discovery
Route de l'Orme aux Merisiers RD 128 / 91190 Saint-Aubin, France